Design, Construction and Control of a Large Quadrotor Micro Air Vehicle

Paul Edward Ian Pounds

September 2007

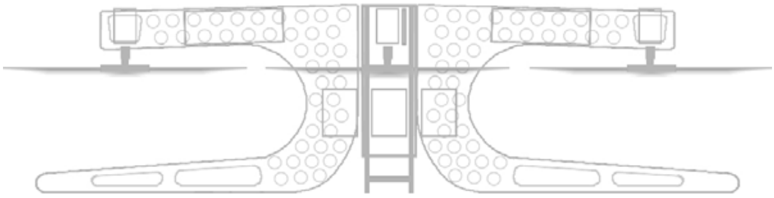

A thesis submitted for the degree of Doctor of Philosophy
of the Australian National University

THE AUSTRALIAN NATIONAL UNIVERSITY

Declaration

The work in this thesis is my own except where otherwise stated.

Paul Pounds

Dedication

For the past four years, I have been dogged by a single question. It was never far away - always on the lips of my friends and family, forever in my mind. This question haunted my days, kept me up at night and shadowed my every move.

“Does it fly?”

Without a doubt, the tenacity of this question played a pivotal role in my thesis. Its persistence and ubiquity beguiled me to go on and on, driving me to finish when I would have liked to have given up. I owe those people who voiced it gratitude for their support and motivation. So, I would like to thank you all by way of answering your question:

Yes. Yes, it does.

Acknowledgements

This thesis simply could not have happened without the help of my colleagues, many of whom I have come to regard as not just co-workers, but as friends.

Foremost thanks to my supervisor, Robert Mahony, for his constant support, friendly ear, helpful advice, paper editing skills and frequent trips to France. He's been invaluable in keeping me on the straight and true and preventing me from running off on pointless (yet fascinating) tangents.

Special thanks to the members of my supervisory panel and research partners — Peter Corke, Tarek Hamel and Jongyuk Kim — for fielding questions, explaining maths in detail, reviewing papers and keeping me motivated. Particular gratitude is owed to the CSIRO ICT Robotics group — Les Overs, Jonathan Roberts, and Stephen Brosnan — for their insight was a light in dark times when nothing would compile.

My philosophy is never to let IT, workshop or admin staff feel unappreciated — this pays dividends when you need parts made in a hurry, or someone to explain how to use a fax machine in time-critical circumstances. Also, IT staff are also a rich source of surly wisdom and discarded electrical equipment. Much thanks goes to Andrew Wilkinson, Helen Shelper, Pam Shakespeare, Deb Piotch, Ben Nash, Joel Gresham, and David Tyson-Smith.

Special appreciation is due Michael Eastwood for being my safety back-up during after-hours tests and keeping me sane.

Finally, I must thank my father and editor, Robert Pounds, for spending countless hours pouring over reams of incomprehensible text, before deftly scribing cryptic but precise editorial marks to turn my garble into meaningful prose.

Abstract

This thesis presents research directed towards the development of practical quadrotor robot helicopters. Most existing quadrotor robot vehicles have been based on consumer flying toys that do not offer the performance necessary to consider commercial applications. The Australian National University's 'X-4 Flyer' has been developed to investigate the enabling technologies essential for the next generation of larger (heavier than 2 kg or 1 m in length) quadrotor Unmanned Aerial Vehicles (UAV) capable of undertaking commercial tasks. It combines a custom-built chassis, rotors and avionics with off-the-shelf motors and batteries to provide a reliable experimental platform.

Several major challenges must be overcome to produce a successful, large quadrotor UAV: generation of sufficient lifting thrust with compact rotors, control of rotor dynamics associated with heavier rotor blades, and regulation of the unstable rigid body dynamics using low-cost sensors in a high-vibration environment. In this thesis, I provide solutions to these problems for the X-4 Flyer and demonstrate their effectiveness in operation.

I have developed a design for a complete micro air-vehicle thruster that combines fixed-pitch small-scale rotors and embedded control. This produces a mechanically simple, high-performance thruster with high reliability. The custom rotor design requires a balance between aerodynamic performance, blade rigidity and manufacturability. An iterative steady-state aeroelastic simulator is used for holistic blade design. The aerodynamic load disturbances of the rotor-motor system in normal conditions are experimentally characterised to produce performance metrics for system sensitivity. The motors require fast dynamic response for authorative vehicle flight control. I detail a dynamic compensator that achieves satisfactory closed-loop response time. The experimental rotor-motor plant displays satisfactory thrust performance and dynamic response.

Unlike typical quadrotors, the X-4 uses hinged rotors. By combining hinged rotors with the longitudinal flight dynamics of a helicopter, I develop a complete dynamic model, which includes often over-looked aerodynamic effects. It is shown that placement of the rotors close to the horizontal plane of the centre of mass produces favorable dynamic behaviour. From the fundamental limits of control, I use the Bode integral to identify the ideal mass and rotor configuration of the robot to simplify control design. A linear SISO controller is designed to regulate flyer attitude, and is demonstrated on a gimbal test rig.

Furthermore, commercially viable aerial robotic vehicles require low-cost attitude stabilisation systems that are robust to noise and sensor bias. A typical attitude stabilisation system consists of MEMs accelerometers, gyroscopes linked to separate attitude estimator, and attitude controller algorithms. I implement a non-linear attitude stabiliser for low-cost aerial robotic vehicles that combines attitude and bias estimation with control. The attitude control algorithm is based on a non-linear control Lyapunov function analysis derived directly in terms of the rigid-body attitude dynamics and measurement signals. The combined estimator-controller is shown to function in simulation, even in the presence of noise.

The flyer has successfully flown in the ANU Mechatronics test cage. It demonstrated $\pm 0.5^\circ$ attitude stability and hovered a short distance. The failure of a motor control board while on the ground halted testing before longer flights could be carried out. The X-4 has demonstrated commercially-viable attitude stabilisation precision, payload capacity and flight-time performance.

Contents

Nomenclature

List of Symbols

a	Airfoil polar lift slope
a_0	Airfoil polar lift slope operating point
a_0	Blade coning angle, rad
a	Nonlinear cross-coupling term
$\widehat{a}$	Nonlinear cross-coupling estimate
$\widetilde{a}$	Nonlinear cross-coupling error
a^y	Inertial gravity measurement vector
a_{1_s}	Longitudinal flapping angle, rad
$\overline{a}_{1_s}$	Longitudinal flapping angle due to translation, rad
A	Rotor disc area, m^2
A_1	First longitudinal blade feathering harmonic, rad
A_b	Blade area, m^2
$\mathcal{A}$	Body fixed frame
b	Amalgamated thrust coefficient, N/rad$\cdot$s^{-1}
b	Number of blades per rotor
b	Gyro sensor bias vector
$\widehat{b}$	Gyro sensor bias estimate
$\widetilde{b}$	Gyro sensor bias error
b_{1_s}	Lateral flapping angle, rad
$\overline{b}_{1_s}$	Lateral flapping angle due to translation, rad
B	Slew rate bound, units$\cdot$s^{-1}
B_1	First lateral blade feathering harmonic, rad
$\mathcal{B}$	Rotor fixed frame
c	Blade chord, m
c_{t}	Blade tip chord, m
c_d	Non-dimensionalised drag coefficient
c_l	Non-dimensionalised lift coefficient

c_m	Non-dimensionalised moment coefficient
C	Controller transfer function
C	Aeroelastic damping matrix
C_H	Non-dimensionalised H-force coefficient
C_T	Non-dimensionalised thrust coefficient
C_Q	Non-dimensionalised torque coefficient
d	Rotor arm length, m
d	Disturbance signal
D	Blade drag, N
D	Rotor displacement vector, m
D	Noise colour filter
e	Flapping hinge offset, m
e_{spring}	Sprung rotor hub virtual hinge offset, m
$e_{1,2,3}$	Local frame directions
$e_{x,y,z}$	Inertial frame directions
E	Global sensor cost
$E_{1,2,3}$	Local frame directions
$E_{x,y,z}$	Inertial frame directions
F	Force vector, N
$F(t)$	Aeroelastic driving load function, N
g	Acceleration due to gravity, $\mathrm{m{\cdot}s^{-2}}$
G	Shear modulus, Pa
G	Discretised plant transfer function
h	Height of rotor above CoG, m
H	Plant transfer function
i	Index
I	Electrical current, A
I	Rotational inertia matrix, $\mathrm{kgm^2}$
I_b	Blade rotational inertia, $\mathrm{kgm^2}$
I_R	Rotor rotational inertia, $\mathrm{kgm^2}$
$\mathcal{I}$	Inertial frame
J	Rotor to body fixed frame mapping matrix
k	Amalgamated torque coefficient, $\mathrm{Nm/rad{\cdot}s^{-1}}$
k	Gain
k_0	Hub spring stiffness, $\mathrm{Nm^{-1}}$
k_i	Sensor measurement weighting
k_a, k_b	Bias and cross-coupling estimation gains

k_R, k_e	Control gains
K	Glauert coefficient, ‘distortion factor’
K	Aeroelastic stiffness matrix, Nm^{-1}
L	Blade lift, N
L	Lyapunov function
$L(x)$	Laplace transform of x
m	Vehicle mass, kg
m^y	Inertial magnetometer measurement vector
M	Blade moment, Nm
M	Rotor flapping moment, Nm
M	Aeroelastic mass matrix, kg
M	Cost transformation matrix
M_0	Constant transformation matrix
M_A	Aerodynamic blade moment, Nm
M_b	Static blade moment, Nm
$M_{\mathrm{C.F.}}$	Blade flapping moment, Nm
M_M	Rotor flapping stiffness moment, Nm
$M(r)$	Twisting moment along the blade, Nm
M_{spring}	Sprung rotor stiffness moment, Nm
M_W	Rotor weight moment, Nm
p	Roll angular velocity, $\mathrm{rad{\cdot}s}^{-1}$
p	Unstable transfer function pole
p_{b}	Battery pole
p_{m}	Motor pole
P_i	Induced rotor power, W
$\mathbb{P}_a(A)$	Anti-symmetric part of matrix A
q	Pitch angular velocity, $\mathrm{rad{\cdot}s}^{-1}$
q	Torque factor
Q	Rotor torque, Nm
r	Blade radius station, m
r	Input reference signal
R	Rotor radius, m
R	Rotation matrix
$\widetilde{R}$	Orientation error matrix
R^d	Desired rotation matrix
R_{bat}	Battery internal resistance, Ω
s	Laplace transform of the differential operator

s_x, c_x	$\sin(x)$ and $\cos(x)$ shorthand
S	Sensitivity transfer function
T	Rotor thrust, N
u	Aeroelastic member displacement, m
u	Plant demand signal
u_{1_s}	Rotor local frame longitudinal flapping angle, rad
U_P	Rotor perpendicular flow velocity, ms^{-1}
U_T	Rotor tangential flow velocity, ms^{-1}
v_{1_s}	Rotor local frame lateral flapping angle, rad
v_i	Inflow velocity, ms^{-1}
V_r	Rotor velocity, ms^{-1}
v_l	Local inflow velocity, ms^{-1}
v_i	Sensor measurement direction vector
v_{0i}	Sensor measurement inertial direction vector
v^d	Desired sensor measurement
V	Velocity vector, ms^{-1}
V	Motor drive voltage, V
V	Lyapunov energy-like function
W	Laplace transform of $\delta\omega$
x	X displacement, m
X	Longitudinal position-pitch transfer function
X	Speed sensor transfer function
y	Y displacement, m
Y	Lateral position
z	z-Transform of unit delay operator
z	Z displacement, m
z_b	Battery zero
Z	Vertical position
α	Angle of attack, rad
α_s	Shaft tilt angle, rad
β	Blade flapping angle, rad
γ	Lock number
Γ	Applied torque vector
$\overline{\Gamma}$	Known torque parameters
ε	Back-EMF, V
ε	Innovation term
η	White noise signal

η	Euler angle vector, rad
θ	Pitch Euler angle, rad
θ	Geometric blade pitch angle, rad
θ_0	Linear blade twist geometric equivilent angle at rotor axis, rad
θ_1	Linear blade twist geometric washout angle, rad
θ_t	Ideal rotor twist blade geometric tip angle, rad
Θ	Laplace transform of θ
$\kappa(r)$	Strain angle, rad
λ	Motor flux-linkage coefficient
λ	Non-dimensionalised inflow ratio
μ	Rotor advance ratio
μ_r	Rotor advance ratio
μ_Ω	Gyro sensor noise vector
ξ	Position vector, m
ρ	Density of air, kg/m^3
σ	Rotor disc solidity ratio
$\tau(r)$	Applied torque, Nm
τ^d	Desired applied torque vector
ϕ	Roll Euler angle, rad
ϕ	Inflow angle, rad
ψ	Yaw Euler angle, rad
ψ	Azimuthal angle, rad
ψ_r	Rotor azimuthal direction of motion, rad
ω	Rotor angular velocity, rad·s^{-1}
ω_0	Rotor angular velocity at hover, rad·s^{-1}
Ω	Angular velocity vector, rad·s^{-1}
Ω^d	Desired angular velocity vector
Ω^y	Gyro sensor measurement vector
$\overline{\Omega}$	Biased noise-free gyro sensor measurement

List of Acronyms

ADC	Analog to Digital Converter
AoA	Angle of Attack, rad
BEM	Blade Element Method
BEMT	Blade Element Momentum Theory
C2S	CAN-to-Serial
CAN	Controller Area Network
CAT5	Catagory 5
C.F.	Centripedal Force
CFD	Computational Fluid Dynamics
CoG	Centre of Gravity
CON	Concatenated CAN
COS	CAN-over-Serial
COTS	Commercial-Off-the-Shelf
CNC	Computer Numerical Control
n-DoF	n Degrees of Freedom
DSP	Digital Signal Processor
EMF	Electro-Motive Force
F.M.	Figure of Merit
GPS	Global Positioning System
ID	System Identification
INS	Inertial Navigation System
IMU	Inertial Measurement Unit
LQ	Linear Quadratic
LSB	Least Significant Byte
MAV	Micro Air Vehicle
MEMS	Micro Electro-Mechanical System
MIMO	Multiple-Input Multiple-Output
MSB	Most Significant Byte
ODE	Ordinary Differential Equation
PD	Proportional-Derivative
PID	Proportional-Integral-Derivative
PSD	Power Spectral Density
PWM	Pulse Width Modulated
RC	Radio Control
R.D.	Routh's Discriminant

RE	Reynold's Number
RPV	Remote-Piloted Vehicle
SISO	Single-Input Single-Output
$SO(3)$	Special Orthogonal Group 3
SNR	Signal-to-Noise Ratio
SPI	Serial Peripheral Bus
UAV	Unmanned Aerial Vehicle
UGV	Unmanned Ground Vehicle
USB	Universal Serial Bus
VTOL	Vertical Take-Off and Landing

Chapter 1

Introduction

1.1 Why UAVs?

Unmanned Aerial Vehicles (UAVs) are autonomous or remotely piloted aircraft. They range in size from full-scale craft, similar to those flown by humans, to miniature aircraft centimeters in size. UAVs are driven by a variety of power plants, including petrol engines, gas turbines and electric motors. Both fixed-wing and rotorcraft UAVs have seen service.

The utility of UAVs in military applications is readily apparent — UAVs can potentially carry out the range of tasks normally executed by piloted aircraft without placing human pilots in jeopardy. However, these benefits also carry over to civilian aircraft that operate in hazardous conditions or require tedious or onerous piloting during lengthy operations. For example, unmanned aircraft could carry out power-line inspection in close proximity to live electrical cables, a task currently performed by manned aircraft [Golightly and Jones 2005]. Autonomous rotorcraft also have the potential to revolutionise commercial practice in a variety of fields such as mining, infrastructure and agriculture, which do not presently employ aircraft due to the size and expense of full-scale vehicles [Herwitz *et al* 2002].

Small-scale UAVs, or 'Micro Air Vehicles' (MAVs), expand the range of possible aero-robot duties further with their high portability and ability to operate in small spaces [Bouabdallah and Siegwart 2005a]. Recent advances in miniaturisation, battery and control technology have made very small rotorcraft possible.

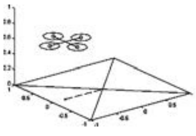

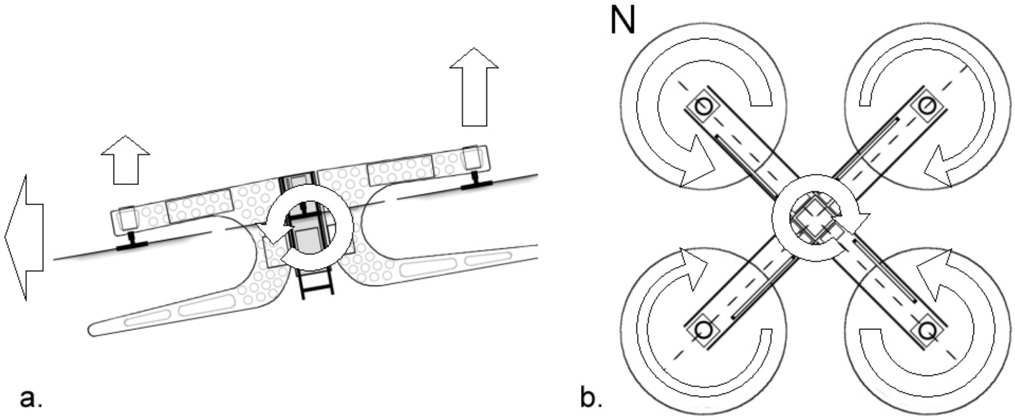

Figure 1.1: Quadrotor Rotor Directions and Motion.

1.2 Why Quadrotors?

Quadrotors are a special form of rotorcraft UAV that use two pairs of contra-rotating rotors to provide lift and directional control (indexed by ‘North’, ‘South’, ‘East’ and ‘West’). Unlike conventional helicopters, quadrotors typically have fixed-pitch blades and vary their thrust by changing rotor speed. Flight attitude is regulated entirely by rotor speed. To tilt the helicopter, the speed of one motor is increased and the opposite motor decreased — the difference in thrust causes the craft to pitch or roll. When the vehicle tilts, a component of the thrust is directed sideways and the aircraft translates horizontally (see Fig. 1.1).

Two major motivators for quadrotors are reliability and compactness — both are essential for a system that will be portable and useful in close proximity to people and structures in commercial applications. Conventional helicopters are mechanically very complex. They rely on a complex, adjustable mechanism that causes each blade to go through a complete pitch cycle each revolution of the rotor, providing attitude control of the rotor plane that, in turn, is used to control airframe attitude. The most common system used is a ‘swashplate’ structure that consists of two parallel moving bearings fixed on the rotor mast to transmit angular displacement to the pitch horns of the rotor blades (see Fig. 1.2). Small helicopters may further require a Bell-Hillier stabilizer linkage to slow the natural dynamic response of the rotor. Swashplates are sophisticated pieces of high-speed machinery operating in a vibrating environment and are highly prone to failure without constant maintenance. Failure of the swashplate causes catastrophic loss of cyclic control and, typically, destruction of the vehicle.

The inherent mechanical robustness of electric quadrotor helicopters stems

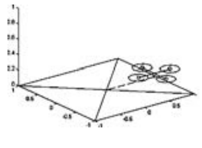

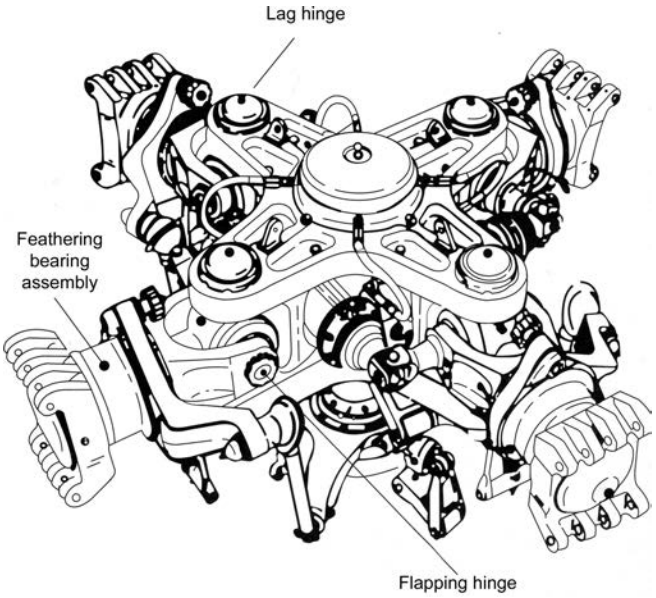

Figure 1.2: Full-Scale Helicopter Swashplate [Done and Balmford 2001].

from the simplicity of the rotor head. Without a complex swashplate, a direct-drive electric quadrotor may have only four moving parts — the rotors themselves. This has an almost negligible chance of catastrophic failure in flight. The easy and inexpensive maintenance required by quadrotors is a key consideration for civilian craft that must operate reliably in proximity to humans, without regular skilled maintenance.

The compactness of quadrotor helicopters is due to reduced rotor diameters and closely spaced layout. They do not have a single large rotor or long tail boom that can readily collide with nearby obstacles, and instead use small rotors that are easily shrouded for protection. This makes them ideal for tasks indoors or in enclosed spaces, such as inspecting ceilings of a factory, flying down mine shafts or scanning close to civil infrastructure such as bridges or dam walls.

As a result of these factors, I believe quadrotors offer an inherently safer option for commercial robotic operation than equivalently sized helicopters.

1.3 Why the X-4 Flyer?

The X-4 Flyer developed at the Australian National University (ANU) [Pounds *et al* 2004] emphasises the focus on quadrotor UAVs for commercial applications. It was conceived as an experimental platform for aerial robot research (see Fig. 1.3) and so is designed to lift up to 1 kg of payload with the aim of

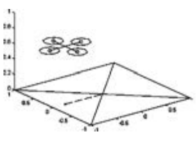

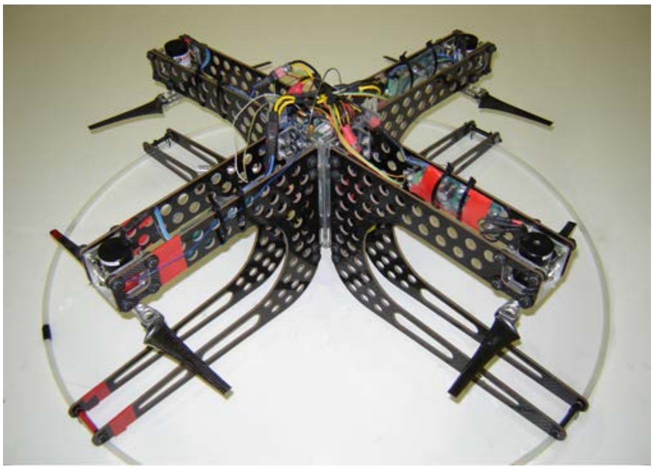

Figure 1.3: Australian National University X-4 Flyer.

carrying modular sensor packages independent from the core avionics. It has particularly small rotors, making it similar in size to much lighter craft. It is 1.00 m from furthest rotor-tip to rotor-tip.

The X-4 is designed to be reliable and robust – the only moving parts are the four motor shafts and teetering rotor assemblies, making it low-maintenance and easy to prepare for operation. The flyer is intended to be used indoors, but is also robust and heavy enough for outdoor flight. It has a flight time greater than 10 minutes in hover, and future developments of the vehicle should extend this to 20–30 minutes.

To accommodate its large payload, the X-4 must be relatively heavy. At 4.34 kg, the flyer weighs ten times as much as the common Draganflyer IV, but with a rotor area only 20 per cent larger (0.34 m^2 compared with 0.28 m^2). Consequently, the X-4's rotors have eight times the disc loading — 12.7 kgm^{-2}, very high by the standards of conventional helicopters [Prouty 2002, p 644].

In its current configuration, the X-4 is a tele-operated robotic vehicle. It regulates its flight attitude but does not perform position keeping or autonomous navigation. However, computer inputs can be easily substituted for human-issued attitude references without any changes to hardware.

1.4 Problems and Objectives

This thesis considers key enabling technologies required to build larger quadrotors: *thrust generation*, *rotor speed control* and *attitude control*.

Solving the thrust problem demands specific focus on the design of compact

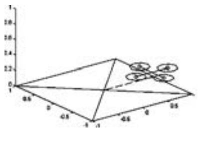

rotors. Small custom-designed blades can take advantage of ideal chord and twist geometry, where structural limitations make this impractical for full-scale aircraft. However, the optimal airfoils for the low Reynold's Number flow conditions encountered by small quadrotors are very thin and it is difficult to manufacture such blades. The aerodynamic torque on the blades will cause them to deform under load conditions — a problem that is usually ignored in traditional helicopter systems, where the variable pitch mechanism is used to adjust blade twist. The design of high-performance rotors for small-scale UAVs is a trade-off between ease of manufacture, mechanical properties of the airfoil and optimal aerodynamic performance. A detailed discussion of rotor design for the X-4 Flyer is given in Chapter 4.

As flight control of the helicopter is directly linked to changes in thrust, fast thrust changes are essential for acceptable flyer performance. The rotors are fixed-pitch for mechanical simplicity, and so the robot must be able to speed up and slow down its rotors quickly. Light-weight quadrotors have fast drive-system dynamics that make their attitude control straight-forward, but comparatively large payload-carrying quadrotor UAVs, like the X-4, must incorporate some schema to improve the bandwidth of the rotor response. The speed control design for the X-4 is described in Chapter 4.

Given sufficient drive-system bandwidth, the attitude controller must also deal with the intrinsically unstable dynamics of rotorcraft. Attitude compensators must regulate the aircraft's flight with sufficient stability for sensor payloads to be useful. A common misconception about quadrotors is that they are easier to control than a conventional helicopter. A quadrotor is potentially less manoeuvrable than a helicopter due to the need to change rotor speeds to pitch or translate, whereas the swashplate on a conventional helicopter can be adjusted almost instantaneously. Two attitude control schemes are discussed in Chapters 5 and 6.

Designing these controllers requires plant models that represent the essential dynamics in roll, pitch and yaw. Existing treatments do not fully model the flapping and inflow dynamics specific to quadrotors. These dynamics are important, as they can be exploited to design quadrotors in such a way that the craft's geometry simplifies the control design and maximises its performance. These effects and their dynamics equations are explained in Chapter 5.

Once the key technology problems have been solved, the remaining technical challenges are relatively straight forward. Nonetheless, designing a rotorcraft is not a trivial process and an outline of the engineering undertaken is given in

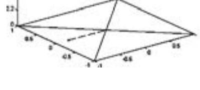

Chapter 3. My overall goals in this thesis are as follows:

1. Produce mechanically simple rotors to generate the required lift.
2. Produce motor controllers for fast dynamic speed response.
3. Devise a dynamic model with the important flapping effects of quadrotors.
4. Find the flyer configuration with the most favourable attitude dynamics.
5. Build the complete flyer hardware system.
6. Design and implement onboard attitude control.
7. Improve attitude control with nonlinear control-estimation methods.
8. Demonstrate the X-4 Flyer's flight worthiness.

1.5 Papers and Publications

Papers and publications written in the course of this thesis are:

- P. Pounds, R. Mahony, J. Gresham, P. Corke, J. Roberts, Towards Dynamically-Favourable Quad-Rotor Aerial Robots, In *Proc. Australasian Conference on Robotics and Automation*, Canberra, Australia, Dec. 2004.
- P. Pounds and R. Mahony, Small-Scale Aeroelastic Rotor Simulation, Design and Fabrication, In *Proc. Australasian Conference on Robotics and Automation*, Sydney, Australia, Dec. 2005.
- P. Pounds, R. Mahony and P. Corke, A Practical Quad-Rotor Robot, In *Proc. Australasian Conference on Robotics and Automation*, Auckland, New Zealand, Dec. 2006.
- P. Pounds, R. Mahony and P. Corke, System Identification and Control of an Aerobot Drive System, In *Proc. Information, Decision and Control*, Adelaide, Australia, Feb. 2007.
- P. Pounds, T. Hamel and R. Mahony, Attitude Control of Rigid Body Dynamics From Biased IMU Measurements, IEEE Conference on Decision and Control, New Orleans, Louisiana, United States, Dec. 2007.

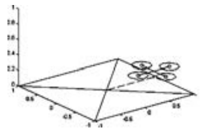

- P. Pounds, R. Mahony and P. Corke, Design of a Static Thruster for Micro Air Vehicle Rotorcraft, *Journal of Aerospace Engineering*, 2007, accepted awaiting publication.

1.6 Roadmap

This thesis comprises seven chapters, including this introduction. Chapter 2 is a literature review that surveys the body of scientific work relevant to quadrotor design, aerodynamics and control, as well as allied fields of study related to UAVs. Chapter 3 describes the hardware and systems of the X-4 Flyer in detail. Chapter 4 reports on the science, design, fabrication and testing results of a combined rotor-motor drive system for the X-4 Flyer. Chapter 5 provides a quadrotor dynamic model with estimated parameters, and details a Single Input Single Output (SISO) controller for attitude stabilisation. Chapter 6 presents a combined nonlinear control-estimator which uses the direct vector measurements from the flyer's inertial sensors. Chapter 7 concludes the thesis, summarising the results and findings of this research. Appendix A derives the full flapping equations for convenitional helicopters. Appendix B and Appendix C provide additional details of the X-4's avionics subsystems and interfaces. Appendix D provides keys stability derivatives for quad-rotor helicopters. A compact-disc containing design files and data is included at the back of the thesis.

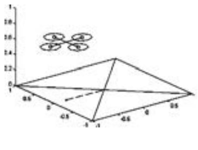

Chapter 2

Literature Review

In this chapter, I provide the historical and theoretical context for the X-4 Flyer. Section 2.1 gives a short synopsis of the concurrent development of vehicles and enabling technology that led to modern UAVs, and a brief history of manned quadrotors and micro quadrotor research projects. Section 2.2 provides a survey of other rotorcraft UAV configurations in competition with quadrotors, and their relative benefits and drawbacks. Section 2.3 discusses underlying concepts for high-level UAV design and which formulative process is appropriate to the X-4 Flyer. Section 2.4 presents the principal theory behind fundamental rotor aerodynamics, and this is expanded in Section 2.5 with a description of aeroelastic and unsteady aerodynamic effects. Section 2.6 outlines the basic models developed to represent quadrotor dynamics and behaviour. Section 2.7 surveys the variety and performance of controllers used to stabilise quadrotors. Finally, Section 2.8 relates specific conclusions and insights drawn from the literature review.

2.1 Historial Context

2.1.1 Early UAVs and Enabling Technologies

The utility of unmanned aerial vehicles has always been dictated by the technology available to control and direct the craft. As early as 1917 (only 14 years after the invention of the aeroplane itself) Elmer Sperry constructed a self-stabilising aircraft using gyroscopes, barometers and servo-motor control [Armitage 1988]. After take-off controlled by a human, the Hewitt-Sperry Automatic Aeroplane was capable of flying up to 48 km and dropping a bag of sand within 3.2 km of a predefined target. The first fully-unmanned flight was the 1918 Curtis-Sperry

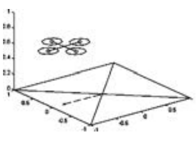

Flying Bomb, which was launched from a moving car and flew a preset distance of 900 m [Parsch 2005]. In the 1930s, development continued on both sides of the Atlantic, but the emphasis was on radio-controlled drones for target practice rather than on autonomous vehicles.

The outbreak of the Second World War in 1939 prompted renewed interest in flying bombs. Advances in radio, gyroscopic control technology and television produced more sophisticated weapons, but with mixed results. The Allies focussed on radio-control of modified bombers, using telemetry taken from cameras in the nose looking forward and in the cockpit pointed at the instruments [Armitage 1988]. These attempts had only limited success. The Axis flying bombs, specifically the V-1, enjoyed great notoriety for their part in the London blitz. The V-1 used a weighted pendulum for attitude control, a gas-powered gyroscope compass for bearing and a barometer for altitude control [Armitage 1988]. A free-wheeling propeller at the front of the craft estimated distance and caused the bomb to dive when a preset number of rotations was reached. In practice the V-1 was as inaccurate as other flying bombs of the era, but the sheer number of launches accounted for more than 6,000 casualties [Armitage 1988]. Captured V-1s catalysed the Allies to continue developing cruise-missile, Remote-Piloted Vehicle (RPV) and radio-controlled drone technology, which formed the basis of modern UAVs.

Notable among the early post-war RPVs was the QH-50 Gyrodyne (see Fig. 2.1), the first unmanned helicopter. Developed for anti-submarine warfare in 1950, the Gyrodyne was remotely piloted from ships and used gyroscope feedback control stability in the air [GHHF 2007].

Post-war cruise-missiles such as Navaho and Matador advanced the capabilities of fixed-wing drones. The N-69 Snark and X-10 Navaho introduced an Inertial Navigation System (INS) to manoeuvre through a trajectory on approach to its target [Armitage 1988]. The TM-61C Matador had a microwave-based positioning system that allowed it to map its location using signals received from known transmitters [Armitage 1988]. The TM-76A had INS and down-looking terrain-following radar. Drones such as the MQM-57 Falconer and Model 147J Lightning Bug added cameras and automated flight capability to remotely-piloted aircraft, and were used for reconnaissance missions over China and the Soviet Union after the loss of several U-2 spyplanes in the 1960s. This technology culminated in the SLCM Tomahawk missile, which features INS, Global Positioning System (GPS), terrain-following radar and terminal guidance based on video feature recognition. The Tomahawk was used to good effect during the 1992

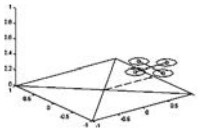

Figure 2.1: QH-50 Gyrodyne ASW UAV.

Gulf War, demonstrating a 94 per cent strike rate in its first combat deployment [Goebel 2007].

Today, robot aircraft combine modern computer power with technology originally developed for drones and cruise missiles to perform a variety of roles including reconnaissance, surveillance, and air-to-ground and air-to-air attack missions. Progress in computers, light-weight cameras and Micro Electro-Mechanical System (MEMS) inertial sensors has now made UAV technology affordable for non-military use. Consequently, the new frontier of research is in developing flying robots for generalised use, outside of expensive military budgets.

2.1.2 Manned Quadrotors

The first manned quadrotor was the Bréguet-Richet ‘Gyroplane No. 1’ constructed in 1907 (see Fig. 2.2). The gyroplane consisted of a cross-beam fuselage with four bi-plane rotors (for a total of 32 blades) at each end. The machine could carry a small person but it never flew outside of ground effect. Its handling was reported to be poor and it required a team of men to stabilise it during hovering flight [Leishman 2002a]. Other early quadrotors that achieved flight were the 1921 Æhmichen quadrotor and 1922 Jerome-de Bothezat quadrotor ‘Flying Octopus’ [Leishman 2006, pp 25–26].

Two notable manned quadrotor craft were built during the 1960s as part of the United States ‘X-Plane’ research vehicle series. The Curtiss-Wright X-19 was a quad tilt-rotor the size of a business jet. It used a special type of radial propeller

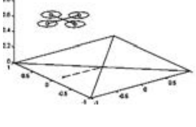

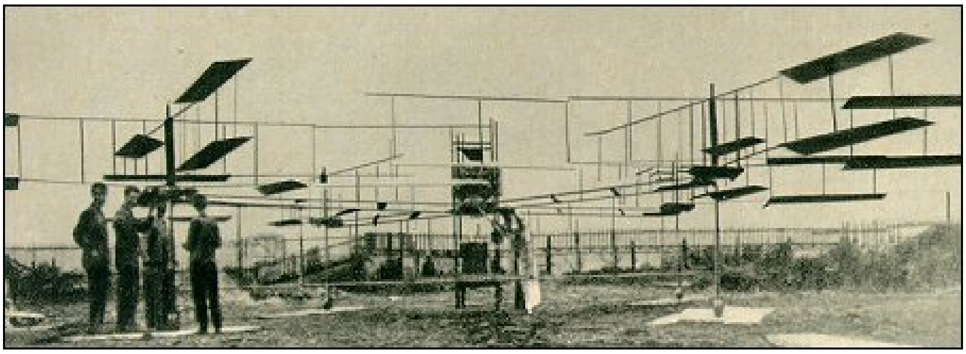

Figure 2.2: Bréguet-Richet Gyroplan No.1 — The First Quadrotor

Figure 2.3: Curtiss-Wright X-19 Radial Propeller Craft.

(see Fig. 2.3). The propellers used high-angle high-twist rotors to induce vertical thrust even when the rotors were aligned horizontally [Starostin 2004]. The X-19 was destroyed on its first test flight and the radial lift rotor technology was not developed further [Winchester 2005].

The Bell X-22 was a quad ducted-fan craft that saw long service as a research vehicle (see Fig. 2.4). The X-22 could be configured to emulate the flight behaviour of theoretical aircraft and was used a test-bed for the Hawker Siddeley GR.1 Harrier [Winchester 2005]. Both the X-19 and the X-22 used variable pitch rotors for attitude control, and the X-22 had additional vanes in its outflow to allow for low-speed yaw control [Starostin 2004].

Following the success of the V-22 Osprey tilt-rotor, Boeing produced conceptual designs for a quad tilt-rotor based on the same technology. Although no aircraft has yet been built, quad tilt-rotor models have been tested in wind tunnels for aeroelastic loading of its wings and surfaces (see Fig. 2.5) as well as in simulation with complex Computational Fluid Dynamics (CFD) programs for analysis of inflow behaviour and vortex-ring states that plagued the V-22.

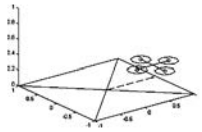

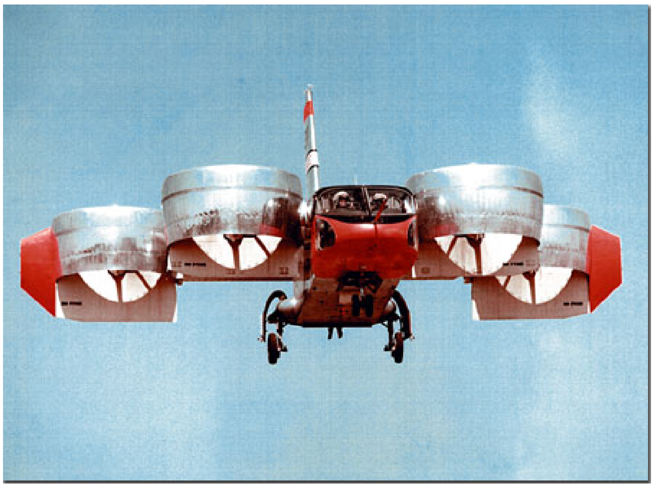

Figure 2.4: Bell X-22 Ducted Fan Research Vehicle.

Figure 2.5: Boeing Quad Tilt-rotor Half-model in the Langley Wind Tunnel.

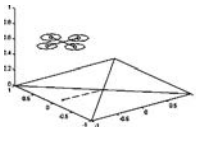

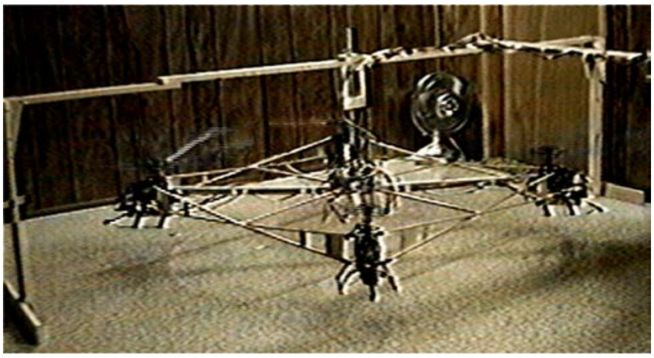

Figure 2.6: Borenstein Hoverbot.

2.1.3 Micro Quadrotors

In the last 15 years the number and variety of micro quadrotor vehicles has increased substantially. Early efforts to build small quadrotors were based around radio-controlled toys. The Hoverbot, built in 1992, was constructed from four radio-controlled helicopters joined at the tail [Borenstein 1992] (see Fig. 2.6). The aircraft could lift off in a test frame and stabilise itself in orientation using potentiometers built into its test gimbal. It used variable pitch on all four rotors to change thrust.

The mid-90s ‘Roswell Flyer’ and ‘HMX-4’, later to become the ‘Draganflyer’, consisted of cheap motors and rotors, a foam frame and early MEMS gyros in feedback for pilot-assist. The craft were very light and small, limited to carrying tens of grams of payload. Flying the craft required continuous pilot attention. This craft has formed the basis of numerous research vehicles.

The Mesicopter was a late-90s Standford University project aimed at creating centimetre-scale quadrotors. The total aircraft weight was of the order of a gram, and special wafer-cut moulds were required to fabricate its rotors. The first Mesicopter prototypes had fixed-pitch rotors in a conventional quadrotor configuration, but later models used shrouded rotors with inverted mass and a “passive aerodynamic system with rotor cowls and fixed vanes” for control [Kroo *et al* 2000] (see Fig. 2.7).

Post-2000, quadrotors have proliferated as toys and research tools. The Draganfly Innovations Draganflyer is now in its fifth incarnation along with larger derivative versions aimed at professional applications (see Fig. 2.8). The basic Draganflyer lifts approximately 100 g of payload for 5–10 minutes. The pilot must stabilise the craft with the assistance of damping from rate gyros, although more advanced models can self-stabilise using ultrasonic sensors.

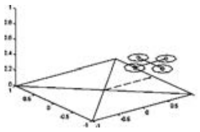

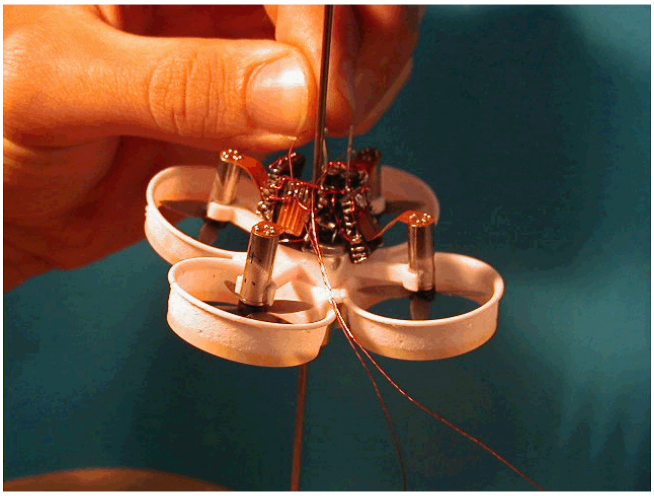

Figure 2.7: Stanford Mesicopter Micro UAV.

Figure 2.8: Draganfly Innovations Draganflyer IV

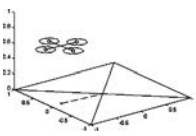

Figure 2.9: CEA X4-Flyer.

Draganflyer parts are used by many control and robotics researchers around the world. The number of purpose-built quadrotors is low, compared with derivative craft, due to the high overheads involved in constructing aircraft from scratch. Typically, a research quadrotor will consist of Draganflyer chassis, rotors and motors complemented by custom avionics and control.

Numerous universities have used quadrotors for research into attitude control, visual servoing, swarm control and aerodynamics. The following is only a brief overview of selected quadrotor research projects.

CEA's 'X4-Flyer' project seeks to develop quadrotor technology for intuitive pilot operation and operation in hazardous environments [Guenard *et al* 2005]. This quadrotor is a novel departure from other modified Draganflyers in that it doubles the number of blades on each motor and replaces the individual Draganflyer motors with pairs of motors, for a total of eight motors (see Fig. 2.9). It also has custom drive electronics consisting of a GigaHertz Discrete Signal Processor (DSP) card that provides excellent flight stability. The current X4-Flyer incarnation has four ducts around its rotors [Guenard *et al* 2007]. Bourquardez *et al* use visual feedback in an outer control loop for position and altitude [Bourquardez *et al* 2007]; the system can guide the CEA quadrotor through waypoints using a single down-facing camera.

The EPFL 'OS4' project is aimed at developing autonomous indoor Vertical Take-Off and Landing (VTOL) vehicles [Bouabdallah and Siegwart 2005a], capable of using different navigation schemes. The OS4 quadrotor began as a Draganflyer test-bed on a gimbal but has since evolved into an entirely original vehicle, including custom avionics, airframe and rotors (see Fig. 2.10). The craft has been

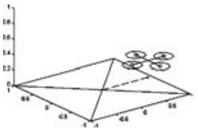

Figure 2.10: EPFL 'OS4' Quadrotor.

used successfully for testing a variety of control schemes [Bouabdallah *et al* 2004b] [Bouabdallah and Siegwart 2005b].

Tayebei and McGilvray have done much work on quadrotors, focussing on quaternion and nonlinear control [Tayebi and McGilvray 2004]. Their experimental apparatus consists of a non-flying modified Draganflyer with original airframe and drive systems, but with custom avionics. The quadrotor is fixed to a ball-joint test rig with off-board power that allows limited rotation in all three axes [Tayebi and McGilvray 2006].

The Standford Testbed of Autonomous Rotorcraft for Multi-Agent Control (STARMAC) project uses multiple vehicles flying in formation for collision and obstacle avoidance [Hoffmann *et al* 2004]. Quadrotors were chosen for this project because they are not as cumbersome as other rotorcraft and can operate in small environments. The STARMAC quadrotors uses Draganflyer rotors and motors (see Fig. 2.11), but incorporate a sliding-mode controller for attitude stability [Waslander *et al* 2005].

MIT's Aerospace Controls Laboratory uses quadrotors for UAV swarm experiments. As many as five quadrotors may fly simultaneously and cooperate with Unmanned Ground Vehicles (UGVs). In one experiment, a quadrotor was landed successfully on a moving UGV. MIT uses unmodified Draganflyers with onboard video, which are controlled by off-the-shelf hobby radios via a PC interface connected to the handset's 'trainer port' [Tournier *et al* 2006].

KITECH's Division of Applied Robotic Technology Quad-Rotor Type (QRT) is designed to investigate quadrotor technology for use in indoor emergency obser-

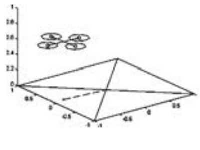

Figure 2.11: Stanford STARMAC Quadrotor.

vation applications [Park *et al* 2005]. The QRT consists of a 1.5 kg custom-made flyer built around a Draganflyer chassis. It uses rigid hobby propellers, driven by geared motors with encoders, that produce a total maximum thrust of 1.8 kg for 20 per cent headroom; no information is given on flight time or non-battery payload. The QRT uses custom avionics and INS and has an onboard camera, IR and ultrasonic sensors.

UTC's Centre de Recherche de Royallieu quadrotor project aims to develop simple control strategies for four-rotor helicopters [Castillo *et al* 2004a] [Salazar-Cruz *et al* 2005]. The early hardware setup was similar to that used by MIT — the quadrotor was an unmodified Draganflyer with mounted inertial sensors transmitting wirelessly to a PC interfaced to a hobby radio handset. In this case, the PC interface card is connected to the handset potentiometers, rather than to a 'trainer port' [Castillo *et al* 2004b]. More recently, the onboard system was replaced with custom electronics built around the Rabbit Microprocessor RCM3400 core, which reads inertial sensors, controls the motors and communicates over a wireless modem [Romero *et al* 2003]. It includes onboard video transmitting to an offboard PC that sends command signals via the radio handset.

The University of Pennsylvania quadrotor project focusses on vison control for autonomous UAV rotorcraft. The quadrotor consists of an HMX-4 connected to a tether that allows it to fly vertically and pitch, roll and yaw without lateral translation [Altŭg *et al* 2002]. A pair of cameras connected to a PC detect flyer position and pose, using coloured blobs attached to the craft. A second PC

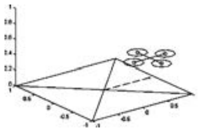

Figure 2.12: Draganfly Innovations Draganflyer XPro

receives the pose information and controls the orientation of the flyer via a parallel port “remote control device” [Altŭg *et al* 2003].

Next to the Hoverbot, the largest quadrotor found was the 6.2 kg Cornell Autonomous Flying Vehicle ‘AFV’. The craft was custom-built and consisted of hobby rotors, motors, speed controllers and early lithium polymer batteries. A try-and-see method was used to find the best mix of rotors, motors and gearing. The craft used rotor speed control loops via shaft encoders, and performed bias estimation for its inertial sensors using Kalman filters [Nice 2004]. Although the vehicle achieved hover stability on a test platform with tethered power, damage during testing prevented free flight experiments.

Outside of research, two commercially targeted quadrotors are currently in operation: the Draganfly Innovations Draganflyer X-Pro (see Fig. 2.12) and the SIM Sky Eye (see Fig. 2.13). The Sky Eye is operated by a human controller and is designed for use as a remote surveillance drone. To date more than 30 Sky Eye craft have been sold, including units destined for Chinese police use.

2.2 Quadrotor Alternatives

Quadrotor UAVs are not the only rotorcraft being investigated for use in commercial applications. Other craft are being developed to reduce or eliminate some of the drawbacks of conventional helicopters, most often limited cruise velocity. Rotorcraft UAVs are designed as either predominantly hovering vehicles or as transitional vehicles. Tilt-rotor, tail-sitter and stopped-rotor craft move between

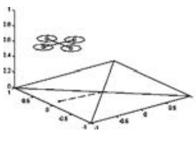

Figure 2.13: SIM Sky Eye Commercial quadrotor

hover and cruising flight. The inevitable tradeoff between hover efficiency and cruise performance means that transitional vehicles will never loiter as efficiently as a purpose-designed hovering vehicle.

A brief description of the competing rotorcraft types (including conventional helicopters), example systems, and their advantages and disadvantages with respect to quadrotors is given below.

- *Conventional Rotors*

  Progress in developing conventional helicopter UAV systems has been swift — some helicopter UAVs have already seen limited use in civilian roles. The Yamaha RMAX is a well-known system, used for agricultural work, crop-dusting terraced rice paddys in Japan, aerial photography and flight research [UAD 2001] (see Fig. 2.14). It features fully autonomous hover and autopilot, while high-end versions include GPS and position-holding capabilities.

  Advantages of conventional helicopters compared with quadrotors are the ready availability of commercial systems, well understood dynamics and efficient thrust generation. Their disadvantages, as discussed in Chapter 1, are their intensive maintenance requirements and bulk. The size of their rotors and tail boom limits them to flying in open areas. The exclusion zone of the main rotor requires that any cameras or sensors onboard be far away from objects the UAV may wish to investigate.

- *Coaxial Rotors*

  Closely related to conventional helicopters, co-axial helicopters eliminate

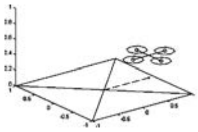

Figure 2.14: Yamaha RMAX Commercial UAV.

Figure 2.15: Bombardier Guardian UAV.

the need for a tail-rotor by combining two main rotors on one axis.Well-known examples of this are the Bombardier CL-327 Guardian UAV (see Fig. 2.15) [AHS 2006] and QH-50 Gyrodyne anti-submarine warfare UAV (see Fig. 2.1).

Advantages of co-axial UAVs are their favourable dynamics[1], compact rotor discs and high manoeuvrability. However, the rotor mast complexity of a co-axial UAV is twice that of an equivalent conventional helicopter, exacerbating the problems of UAV maintenance and reliability.

- *Ducted Fan and Shrouded Rotor*

  Ducted fan and shrouded rotor craft are a popular format of VTOL UAV.

---

[1] Specially designed co-axial helicopters can be made dynamically stable in attitude.

Figure 2.16: Bertin Hovereye.

They offer improved efficiency by eliminating vortex losses at their rotor tips. Examples are the Bertin Hovereye [Pflimlin *et al* 1997] (see Fig. 2.16). Other ducted fan UAVs include the Sikorsky Cypher UAV, Honeywell MAV, NORD 500 and Solo Trek XFV.

Ducted fans offer the closest performance match to quadrotor alternatives. They have high-disc loadings (similar to quadrotors) and are designed for hover flight. The shroud makes them exceptionally safe vehicles to operate — they can approach obstacles closely, even to touching. However, they are mechanically more complex than quadrotors, due to the need for vanes to direct their rotor thrust, and pose difficult aerodynamics problems in shroud design.

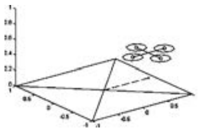

Figure 2.17: Bell Eagle Eye tilt-rotor.

- *Tilt-Rotor*

Tilt-rotors are a tandem configuration that uses rotors tilted through 90 degrees to drive the aircraft to aeroplane-like speeds, with lift generated by a conventional wing. Examples include the Bell-Boeing Eagle Eye (see Fig. 2.17) [Bell 2006], the Fulton School of Engineering HARVee [Wells 2004] and AeroCopter tilt-disc MAV [Yassini and Syrovy 2002].

Tilt-rotors typically include the full cyclic and collective control used in conventional helicopters (and their attendant problems) in addition to the rotor tilt mechanisms. Although they have more compact rotors in a tandem configuration, the wide spacing of the rotors restricts them to open spaces.

- *Tail-sitter*

A tail-sitter UAV, such as the Boeing Heliwing [AHS 2006], is a craft that takes off vertically like a helicopter but then transitions into horizontal flight with lift being generated by wings (see Fig. 2.18). Other UAVs that use this method include the University of Sydney T-Wing [Anderson and Stone 2007], Drexel University MAV [Green and Oh 2005] and the NASA quadrotor [Young *et al* 2002].

In hover, the performance and dynamics of tail-sitters is very similar to that

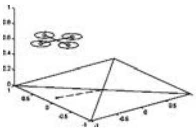

Figure 2.18: Boeing Heliwing Tailsitter.

of ducted fans. However, the dual operation of the prop-rotor makes them uncompetitive for long-term hovering. In addition, they do not possess the safety advantages of a shroud.

- *Stopped-Rotor*
  Stopped rotors use a spinning rotor surface that is halted mid-flight and then used to provide lift like a wing. The Boeing X-50 Dragonfly UAV uses a single turbine power-plant to drive the rotor and provide horizontal thrust [Boeing 2006] (see Fig. 2.19). A cyclic mechanism is used to pitch the entire middle wing segment in helicopter mode. Similar concepts include the ANU Hybrid-Concept Flyer [Pope 2002] and the Phantom rotorcraft UAV [Veratech 2007].

  Compared with quadrotors, stopped-rotors are more complex due to the need to spin, feather, stop and lock the rotor-wing. Like the tilt-rotor, they inherit all the difficulties of a conventional helicopter, but must also carry the additional weight and complexity of maneouvering fins and control surfaces. Consequently, stopped-rotors are not viable competitors for quadrotor tasks.

Of the alternatives cited, only the ducted fan has similar performance capabilities for operating in close environments without substantial complexity. However, quadrotors still offer greater mechanical simplicity and potential reliability that makes them more desirable for the applications in mind. Quadrotors and ducted

Figure 2.19: Boeing X-50 Dragonfly Stopped-Rotor UAV.

fan craft can be combined into a shrouded quadrotor that combines the benefits of rotor safety with simple mechanical design, at the expense of the added weight of four shrouds. This may be a direction of future research.

2.3 UAV Systems Design

UAV design has become an increasingly common task for aerospace and robotics engineers. Consequently, an accumulating body of experience in developing these systems is available to prospective designers.

The key technical challenges of UAV hardware engineering are numerous and familiar. Foremost, Young *et al* posit thrust and flight endurance as limiting factors for MAVs, going so far as to equip their quadrotor with a partial wing for cruise capability [Young *et al* 2002]. Rutherford and Wells cite logistics and endurance as limitations of UAVs, and suggest that custom designs are essential to meet specific real world goals [Rutherford and Wells 1999]. In the case of quadrotors, this translates into a need for efficient rotor design to maximise flight time and payload.

As stated in Chapter 1, there is an increasingly recognised need for improved logistics, reliability and maintainability, possibly by unskilled service staff [Pounds and Mahony 2005]. Gordon *et al* report that miniaturisation, maintainability, logistics and control are major obstacles to VTOL UAVs carrying out practical missions [Gordon *et al* 1993]. Essential facets of logistics improve-

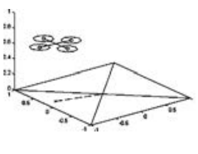

ment, such as use of modular subsystems and centralised complexity, fit well with quadrotors and are core to the underlying philosophy of the X-4 project.

The challenges facing UAV designers divide into component-level design (e.g. developing efficient rotors or better sensors) and system level design (e.g. reducing aerodynamic drag, making the system easy to service). I identify two methodologies in UAV development as it is currently practised: bottom-up and top-down design.

Bottom-up design consists of assembling known subsystems and components into a functioning design, focussing on Commercial-Off-The-Shelf (COTS) parts and rapid turn-around. This process typifies lower-budget research work where the scope for developing custom systems to spec does not exist. Here COTS drive systems, sensors, airframes, and even entire vehicles are the norm. Gordon *et al*, Bhandari and Colgren, and Taamallah *et al* use commercially available radio-control helicopters as the basis of their helicopter UAVs [Gordon *et al* 1993] [Bhandari and Colgren 2006] [Taamallah *et al* 2005]. Jung *et al* use an off-the-shelf radio-control aeroplane [Jung *et al* 2006]. In particular, the X-Cell model helicopter used by Gordon *et al* and Mettler *et al* has seen use in numerous projects [Mettler *et al* 2004], much like the quadrotor Draganflyer, as discussed in Section 2.1.2. Bottom-up design has the advantage of speeding development time and allowing for rapid replacement of readily available parts. However, it also burdens the engineer with imperfect knowledge of components and systems not specifically design for the application.

Top-down design consists of identifying target aircraft performance and structure, and then specifying what subsystems are necessary to meet the requirements. For example, Rutherford and Wells provide a set of criteria for an air-launched drone rotorcraft that could not be met by existing commercial designs [Rutherford and Wells 1999]. Martinez-Val and Hernández derive analytical performance curves for a long-range surveillance RPV and choose design parameters to meet their operational requirements [Martinez-Val and Hernández 1999].

Top-down design is the prevailing methodology among large, well-resourced aerospace firms accustomed to long development cycles. Top-down design is not limited by the capabilities of existing components, although it is expected that some COTS parts may be used. Every UAV currently deployed has been tailored for its target application. This style of global design provides the user and maintainer complete information about the system — “If you build it, you understand it” [Gordon *et al* 1993] — but the required overheads in time and manufacturing make it impractical for many university-level research vehicles.

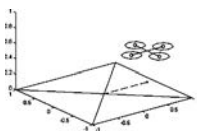

In the case of the ANU X-4 Flyer, where drive system and avionics performance needs are all predetermined, the vehicle must be developed from a top-down perspective to satisfy the challenging performance goals. In many cases the needs can be met with off-the-shelf parts (such as motors and batteries) but in the case of rotors, motor controllers and vibration isolators, purpose-built components were required. The symmetrical nature of quadrotors greatly facilitates the reuse of custom parts that need only be designed once, and then fabricated four times.

2.4 Classic Aerodynamics and Design

2.4.1 Rotor Modelling and Design

The basics of full-scale helicopter design are well established and the field of available texts is large. Perhaps the most prominent engineering text is Prouty's 'Helicopter Performance Stability and Control' [Prouty 2002] which provides a detailed derivation of momentum theory and Blade Element Method (BEM) of rotors in addition to trim and control topics. Another notable text is 'Rotary-Wing Aerodynamics' [Stepniewski and Keys 1984], which examines vortex theory and potential theory as well as providing details on tandem rotor configurations. In addition to fundamentals, 'Principles of Helicopter Aerodynamics' [Leishman 2006] includes detailed rotor and airfoil design and contemporary topics such as aeroelasticity and dynamic stall. 'Bramwell's Helicopter Dynamics' by Done and Balmford [Done and Balmford 2001] focusses on stability and control, with a section on aeromechanical behaviour. Several other texts, such as those by Seddon, Honnery and McCormick, are useful primers and quick references [Seddon 1996] [Honnery 2000] [McCormick 1999].

The most basic theory — momentum theory — treats the rotor as an 'actuator disc' in a flow that causes an instantaneous change in pressure. By balancing the flow momentum and energy, it can be shown that the velocity of the flow at infinity downstream will be twice the induced flow velocity at the disc. Consequently, equations can be derived that relate the rotor thrust to required power and disc area [Seddon 1996].

Blade element method divides the actuator disc into a set of annuli spaced along the blade. Using airfoil theory developed for fixed-wing aircraft, the lift at each point along the blade can be integrated to give the total thrust across the rotor [Prouty 2002, pp 13–15] [Done and Balmford 2001, p 46]. Blade element

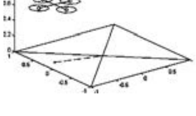

theory incorporates the specific airfoil lift and drag characteristics, and rotor planform geometry, which makes it suitable for designing rotors and propellers to optimise the operation of airfoils given experimental or computed performance data [Stepniewski and Keys 1984, p 91]. Blade Element Momentum Theory (BEMT) combines BEM with momentum theory for non-uniform induced velocity analysis [Prouty 2002, pp 36–76] [Leishman 2006, pp 125-152].

More complicated methods, such as vortex theory and potential theory [Stepniewski and Keys 1984], were originally developed to solve curved and unsteady flow problems. These techniques have since proven adaptable to computer algorithms for analysing flow geometry and performance.

While there is extensive research into full-scale rotors and drive systems, investigation into the special problems of small-scale UAV rotorcraft propulsion is quite sparse, at least in the public domain. One important question is whether rotor design tools developed for large helicopters are applicable to miniature helicopter UAVs. Bohorquez *et al* use CFD modelling and BEMT analysis to estimate the performance of several small-scale rotors with low Reynold's Numbers [Bohorquez and Pines 2003]. They found that the modelled performances generally agree with the experiments, although the CFD-calculated efficiencies differ by as much as 20 per cent. Mettler *et al* analyses the dynamics of several small rotorcraft and the relationship between their size and dynamic behaviour [Mettler *et al* 2004].

Methods for small craft rotor design vary in sophistication, ranging from trial and error to analytical aerodynamic simulation. Bouabdallah *et al* use a COTS try-and-see matching of a range of propellers and gearing to achieve the best results [Bouabdallah *et al* 2004a]. Prouty provides a top-down classical aerodynamics analytical method for designing rotors and choosing engines for full-scale helicopters [Prouty 2002]. Nicoud and Zufferey use a basic idealised analytical approach to design balsa wood propellors for a very small indoor aeroplane [Nicoud and Zuffery 2002]. Vanessa Wells' HARVee tilt-rotor UAV used a multi-dimensional BEM simulation and search algorithm to identify the optimal blade planform for small-scale proprotors [Wells 2004]. Drela used a set of airfoil panel-based simulation and modelling tools to design the MIT demonstrator quadrotor [Drela 2003]. Pounds and Mahony combine the analytical simulation tools developed by Drela and Well's simulation-search method, and expand them to include the effects of aerodynamic distortion of the rotor [Pounds and Mahony 2005] (see Chapter 4).

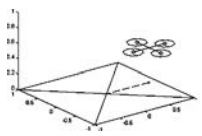

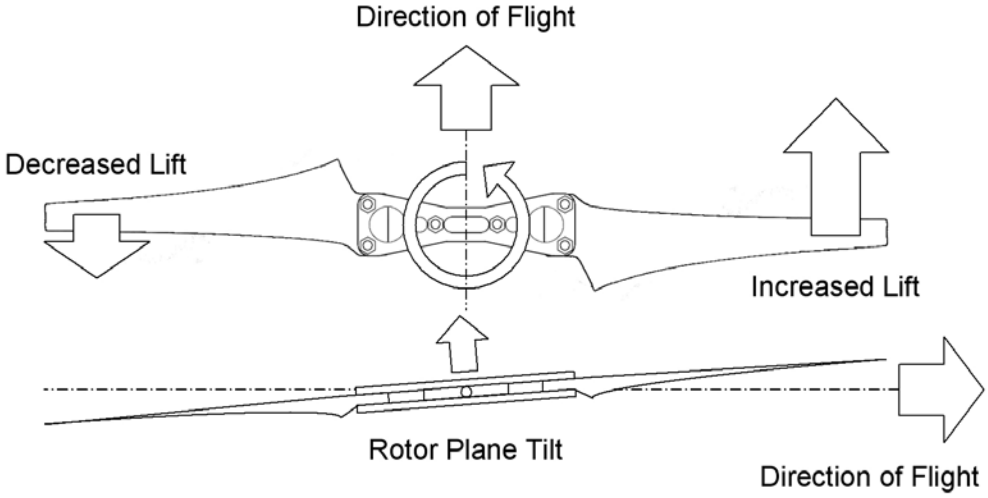

Figure 2.20: Rotor Flapping Due to Horizontal Translation.

2.4.2 Rotor Flapping

An important aspect of rotor dynamic modelling is the flapping effect caused by horizontal translation of the rotor in air. When a rotor translates, one blade — the ‘advancing blade’ — will move in the direction of translation and one blade — the ‘retreating blade’ — will move opposite the direction of motion. The advancing blade will have a net velocity increase and the retreating blade will have a net velocity decrease relative to the air (see Fig. 2.20). This creates a disparity of lift between the advancing side of the rotor and the retreating side of the rotor — if the rotor disc is perfectly rigid this causes the helicopter to flip, as was the case in very early autogyro experiments [Leishman 2006, p 20].

Rotor flapping is the process by which a rotor blade balances the lift imbalance (aerodynamic force), centripedal force and blade weight force by allowing free rotation around a hinge or flexure. The lift imbalance causes the advancing blade to rise, and the retreating blade to fall — leading the rotor plane to tilt until a new equilibrium is met. Increasing translational velocity leads to increasing rotor tilt. When the rotor plane tilts, the combined lift force generated by the blades is correspondingly tilted, resulting in a horizontal component of thrust that opposes the direction of translation. To enter forward flight, a helicopter uses its cyclic control to create a similar lift imbalance through differential blade pitch that opposes and cancels the rotor flapping caused by the translation of the vehicle [Prouty 2002, pp 445-447].

The angles subtended by the tilted rotor disc and vehicle axes through the

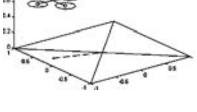

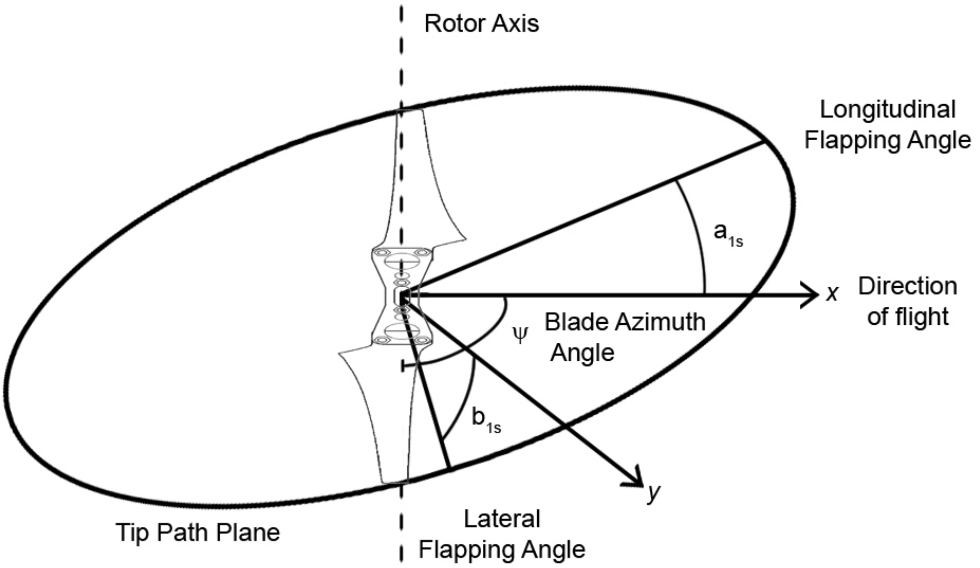

Figure 2.21: Rotor Flapping Angles.

longitudinal and lateral planes due to rotor flapping are referred to as the rotor flapping angles, a_{1_s} and b_{1_s} (see Fig. 2.21). At equilibrium, the vertical lift force generated by the blades causes the blades to angle slightly upwards, called the 'coning angle' [2].

In hover, unactuated flapping rotors will always return to the plane perpendicular to the rotor axis [Prouty 2002, p 450]. If the aircraft is pitched or rolled, the blade inclination relative to the inflow will causes the rotor plane to match the rotor mast attitude. Additionally, if the blade pivot is offset from the rotor axis of rotation, the centripedal force of the blades will pull against the hub such that the fuselage is pulled to align with the rotors — the corresponding reaction torque causes the lighter blades to return to level rotation relative to the helicopter [Done and Balmford 2001, p 25].

Virtually all helicopters are constructed with mechanical linkages to accomodate the motion of the blades with respect to the vehicle during flapping. There are several types of flapping hinge (see Fig. 2.22). Most rotor blades do not pivot at the rotor axis, but rather some small distance outboard. In the case of two-blade rotors, the blades can be pivoted at the middle like a 'see-saw'; this is called a teetering hinge. Some advanced rotors forgo a hinge entirely and use the compliance of the rotor blades to effect rotor tilt; these have a virtual hinge offset

---

[2] In the case of the X-4 Flyer, the coning angle is very small — 1.1° — and so the rotor is generally treated as a flat disc; the equation for coning angle is given in Appendix A.

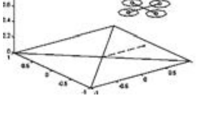

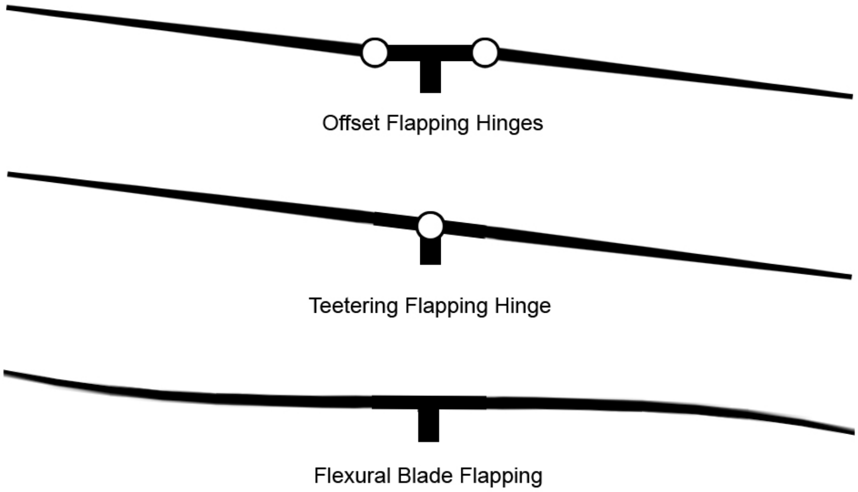

Figure 2.22: Rotor Flapping Hinges — Offset, Teetering and Flexural.

determined by the length and elasticity of the blades. In practice, even apparently rigid unhinged rotors exhibit flexure flapping. The length of the hinge offset dictates the cross-coupling of longitudinal and lateral flapping and the magnitude of coupled torques applied to the rotor shaft.

2.4.3 Longitudinal and Lateral Flapping Equations

The combination of the flapping forces and effects is modelled mathematically by equating the lift, weight and centripetal moments about the blade hinge to zero at all points around the rotor azimuth. The resultant longitudinal and lateral flapping angles, a_{1_s} and b_{1_s} respectively, can be found by simultaneously solving the constant and sinusoidal components of the blade centrifugal-aerodynamic-static balance.

Prouty provides a generalised model for flapping [Prouty 2002, p 469]; a derivation of these equations is provided in Appendix A:

$$a_{1_s} = \frac{\frac{8}{3}\theta_0\mu + 2\theta_1\mu - B_1\left(1+\frac{3}{2}\mu^2\right) + 2\mu\left(\mu\alpha_s - C_T/\sigma\frac{\sigma}{2\mu}\right)}{\left(1-\frac{\mu^2}{2}\right)}$$

$$+\frac{12\left(\frac{e}{R}\right)}{\gamma\left(1-\frac{e}{R}\right)^3\left(1+\frac{\mu^2}{2}\right)} \times \left[A_1\left(1+\frac{\mu^2}{2}\right)+\frac{4}{3}C_T/\sigma\left(\frac{\frac{2}{3}\frac{\mu\gamma}{a}}{1+\frac{3}{2}\frac{e}{R}}+\frac{\sigma}{2\mu}\right)\right] \quad (2.1)$$

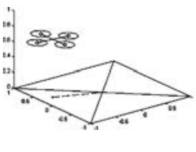

$$b_{1_s} = A_1 + \frac{\frac{4}{3}C_T/\sigma}{1+\frac{\mu^2}{2}}\left(\frac{\frac{2}{3}\frac{\mu\gamma}{a}}{1+\frac{3}{2}\frac{e}{R}} + \frac{\sigma}{2\mu}\right) + \frac{12\left(\frac{e}{R}\right)}{\gamma\left(1-\frac{e}{R}\right)^3\left(1-\frac{\mu^4}{4}\right)}$$
$$\times\left[\frac{8}{3}\theta_0\mu + 2\theta_1\mu - B_1\left(1+\frac{3}{2}\mu^2\right) + 2\mu\left(\mu\alpha_s - C_T/\sigma\frac{\sigma}{2\mu}\right)\right] \tag{2.2}$$

where A_1 and B_1 are longitudinal and lateral blade feathering control input angles, θ_0 is the equivalent blade pitch at the rotor axis and θ_1 is the washout of a linear twist blade [Prouty 2002, p 20], α_s is the shaft tilt angle, σ is the rotor disc solidity and C_T is the non-dimensionalised thrust coefficient, e is the hinge offset, R is the rotor radius, μ is the advance ratio, a is the polar lift slope of the blade airfoil and γ is the Lock Number:

$$\gamma = \frac{\rho a c R^4}{\mathrm{I}_b} \tag{2.3}$$

where I_b is the rotational inertia of the blade about the flapping hinge, ρ is the density of air and c is the chord length. This model for flapping assumes steady forward flight, linear rotor twist and slow acceleration.

The flapping angles are functions of the ‘advance ratio’, $\mu = V/\omega R$ — the ratio between horizontal speed and blade tip speed, where ω is the rotor angular velocity and R is the rotor radius.

Prouty’s equations represent the full complexity of the first harmonic flapping angles for variable pitch blades subject to linear motion. As flapping is fundamental to helicopter aerodynamics, numerous other texts provide similar derivations for these dynamics; Leishman and Done and Balmford, particularly, give excellent coverage of flapping dynamics [Leishman 2006][Done and Balmford 2001].

In this work, I propose a treatment tailored to quadrotors that greatly simplifies the forward velocity-flapping relation [Pounds *et al* 2004]. The following modifications are made:

- In helicopters with cyclic rotor pitch, changing the pitch angle of the blades causes a one-to-one pitch angle change in the rotor tilt [Prouty 2002, pp 445-447] — this is what allows a helicopter to change its velocity and hover in arbitrary directions. In the case of fixed-pitch blades, blade feathering is discarded:

$$A_1 = 0 \tag{2.4}$$
$$B_1 = 0 \tag{2.5}$$

- The blade element linear twist distribution given in Prouty's flapping equations can be directly replaced with ideal twist:

  $$\theta_t = \frac{2}{3}\theta_0 + \frac{1}{2}\theta_1 \tag{2.6}$$

  where θ_t is the blade tip angle of an ideal twist rotor.

- Using Coleman's inflow model [Coleman *et al* 1945] (see Section 2.4.4) and small shaft angle relative to the direction of travel[3], the vertical flow component of the flapping balance can be rewritten in terms of the non-dimensionalised inflow ratio, $\lambda = v_i/\omega R$ [Prouty 2002, p 167]:

  $$\mu\alpha_s = 0 \tag{2.7}$$

  $$\lambda = C_T/2\mu \tag{2.8}$$

  where v_i is the inflow velocity.

The simplified equations for the first harmonic flapping longitudinal and lateral angle solutions due to forward flight, $\overline{a}_{1_s}$ and $\overline{b}_{1_s}$, become:

$$\overline{a}_{1_s} = \frac{1}{\left(1-\frac{\mu^2}{2}\right)}\mu\left(4\theta_t - 2\lambda\right) + \frac{12\left(\frac{e}{R}\right)}{\gamma\left(1-\frac{e}{R}\right)^3\left(1+\frac{\mu^4}{4}\right)} \times \frac{4}{3}\left(C_T/\sigma\frac{\frac{2}{3}\frac{\mu\gamma}{a}}{1+\frac{3}{2}\frac{e}{R}} + \mu\right) \tag{2.9}$$

$$\overline{b}_{1_s} = \frac{1}{\left(1+\frac{\mu^2}{2}\right)}\frac{4}{3}\left(C_T/\sigma\frac{\frac{2}{3}\frac{\mu\gamma}{a}}{1+\frac{3}{2}\frac{e}{R}} + \mu\right) + \frac{12\left(\frac{e}{R}\right)}{\gamma\left(1-\frac{e}{R}\right)^3\left(1-\frac{\mu^4}{4}\right)} \times \mu\left(4\theta_t - 2\lambda\right) \tag{2.10}$$

These equations are further discussed in Subsection 5.2.4. It is interesting to note that, for small values of μ, the flapping equation is approximately linear with velocity.

The components of the flapping angles produced by the craft's pitch and roll rates, q and p respectively, are added to those of forward flight, (2.10) and (2.10), to obtain a final expression for the flapping angle:

$$a_{1_s} = \overline{a}_{1_s} + \frac{\frac{-\frac{16}{\gamma}\left(\frac{q}{\omega}\right)}{\left(1-\frac{e}{R}\right)^2} + \left(\frac{p}{\omega}\right)}{1-\frac{\mu^2}{2}} + \frac{\frac{\frac{12}{\gamma}\frac{e}{R}}{\left(1-\frac{e}{R}\right)^3}\left[\frac{-\frac{16}{\gamma}\left(\frac{p}{\omega}\right)}{\left(1-\frac{e}{R}\right)^2} - \left(\frac{q}{\omega}\right)\right]}{1-\frac{\mu^4}{4}} \tag{2.11}$$

$$b_{1_s} = \overline{b}_{1_s} + \frac{\frac{-\frac{16}{\gamma}\left(\frac{p}{\omega}\right)}{\left(1-\frac{e}{R}\right)^2} + \left(\frac{p}{\omega}\right)}{1-\frac{\mu^2}{2}} + \frac{\frac{\frac{12}{\gamma}\frac{e}{R}}{\left(1-\frac{e}{R}\right)^3}\left[\frac{-\frac{16}{\gamma}\left(\frac{q}{\omega}\right)}{\left(1-\frac{e}{R}\right)^2} - \left(\frac{p}{\omega}\right)\right]}{1-\frac{\mu^4}{4}} \tag{2.12}$$

---

[3] This is true for the X-4 in slow hovering flight, but some quadrotors, like the Stanford Mesicopter, have angled rotor shafts and must include shaft angle.

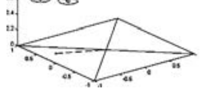

The reaction moments produced by the rotor flapping comprise two components - the rotor hub stiffness and the thrust vector acting around a displacement from the vehicle's centre of gravity:

$$M = \frac{\partial M_M}{\partial a_{1_s}} a_{1_s} + D \times T \tag{2.13}$$

where M_M is the angular moment induced at the mast by the centripedal forces of the blades ('hub stiffness'), T is the total thrust of the rotor and D is the rotor displacement from the helicopter centre of mass:

$$D = (x\ y\ z)^{\mathrm{T}} \tag{2.14}$$

The rotor stiffness, $\partial M_M / \partial a_{1s}$, is due to physical stiffness of the rotor and centrifugal forces derived from the effective hinge offset e of the rotor. The rotor stiffness due to hinge offset is given by Prouty as:

$$\frac{\partial M_M}{\partial a_{1si}} = \frac{3}{4}\left(\frac{e}{R}\right)\frac{A_b \rho R \left(\omega R\right)^2 a}{\gamma} \tag{2.15}$$

where A_b is the area of the rotor disc occupied up by the blades.

The moment about the blade flapping hinge is given by:

$$M_{\mathrm{C.F.}} = \omega^2 \beta \left(\mathrm{I_b} + \frac{eM_b}{g}\right) \tag{2.16}$$

where β is the blade flapping angle and M_b is the static moment of the blade about the hinge [Prouty 2002, pp 455–456].

Most small-scale and all full-scale conventional UAV helicopters use flapping hinges, and Bhandari and Colgren provide a six Degree of Freedom (6-DoF) flapping model for small UAVs with good experimental agreement [Bhandari and Colgren 2006], but I have not to date read any text describing the use of flapping hinges in small-scale quadrotors beside the X-4. The size of the forces involved in flapping guarantees that practically all rotors flap in translation; the light blades of the Draganflyer, although not equipped with flapping hinges, exhibit elastic flapping due to their flimsy construction. Previously experiments with very solid rotors found that pitch and roll motion induced very strong gyroscopic torques along the axis of the rotor arms, which led to structural damage of the aircraft during rapid manoeuvres [Pounds *et al* 2002].

2.4.4 Rotor Inflow Distortion

For helicopters that operate around hover, the inflow skew effects from translation have been found to have significant effects on performance. The ratio

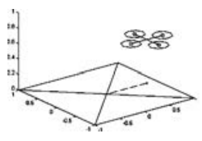

of induced rotor velocity to horizontal velocity of the wake is measured by the induced velocity distortion factor:

$$v_l = v_i \left(1 + K\frac{r}{R}\cos\psi\right) \tag{2.17}$$

where v_l is the local velocity at azimuthal position ψ and radial distance r, for a rotor with radius R, given induced flow velocity v_i and a ‘distortion factor’ K.

Prouty’s analysis [Prouty 2002, p 124] approximates the distortion factor, or Glauert Coefficient, as zero in hover or unity for forward flight. As was found in the Advancing Blade Concept helicopter, a special type of co-axial helicopter [Ruddell 1976], this assumption is not rigorous and does not hold for slow, hovering flight [Coleman 1997]. Chen gives an overview of several alternative models proposed for the Glauert Coefficient [Chen 1990].

Classical models of inflow distortion include those developed by Glauert, Coleman [Coleman *et al* 1945], Castles [Castles and De Leeuw 1954] and Heyson [Heyson and Katzoff 1957]. Modern inflow analysis extends to vortex analysis, rigid and free wake analysis and CFD techniques [Yang *et al* 2000] [Brown and Houston 2000]. The linear-skew inflow model produced by Coleman is particularly suitable to low-speed flight analysis:

$$K = \frac{1}{2}\tan^{-1}\left(\frac{v_i}{\omega r}\right) \tag{2.18}$$

where v_i is the induced flow velocity at the rotor plane.

2.5 Modern Aerodynamics

2.5.1 Aeroelasticity

Aeroelasticity is the deformation of aerodynamic structures due to the forces and torques produced during flight. The phenomenon has been understood since the 1960s, but the past decade has seen much effort towards modelling the unsteady aeroelastic problem, with the availability of sophisticated computational tools and its growing importance in the design of lighter, flexible airframes. Loewy provides an early overview of aeroelasticity problems in rotorcraft [Loewy 1969], later updated by Friedmann [Friedmann 1977].

Hyvārinen and Kjellgren describe aeroelasticity as the interaction between inertial, elastic and aerodynamic forces. The equation of motion for an elastic system of nodes is a second order system [Hyvārinen and Kjellgren 1997]:

$$M\ddot{u} + C\dot{u} + Ku = F(t) \tag{2.19}$$

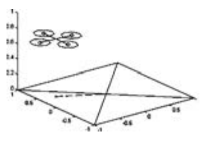

where M is a mass matrix, C is a damping matrix, K is an elasticity matrix, u is the member displacement, and $F(t)$ is the aerodynamic load. The driving load function is computed from both the aerodynamic model and deformation matrix.

Although all aspects are present in real systems, computations can be simplified by making assumptions about the coefficients. For very light members the first term will be dominated by the damping and elastic components. For systems with constant or very fast aerodynamic states, the unsteady loading function can be simplified to produce an equilibrium equation [Hyvārinen and Kjellgren 1997]. Given known structural parameters, the stability of the full system can be determined analytically.

Cutting-edge aeroelastic analysis software typically combine a CFD algorithm with the dynamic Finite Element Analysis (FEA) to compute unsteady the aerodynamic state and loads [Quackenbush *et al* 2004]. This is a computationally-intensive task, even for modern supercomputers.

Although the aeroelastic behaviour of blades is of particular interest to helicopter designers, little attention is paid to steady-state loading conditions of highly deformable wings – Leishman explains that the steady-state twisting on variable pitch blades is simply countered by increasing collective pitch [Leishman 2006, pp 378–379]. A fixed-pitch rotor, however, must be designed to compensate for static aerodynamic loading under normal flight conditions [Pounds and Mahony 2005] (see Chapter 4).

2.5.2 Unsteady Aerodynamics

The aerodynamics of rotor thrust change from given speed changes are very important for quadrotors. The non-equilibrium unsteady air flow in an accelerating rotor is due to the compressive and viscous effects of the accelerating airfoil sections parallel to the rotor plane, and the propagation of accelerating air flow through the rotor plane.

Early work on the aerodynamics of accelerating airfoils can be traced back to Wagner's 1925 potential theory for airfoils in non-uniform motion and characterisation of unsteady flat plate lift and drag [Wagner 1925]. Jones uses integral methods to extend the formulation to finite wings [Jones 1940]. More recently, several papers have analysed unsteady lift of flat plate wings applied to insect flight [Pullin and Wang 2003] [Wang 2005]. This theory can be adapted to calculate the time response of a blade's induced drag and rotor torque. However, for the X-4, the rise-time is very small, and may be ignored in modelling for control.

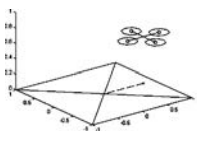

The response of the inflow velocity to rotor speed has been found to have a small dynamic effect[4]. Carpenter and Fridovitch conducted experiments into rapid pitch changes in full-scale helicopter rotors and noticed a delay in the flow response which they modelled with an “apparent mass” of the air [Carpenter and Fridovitch 1953]. Leishman, however, disagrees with the interpretation of the observations [Leishman 2002b] and instead attributes the effect to delay in the propagation of vorticity in the wake. The vortex field convection was found to be critical in estimating the transient flow of the wake during manoeuvring flight. Again, in the case of the X-4, this is found to be a fast effect, and can be neglected in dynamic modelling for normal performance (see Section 4.2).

2.5.3 Aerodynamic Disturbance Modelling

Wind, turbulence, and large aircraft wakes can have a major effect on the handling of small aircraft. There is a growing body of research that models statistical characteristics of gusts and eddies for rotor-disturbance interaction and global disturbance phenomena. Grace provides an analysis contrasting common blade-vortex interaction models and gust models for wings [Grace 2001]. These can be combined with boundary element method analysis to compute wing lift behaviour as a time-evolution of vortex interaction. A similar spectrum is provided in Shiau and Chen for natural gust velocity at ground level [Shiau and Chen 1991]. The general behaviour is of zero DC strength, a peak of low frequency power and roll-off with increasing frequency. An example spectral response from Shiau and Chen is shown in Fig. 2.23.

The behaviour of small rotors in dynamic and turbulent flow conditions has not been widely examined. Quadrotor researchers dealing with wind effects have typically treated aerodynamic disturbances as slowly varying or constant loads [Mistler *et al* 2001]. Mokhtari and Benallegue use an adaptive approach to compensate for wind disturbances, but this is not targeted at rapidly-changing dynamic wind conditions [Mokhtari and Benallegue 2004]. Hamel *et al* develop a series of tables, based on wind tunnel tests, for use in the control of ducted fan craft in changing flow conditions [Pflimlin *et al* 1997], but their model is not appropriate to free-air rotors. A spectral characterisation of free-air small-scale rotor speed variation due to noise, motion and obstacles has been experimentally

---

[4] This effect is distinct from dynamic inflow velocity as a result of craft velocity, which is often a steady-state phenomenon.

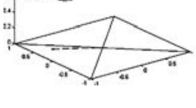

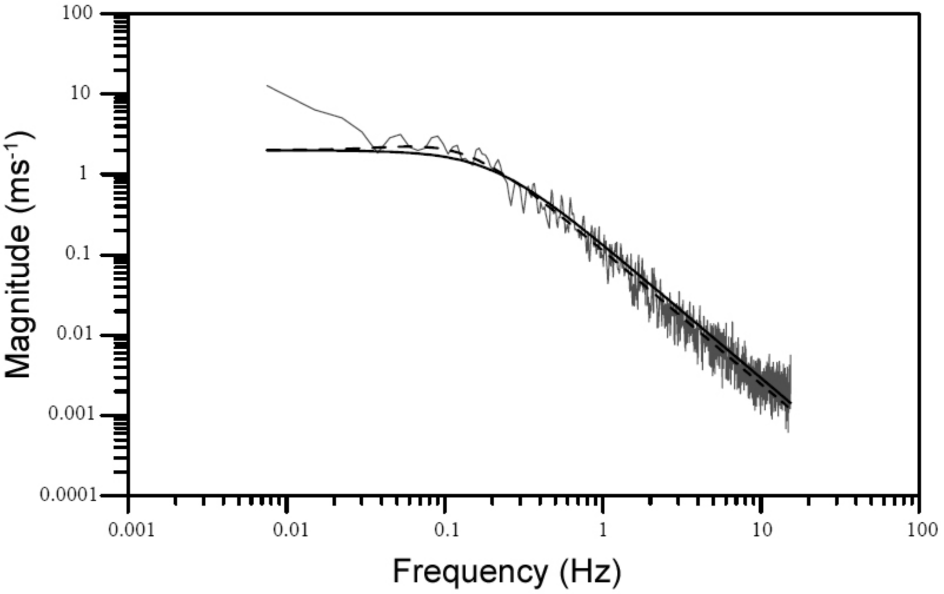

Figure 2.23: Typical Airfoil Gust Spectral Response [Shiau and Chen 1991].

derived to model typical quadrotor operating conditions [Pounds *et al* 2007a] (see Section 4.3.2).

2.6 Typical Quadrotor Models

Mathematical dynamic models of flight behaviour are essential for good control design and analysis. In this section I provide the most common model used to represent quadrotor behaviour, based primarily on Hamel *et al* [Hamel *et al* 2002], with reference to notable variations by other researchers.

2.6.1 Rigid Body Dynamics

The most basic quadrotor model used consists only of rigid body dynamics with abstract force and torque actuators and no aerodynamics — sometimes called the 'flying brick' model [Bradley 1996]. The quadrotor is represented as a mass with inertia and autogyroscopics, acted upon by gravity and control torques and forces. The rigid body dynamics of a quadrotor are easily derived from the Newton-Euler model [Hamel *et al* 2002], and equivalent derivations exist using the Lagrangian

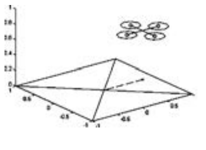

approach [Castillo *et al* 2004a] [Bouabdallah *et al* 2004b]:

$$\begin{aligned} \dot{\xi} &= RV & (2.20)\\ \dot{R} &= R \cdot \Omega_{\times} & (2.21)\\ m\dot{V} &= mge_3 - RF & (2.22)\\ \mathrm{I}\dot{\Omega} &= -\Omega \times \mathrm{I}\Omega + \Gamma & (2.23) \end{aligned}$$

where ξ is position vector, R is the rotation matrix, V is the velocity vector, Ω is the rotational velocity vector, m is the mass, I is the inertia, g is acceleration due to gravity in inertial direction e_3, and F and Γ are the applied force and torque. Here $x_{\times}$ is the skew-symmetric matrix such that $a_{\times}b = a \times b$ for vectors in $\Re^3$. These dynamics can also be written in matrix form [Bouabdallah *et al* 2004a]:

$$\begin{pmatrix} mI_3 & 0 \\ 0 & \mathrm{I} \end{pmatrix} \begin{pmatrix} \dot{V} \\ \dot{\Omega} \end{pmatrix} + \begin{pmatrix} \Omega \times mV \\ \Omega \times \mathrm{I}\Omega \end{pmatrix} = \begin{pmatrix} F \\ \Gamma \end{pmatrix} \tag{2.24}$$

The rotational dynamics can be written as Equations (2.21) and (2.23), or in a quaternion representation [Tayebi and McGilvray 2004].

2.6.2 Rotor Dynamics

The driving forces and torques of the rigid body dynamics are further modelled to better represent the craft behaviour. Complete models include a basic representation of the aerodynamics and mechanics associated with the rotors — thrust, torque and gyroscopics — and motor dynamics [Hamel *et al* 2002] [Tayebi and McGilvray 2004] [Bouabdallah *et al* 2004a].

Rotor force and torque are modelled as quadratic functions of rotor speed, without specific consideration of the underlying aerodynamic coefficients [Hamel *et al* 2002] [McKerrow 2004]:

$$T_i = b\omega_i^2 \tag{2.25}$$

$$Q_i = k\omega_i^2 \tag{2.26}$$

where T and Q are thrust and torque, k and b are amalgamated coefficients and ω is the rotor speed or the ith rotor.

The force and torque vectors, F, is the summation of the individual rotor thrusts in the vertical direction:

$$F = \sum_{i=\mathrm{N,S,E,W}} T_i e_3 \tag{2.27}$$

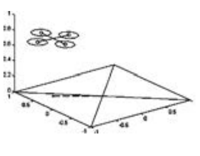

The torque, Γ, is the summation of the rotor thrust couple and gyroscopic moments. The torques produced by the thrust vectors are implemented as a multiplication between a rotor speed vector and a hub displacement [Pounds *et al* 2002]:

$$\Gamma_T = \begin{pmatrix} 0 & 0 & bd & -bd \\ bd & -bd & 0 & 0 \\ k & k & -k & -k \end{pmatrix} \begin{pmatrix} \omega_{\mathrm{N}}^2 \\ \omega_{\mathrm{S}}^2 \\ \omega_{\mathrm{E}}^2 \\ \omega_{\mathrm{W}}^2 \end{pmatrix} \tag{2.28}$$

where d is the displacement of the rotor hub from the craft centre of gravity.

Hamel *et al* substitute a rigid rotor model with gyroscopic effects in place of the flapping behaviour of flexible rotors [Hamel *et al* 2002]:

$$\Gamma_{\mathrm{gyro}} = \sum_{i=\mathrm{N,S,E,W}} \mathrm{I}_R(\omega_i \times e_3)\Omega \tag{2.29}$$

I_R is the rotor inertia. Bouabdallah *et al* do cite flapping as a quadrotor dynamic effect, but do not model the dynamics and instead use a rigid model for their control [Bouabdallah *et al* 2004a].

Motor dynamics are given as a function of drive torque [Hamel *et al* 2002]:

$$\mathrm{I}_R\dot{\omega} = \tau - Q \tag{2.30}$$

where τ is the drive torque.

A model that uses rotor flapping modifies (2.27) to include a directed thrust component due to rotor tilt [Pounds *et al* 2004]:

$$F = \sum_{i=\mathrm{N,S,E,W}} T_i \begin{pmatrix} -\sin a_{1_s i} \\ \cos a_{1_s i} \sin b_{1_s i} \\ \cos b_{1_s i} \cos a_{1_s i} \end{pmatrix} \tag{2.31}$$

where the s_x and c_x notations represent $\sin x$ and $\cos x$ respectively. The flapping angles are calculated using the equations in Section 2.4.3, modified to account for generalised lateral and rotational motion of the craft (see Section 5.2.4).

2.7 Control

The control of quadrotors, and UAVs in general, is an active field of study with many recent papers. Three areas of control research are touched on by the X-4's development: attitude estimation, attitude control, and limitations of control. Progress in these fields is outlined below.

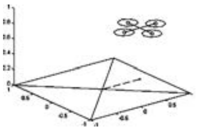

2.7.1 Attitude Estimation

As accurate inertial navigation systems developed by military research are unavailable to small and affordable civilian UAVs, low-cost sensors with possibly biased or noisy measurements must be used instead. Estimation schemes have been developed to filter multiple sensor inputs to produce reliable estimates of flight attitude [Roberts *et al* 2003].

Linear and Kalman filtering techniques have been in use for many years. Extended Kalman filters have proven popular for attitude estimation of spacecraft, typically with a three-dimensional representation of full Special Orthogonal Group-3 ($SO(3)$) coordinates [Crassidis *et al* 2007]. Jun *et al* use a Kalman filter with gyroscope and accelerometer data for a model-independent estimator for robot helicopters [Jun *et al* 2006]. Bachmann *et al* use a quaternion extended Kalman filter with gyroscope, accelerometer and magnetometer data [Bachmann *et al* 2001]. However, the unpredictable nature of extended Kalman filters for nonlinear problems such as walking robots or helicopters makes them difficult to tune [Rehbinder and Hu 2004].

Nonlinear techniques have been developed for cases where pose singularities, instabilities and gyroscope bias errors become significant, such as satellite attitude kinematics [Crassidis *et al* 2007]. Nonlinear observer formulations have shown good robustness and bias rejection performance [Mahony *et al* 2008]. Vik and Fossen use a nonlinear observer to fuse INS and GPS measurements, combining the long-term stability of GPS with the short-term accuracy of inertial sensors [Vik and Fossen 2001]. Thienel and Sanner proved exponential stability of bias estimates for a nonlinear observer with closed loop control [Thienel and Sanner 2003].

Section 2.7.2 discusses the combination of estimation algorithms with closed loop control.

2.7.2 Attitude Control

Attitude control is the foremost enabling technology for autonomous helicopters. The controllability of a helicopter by a human is directly related to the bandwidth of the open-loop pitch and roll dynamics. Conventional radio-control helicopters and UAV rotorcraft employ Bell-Hillier linkages to add damping to slow down the dynamics [Done and Balmford 2001, pp 175–178]. Small quadrotors without these features cannot fly without some form of feedback control to provide artificial damping.

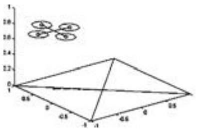

The earliest control systems used on quadrotor toys in the early 90s provided pilot augmentation via rate gyro feedback. Since their adoption by UAV researchers around the world, these toys have been flown with a variety of controllers. Most controllers are orthogonal SISO designs with independently acting pitch and roll, however Multiple-Input Multiple-Output (MIMO), nonlinear controllers, robust controllers and vision-based schemes have also been implemented.

By far the most common control scheme used for quadrotors is the linear Proportional-Integral-Derivative (PID) controller. Numerous researchers and hobbyists have used this type of compensator with success. Bouabdallah *et al* compared PID against an Linear Quadratic (LQ) scheme and found the two performed comparably [Bouabdallah *et al* 2004b]. Altŭg *et al* use a linear Proportional-Derivative controller to control yaw on a vehicle constrained to vertical and yaw motion, but deviations introduced by the test rig make the performance difficult to gauge [Altŭg *et al* 2002].

Stanford's STARMAC flyer uses LQ regulator attitude control inside an integral sliding-mode position control [Hoffmann *et al* 2004] [Waslander *et al* 2005]. The controller was found to give good control at low rotor speeds but 'degraded' at higher speeds reportedly due to the increased vibrations. They report, "This was solved by implementing a softer attitude controller with lower costs on attitude deviations. This improved noise rejection at the cost of tracking performance."

Nonlinear control is common in quadrotor attitude control research. Mistler *et al* show that the nonlinear dynamics of quadrotors cannot be exactly linearised or decoupled into a nonlinear SISO system, but go on to use a dynamic feedback technique to linearise the behaviour [Mistler *et al* 2001]. They state that this method is not as flexible as Lyapunov control techniques for nonlinear systems, as it cancels beneficial nonlinearities in the system and requires feedback of all the states. Linearisation via feedback is a common method used to control the nonlinear dynamics.

Papers by Tayebei and McGilvray have demonstrated test-rig control of Draganflyers using nonlinear PD and PD^2 schemes, both in $SO(3)$ and quaternion characterisations, derived with Lyapunov stability analysis. The PD^2 controllers demonstrated ±2 degrees tracking [Tayebi and McGilvray 2004] [Tayebi and McGilvray 2006]. Bouabdallah *et al* also implements a PD^2 controller on the 'OS4' craft built at EPFL [Bouabdallah *et al* 2004a] with similar performance.

Guenard *et al* use a Lyapunov approach to design a quaternion controller with backstepping techniques for the CEA X4-Flyer with good results

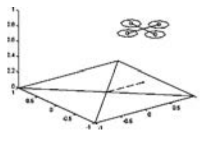

[Guenard *et al* 2005]. The aircraft also has adaptive Lyapunov-derived altitude control via an ultrasonic sensor [Guenard *et al* 2006].

Mokhtari and Benallegue also use a Lyapunov approach to control their nonlinear model in position, combined with an adaptive control to compensate for wind disturbances [Mokhtari and Benallegue 2004]. They hold that attitude should be controlled directly, as it can be measured more accurately and is the variable directly acted upon by the thrusters. Although they do not have experimental data, their simulation shows that a quadrotor can track a position curve using attitude control, in the presence of wind.

Castillo *et al* employ a Lagrangian approach to deriving the flyer model and a Lyapunov-derived PD compensator, producing a smooth controller with ±1 degree tracking and a small offset [Castillo *et al* 2004a] [Castillo *et al* 2004b]. Salazar-Cruz *et al* advance on these results and show that a small quadrotor with ±3 degrees roll-pitch angle tracking can follow an X-Y position trajectory with an accuracy of ±100 mm [Salazar-Cruz *et al* 2005].

Many of these researchers have also used sliding-mode controllers for quadrotors. Bouabdallah and Siegwart have implemented backstepping and slide-mode control on the ‘OS4’ with ±1 degree pitch-roll performance [Bouabdallah and Siegwart 2005b]. Benallegue *et al* have implemented a feedback linearised controller with a sliding mode observer running in parallel on their quadrotor simulator [Benallegue *et al* 2006]. Their approach aims to reduce the number of sensors required by the quadrotor and still be robust to disturbances — the sliding-mode observer acts to estimate the influence of external disturbances and reject them.

Another popular branch of control research for quadrotors is robust control. Mokhtari *et al* combine a feedback linearisation scheme with an H_∞ controller [Mokhtari *et al* 2005]. They show that this combination can make the whole aircraft robust to disturbances and design uncertainty, and provide a sensitivity analysis for their physical system. Park *et al* developed a Robust-Interal Loop controller to operate in conjunction with PID, as the PID compensator did not adequately handle noise and disturbances in flight [Park *et al* 2005]. The inner loop controller causes the plant to track the model around which the PID is designed. Their 1.8 kg custom-built flyer, using rigid hobby propellors, demonstrated flight with unspecified attitude tracking error.

Although the predominant control scheme for quadrotors uses MEMS gyroscopes and accelerometers to sense the motion of the craft, visual control schemes have also been used to detect motion and provide feedback. The trend of these

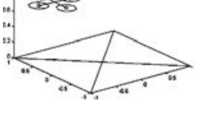

experiments is to use MEMs devices to control attitude and close the loop around position, even though many of the estimation schemes can extract pose directly.

Altŭg *et al* use a camera on the ground observing the quadrotor to estimate pose and position, although a set of onboard MEMS gyros were also used to control attitude [Altŭg *et al* 2002]. The attitude regulator used was a feedback linearisation controller. This system was expanded to include an onboard camera that tracks the position of the ground station — this improved the attitude control to a ±5 degrees and the position tracking to ±130 mm [Altŭg *et al* 2003]. Although it has yet to be implemented in hardware, Shakernia *et al* have shown that a UAV can land using motion reconstruction from visual observation of markers on a landing pad [Shakernia *et al* 1999], although onboard accelerometers are still required for pose extraction. Their egomotion estimator was used inside the control loop to recover pose and position information. In simulation their system was able to control both quadrotor position and pose given noisy target data. Romero *et al* use a similar 'N-points' and '2D planar' technique, but with full 6-axis INS data for control [Romero *et al* 2003]. The first method uses a set of points of known relative position, and the second uses a cluster of unknown points constrained to lie in a known 2D plane to extract pose. Both of these provide ±100 mm position tracking, but no pitch-roll accuracy is given.

It is possible to combine pose estimation with a control scheme by adding an output driving term to the estimation algorithm. Mahony *et al* demonstrate this for nonlinear rigid-body dynamics on $SO(3)$ [Mahony *et al* 2005] [Hamel and Mahony 2002]. This work is closely related to work that uses the quaternion formulation for the design of nonlinear attitude filters [Salcudean 1991] [Vik and Fossen 2001] [Thienel and Sanner 2003]. Tayebi and McGilvary develop a quaternion nonlinear algorithm to stabilise their quadrotor [Tayebi and McGilvray 2004] [Tayebi and McGilvray 2006], but early work in this area predates the development of quaternion-based filters [Wie *et al* 1989] [Wen and Kreutz-Delgado 1991] [Fjellstad and Fossen 1994].

Mahony *et al* developed these ideas further, producing a nonlinear explicit complementary filter that separated the estimation problem from the control problem [Hamel and Mahony 2002]. Building on this, they produced a combined nonlinear control-estimator for MAVs [Mahony *et al* 2006] that did not require numerical reconstruction of attitude and provided weightings for observer response tuning for the system noise characteristics.

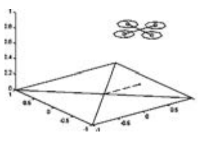

2.7.3 Fundamental Limits of Control

The basic premise of the fundamental limits of control is that there is an intrinsic ceiling to the performance obtainable by a control system, irrespective of the control scheme used. The concept is recorded by Bode in 1945 [Bode 1945] and was understood by practising engineers through the following decades [Stein 2003], although it was somewhat ignored by researchers during the development of state-space methods from the late 50s through to the late 80s. In the 1990s Goodwin and others reconsidered the fundamental limits of control from a modern perspective [Seron and Goodwin 1995] [Seron and Goodwin 1996] [Middleton and Goodwin 1990] [Middleton 1991].

Bode's eponymous integral relates the sensitivity function of a closed-loop system to the number of unstable poles of the open-loop system [Seron *et al* 1997]:

$$\int_0^\infty \log|S(e^{j\omega})|d\omega = \pi \sum_{i=1}^{n_p} p_i \tag{2.32}$$

where S is the sensitivity function of the closed-loop system, p_i are the poles of the open loop plant, and ω is frequency.

A result of this relationship is that control action to decrease sensitivity at one frequency must intrinsically increase sensitivity elsewhere in the spectrum — the so-called 'water-bed effect' [Francis and Zames 1984] [Freudenberg and Looze 1987]. Consequently, it is not possible to specify arbitrarily sensitivity targets for the closed-loop system across the whole frequency range.

This has important implications for aircraft design, in that the natural instability of the open-loop system must be minimised for best closed-loop sensitivity performance (see Section 5.4).

2.8 Perspectives on Quadrotor Design

The evolutionary niche of the X-4 amongst UAVs is in the early civilian adoption of aerobots capable of performing real tasks. As stated in Section 2.3, simplicity and reliability are key factors for practical flying robots to be used in the commercial sector. This leads naturally to a top-down approach in which the global aircraft is designed from the outset to be robust and adhere to predetermined performance specifications.

The detail in which full-scale helicopter aerodynamicists model rotorcraft behaviour with analytical models and CFD is indicative of the importance of

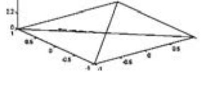

representing the complex aspects of the entire system. Consequently, the obvious question is why do quadrotor designers neglect these terms? Although the desire for concise simplicity when designing small-scale vehicle control systems leads to purposefully ignoring of some of the complexity of larger aerodynamic systems, the results of Bohorquez *et al* suggest that full-scale phenomena are applicable to small-scale rotorcraft and thus bear modelling and investigation [Bohorquez and Pines 2003].

All of the quadrotor control papers surveyed make the assumption that there is no relation between horizontal translation and pitch-roll attitude dynamics, but the physics of rotor flapping show that, even around hover, this is a false assumption. Bouabdallah *et al* goes so far as to list rotor flapping as a dynamic influence on the craft, only to omit it in the derivation of the controller [Bouabdallah *et al* 2004a]. I believe there is a need to correct the oversight in the literature and provide a model and control scheme with flapping dynamics in mind.

PID control is the benchmark control scheme and has shown good performance with low complexity — this makes it an obvious starting point for practical flight control. Mokhtari and Benallegue hold that attitude should be controlled directly, inside a position loop, as it can be measured more easily than position and is the variable directly acted upon by the thrusters [Mokhtari and Benallegue 2004]. Tayebei and McGilvray make the observation that for good attitude performance the rotor speed should converge to its target faster than the attitude diverges [Tayebi and McGilvray 2004]. The implication is that fast motor response is essential, and dynamic motor control is a logical step towards improving quadrotor attitude regulation.

Benallegue *et al* raise the importance of quadrotor performance with reduced sensors [Benallegue *et al* 2006]. The philosophy behind reducing the complexity of mechanical systems can be equally employed to reduce the complexity of avionics systems. Improving the sensors through better estimation schemes and minimising the number of sensors necessary to control the craft can potentially improve the reliability of the system. In the same vein, the technology for combining estimation with attitude control potentially eliminates the processing and communications overhead inherent in distinct sensor-estimation-control schemes. From the work of Mahony *et al*, it is possible to bring together nonlinear complementary filtering and attitude estimation in a nonlinear framework to solve the coupled attitude estimation and control problem without explicitly calculating the pose matrix [Mahony *et al* 2006].

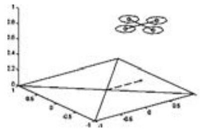

Chapter 3

X-4 Hardware

In this chapter I outline the X-4 Flyer's hardware systems and principal design concepts. I describe the functionality and interconnections of vehicle subsystems and provide the rational behind design aspects uncommon to other quadrotors. Additional details of specific avionic systems and interfaces are provided in Appendix B and C.

The X-4 Flyer has several key differences from other quadrotors that make it unique. The flyer weighs 4.34 kg compared with less than 1 kg for most other documented quadrotors. It carries a much larger, non-integrated and flexible payload than other quadrotors — up to 1 kg compared with approximately 100 g for smaller vehicles. These design decisions make the X-4 Flyer a heavier, higher-powered vehicle than other quadrotors of similar footprint.

An important design feature of the X-4 is its mechanical simplicity. It has no complex moving assemblies that must be maintained. The only maintenance required between flights is recharging of the batteries, ensuring electrical connections and chassis fasteners are tight, and a periodic bearing change.

This chapter is divided into six sections. Section 3.1 presents the system-level specifications fo the X-4. Section 3.2 describes the airframe and chassis hardware. Section 3.3 outlines the hardware and requirements of the rotors and motors. Section 3.4 outlines the avionics architecture, onboard electronics and communications subsystems. Offboard communications, electronics and human interface hardware is given in Section 3.5. Finally, Section 3.6 reports the safety systems built into the flyer and the secure operating cage.

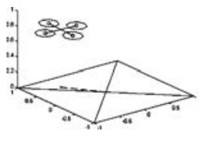

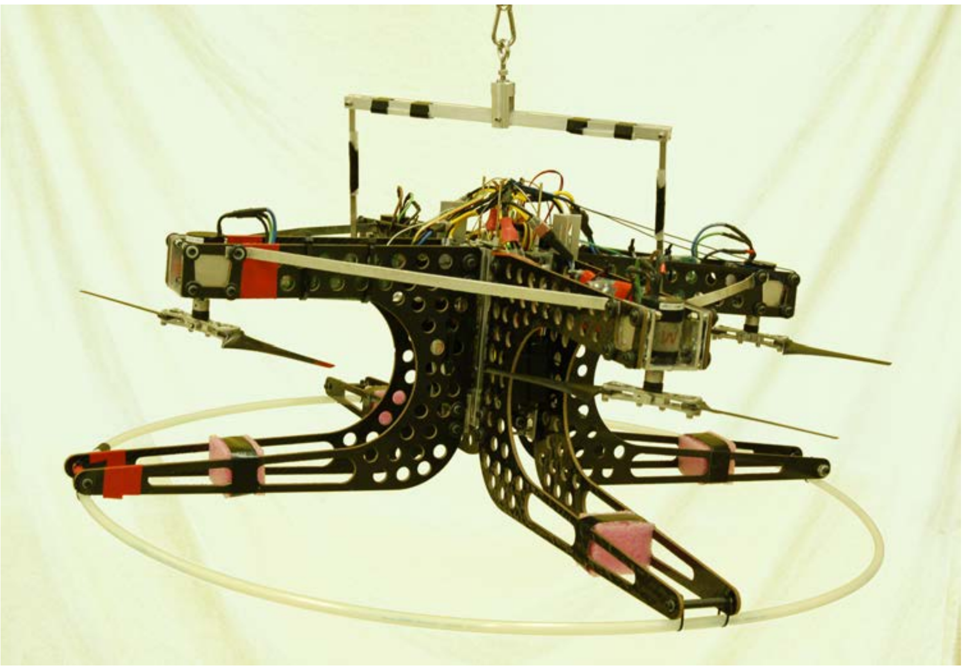

Figure 3.1: X-4 Flyer Quadrotor Helicopter.

3.1 X-4 Flyer Overview

As discussed in Chapter 1, two design parameters drive the X-4's design:

- 1 m maximum width rotor-tip to rotor-tip.
- 0.5 to 1 kg payload.

Given its intended use as an experimental platform, and the projected functionality of commercial quadrotors operating in enclosed spaces, the X-4 was sized to be small enough for flying indoors and tight spaces, but large enough to fly outdoors as well. A minimum payload of 0.5 kg allows for a variety of sensors to be mounted onboard, while a full kilogram of payload allows for sophisticated sensors systems such as a laser scanner or vibration-isolated gimbal mounts for precision sensor systems.

The X-4 must be significantly heavier than other small quadrotors in order to accommodate 1 kg of payload. The flyer's weight is 3.5 kg unloaded, for a loaded weight of 4–4.5 kg. The X-4 must lift its weight with a 30 per cent control margin, requiring 5.85 kg maxmimum thrust.

The present version of the flyer weighs 4.34 kg, unladen, and is capable of lifting up to 4.6 kg with a 30 per cent control margin. It comprises a chassis made from aluminium and carbon-fibre, off-the-shelf brushless motors, and

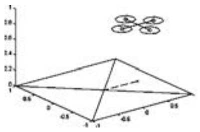

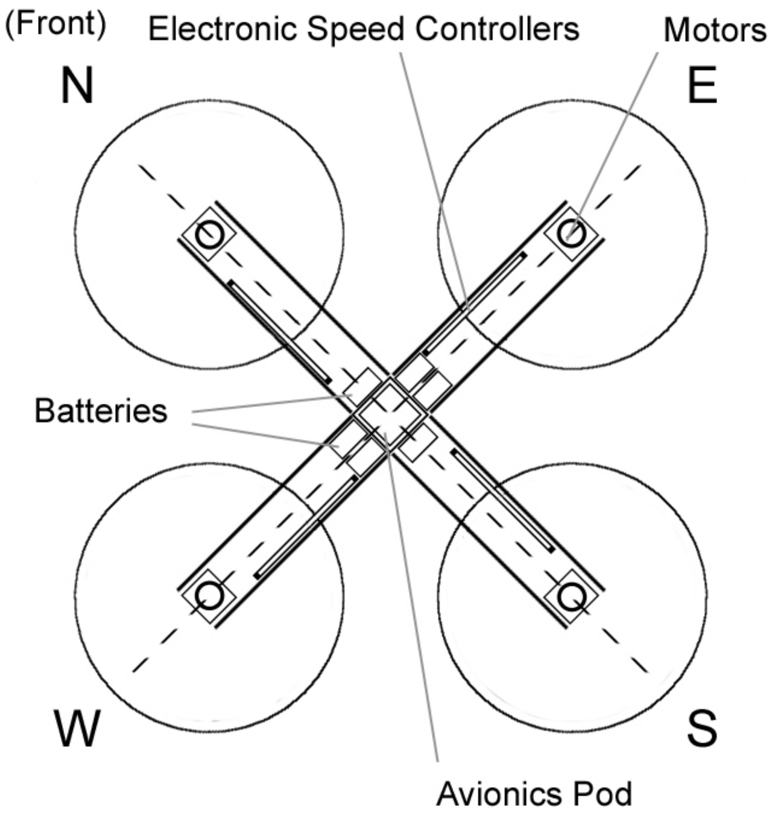

Figure 3.2: X-4 Flyer Layout and Subsystems.

lithium polymer batteries and custom-built avionics and controllers. The 800 g weight above the design target is the result of excess weight in the airframe and avionics vibration-isolation units.

3.2 Chassis

3.2.1 Airframe

The X-4's airframe is immediately distinctive because of its inverted, mid-mounted rotors (see Fig. 3.1). These features are unusual amongst quadrotors, which typically mount their rotors above the frame and other components. This rotor placement was specifically chosen to position the rotor plane close to the vehicle's centre of mass, leading to improved dynamic properties (see Chapter 5).

The inversion of the motors — placing the motors above the rotors — serves two purposes. Firstly, it raises the centre of mass so that the top and bottom half

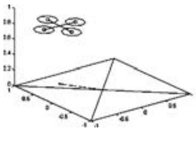

of the flyer are balanced about the rotors. Secondly, it causes the rotor to push up against the motor end-stop so that, even if a rotor mounting screw should loosen in flight, the rotor will be remain on the shaft rather than flying off the vehicle and posing a hazard to operators.

Following from the low-mounted rotors, the X-4 sports four landing legs that keep the rotor plane clear of the ground. Typical quadrotors land on a central pedestal or rigid legs attached to the frame, but these rarely extend beyond the hub of the rotors and heavy side-ways landings can allow the rotor blades to strike the ground. The X-4's legs extend well beyond the rotor hubs — the flyer must pitch more than 60 degrees before the rotors will strike the ground. A plastic hoop is attached at the base of the legs to enable them to slide freely on the landing platform and so prevent them from catching on the ground and flipping the flyer.

The X-4's airframe design and fabrication are documented in Green [Green 2003]. The total mass of the airframe, by itself, is 1.2 kg. It consists of an aluminium core, four cross-linked carbon fibre arms and four motor pods. The flyer's arms and avionics pod bolt onto the central aluminium core. The all-metal centre frame is very strong and rigid, but its 0.5 kg weight was heavier than anticipated. The flyer's arms are made of milled foam carbon-fibre sandwich sheet, and offer convenient mounting points for motor pods, controllers and batteries. Four cross-braces connect the arms into a box-car truss to reduce oscillations.

3.2.2 Vibration Isolation

At flight speeds, the rotors induce significant vibration in the airframe and it is necessary to mechanically isolate the sensitive avionics and sensors [Dunbabin *et al* 2004]. The mounting space inside the chassis houses a suspended avionics stack built on brass rod with nylon spacers fixed in Delrin mounts (see Fig. 3.3). The Delrin brackets are screwed into four rubber isolator mounts, arranged at the top and bottom of the stack in a tetrahedron geometry, and attached to the central aluminium core.

The rubber mounts are commercially available McMaster-Carr vibration insulation products rated with a frequency cut-off of 50 Hz. The mechanical damping provided by this installation eliminates the induced vibration noise associated with the 135 Hz rotation of the rotors.

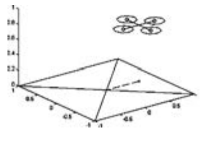

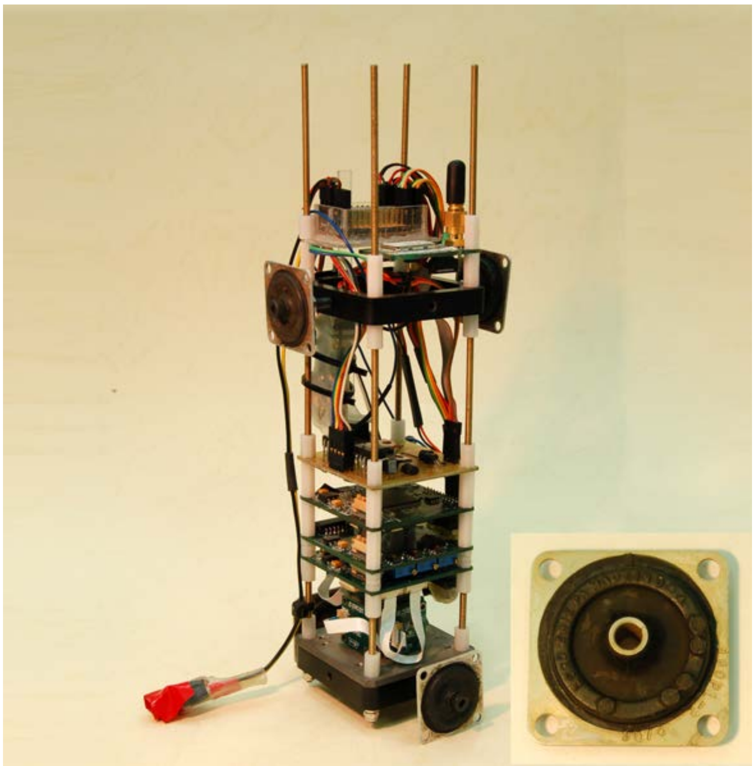

Figure 3.3: Avionics Vibration-Isolation Pod and Rubber Mount (Inset).

3.2.3 Test Gimbal

The chassis has mounting points for an attitude control test gimbal (see Fig. 3.4). The gimbal allows the robot to be freely rotated around its centre of mass, whilst firmly tethered in place so that it can be tested safely in a cage. The gimbal mounting rails are removed prior to free flight.

The flyer gimbal is unusual compared with other quadrotor test rigs. The X-4's gimbal consists of parallel links that produce a virtual joint which allows the craft to rotate freely on all three axes, aligned with the flyer's centre of mass. The rotational behaviour of the X-4 mounted in the gimbal provides a good representation of the attitude dynamics the flyer would experience in flight. Other typical test rigs consist of a ball-joint mounted underneath the quadrotor, which adds an inverted-pendulum dynamic.

The frame is made of solid links that add slightly to the rotational inertia of the flyer system but prevent the frame from flexing in operation. Rather than rotating about the long pitch and roll axes of the flyer, the axes of the gimbal are offset 45°. This provides the widest rotational range with the smallest and lightest gimbal. The geometry of the frame allows the flyer to pitch and roll by

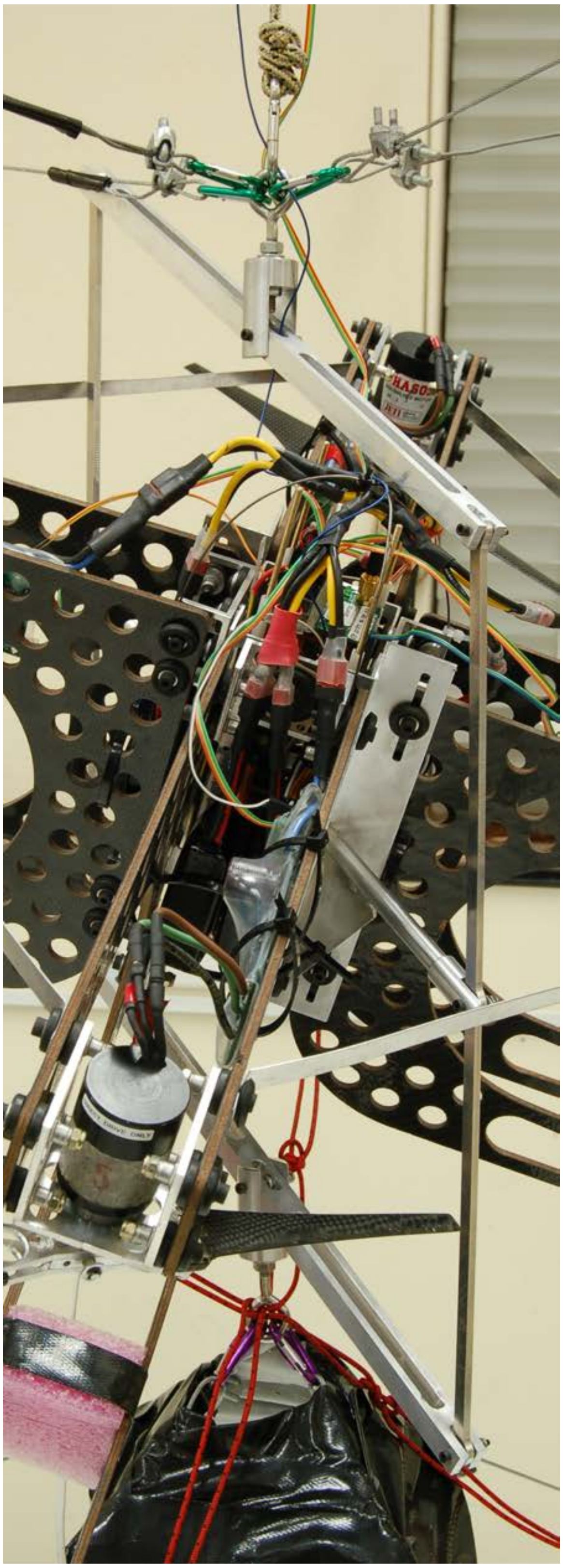

Figure 3.4: Flyer Gimbal Mount.

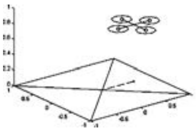

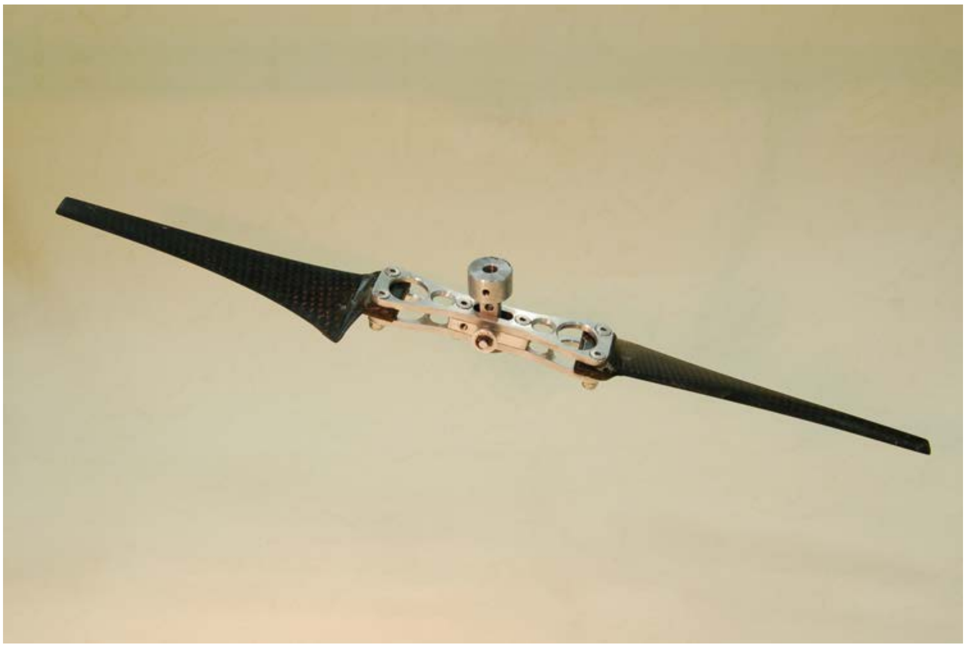

Figure 3.5: ANUX2 Teetering Hub Rotor.

up to 25° and rotate 360° in yaw. During operation, pitch and roll are limited to 15° deflection by guy-lines. A bolt clamp can be used to prevent the flyer from yaw motion. All gimbal joints use ball bearings to reduce friction.

3.3 Drive System

3.3.1 Rotors

Rotors are a key aspect of the X-4, given the performance demanded by the size and weight specifications. The combination of small rotors, fixed-pitch blades and high loading create a difficult design problem. The high disc-loading of the flyer's rotors produces concentrated aerodynamic pressure at the leading edges of the rotor blades, causing them to twist about their radial axis. The X-4's blades must be specially designed to twist into the correct angle under load. Chapter 4 reports the process used to produce these rotors.

The power needed to generate the required amount of thrust increases with decreasing rotor size, and so the largest rotors that fit within the design limitations should be used. The maximum size of the rotors is also constrained by the need to avoid closely-spaced rotor tips interfering with each other. The spacing of the rotors was chosen to provide a clearance of $R\sqrt{2}$ from the rotor

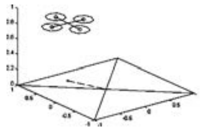

hub, where R is the rotor radius, based on the assertion that the velocity of the potentially-interfering flow upstream is half that at the rotor plane [Green 2003].

The limited size of the rotors requires a high inflow velocity to move the necessary volume of air to support the weight of the craft [Prouty 2002, p 4]. Consequently, quadrotor designs must optimise their rotors to be efficient at higher inflow speeds than conventional helicopters. Early tests with off-the-shelf hobby propellers demonstrated that properly engineered rotors were essential to meet these performance requirements [Pounds *et al* 2002].

For a quadrotor helicopter weighing 4 kg with a 30 per cent control margin, each motor must produce 12.7 N of thrust. The rotor radius can be no greater than 0.165 m, due to the size of the robot. The power requirement can be calculated from classical rotor momentum theory [Seddon 1996, p 6]:

$$P_i = \frac{T^{3/2}}{\sqrt{2\rho A}} \tag{3.1}$$

where P_i is the power induced in the air, T is the rotor thrust, ρ is the density of air and A is the area of the rotor disc. For the X-4 Flyer specifications, each rotor requires 101.2 W of power induced in the air.

Honnery [Honnery 2000] gives Mach 0.3–0.4 as the onset velocity of fluid flow compressibility effects; thus, the rotational velocity should ideally be less than 800–1000 rad·s^{-1}. The original batteries selected for the X-4 had a steady-state current limit of 22 A, which limits the motor to a maximum torque of 0.1749 Nm, and hence a top shaft power of 148 W at a target speed of 850 rad·s^{-1}. See Subsection 3.3.2 for a discussion of motor torque theory.

An ideal rotor's thrust and torque are related to its rotational velocity by quadratic relations [Prouty 2002, p 15]:

$$T = C_T \rho A R^2 \omega^2 \tag{3.2}$$

$$Q = C_Q \rho A R^3 \omega^2 \tag{3.3}$$

where T is the thrust, Q is the torque, C_T and C_Q are non-dimensionalised thrust and torque coefficients, R is the rotor radius and ω is the rotor speed. The coefficients C_T and C_Q are constants determined from airfoil data or empirical tests. Given an estimated rotor speed of 850 rad·s^{-1}, the minimum C_T required is 0.005. The coefficients are related by:

$$C_Q = C_T \sqrt{C_T/2} \tag{3.4}$$

The required torque is 0.082 Nm, leading to 70 W of induced power in the air to hover.

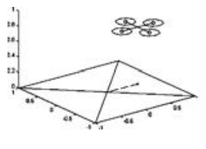

Assuming a perfect rotor Figure of Merit (F.M.) of 1 — the ratio of output power in the air, over the input shaft power [Done and Balmford 2001, p 55] — the maximum achievable theoretical thrust is 15.1 N per motor. In practice, a F.M. of 1 is impossible to achieve. Typical helicopters operate with F.M.s of 0.6–0.8 [Prouty 2002, p 5]. A commercial quadrotor such as the Draganflyer IV has an estimated F.M. of 0.4–0.5. For the X-4, the design F.M. must be no less than 0.77. This was recognised as a challenging but realistic goal; the production rotors achieved a F.M. of 0.75.

Unlike virtually all other small-scale quadrotors, the X-4 Flyer uses mechanical flapping hinges (see Fig. 3.5). These allow the blades to rotate about the rotor mount in response to changing aerodynamic conditions — they are essential to the function of all helicopters in translational flight. All rotorcraft exhibit flapping behaviour, but those lacking mechanical hinges flap by means of the elastic flex of the rotors. The causes and effects of blade flapping are described in detail in Section 2.4 and expanded on in Section 5.2.

The flapping hinge used in the flyer is a teetering hinge consisting of a blade mount on a single pivot through the centre of the rotor hub. This allows one blade to ascend as the other descends in concert. The symmetry of two-blade flapping ensures that there is no need for lead-lag flex between the blades. A rubber stop prevents the blades from flapping so far as to strike the structure of the flyer.

Unlike designs with two separate hinges, as typically used in full-scale helicopters, this configuration has no hinge offset and so produces no blade-couple moment in flapping. Fixed rotorheads with no hinges induce very strong gyroscopic moments on the rotor mast. In the case of the original X-4 flyer with solid hobby aeroplane propellors for rotors, the gyroscopic torques were sufficient to break the structure of the craft [Pounds *et al* 2002]. The elimination of these torques, along with their inherent mechanical simplicity, makes teetering hinges an obvious choice for the X-4.

3.3.2 Motors

The rotors are driven by JETI Phasor 30/3 hobby aircraft brushless motors (see Fig. 3.6). The Phasor 30/3 is a six-pole, 18-stator-coil motor designed for direct propeller drive without a gearbox. They were selected for their maximum power rating of 350 W, low-speed, high-torque performance and availability at the time. The motors are sensorless and must be commutated electronically via

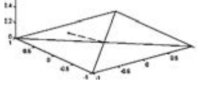

Figure 3.6: Jeti Phasor 30/3 Brushless Motor.

back-EMF or with external sensors.

The motors are mounted on pods that screw into the carbon-fibre arms. The pods can be shimmed so that the motor axis is tilted side to side. This allows for a mechanical yaw trim to be introduced to offset the natural imbalance in rotor torques between the sets of contra-rotating blades. Each motor is 35x55 mm and weighs 290 g.

From the manufacturer's data, and verified by testing, the flux-linkage coefficient of the motor is $\lambda = 0.00795$. The torque produced by the motor is proportional to the current flow [Cogdell 1999, p 853]:

$$\tau = \lambda I \tag{3.5}$$

where τ is the torque, and I is the current. Given a limited battery current of 22 A, this sets a maximum available torque of 0.1749 Nm. The shaft speed is determined by the drive voltage, and can be calculated using the back-EMF of the coils:

$$\varepsilon = \lambda \omega \tag{3.6}$$

where ε is the motor back-EMF. Using the rotor torque equation (3.3), the speed of the motor under load is found by solving the simple quadratic:

$$V = \frac{C_Q \rho A R^3 \omega^2}{\lambda} R_{\text{bat}} + \lambda \omega \tag{3.7}$$

where V is the applied voltage, R_{bat} is the internal resistance of each lithium polymer cell. Given unlimited current and a 16.8 V supply with a combined internal resistance of 0.03 Ω, the maximum speed of the target rotor described in Section 3.3.1 is 1580 rad·s^{-1}. However, as the batteries have a current draw ceiling of 22 A, the actual speed cannot be greater than 1240 rad·s^{-1}.

In operation, the motors have proven to be very robust and have operated for hundreds of hours each, with two bearing changes, and only one motor failure

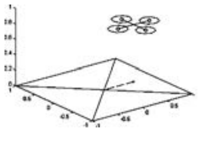

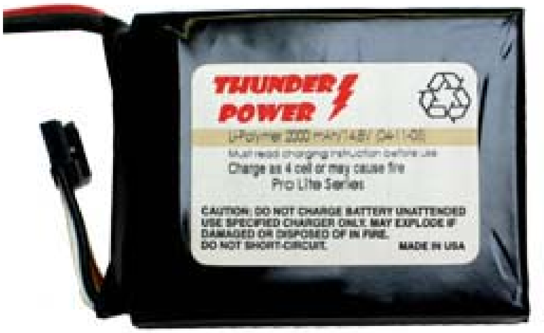

Figure 3.7: 14.8 Volt 2000 mAHr Lithium Polymer Battery Pack.

in the life of the project[1]. More advanced motors are now available and have been specified to replace the aging (and now unavailable) Phasor motors. The Torcman 280-15 outrunner motor has been tested with the ANUX2 rotors and found to produce the same thrust performance. The 280-15 is 35x40 mm and weighs 160 g, offering a net weight saving of 0.5 kg for all four motors.

3.3.3 Batteries

Lithium polymer cells are currently the only practical choice for light-weight, high-current, high-capacity power storage. The X-4 uses six parallel battery packs of four cells, connected in series. Each cell produces 3.7 V and 40 A continuous current draw. The internal resistance of each cell is approximately 0.03 Ω. Each Thunder Power battery (see Fig. 3.7) provides a nominal 14.8 V and 2000 mAHrs of energy, giving the X-4 an endurance of more than 11 minutes flight time.

Lithium polymer battery technology moves quickly — the first set of cells used had an absolute maximum current draw of 24 A, only 1500 mAHrs capacity and weighed 1.10 kg. The latest cells weigh 0.98 kg, a saving of 12 per cent. Even with the latest technology, the cells remain the heaviest subsystem of the flyer and the bottle-neck of system performance. The flyer's endurance and payload capacity are expected to rise significantly as further improvements in battery technology are made.

---

[1] The failed motor had a fractured coil winding that was detected on the ground, prior to testing.

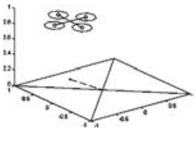

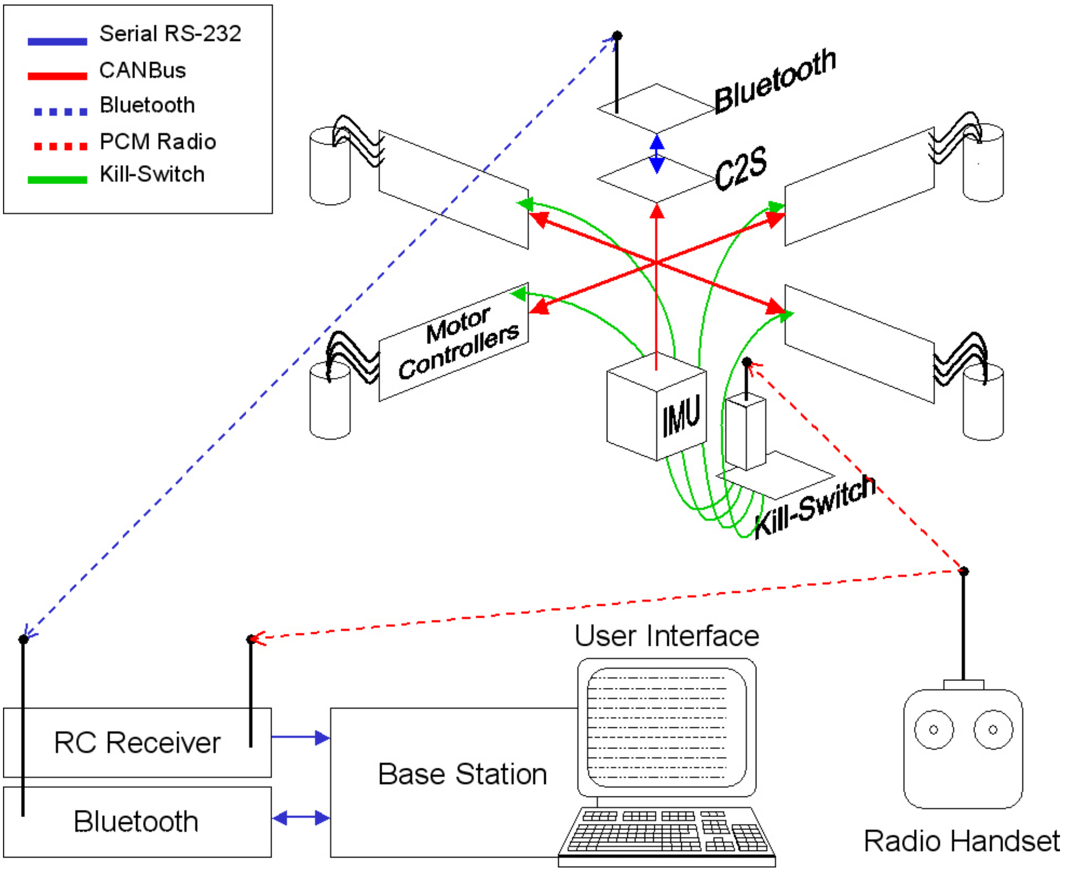

Figure 3.8: Avionics Communications Structure and Subsystems.

3.4 Avionics

Electronic flight systems (avionics) include sensors, processors, actuator controllers and communications systems. The X-4's avionics consist of four speed controllers, an inertial measurement unit, communications board, radio transmitter and safety kill-switch. The flyer has a distributed architecture that embeds high-level control functions in the separate motor-control boards, rather than routing data through a single centralised controller. The various subsystems are connected via a standard industrial communications bus protocol with packetisation and parity. The avionics systems and interconnections are shown in Fig 3.8.

3.4.1 Communications

A 'Controller Area Network' (CAN), or CANbus network, is used for onboard communications. The CANbus is a packetised communications protocol that allows for up to 8 bytes of data to be transmitted in a frame, with extensive

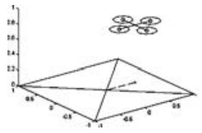

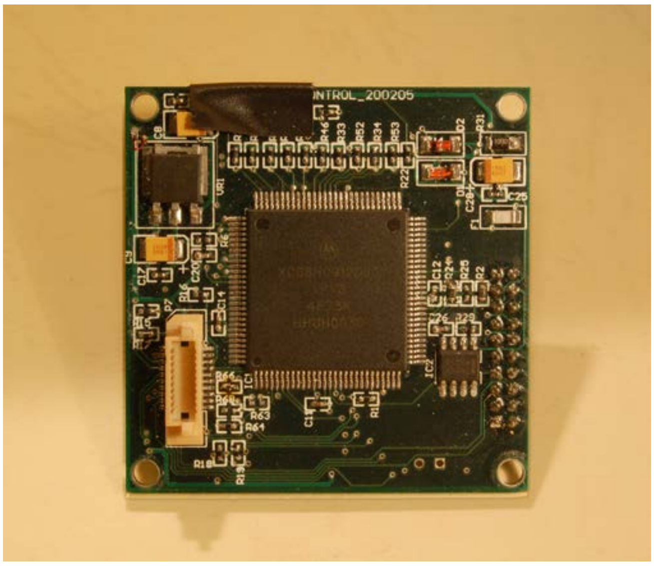

Figure 3.9: CANbus to RS-232 Serial Converter Board.

parity. The X-4's bus runs at the 1 Mbit per second rate, allowing for up to 9250 full-length packets to be transmitted each second. Appendix B details the CANbus protocol specification.

CANbus is an addressed bus — each actuator, sensor and processor has its own unique address. The X-4 uses a two-part addressing scheme that routes packets by location and type, allowing packets to be filtered and routed appropriately for different classes of subsystem. Appendix B details the addressing and filtering scheme.

When designing the avionics, care was taken to ensure that the bus design did not introduce latency into the digital control path. The X-4 uses onboard distributed control, rather than off-board or centralised control, on a single communications bus that ensures packets from the IMU are quickly disseminated over the bus without any unnecessary double-handling of data.

The CANbus interfaces with a radio downlink via a dedicated CAN-to-Serial (C2S) converter card (see Fig. 3.9). The card takes in CANbus packets and translates them into virtualised CAN Over Serial (COS) packets that are then transmitted over a Bluetooth link. Appendix B describes the COS protocol in more depth. The C2S board is 50x50 mm and weighs 20 g.

The radio telemetry link consists of a Bluewave Bluetooth 'serial-replacement' tranceiver (see Fig. 3.10). The Bluewave board is 25x35 mm and weighs 15 g. The Bluetooth transceiver has an RS-232 serial interface, and sends and receives packets at 2.45 GHz radio frequency. The modules are capable of up to 1 Mbps

Figure 3.10: Bluewave Serial Bluetooth Transceiver.

data rates. The bandwidth of the downlink is limited to 56 Kbps by the RS-232 interface of the C2S card, but given the total traffic load of the onboard communications bus is 26 Kbps, it is not expected that any data will be lost.

It has been found that the data link has variable latency due to retransmission of missing packets, with delays as long as 0.16 seconds not uncommon. Consequently, the Bluetooth link is not suitable for real-time control and care must be taken to time-stamp data for signal reconstruction.

An additional hobby radio-control (RC) receiver (see Fig. 3.11) forms part of the redundant safety shutdown system described in Section 3.6. It is used to disable the X-4's motor control electronics and ensure emergency shutdown independently of software crashes or Bluetooth communications failure. The onboard receiver is a seven-channel JR R700 36.560 MHz radio receiver. It is used solely for safety cut-off and does not act as a data device. The receiver has been removed from its casing to save weight, and is 50x25x15 mm and weighs 15 g.

3.4.2 Inertial Measurement Unit

The EiMU is a 6-axis Inertial Measurement Unit (IMU), designed and fabricated by the CSIRO Queensland Centre for Advanced Technologies (QCAT) ICT Robotics group (see Fig. 3.12). It acts like the inner-ear of the robot, measuring the roll, pitch and yaw rates, and x, y and z accelerations. Combined with three-axis magnetic field measurements, this data is used to compute the flight attitude

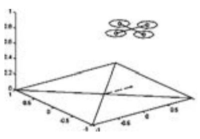

Figure 3.11: JR R700 Hobby Radio Receiver.

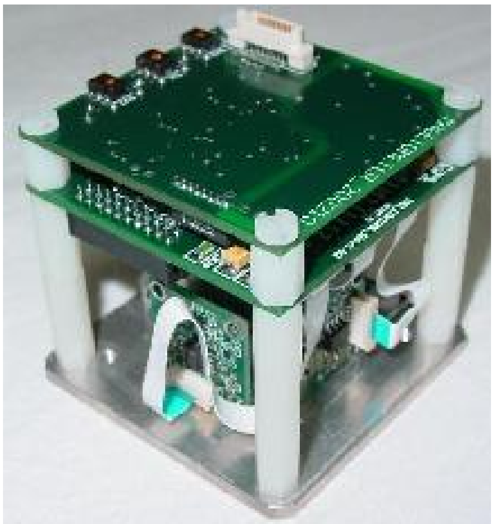

Figure 3.12: CSIRO EiMU Inertial Measurement Unit.

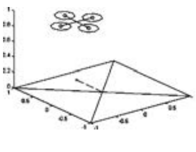

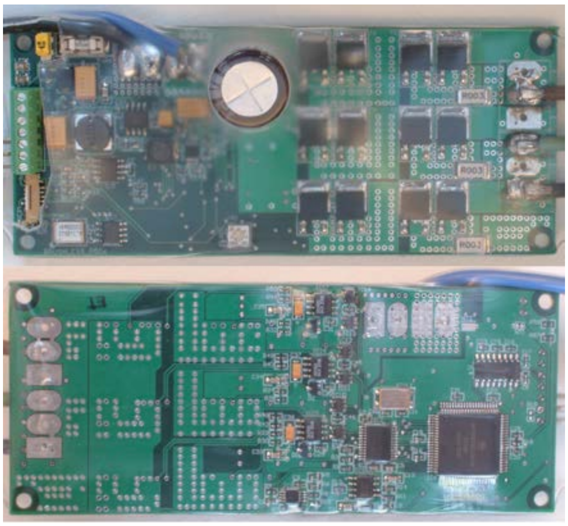

Figure 3.13: Electronic Speed Control Boards, Top and Bottom Sides.

of the craft using a complementary filter [Roberts *et al* 2003]. The EiMU unit measures 50x50x60 mm and weighs 60 g.

The IMU outputs raw sensor measurements and resolved angle estimates at 50 Hz. If only raw measurements are transmitted, the data rate can be increased to 100 Hz. Unlike standard CANbus devices, the EiMU transmits in an extended packet format, where 28 bytes of packet data are broken up over four 8-byte CAN packets — 1 sequence byte and 7 payload bytes. Refer to Appendix C for detailed EiMU communication specifications.

The inertial measurement packets are also used as a 'heartbeat' for the avionics and base station, with received EiMU packets signifying an active and healthy communications link.

3.4.3 Motor Controllers

The motor controllers read in operation instructions and speed references from the CANbus and control the motors in a high gain local feedback loop (see Fig. 3.13). Specifically, the speed controllers do four tasks: motor commutation, speed control, voltage bus monitoring and safety interlock. The motor control boards were custom made for the X-4 Flyer, and are 120x50 mm and weigh 75 g.

A Toshiba TB9060 brushless motor control chip synchronises the motor's magnetic phases by switching a three-phase MOSFET H-bridge. To sense motor position, the back-EMF of the phases are monitored and fed into a comparator. The TB9060 receives a Pulse Width Modulated (PWM) 'demand' signal from a

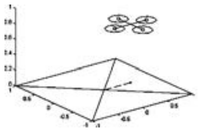

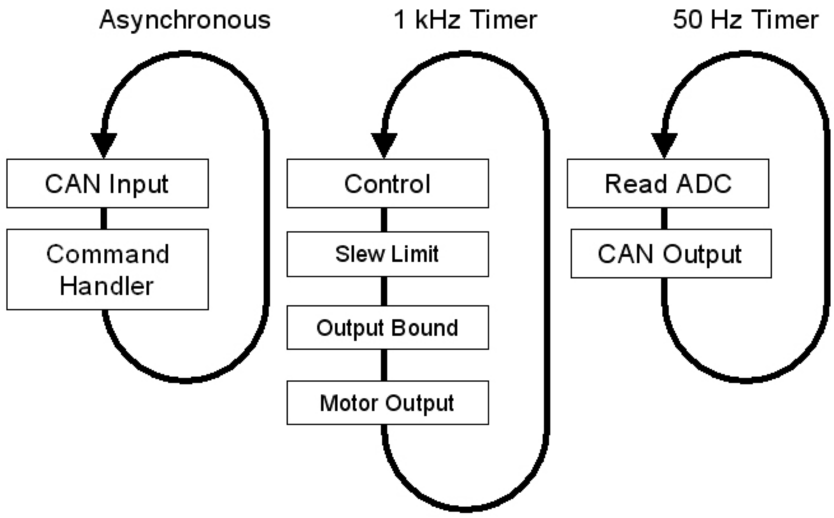

Figure 3.14: Brushless Motor Controller Thread Functionality.

multi-threaded HC12D60A microprocessor specifying the drive voltage-chopping duty-cycle and, consequently, motor torque.

The HC12 microprocessor also reads the back-EMF comparators via an Analog-Digital Converter (ADC) and computes the frequency of the motor rotation (see Fig. 3.14). This provides an accurate speed measurement for regulation of the angular velocity of the rotor. A control algorithm updates the demand signal to the TB9060 chip at 1 kHz. The controller's task is to improve the response time of the motors, allowing for better attitude control authority. Speed control also ensures that the thrust produced by each rotor is kept constant, irrespective of decreasing power bus voltage. A detailed description of motor speed control is given in Section 4.3.

Sense resistors on the power lines feeding the H-bridge measure the bus voltage and current flow. The HC12 uses an onboard analog-to-digital converter to read the values, and then reports the voltage, current, rotor speed and demand over the CANbus.

The motor controller boards include a software lock-out as part of the redundant emergency shutdown system described in Section 3.6. In an emergency, the motors are disabled by instructions sent over the Bluetooth radio link, via the CANbus. The lockout writes repeatedly writes zero speed to the TB9060 and refuses any other instruction. After the lockout is engaged, it cannot be cleared short of power-cycling the boards. When the motors boards receive the 'panic' instruction, they write out a packet acknowledging receipt of the command.

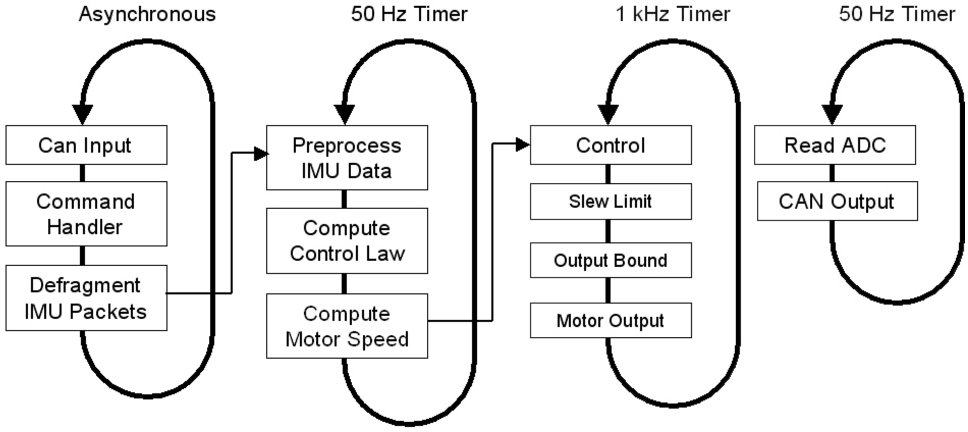

Figure 3.15: Attitude Controller Functional Diagram.

The boards are powered by the flyer's primary cells. A regulator circuit steps down the 16 V bus to 5 V for board power — this eliminates the need for additional batteries (although the other avionics must draw their power through a separate low-voltage bus). A consequence of this design is that large surges in motor current draw cause the power bus voltage to drop below 5 V, which results in the regulator being unable to supply the motor controller board. If the microprocessor is undersupplied it will reset, causing the motor to stall. This imposes a voltage bus constraint on the motor control design, described in detail in Section 4.3.

3.4.4 Attitude Controller

The flyer is stabilised in roll and pitch by a distributed attitude controller embedded on the motor control boards. Two control algorithms have been devised:

- linear PID controller using the EiMU's complementary-filtered attitude estimates and filtered gyro rates; and
- nonlinear combined control-estimator using raw accelerometer and gyro data.

Only the linear controller has been implemented on the motor boards, thus far.

The control boards read EiMU data over the CANbus at 50 Hz and calculate the corresponding output speed reference for their respective rotor. The control and write loops in the controller are clocked to 50 Hz to ensure even computation of integral states (see Fig. 3.15).

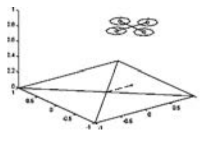

The attitude controller system also arbitrates flyer modes of operation and reads user handset inputs over the CANbus. There are four operating modes. In 'stopped' mode, the motors may be started to idle, their directions reversed, sent manual speed or demand instructions, or stopped. No reference speeds are sent from the controller. Under 'manual' mode, the attitude controller sends motors speed references derived from handset stick position. Raising the throttle increases all the rotor speeds by an equal amount. Moving the pitch joystick forward slows the North rotor and speeds the South rotor equally; no IMU feedback is used.

'Autonomous' mode can take commands from either the radio handset or the base-station computer. Commands take the form of pitch and roll reference angles and throttle value derived either from joystick positions or computer-generated trajectory points. Moving the pitch stick back by 10 degrees causes the robot to track 10 degrees pitch angle. Provision exists for an 'augmented' control mode that will use gyro feedback to assist a human pilot to manually stabilise the robot.

Chapter 5 reports the science and engineering used to estimate the X-4's dynamic model and produce attitude control algorithms. Chapter 6 develops a combined nonlinear control-estimator algorithm for a basic 'flying brick' model of the flyer.

3.4.5 Sensor Payloads

Due to the light weight of their design, many small quadrotors integrate their sensors into their avionics. This saves weight and reduces communications overhead but also decreases the flexibility of the payload. Larger payloads can accommodate sensors that are not optimised for weight or deeply integrated. Consequently, the X-4's kilogram of lift capacity can take a variety of possible sensors without concern for fractional weight savings.

Cameras and other vision sensors are the expected main payload of the vehicle. These have yet to be fitted to the X-4, but they will consist of at least one camera facing downwards on the bottom of the robot. This camera will be used for tracking objects on the ground, automatic landing and other visual servoing tasks. Additional cameras may be mounted underneath for stereo vision, or peripherally around the helicopter for horizon scanning. Other sensors that could potentially be mounted include laser range-finder scanners, ultrasonic transceivers, polarised light sensors and GPS. In the case of low-bandwidth sensors, provision exists for telemetry to be sent over the CANbus to onboard controllers or to the base

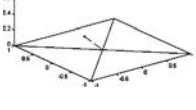

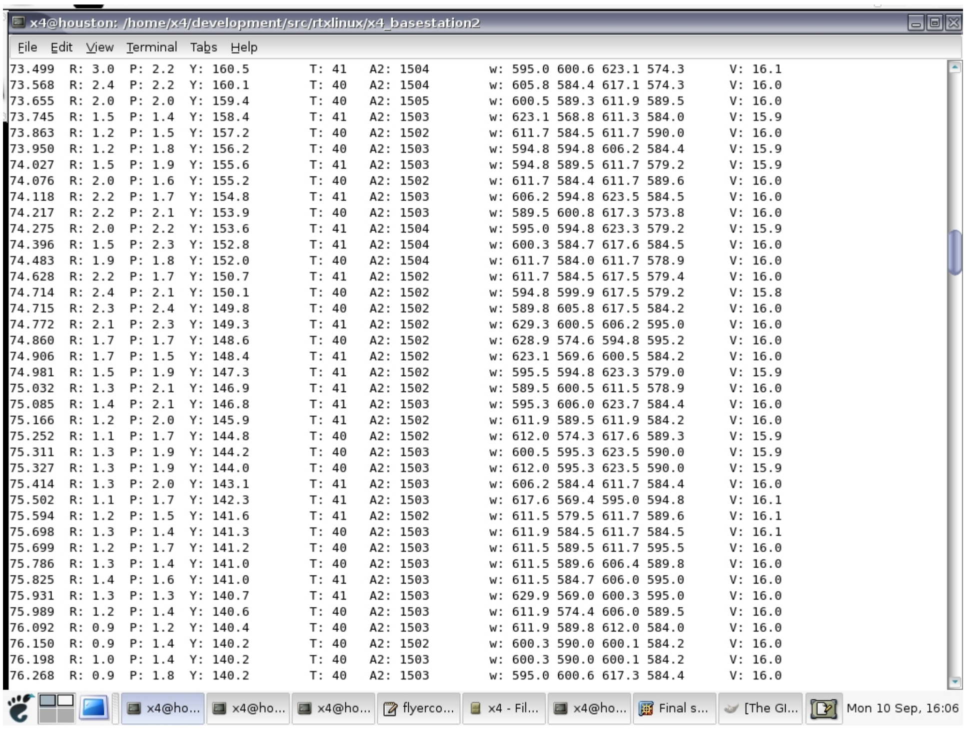

```
73.499  R: 3.0  P: 2.2  Y: 160.5       T: 41   A2: 1504       w: 595.0 600.6 623.1 574.3      V: 16.1
73.568  R: 2.4  P: 2.2  Y: 160.1       T: 40   A2: 1504       w: 605.8 584.4 617.1 574.3      V: 16.0
73.655  R: 2.0  P: 2.0  Y: 159.4       T: 40   A2: 1505       w: 600.5 589.3 611.9 589.5      V: 16.0
73.745  R: 1.5  P: 1.4  Y: 158.4       T: 41   A2: 1503       w: 623.1 568.8 611.3 584.0      V: 15.9
73.863  R: 1.2  P: 1.5  Y: 157.2       T: 40   A2: 1502       w: 611.7 584.5 611.7 590.0      V: 16.0
73.950  R: 1.2  P: 1.8  Y: 156.2       T: 40   A2: 1503       w: 594.8 594.8 606.2 584.4      V: 15.9
74.027  R: 1.5  P: 1.9  Y: 155.6       T: 41   A2: 1503       w: 594.8 589.5 611.7 579.2      V: 15.9
74.076  R: 2.0  P: 1.6  Y: 155.2       T: 40   A2: 1502       w: 611.7 584.4 611.7 589.6      V: 16.0
74.118  R: 2.2  P: 1.7  Y: 154.8       T: 41   A2: 1503       w: 606.2 594.8 623.5 584.5      V: 16.0
74.217  R: 2.2  P: 2.1  Y: 153.9       T: 40   A2: 1503       w: 589.5 600.8 617.3 573.8      V: 16.0
74.275  R: 2.0  P: 2.2  Y: 153.6       T: 41   A2: 1504       w: 595.0 594.8 623.3 579.2      V: 15.9
74.396  R: 1.5  P: 2.3  Y: 152.8       T: 41   A2: 1504       w: 600.3 584.7 617.6 584.5      V: 16.0
74.483  R: 1.9  P: 1.8  Y: 152.0       T: 40   A2: 1504       w: 611.7 584.0 611.7 578.9      V: 16.0
74.628  R: 2.2  P: 1.7  Y: 150.7       T: 41   A2: 1502       w: 611.7 584.5 617.5 579.4      V: 16.0
74.714  R: 2.4  P: 2.1  Y: 150.1       T: 40   A2: 1502       w: 594.8 599.9 617.5 579.2      V: 15.8
74.715  R: 2.3  P: 2.4  Y: 149.8       T: 40   A2: 1502       w: 589.8 605.8 617.5 584.2      V: 16.0
74.772  R: 2.1  P: 2.3  Y: 149.3       T: 41   A2: 1502       w: 629.3 600.5 606.2 595.0      V: 16.0
74.860  R: 1.7  P: 1.7  Y: 148.6       T: 40   A2: 1502       w: 628.9 574.6 594.8 595.2      V: 16.0
74.906  R: 1.7  P: 1.5  Y: 148.4       T: 41   A2: 1502       w: 623.1 569.6 600.5 584.2      V: 16.0
74.981  R: 1.5  P: 1.9  Y: 147.3       T: 41   A2: 1502       w: 595.5 594.8 623.3 579.0      V: 15.9
75.032  R: 1.3  P: 2.1  Y: 146.9       T: 41   A2: 1502       w: 589.5 600.5 611.5 578.9      V: 16.0
75.085  R: 1.4  P: 2.1  Y: 146.8       T: 41   A2: 1503       w: 595.3 606.0 623.7 584.4      V: 16.0
75.166  R: 1.2  P: 2.0  Y: 145.9       T: 41   A2: 1502       w: 611.9 589.5 611.9 584.2      V: 16.0
75.252  R: 1.1  P: 1.7  Y: 144.8       T: 40   A2: 1502       w: 612.0 574.3 617.6 589.3      V: 15.9
75.311  R: 1.3  P: 1.9  Y: 144.2       T: 40   A2: 1503       w: 600.5 595.3 623.5 590.0      V: 15.9
75.327  R: 1.3  P: 1.9  Y: 144.0       T: 40   A2: 1503       w: 612.0 595.3 623.5 590.0      V: 15.9
75.414  R: 1.3  P: 2.0  Y: 143.1       T: 41   A2: 1503       w: 606.2 584.4 611.7 584.4      V: 16.0
75.502  R: 1.1  P: 1.7  Y: 142.3       T: 41   A2: 1503       w: 617.6 569.4 595.0 594.8      V: 16.1
75.594  R: 1.2  P: 1.5  Y: 141.6       T: 41   A2: 1502       w: 611.5 579.5 611.7 589.6      V: 16.1
75.698  R: 1.3  P: 1.4  Y: 141.3       T: 40   A2: 1503       w: 611.9 584.5 611.7 584.5      V: 16.1
75.699  R: 1.2  P: 1.7  Y: 141.2       T: 40   A2: 1503       w: 611.5 589.5 611.7 595.5      V: 16.0
75.786  R: 1.3  P: 1.4  Y: 141.0       T: 40   A2: 1503       w: 611.5 589.6 606.4 589.8      V: 16.0
75.825  R: 1.4  P: 1.6  Y: 141.0       T: 41   A2: 1503       w: 611.5 584.7 606.0 595.0      V: 16.0
75.931  R: 1.3  P: 1.3  Y: 140.7       T: 41   A2: 1503       w: 629.9 569.0 600.3 595.0      V: 16.0
75.989  R: 1.2  P: 1.4  Y: 140.6       T: 40   A2: 1503       w: 611.9 574.4 606.0 589.5      V: 16.0
76.092  R: 0.9  P: 1.2  Y: 140.4       T: 40   A2: 1503       w: 611.9 589.8 612.0 584.0      V: 16.0
76.150  R: 0.9  P: 1.4  Y: 140.2       T: 40   A2: 1502       w: 600.3 590.0 600.1 584.2      V: 16.0
76.198  R: 1.0  P: 1.4  Y: 140.2       T: 40   A2: 1503       w: 600.3 590.0 600.1 584.2      V: 16.0
76.268  R: 0.9  P: 1.8  Y: 140.2       T: 40   A2: 1503       w: 595.0 600.6 617.3 584.4      V: 16.0
```

Figure 3.16: Telemetry Console and UI Screenshot.

station via the Bluetooth link. However, higher-bandwidth sensors will require separate onboard channels or dedicated wireless telemetry links to ground.

3.5 Base Station

3.5.1 Command and Telemetry Console

The base station is the operator station on the ground, and serves as a user interface, telemetry output and data-logger, as well as a router for a hobby RC radio handset signals. It can be either a desktop PC running Debian Linux or laptop for use in the field. The user interface takes the form of a command terminal that displays flight data (see Fig. 3.16). Each time new IMU data is received the vehicle status is updated on a new line. The user operates the system by pressing keys to stop, start and reverse motors, change flyer operation modes and send software emergency shutdown instructions. Vehicle roll, pitch and yaw reference angles and throttle position are input via a hobby radio handset.

The flyer status display is updated as new IMU packets are received. Each telemetry update is time-stamped so that reported events can be easily cross-

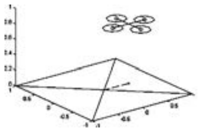

Figure 3.17: Base Station Communications Stack.

referenced against stored telemetry data. All packets read by the base station are stored so that a complete record of all communications and system states are available for later analysis. Information on telemetry logfiles is given in Appendix B.

3.5.2 Communications Stack

Two radio links connect the base station to the flyer and radio handset (see Fig. 3.17). A Bluetooth link transmits and receives commands and telemetry data to and from the flyer. A hobby radio receiver listens for signals from a radio handset transmitter.

The base station Bluetooth module is a 2.45 GHz Bluewave serial Bluetooth transceiver identical to that onboard the flyer. It carries all the data traffic to and from the flyer. The Bluewave transceivers are Class 1 devices with a range of up to 100 m. Brief experiments have confirmed connection reliability at distances up to 20 m through brick and mortar buildings. The base station Bluewave module is designated ‘master’ and is responsible for initiating and resuming communications with the ‘slave’ on the X-4. A shared passkey encrypts traffic between the two devices — a standard feature of this device.

The offboard Bluetooth unit is housed in a protective casing and powered from rectified mains via a 9 V DC power jack. It connects to the base station through an RS-232 serial cable, interfaced to Universal Serial Bus (USB) via an Alloy two-channel USB-to-RS-232 serial converter.

A 36.560 MHz JR R700 radio receiver, identical to the unit onboard the X-4, captures joystick, throttle and switch positions from a hobby radio handset. The radio instructions are output as seven parallel PWM signals that are read by an

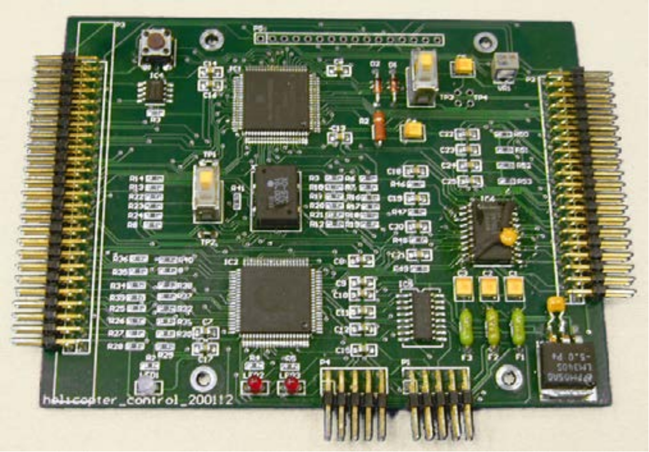

Figure 3.18: RC Receiver Interface Board.

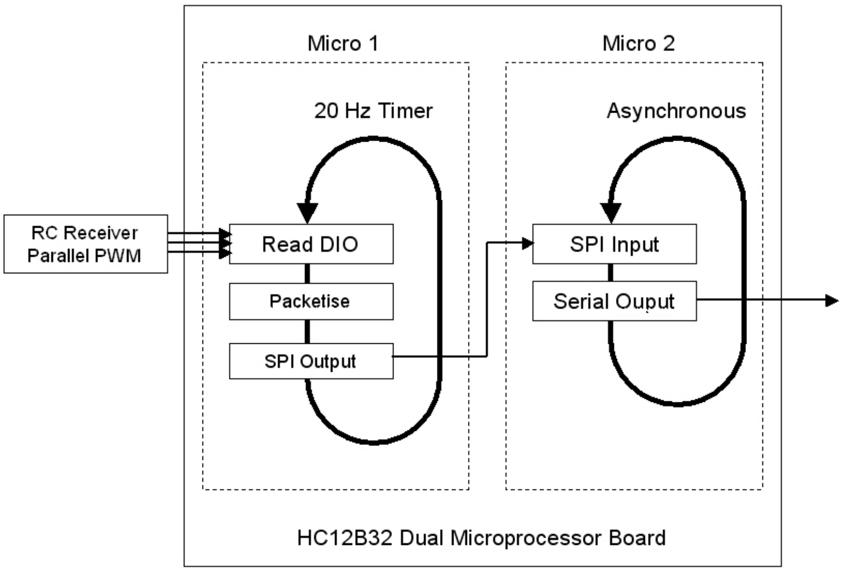

Figure 3.19: RC Receiver Board Functional Diagram.

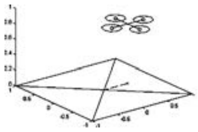

Figure 3.20: JR X3810 RC Handset.

embedded dual HC12B32 microcontroller board (see Fig. 3.18 and 3.19). One B32 chip reads digital input pins to capture the PWM waveforms and then packetises the values into Extended COS packets. The packets are transmitted over Serial Peripheral Interface (SPI) to the second processor which reads bytes off the SPI bus and immediately retransmits them over serial RS-232 to the base station, via a Serial-USB converter. Appendix C details the RC receiver packet structure.

3.5.3 RC Handset

Operator flight commands are input via a JR X3810 RC handset (see Fig. 3.20). The handset transmits 36.560 MHz pulse code modulated signals to the flyer and a base station radio receiver. The radio transmitter has a range in excess of 1 km. The handset has four stick directions for throttle, roll, pitch and yaw, as well as a gear switch and two auxiliary switches. The gear switch is used as a flight mode or function select switch and the second auxiliary switch is used to trigger a hardware/software kill-switch.

3.6 Safety

Helicopters are inherently dangerous vehicles, and the high-speed rotors of the X-4 Flyer make it especially important that safety be incorporated into the design.

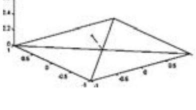

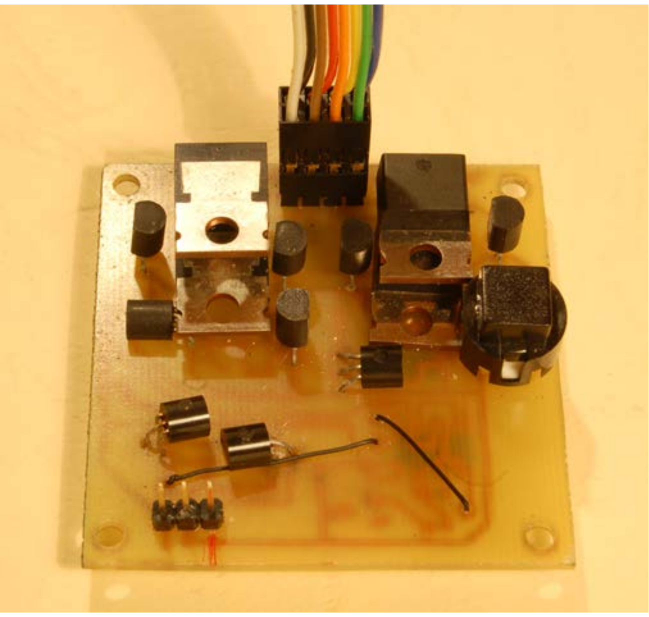

Figure 3.21: Hardware Emergency Kill-switch.

The avionics of the robot are fail-safe and default to shutting down entirely if a critical condition is registered. System-wide shutdown instructions, or ‘panics’, have the highest CANbus address priority. When a panic is sent, all motor controllers will immediately stop the rotors and put them into a state where they cannot be started again, short of a hardware reset (see Section 3.3.2). Panics can be issued either by a manual switch (software kill-switch) or issued automatically by a subsystem that detects a fault.

The flyer can also be disabled by a hardware kill-switch (see Fig. 3.21). The kill-switch is connected to the motor control board power switches — when the kill-switch is triggered, MOSFETs directly disconnect the motor drive circuitry. Once armed, the kill-switch monitors a PWM signal from a dedicated radio receiving signals from a hobby RC handset, allowing the user to remotely make the vehicle safe before approaching (see Section 3.4.1). As the radio handset instructions are also captured by the off-board radio receiver, when the kill-switch is activated, the base station will automatically issue a software panic. Once triggered, the enabling circuit latches off, preventing the motors from being enabled again, until the switch is rearmed. Together the software and hardware kill-switches disable the flyer and prevent it from inadvertently reactivating.

Automatic panics are sent when system errors are detected. In normal operation, the flyer avionics produce regularly timed status data sent over the downlink. If one or more device produces few or no packets, it may indicate that the

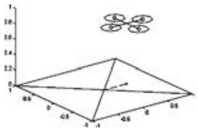

Figure 3.22: ANU Mechatronics Research Laboratory Test Cage.

communications link is degraded or subsystems may be malfunctioning. However, latency in the wireless link does not necessarily imply a problem. To monitor global system health, a ‘pulse’ function on the base station reads the number of packets received from each device — their heartbeat — every second. Similarly, an embedded process in the distributed controller monitors all onboard data traffic and received base station instructions and reports back packet counts every second. If the number of packets is below a set threshold for each subsystem, an alarm or panic is raised and the user is notified on-screen.

For the safety of the operators, the X-4’s rotor performance and attitude stability tests were performed in an enclosed cage (see Fig. 3.22). The case is made of steel square section tubing, particle-board sides and plexiglass windows. The cage is 2.1 m high and is bound on two sides by walls and barred windows. A large door allows access to the cage. Inside, the cage has mains power, CAT5 data patch panels and wired emergency-stop switch. A smooth melamine test pad has been constructed to test the flyer on the ground, which allows the bottom hoop of the flyer to slide easily and so avoid the craft from catching and flipping. A block and tackle system has been installed on rails in the roof, from which the X-4 can be suspended. During suspended tests a series of tie-points around the top of the cage and the edges of the test pad restrain the flyer from approaching the walls of the enclosure, or from moving at all when used with the gimbal mount.

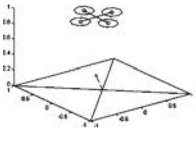

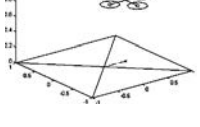

Chapter 4

Rotor Design and Motor Speed Control

In this chapter I present the design of an integrated rotor-motor thruster system for use on the X-4 Flyer. The philosophy of the X-4 Flyer is that it should be operated without regular skilled maintenance. This implies that the mechanical complexity of the drive system should be minimal, and this has significant ramifications for the design. The combination of fixed-pitch blades, small rotor size, and high take-off weight make the X-4 Flyer's drive system a unique design challenge.

4.1 Introduction

Mechanical simplicity is a crucial requirement for commercial UAV systems that will have to operate reliably and safely without regular skilled maintenance [Gordon *et al* 1993]. The complex swash-plate mechanisms of conventional helicopters (see Fig. 4.1) are maintenance-intensive and the risk of catastrophic system failure due to improper maintenance is high. A means of reducing complexity is to use fixed-pitch rotors. Rather than changing thrust by altering the pitch of the blades, the rotor varies thrust by changing rotor speed [Hamel *et al* 2002].

An advantage of working with small-scale fixed-pitch rotors is that they can be designed to have optimal aerodynamic profile for the flow conditions expected in normal flight. Wells [Wells 2004] provides a framework for parameterising simulated blades to find the best profile. For thin, high-performance blades, large aerodynamic loads will cause the profile to deform [Pounds and Mahony 2005], sacrificing performance. This is a steady-state aeroelastic problem inherent in

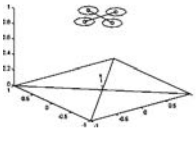

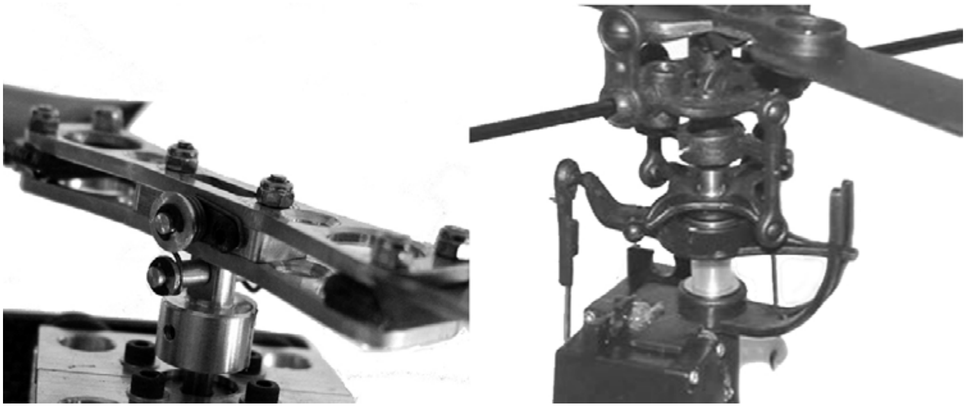

Figure 4.1: X-4 Flyer Mast (left) and Conventional RC Heli Mast (Right).

light-weight fixed-pitch rotors [Prouty 2002, p 43] [Quackenbush *et al* 2004] and good blade design is a tradeoff between aerodynamic performance, structural strength and manufacturability.

In addition to being robust, efficient and compact, miniature UAV drive systems must provide fast thrust changes for manoeuvering flight [Young *et al* 2002] [Pounds *et al* 2007a]. This is critical for craft that rely solely on thrust for manoeuvering, such as tandems, quadrotors or blimps. Quadrotor drives in particular demand fast dynamic performance as they use no other control surfaces for flight stability [Hamel *et al* 2002]. Properly engineered actuators and controllers are required to extract maximum performance.

In this chapter I detail the system design of a small-scale thrust actuator, comprising a fixed-pitch rotor driven directly by a brushless motor with associated control circuitry. The rotor flapping assembly has only two moving parts (see Fig. 4.1) and so the scope for catastrophic mechanical failure is small compared with more complex mechanisms. Efficiency of the rotor was optimised by taking advantage of ideal chord and twist geometries [Prouty 2002, p 46] that are not practical for larger rotors. Rotor deformation under load was overcome by careful choice of the blade profile and manufacturing process as well as incorporation of a pretwist into the design such that the rotors will flex into the correct shape in flight. Control of rotor speed is constrained by a torque limitation, due to load limits on the batteries, that is enforced though a slew-rate constraint on the control demand. A combined feed forward feedback control compensates for the open-loop aerodynamics of the rotor and attenuates disturbances within the imposed slew-rate constraints. The system is implemented on brushless motor control boards designed by the CSIRO ICT Robotics group. The controller is de-

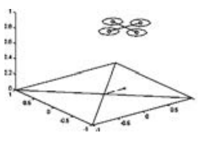

signed for performance within the system limitations and it is shown that more complex algorithms would provide marginal performance advantage.

This chapter is organised into three sections. This section describes the motivation for researching the rotors and drive system, Section 4.2 discusses the key aerodynamic design issues and describes the practical aeromechanical optimisation process used to design the blade geometry. This section also reports the test-bed performance of the complete rotor. Section 4.3 describes the dynamic control problem, provides test results and dynamic models for the open-loop motor-rotor dynamics and disturbances. The design process and logic of the compensator are given, and the measured performance of the implemented controller is presented.

4.2 Blade Design

The design of small-scale fixed-pitch blades is a trade-off between best aerodynamic design and best structural design. The goal of this process is to maximise the thrust produced at steady-state for a given mechanical power supplied to the rotor shaft and imposed system constraints from Chapter 3, Section 3.3 (see Tab. 4.1). In this chapter I consider only the steady-state aeroelastic effects, rather than the full dynamic force balance [Quackenbush *et al* 2004]. The unsteady aerodynamic and aeroelastic effects occur on a timescale of the order of one rotor revolution [Leishman 2006, pp 369–371]. Even during highly aggressive manoeuvres of a UAV the unsteady aerodynamic effects will not have a significant impact on the rotor performance.

The three major facets of the rotor design are tip velocity (as set by blade length and rotor speed), the airfoil section and the planform (chord and twist distribution). Subsection 4.2.1 describes the airfoil and aerodynamic design, Subsection 4.2.2 describes the structural design of the blades and Subsection 4.2.3 discusses practical design issues. Subsection 4.2.3 provides thrust test data of the fabricated rotor.

4.2.1 Aerodynamic Design

Blade length and rotational velocity are the fundamental design parameters of a rotor. The geometry of the UAV limits the rotor radius to 0.165 m. Such small blades need to rotate as fast as possible to generate maximum thrust [Leishman 2006, pp 195-197]. The practical limitations on rotor speed are the motor drive torque and compressibility of air at the blade tip. Assuming the

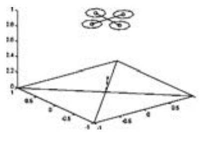

Parameter	Target
Thrust	$\geq$ 11 N
Input Power	$\leq$ 330 W
Current Draw	$\leq$ 22 A
Rotor Speed	800–1000 rad·s^{-1}
Rotor Torque	$\leq$ 0.1749 Nm
F.M.	$\geq$ 0.77

Table 4.1: Rotor Design Parameters.

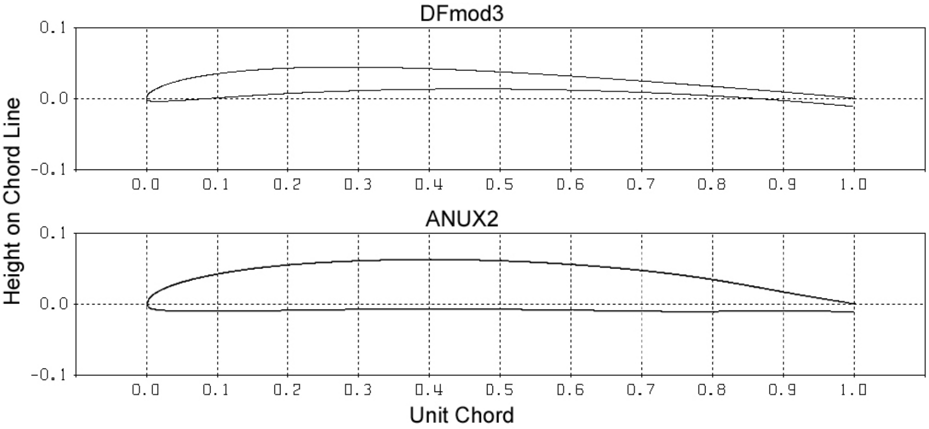

Figure 4.2: DFmod3 and ANUX2 Airfoil Sections, Top and Bottom.

higher Mach 0.4 compressibility bound, the maximum allowable operating speed is 1000 rad·s^{-1}. Assuming a 30 per cent thrust margin, the corresponding operational speed range is 670–1000 rad·s^{-1} (with hover speed at approximately 870 rad·s^{-1}).

The most efficient airfoil shape must be chosen to suit the flow regime at this airspeed. For a rotor of this size at the specified speed the Reynold's Number (RE) is of the order of 100,000. It is expected that the fluid flow will be laminar [Potter and Wiggert 1997, p 99] and the aerodynamics will be largely influenced by viscous effects. For these conditions a high aspect-ratio airfoil sections, such as the DFmod3 (see Fig. 4.2, top) [Drela 2003], VR8 and MA409sm [NASG 2004], are most appropriate. The airfoil should have low camber, a thin cross-section to reduce profile drag, and sharp trailing edges to reduce separation drag.

Unfortunately, such airfoils induce significant aerodynamic moments that dominate the torsional rigidity of the blade. Initial experimental results demonstrated that it was impossible to manufacture a DFmod3, scaled to the X-4 flyer requirements, that was torsionally strong enough to retain its shape under flight loading.

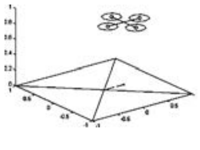

To overcome this problem, a new airfoil design was developed, custom tailored to the X-4's flight profile. The DFmod3 was used as a starting point and its profile was modified to mitigate the effect of twisting on the blade: in particular, altering the design to obtain a lower pitching moment, better rigidity and avoid rapid on-set of stall.

By shifting the airfoil's centre of thickness and camber away from the leading edge, the centre of pressure is moved rearward and the magnitude of the pitching moment is reduced. While it is possible to greatly reduce the pitching moment by adding reflex near the trailing edge, highly reflexed airfoils sacrifice lift; thus only a small amount of reflex is added [Hepperle 2004]. A more rounded leading edge reduces the sudden onset of stall, and a proportionally thicker body and more mass towards the leading and trailing edges stiffen the section. The bottom surface is almost flat to increase thickness and improve manufacturability. The proposed airfoil is a trade-off between maximising lift and minimising moment, with an eye to manufacturability of the design.

The resulting design, the ANUX2, is shown at the bottom of Fig. 4.2. The ANUX2 was tested using Drela's X-foil program [Drela 2004] and found to be the most promising of a range of profiles considered. The section polar plot shows a clear optimal operating Angle of Attack (AoA) at 4.4° and that it performs best at $RE = 94,000$ (see Fig. 4.3). It has a good non-dimensional lift coefficient, c_l, of 0.9 with a 7 per cent thickness ratio.

In parallel with selecting the airfoil, the planform of the rotor is designed to optimise the performance of the blade section. By varying the geometric twist θ and chord c along the length, the AoA α and RE are set to remain ideal as the blade section linear velocity increases with radius r: thus, $\theta = \alpha_{\text{ideal}} + v_i/\omega r$ and $cr = \text{constant}$, where v_i is the inflow velocity and ω is the rotor angular velocity. This is called 'ideal twist' and 'ideal taper', and is the theoretically optimal shape for hover [Prouty 2002, p 46]. Structural constraints prohibit its use on large-scale craft, but small-scale rotors can readily apply it.

The lift, drag and moment of a unit length wing are:

$$L = c_l(\alpha)\frac{1}{2}\rho(\omega r)^2 c(r) \tag{4.1}$$

$$D = c_d(\alpha)\frac{1}{2}\rho\omega^2 r^3 c(r) \tag{4.2}$$

$$M = c_m(\alpha)\frac{1}{2}\rho(\omega r)^2 c(r)^2 \tag{4.3}$$

respectively, where ρ is the density of air and c_l, c_d and c_m are the non-dimensional lift, drag and moment coefficients.

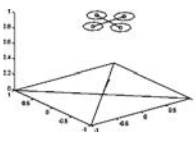

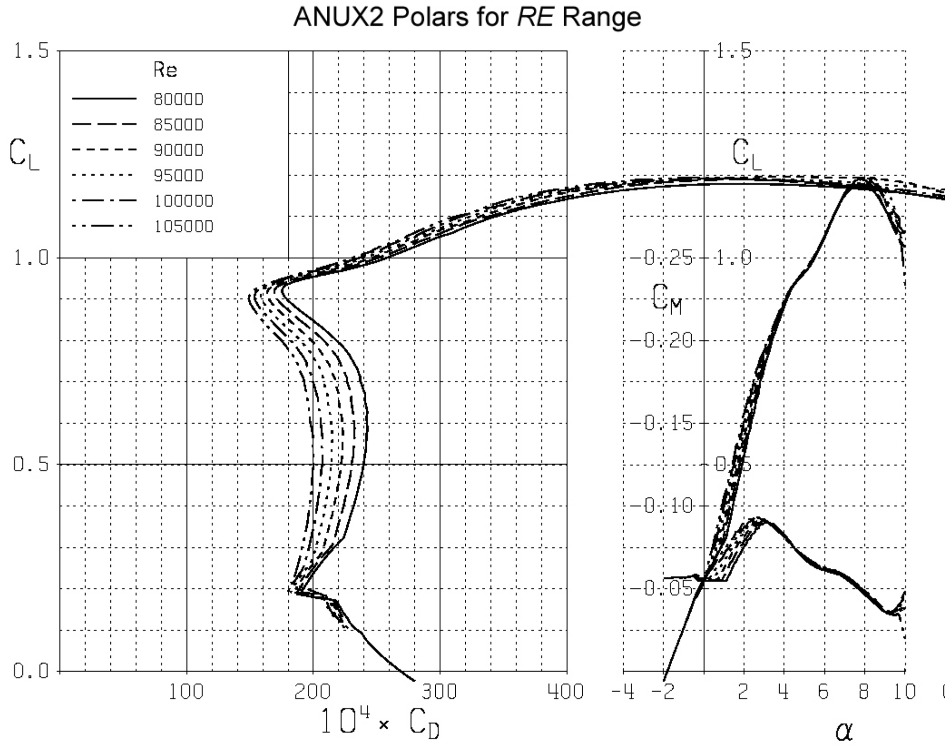

Figure 4.3: ANUX2 Polar Plot.

For a given 3D geometry, the performance of the rotor can be calculated by integrating the lift and drag:

$$T = b\int_0^R c_l(\alpha)\frac{1}{2}\rho(\omega r)^2 c(r)dr \tag{4.4}$$

$$Q = b\int_0^R (c_l(\alpha)\phi(r) + c_d(\alpha))\frac{1}{2}\rho\omega^2 r^3 c(r)dr \tag{4.5}$$

where R is the rotor radius, b is the number of blades, and ϕ is the blade inflow angle.

The moment at a point on the blade can be found by integrating the section moment from the tip inwards:

$$M(r) = \int_r^R c_m \frac{1}{2}\rho\left(\omega r\right)^2 \frac{c^2}{\delta r}dr \tag{4.6}$$

4.2.2 Structural Design

A key aspect of blade design for mini UAVs is designing for best mechanical stiffness and manufacturability of the blade, and to predict and compensate for

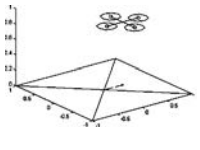

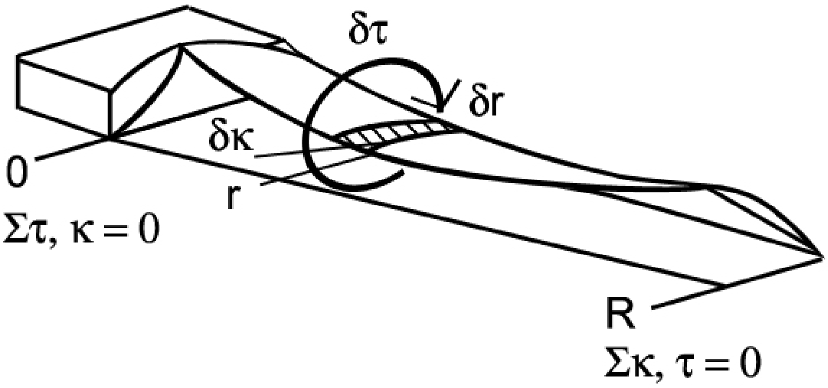

Figure 4.4: Balanced Aerodynamic Moment and Elastic Deformation Integrals.

physical distortion of the blade under load. To compensate for the aeroelastic deformation, the ideal planform is modified by setting the blade angle lower incrementally along the blade, so that the blade will twist up into the correct angle of attack under load. I use the term ‘pretwist’ to describe this modification of the ideal profile. The expected pretwist is calculated by equating the moment on a blade element to the corresponding strain torque. At steady-state, the aerodynamic and twist moments are balanced at all radius stations (fig. 4.4).

The blade material is chosen to maximise shear modulus along the blade axis to minimise κ. Steel and titanium require large overheads to manufacture small sizes with high accuracy, and so are impractical for mini UAV blades. Common plastics are not sufficiently stiff for demanding performance. Composite materials offer good manufacturability and shear modulus, but risk stiffness variability due to hand-fabrication. Nevertheless, carbon-fibre epoxy was found to be ideal for manufacturability and high shear modulus. Carbon-fibre fabric is anisotropic: the torsional stiffness is at a maximum when the weave is 45° to the principal torque axis [Roylance 1996, p 114].

The elastic deformation of a cross-section of length δr in torsion is given by:

$$\tau(r) = \kappa(r)\frac{Gq}{\delta r} \tag{4.7}$$

where τ is the torque, κ is the strain angle, G is the material shear modulus and q is the torque factor. The torque factor of an airfoil is approximated by that of a flat plate of the same size. Consequently:

$$\delta\kappa(r) = \int_r^R c_m \frac{1}{2}\rho\left(\omega r\right)^2 \frac{c^2}{Gq}dr \tag{4.8}$$

In the case of anisotropic materials, the correct material orientation stiffness value must be used — the blade carbon fibre is at 45° to the torsion axis.

In equilibrium, the aerodynamic and twist moments must sum to zero at all points along the blade:

$$M(r) - \tau(r) = 0 \tag{4.9}$$

The theoretical model for twist (4.2–4.8) was used to develop an iterative simulator that computes the steady-state performance of a rotor for given geometric, aerodynamic and mechanical properties [Pounds and Mahony 2005].

Initially, the simulator is provided an unloaded planform geometry, material shear modulus, airfoil polar data and and motor and battery attributes. At each step it uses the flow conditions across the whole rotor to compute the elemental lift, drag, aerodynamic moments and incremental twist deflection at each radius station. From this it computes the new flow state for the next step. At the end of each iteration the rotor state is checked for convergence. Once the state has converged, the thrust, rotor angular velocity and the mechanical deformation of the blade at each radius station are output.

A search routine, using brute-force computation across a range of input parameters, assessed the outputs of the simulator to identify the best planform geometry for a given airfoil, and evaluate the potential merit of candidate airfoils. The ANUX2 produced the best overall performance in the simulator and was chosen for the final design. The software used is available on the CD at the back of this thesis.

For the ANUX2, the optimal geometry was a tip chord of 10.4 mm and tip pitch of 3.9°, given ideal pitch and chord. The simulator calculated a total thrust of 13.87 N at 764 rad·s^{-1}. The length of the blade is 165.1 mm (from the shaft centre), with the hub clamp at 40 mm.

4.2.3 Practical Issues

The blades were manufactured as a three-ply carbon-fibre epoxy composite [Pounds and Mahony 2005]. They were moulded in CNC-milled aluminium dies (see Fig. 4.5), into which carbon-fibre cutouts were laid and wetted by hand. Epoxy was injected into the closed mould to force out any air and allowed to cure. Once cured, the parts were removed and any flash trimmed by hand.

As hand-manufactured carbon-fibre composites properties are prone to fluctuation between batches, the stiffness of each blade is potentially different. Additionally, the blade screw-down mounting bracket was found to be accurate to

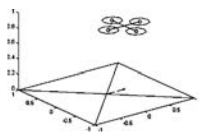

Figure 4.5: X-4 Flyer Blade Die.

no more than 0.5°. The steady-state tip angle must be insensitive to minute variations in these parameters. Robustness of the overall design is improved by applying a small pretwist that sets the AoA lower than optimal in order that unexpected variations will have a greater strain margin before stall. The rounding of the leading edge to reduce stall sensitivity prevents early boundary layer separation, allowing for a wider range of operating AoAs. If the system is accurately parameterised, the drag on the system will be lower for a lower angle of attack, and the rotor will run faster until the aerodynamic and mechanical moments balance at the designed angle.

For the production blade (see Fig. 4.6), the tip angle was reduced to 3.1° to allow for unexpected flex or angular error. Simulation showed that variations of as much as 2° in pitch error can be tolerated.

Due to a manufacturing error in the dies, the shape of the manufactured airfoil section was different from the design. The actual blades exhibit a small ridge along the bottom surface leading and trailing edges that unfortunately compromises the aerodynamic performance of the blades. To understand the consequence of this manufacturing fault, the ridges were modelled in the X-Foil simulator for the same flight conditions. The inviscid simulation mode calculated a c_l of 0.45 at 4.4° AoA; half the predicted lift of the perfect rotors. The expectation was that the blades would run faster, due to lower lift produced, until the blades reach the

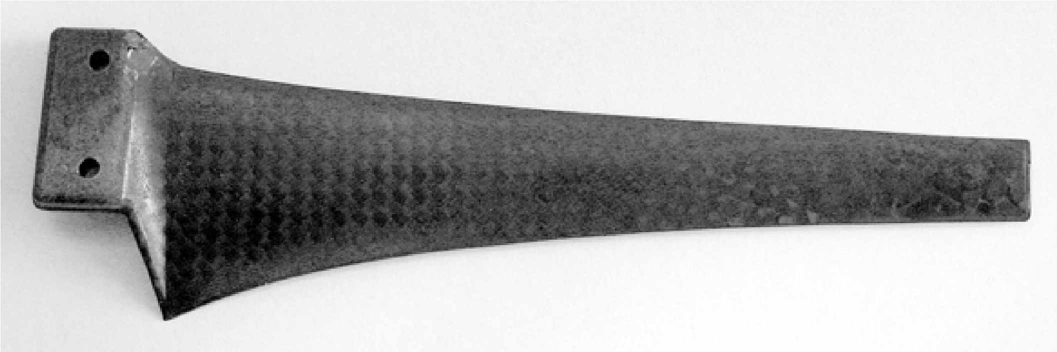

Figure 4.6: ANUX2 Blade With Ideal Chord (Actual Size).

equilibrium twist point, resulting in little reduction in achievable thrust. Financial constraints prevented the flawed mould being replaced.

For the as-fabricated imperfect airfoil, the aeroelastic rotor simulator predicts the rotor will produce a maximum of 14.34 N of thrust at a top speed of 1105 rad$\cdot$s^{-1} and hover thrust at 930 rad$\cdot$s^{-1}. Although it may seem strange that the ‘imperfect’ airfoils should predict a higher thrust than the optimal airfoils, recall that the lower induced drag from decreased lift will undesirably increase the Mach number of the rotor tips.

4.2.4 Rotor Performance

Thrust tests were run to assess the performance of the blades across a range of speeds. The apparatus consisted of a Jeti Phasor 30/3 brushless DC motor mounted on the flyer, which is fixed on a see-saw rig. The other side of the flyer pressed down on a digital scale. The rig was raised one rotor diameter (0.33 m) off the ground. Commands were sent to the motor control boards in the form of PWM signals with 255 quantisation levels. During each test, the drive demand was increased 25 steps, from 50 to 250 PWM units. The motor speed and power data were logged from the speed controller and the digital scale was read directly.

The rotor produced 14.5 N of thrust at full speed, as shown in Tab. 4.2, comparing favourably with the simulator predictions for perfect blades and imperfect blades (+5 and +1 per cent). It was found that the actual blades ran faster than predicted for perfect blades, but slower than predicted for the imperfect blades, requiring 870 rad$\cdot$s^{-1} for hover. The thrust-speed curve follows closely the quadratic relationship (4.4) for rigid rotors (see Fig. 4.7). Current draw measurements from previous tests [Pounds *et al* 2004] give the X-4 more than 10 minutes hovering endurance and more than eight minutes at full throttle.

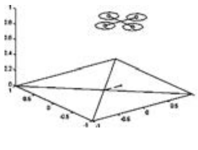

u units	$V_0 \pm 0.1$ V	$V \pm 0.1$ V	$I \pm 0.1$ A	$\omega \pm 1\text{rad}\cdot\text{s}^{-1}$	$T \pm 0.1$N
50	15.4	14.9	1.2	326	1.35
75	15.4	14.5	2.2	429	2.46
100	15.2	13.8	4.3	534	3.52
125	15.1	13.4	6.6	634	5.05
150	15.1	12.8	10.9	722	6.53
175	15.0	12.0	13.4	775	7.74
		Battery change			
185	16.1	13.7	—	921	11.16
200	16.8	12.9	—	926	11.24
225	16.6	12.7	—	1015	13.63
250	16.3	11.7	—	1043	14.53

Table 4.2: Static Rotor Performance. Note that the current sensor was not calibrated for the entire operating range and saturated at 13.8 A.

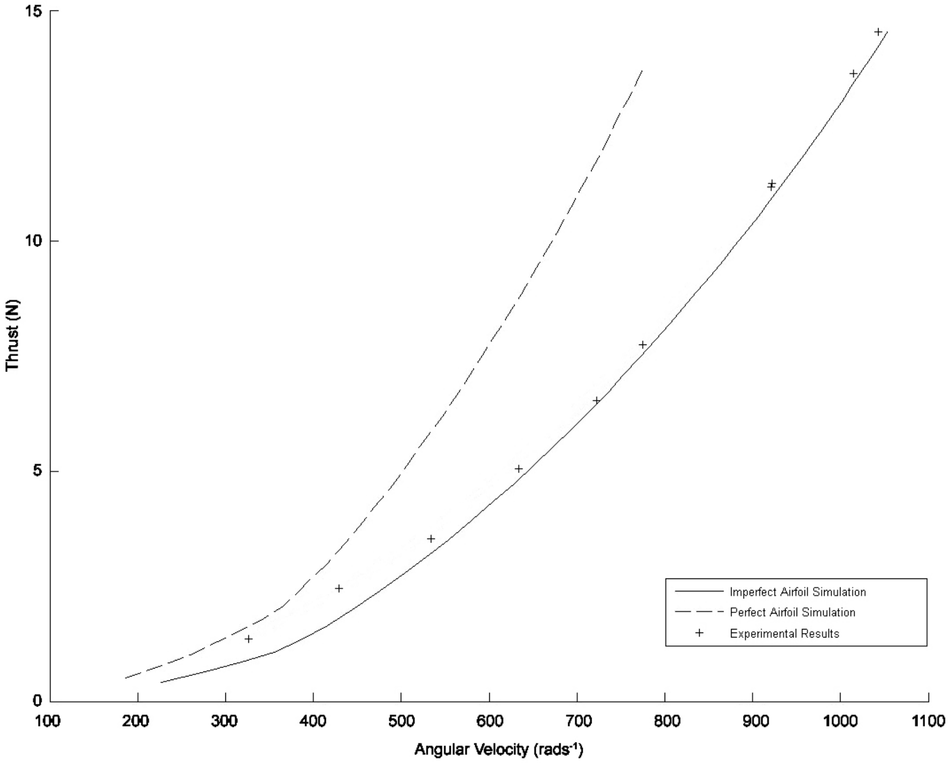

Figure 4.7: Theoretical, Predicted and Experimental Thrust for Given Speed

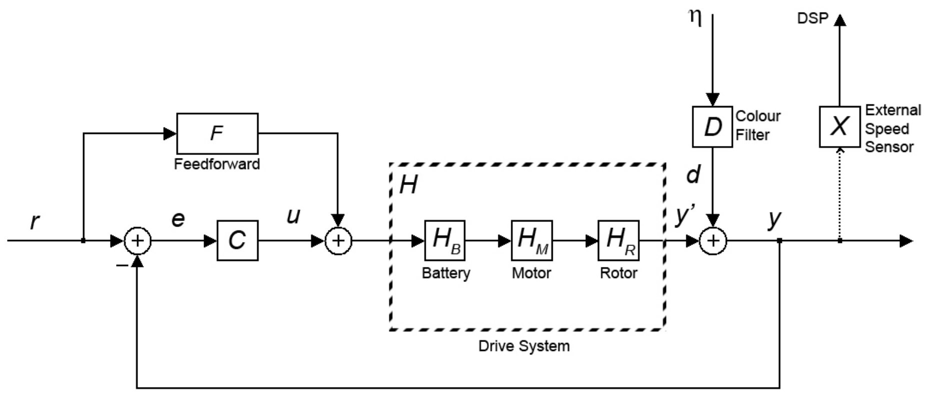

Figure 4.8: Dynamic Model Block Diagram.

4.3 Dynamic Control

Quadrotors must have fast thrust dynamics - the motors must be able to accelerate the rotors quickly to allow authorative attitude stabilisation. Most current quadrotors have light, high-drag rotors that allow for fast speed changes without additional control. This is the case with the popular RCtoys Draganflyer toy [Draganfly Innovations 2006]. Larger quadrotor UAVs such as the X-4 have low-drag rotors with high inertia and need local control to artificially improve the motor response. There are well-developed theories for the control of electric motors driving fans: Cogdell [Cogdell 1999] and Innovatia [Innovatia 2006] give comprehensive overviews of the dynamics of brushless motors, and Franklin and Powell [Franklin *et al* 1994] provide examples of basic motor control. In practice, the closed-loop performance is heavily constrained by limits on the available instantaneous current draw on the batteries and this dominates the control design.

Subsection 4.3.1 provides an experimentally identified plant dynamic model. Subsection 4.3.2 describes experiments to characterise aerodynamic disturbances likely to effect the system. Subsection 4.3.3 gives controller desired performance and physical limitation design bounds. Subsection 4.3.4 presents a control design that satisfies these requirements, and Subsection 4.3.5 reports the performance of the implemented controller.

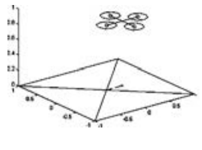

4.3.1 System Identification

The dynamic model of the demand to speed rotor-motor system, H, is composed of a cascade of the rotor aerodynamics, motor dynamics and battery response (see Fig. 4.8). The model is expected to take the form of two poles and one zero:

$$H = \frac{k(s/z_{\mathrm{b}} + 1)}{(s/p_{\mathrm{m}} + 1)(s/p_{\mathrm{b}} + 1)} \tag{4.10}$$

where H is the plant model transfer function, k is the rotor gain, z_{b} is the battery zero and p_{m} and p_{b} are the motor and battery poles.

- Rotor Aerodynamics
  The rotor torque is modelled as a proportional gain at operating conditions. Leishmann provides a quantitative estimate of the timescale of unsteady flow [Leishman 2006, pp 369-371]. The flow rise-time of these rotors was found to be of the order of one blade revolution (less than 8 ms). This is fast compared with the plant mechanics and so is not included in the model.

- Motor Dynamics
  From Cogdell [Cogdell 1999, p 805], the dynamics of an ideal brushless motor system is given to be a two-pole system. One pole is associated with the mechanical dynamics of the motor and the other with the electrical dynamics of the windings. The mechanical pole is governed by the rotational inertia of the drive — the combined total of the rotating motor armature, blades, hub and mast. The electrical dynamic of brushless motors is typically very fast and is omitted.

- Battery Dynamics
  Based on the theory and example cell parameters given in Gao *et al* [Gao *et al* 2002, pp 288-295], the flyer batteries are expected to have a one-pole, one-zero system model. The bus voltage drop due to motor energy consumption is slower than the dynamic effects of the system and is ignored in the dynamic model.

The non-linearities of the motor-rotor system, which include aerodynamic, electrical and mechanical effects, are considered to be small in the vicinity of the operating point and are ignored.

The thruster step response was found using input excitation experiments. The data were used to identify the model parameters, based on the expected model structure.

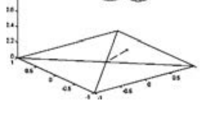

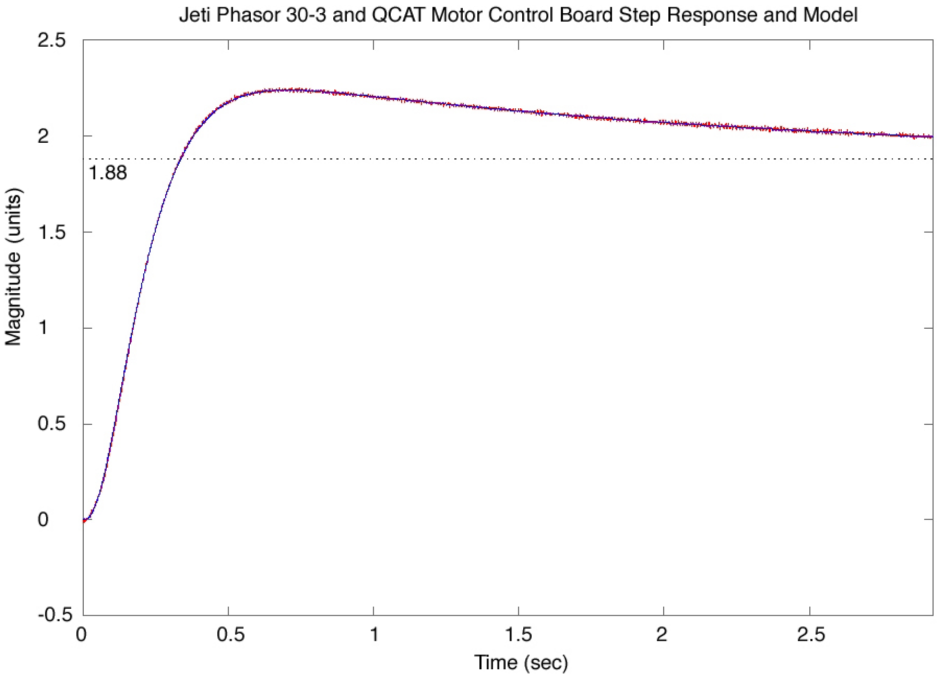

Figure 4.9: Averaged Step Response Data of XH and Identified Model

The experimental rig consisted of the motors (with mounted rotors) connected to the motor control boards. The drive components are mounted on the X-4 Flyer for the test. The flyer is fastened to a testbed that holds it off the ground and allows it to be locked in place or pivoted freely along the pitch axis.

The flyer will predominately operate around hover, with a rotor speed of approximately 870 rad$\cdot$s^{-1}. The reference signal sent was a squarewave between 175 and 225 PWM units, which produce speeds of 820-920 rad$\cdot$s^{-1}, respectively. This is a step across a typical expected speed range of the rotor in operation. The ID experiment was performed over 70 squarewave cycles, each with a period of 6 seconds.

A Digital Signal Processor (DSP) card captured the rotor's speed and input reference signal via a filtered frequency-to-voltage converter that measures the back-EMF frequency of one of the motor phases. The DSP sampled at 1 kHz and the speed sensor can resolve speed differences of 1.2 rad$\cdot$s^{-1}. The sensor board has dynamics associated with low-pass filters and a charge pump with slow electrical dynamics. The sensor board transfer function from sensed speed to analog voltage is:

$$X = \frac{1}{(s/45+1)(s/9.7+1)} \tag{4.11}$$

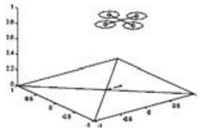

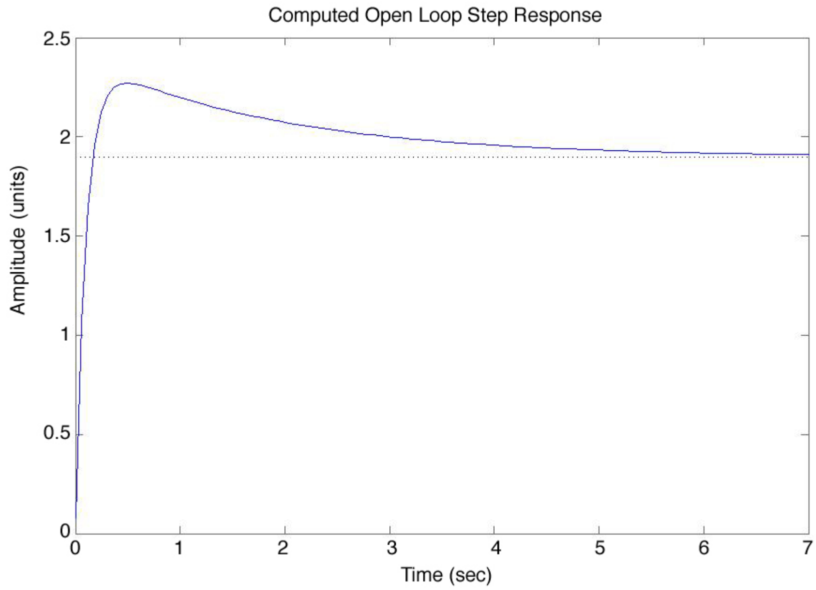

Figure 4.10: Open Loop Plant Step Response

All of the tests were averaged to increase the Signal-to-Noise ratio (SNR) of the data. The noise of the signal has a peak-to-peak magnitude of 10 rad·s^{-1}, for an SNR of 38 dB. Averaging the step responses increases the SNR to 57 dB. The model identified included a 0.02 second time delay in the system; this is attributed to the influence of fast dynamic effects and processor transport delay. The averaged measured response curve data of the combined plant and sensor dynamics, with the estimated sensor-plant model step response super-imposed, is shown in (see Fig. 4.9).

The plant transfer function is found by multiplying the identified system by the inverted known sensor model. The identified thruster response was found to be:

$$H = \frac{1.91(s/0.43+1)}{(s/9.6+1)(s/0.54+1)} \tag{4.12}$$

The $(s/0.43+1)/(s/0.54+1)$ pole-zero pair is attributed to the slow dynamics of the batteries. The dominant pole of the response is the mechanical response of the rotor. The step response and Bode plot of the plant appear in Fig. 4.10 and Fig. 4.11.

Maximum load limits on the lithium ion cells impose a slew rate non-linearity on the allowable control demand. Empirical tests show that constant increasing steps of up to 10 PWM steps per microsecond per time sample can be tolerated.

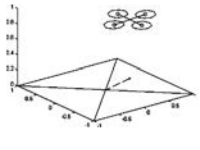

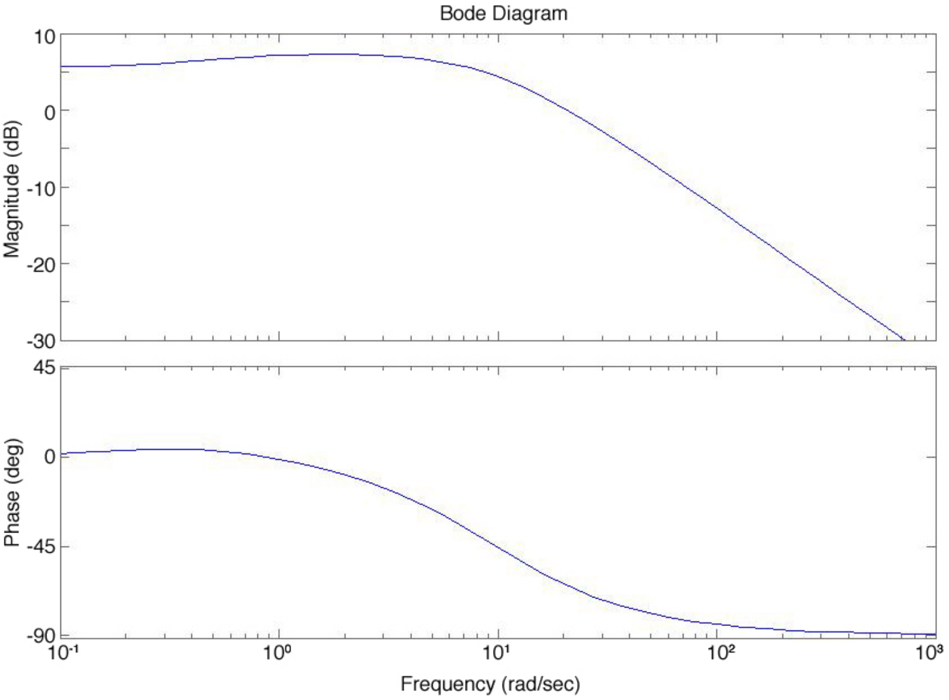

Figure 4.11: Open Loop Plant Bode Plot

The maximum steady state current draw per cells is 12 A. At full throttle, the motor will spin up to a maximum speed of 1050 rad·s^{-1}. The motor electrical phase cannot be reversed during flight for dynamic braking.

4.3.2 Experimental Identification of Disturbance Model

Rotor thrust varies due to environmental effects such as turbulence and cross-winds. Uncontrolled variations in speed are passed as disturbances to the rigid-body dynamics of the helicopter. As thrust cannot be directly measured easily, rotor speed is used as a metric instead.

By analysing variation in the rotor speed from a set of experiments replicating likely noise scenarios, the Power Spectral Density (PSD) distribution of typical disturbances can be determined. A corresponding colour filter is used to generate a disturbance input with an identical PSD that is then used in dynamic modelling of the drive system. Furthermore, these speed disturbances can be passed into the rigid body dynamics of the flyer to provide performance criteria for the global control design.

The rotor disturbances are categorise into four types: environment effects, automotion effects, obstacle effects and sensor noise. Sensor noise is random

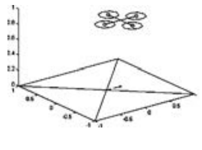

level fluctuation in the measured speed values. Automotion effects are due to the helicopter's motion in the air. Obstacle effects are caused by proximity to objects and surfaces. Environmental effects are due to the dynamic behaviour of the surrounding atmosphere — breezes, updrafts and eddies.

Four tests were performed:

1. Sensor noise test — motor stopped, sensor values recorded.
2. Automotion effects test — constant demand, flyer rocked back and forth by hand.
3. Obstacle effects test — constant demand, static position, a large flat surface moved about the rotor.
4. Environment effects test — constant demand, static position.

In each test, the rotor speed was sampled at 1 kHz with the National Instruments card and Matlab Realtime Windows. Approximately 70 seconds of data was recorded each time.

The PSD of each signal indicates what frequencies are present (see Fig. 4.12). The tests show a body of low frequencies (< 100 rad·s^{-1}) associated with the dynamic disturbances. The sensor noise test produced a flat spectrum of noise. The noise floor of the signals is found to be approximately -30 dB.

Each test exhibited a set of frequency spikes between 150 and 300 rad·s^{-1} associated with noise from a nearby power supply. Frequencies higher than 300 rad·s^{-1} are attenuated by the dynamics of the motor. Slow variation in battery voltage effects the low-frequency part of the PSD, below 1 Hz.

A 600-second-long environment test was performed to improve low-frequency spectrum resolution. It exhibited the same low-frequency power distribution as the other environment test; all of the effects tests produced a similar frequency spectrum, with variations in power. When the PSD is plotted on a log-log graph it shows a linear trend (see Fig. 4.12).

It is interesting to note that the undisturbed test has the greatest levels of higher-frequency noise. It is thought that this is due to circulating air currents and eddies building up over time in a sustained flow. If the flow conditions are constantly disturbed, such systems cannot manifest. As a consequence, stable hover conditions correspond to the worse noise characteristics for the system.

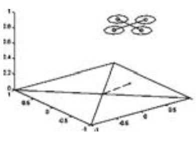

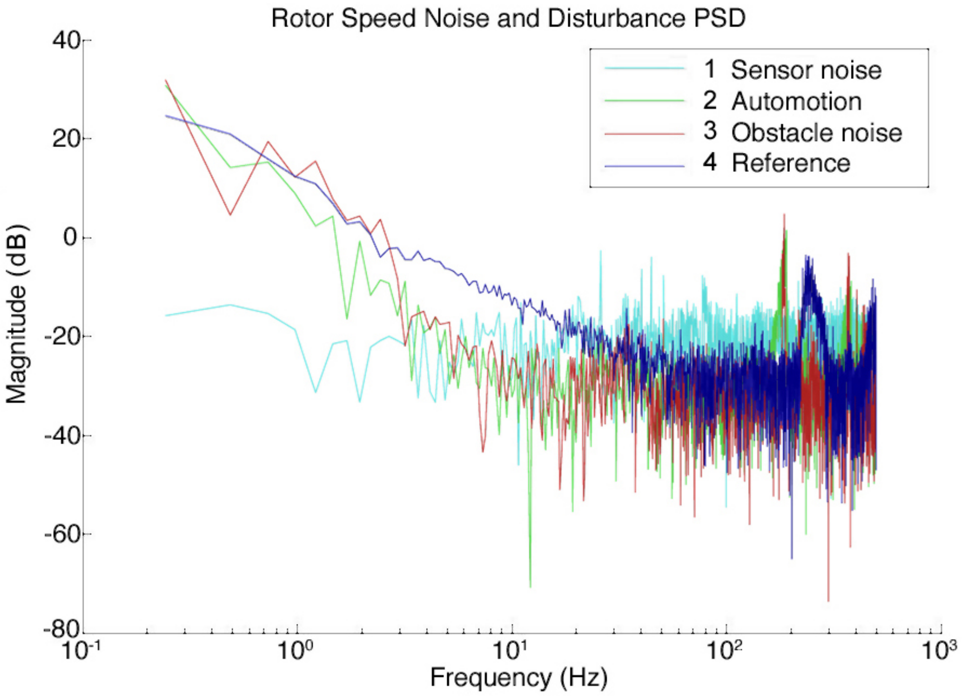

Figure 4.12: Disturbance Power Spectral Density Tests

This worst-case load disturbance noise profile, $d(t)$, is modelled as white noise, $\eta(t)$, passing through a colour filter; $d = D\eta$ (see also Fig. 4.8):

$$D = \frac{0.0143(s+7)}{(s+0.1)} \tag{4.13}$$

4.3.3 Control Requirements and Constraints

The rotor speed controller must provide stable and robust performance with minimal overshoot and good disturbance rejection within the constraints of the system limitations. The controller was implemented in discrete time, running at 1 kHz. The controller frequency is more than twenty times faster than the system dynamics and so the control design is treated as a continuous system [Franklin *et al* 1994, p 609].

Precise reference tracking of the plant is not the foremost task of the controller. The motor-rotor subsystem is designed to be type 0 [Franklin *et al* 1994]; that is, no pure integral term in the controller. The attitude control system for the full UAV will contain integral terms that will compensate motor set-points to ensure flight stability of the vehicle.

The most important design considerations are the constraints following from

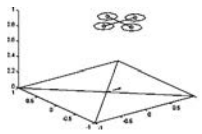

the torque limitation, and the required disturbance rejection. The disturbance rejection requirement places a lower bound on the compensator gain. The control gain that can be realised by the torque-limited plant is bound by the maximum slew-rate that disturbance noise and sinusoidal references may demand.

For disturbance rejection, the aim is for -15 dB gain for attenuation of disturbance inputs across the frequency range of the actuator. Further attenuation reduces the disturbance signal below what can be resolved by the speed sensor. The sensitivity function [Franklin *et al* 1994, p 420] of the controller with respect to uniform white noise disturbance, $\eta(t)$ is:

$$|S| = \frac{|D|}{|1 + CH|} \tag{4.14}$$

The colour filter, D, naturally attenuates the noise signal at higher frequencies, reducing the necessary controller gain at the top end of the spectrum. It is known that $|H| = 1.8$ at low frequencies. Solving for $|C|$ gives a lower gain bound of +8 dB. The disturbance rejection requirement forms the lower bound on the compensated open-loop Bode plot (see Fig. 4.14).

The rate saturation was determined experimentally to be 10 PWM steps/μs. To compute the rate saturation feedback bound on the controller, the closed loop transfer function for $u(t)$, given a reference input $r(t)$ and unit deviation white noise disturbance $\eta(t)$ passed through D, is derived:

$$u = \frac{-CD}{1 + CH}\eta + \frac{C}{1 + CH}r \tag{4.15}$$

Each of these terms can be considered separately to derive the gain bounds associated with each input. In the first case, consider the noise and assume that the rate of change of r is small. Using the Laplace transform, the bound $B =$ 10 PWM steps/μs on the derivative of u becomes:

$$B \geq \frac{|j\omega CD|}{|1 + CH|} \tag{4.16}$$

where $L(\eta) = 1$.

The bound on the compensator open-loop plant is determined by solving this equation in terms of k, the magnitude of the compensator: $C = kC_0(s)$. Squaring both sides of the inequality produces a quadratic that can be solved exactly for k at each frequency:

$$\left(\alpha^2 + \beta^2 - \frac{D^2\omega^2}{B^2}\right)k^2 - 2\alpha k - 1 \leq 0 \tag{4.17}$$

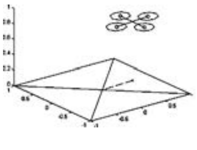

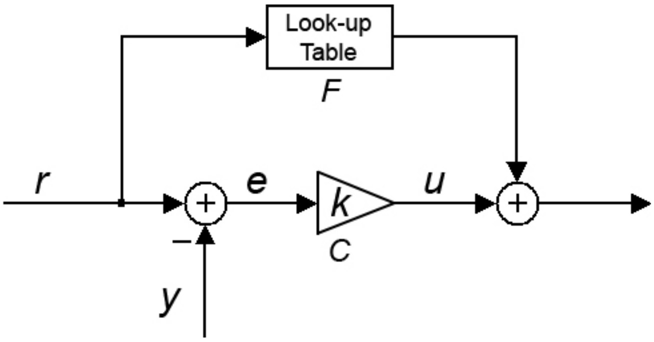

Figure 4.13: Feedback Compensator Structure

where $H = \alpha + j\beta$, and both H and D are functions of ω.

The constraint is complex up to an asymptote at 250 rad·s^{-1} and any compensator magnitude will satisfy this bound up to this frequency. Thus, saturation of the controller due to noise is not a design consideration in the frequency range of interest.

By the same argument, consider the bound due to the allowable rate of change of the reference input and assume η is zero. A bound on the compensated open-loop Bode plot is computed for the reference signal, r, assuming an input sinusoid of amplitude 100 PWM steps across the range of frequencies. Similar to before, the quadratic in k at each frequency is:

$$\left(\alpha^2 + \beta^2 - \frac{r^2\omega^2}{B^2}\right) k^2 - 2\alpha k - 1 \leq 0 \qquad (4.18)$$

The resulting constraint is the upper bound on the compensated open-loop Bode plot (top right, Fig. 4.14), and shows that for frequencies less than the 40 rad·s^{-1} asymptote any gain will track the reference without saturation. Above 60 rad·s^{-1}, the permissible gain rolls off at -20 dB per decade.

4.3.4 Compensator Design

The compensator chosen is a proportional controller with nonlinear feed-forward compensation (see Fig. 4.13). As the plant consists of a single dominant pole and a near pole-zero cancellation, the plant theoretically cannot be destabilised by the application of gain. However, larger gains will introduce limit-cycles in the plant, caused by saturation of the amplitude and slew rate bounds of the controller. From the bounds on the open-loop Bode plot (see Fig. 4.14), it can be seen that complex control designs cannot produce significantly better performance within the physical limitations of the system.

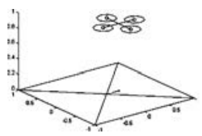

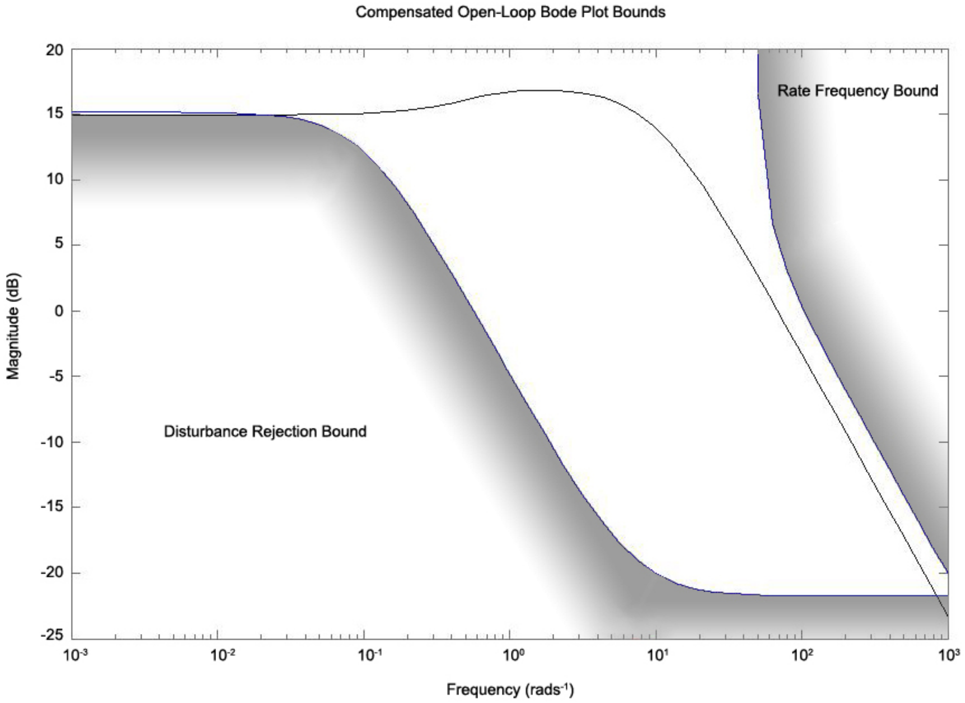

Figure 4.14: Compensated Open-Loop Bode Plot With Bounds

The optimal proportional gain was determined to be 3. From calculation, the minimum gain necessary to satisfy the low frequency disturbance rejection criterion is 2.6 and the maximum gain to satisfy the slew saturation bound across all frequencies is 4.4. A lower gain value was chosen for robustness; in experiment, gains right on the upper bound sometimes produced limit cycles, which were deemed unacceptable.

Remark. For very high performance designs it may be desirable to add control dynamics to raise the gain of the system around 30 rad·s^{-1} to exploit the higher headroom near the rate bound asymptote. If more disturbance rejection is required, the controller may be modified by the addition of a lag controller at low frequencies.

The computed transfer function of the closed loop system between reference and output speed is:

$$H_{cl} = \frac{0.8562(s/0.42+1)}{(s/78.54+1)(s/0.43+1)} \tag{4.19}$$

Although tracking accuracy is not critical, the steady state error of the plant can be reduced by feeding forward the required open-loop demand to drive the system to the vicinity of the desired set-point. This feed-forward term is a non-

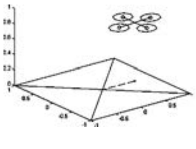

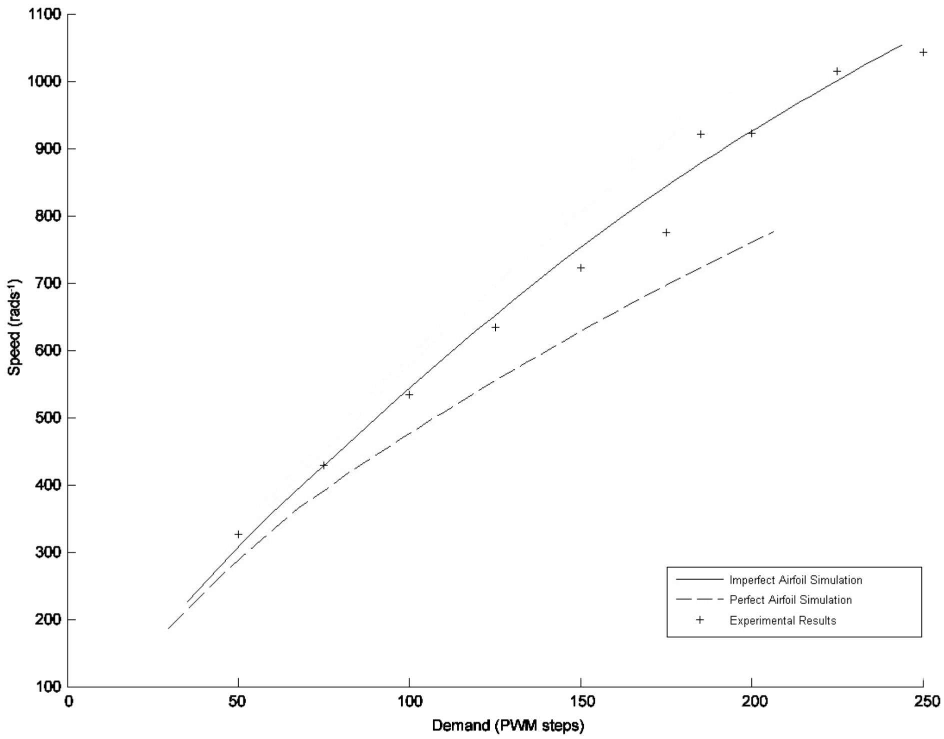

Figure 4.15: Predicted and Experimental Rotor Speeds for Given PWM Input

linear relationship taken from the PWM input vs speed plot (see Fig. 4.15), and is implemented in the controller as a look-up table.

4.3.5 Dynamic Performance

The control design was implemented on the motor control boards and tested in the X-4 thrust test rig. The control loop runs at 1 kHz on the HC12 microprocessor — a speed dictated by the need to smoothly generate the rate-limited ramp output of the controllers. All control computations were performed with float variables, with up to 20-bits computational precision available from the HC12 arithmetic logic unit.

The ID process for the closed loop plant is repeated to confirm that the controller performs as designed. The identification showed good agreement with the calculated system:

$$H_{cl} = \frac{83(s + 0.0046)}{(s + 99)(s + 0.0042)} \tag{4.20}$$

The implemented closed loop system has a rise-time of 0.05 seconds and no overshoot. Higher gains were tested on the controller to investigate the effects

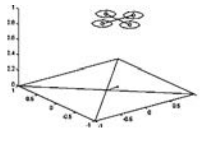

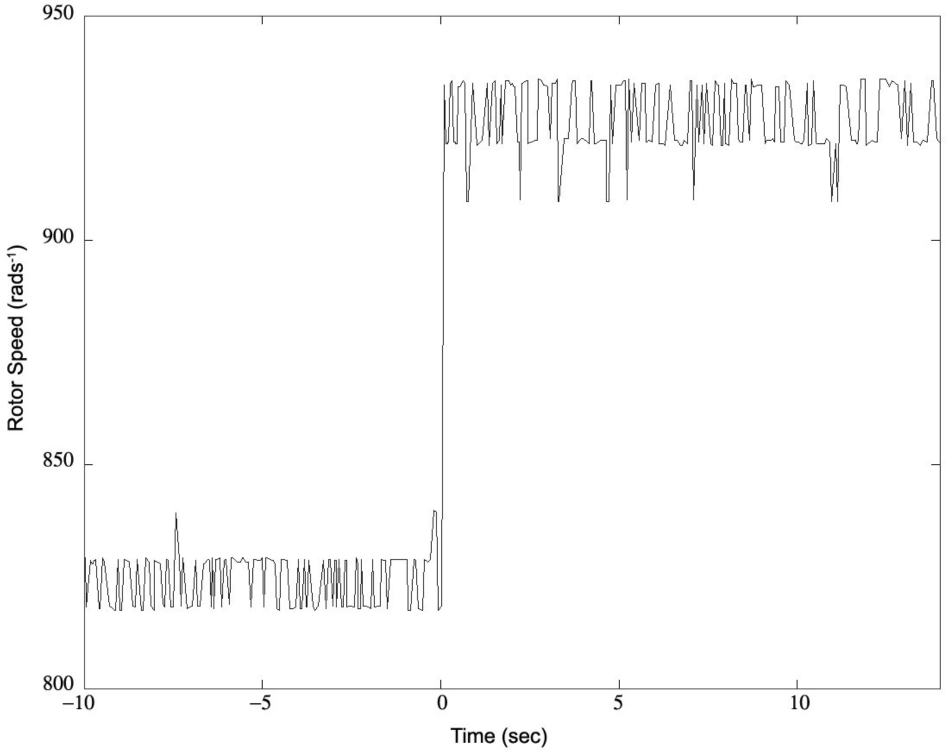

Figure 4.16: Closed-Loop Step Response

of the saturation nonlinearities on the system performance. It was found that, although the system was not destabilised under high gains, the saturation non-linearities led to undesirable limit-cycle behaviour in the vicinity of the set-point. The final gain was chosen to maximise system performance without exciting the saturation non-linearities. The system has a 70 rad·s^{-1} bandwidth and the overall performance of the system was deemed acceptable.

When sampled at the 50 Hz motor board output data-rate, the response occurs within one sample period (see Fig. 4.16). The obtained closed-loop speed response appears to be a 1-step deadbeat response to the avionics attitude control system.

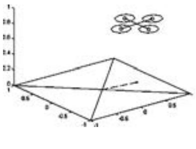

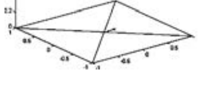

Chapter 5

Quadrotor Dynamics and SISO Control

In this chapter I expand on the classic quadrotor dynamic model and use it to develop a design for the X-4's stability controller. By adding important rotor effects such as flapping and dynamic inflow to the flight model it is possible to show that quadrotors can be made dynamically favourable — that is, made neutral or controllably unstable. This is exploited by using the Bode Integral to find the design parameters that optimise the flyer's configuration.

5.1 Introduction

Helicopters are intrinsically difficult to control — they exhibit unstable oscillating modes associated with the fuselage mass swinging from the rotor. These oscillations are slow enough to be controlled by a pilot in full-scale vehicles, but are much faster in small UAVs. Many small helicopters are impossible for a human to fly without assistance; these typically employ a bell-hillier stabiliser bar to slow these dynamics so that a human can pilot them. However, rotorcraft can be constructed with different rotor configurations that exhibit pure instability and stable oscillations [Prouty 2002, p 603]. Quadrotors are ideal for exploring this.

The simpler quadrotor dynamic models are not capable of representing complex helicopter behaviour. In particular, they omit the blade flapping effect which is critical to understanding the oscillatory helicopter modes. Additional effects unique to quadrotors include rotor flapping due to yaw and variable rotor inflow velocities as a result of craft pitch and roll. These aerodynamic effects are combined with the basic equations to produce a more detailed model.

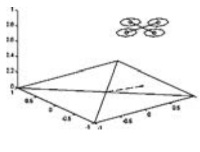

The expanded flapping model is used to design a controller to stabilise the flyer. The flight model decoupled dynamics in longitudinal pitch-roll and azimuthal modes can be derived and used to determine the unforced response in pitch and roll for a range of system configurations. By making careful choices about the set-up of the flyer, the control task can be simplified.

The loose coupling of the pitch and roll axes of a helicopter around hover allow a SISO controller to be used. The system parameters are estimated from data to produce a numerical plant model. From this model a linear PID controller is designed. It was tested in simulation and implemented — it demonstrates successful roll and pitch compensation in tethered tests and free flight.

This chapter is organised into six parts, including this introduction. Section 5.2 presents the dynamics of quadrotor helicopters with blade flapping. Section 5.3 provides a derived plant model based on measured flyer parameters, and analyses the effect of parameter model envelope. Section 5.4 describes how the height of the rotors above the centre of gravity effects the sensitivity of the plant. Sections 5.5 and 5.6 provides a PID control design for the attitude dynamics and reports the performance of the controller on the test gimbal.

5.2 Dynamics and Stability

5.2.1 The Importance of Flapping

When a rotor translates horizontally there is a difference in blade lift between the advancing and retreating blades which causes the rotor tip path plane to tilt. The resulting angle of the rotor plane is obtained by simultaneously solving the constant and sinusoidal components of the blade centrifugal-aerodynamic-static weight moment system.

Most treatments of quadrotor dynamics do not include blade flapping. In fact, all rotors flap to some degree due to blade flexibility. Thin plastic rotors such as those used in the Draganflyer are particularly prone to this effect. Typically, the physical stiffness of a rotor is ignored in flyer analysis and the rotor stiffness is modelled purely as a centrifugal term.

The dynamics of rotor flapping are very fast, occurring within one revolution of the rotor [Leishman 2006], compared with the rigid body dynamics of the helicopter. Consequently, the blade flapping equations can be written as instantaneous functions of the craft's planar velocity.

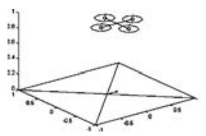

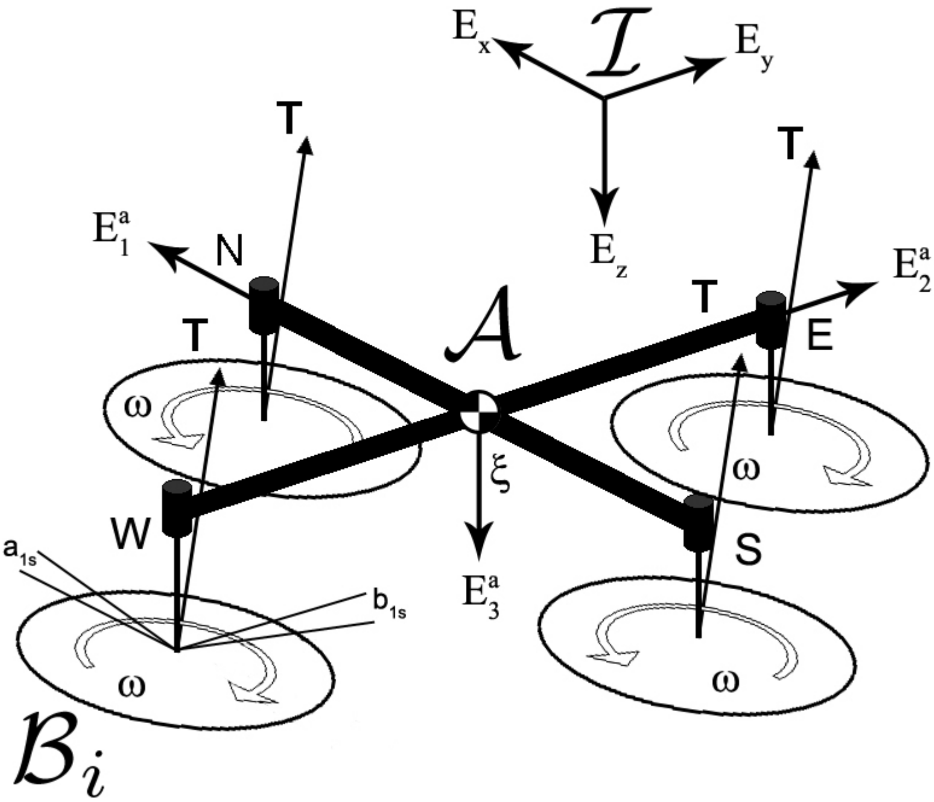

Figure 5.1: Flapping Quadrotor Free-body Diagram.

The flyer behaviour can be modelled using the dynamics of a rigid-rotor quadrotor helicopter modified with additional flapping dynamics. Flapping is important — simulations of the X-4 show that the tilting rotor can introduce significant stability effects for the vehicle [Pounds *et al* 2004].

5.2.2 Basic Dynamics

A basic flyer dynamic model [Pounds *et al* 2002] is modified for articulated rotors by implementing a model of the rotor flapping and generalised rotor force and torque components. The right-hand inertial frame is denoted by $\mathcal{I}= \{E_x, E_y, E_z\}$, where x is aligned with the front of the craft and z is in the direction of gravity, and $\xi = (x, y, z)$ is the origin of the body fixed frame $\mathcal{A} =\{E_1^a, E_2^a, E_3^a\}$. The frame $\mathcal{A}$ is related to $\mathcal{I}$ by the rotation matrix $R : \mathcal{A} \rightarrow \mathcal{I}$. V and Ω are the linear and angular velocities of the frame in $\mathcal{A}$ (see Fig. 5.1).

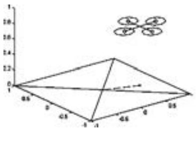

The equations are:

$$\begin{aligned}
\dot{\xi} &= RV && (5.1)\\
m\dot{V} &= -m\Omega \times V + mgR^{\mathrm{T}}e_3 + \sum_{N,S,E,W} T_i && (5.2)\\
\dot{R} &= R \cdot \Omega_\times && (5.3)\\
\mathrm{I}\dot{\Omega} &= -\Omega \times \mathrm{I}\Omega + \sum_{i=\mathrm{N,S,E,W}} [Q_i + M_i] && (5.4)\\
T_i &= C_T \rho A r^2 \omega_i^2 \begin{pmatrix} -\sin a_{1_s i} \\ \cos a_{1_s i} \sin b_{1_s i} \\ \cos b_{1_s i} \cos a_{1_s i} \end{pmatrix} && (5.5)\\
Q_i &= C_Q \rho A r^3 \omega_i |\omega_i| e_3 && (5.6)\\
M_i &= T_i \times D_i && (5.7)
\end{aligned}$$

where m and I are the mass and rotational inertia of the flyer, g is acceleration due to gravity, ρ is the density of air, r is the rotor radius, and A is the rotor disc area. In equation 5.6, ω is multiplied by its magnitude to preserve the sign of rotation for counter-rotating rotors.

Here $x_\times$ represents the skew-symmetric matrix such that $a_\times b = a \times b$ for vectors in $\Re^3$. The rotation matrix R is constructed with the yaw-pitch-roll, $\eta = (\phi, \theta, \psi)$ Euler angles. Rotors are indexed by their corresponding compass directions: North, South, East and West ($NSEW$), where N indicates the front rotor. Correspondingly, D_i is the rotor displacement from the flyer centre of mass:

$$\begin{aligned}
D_N &= \begin{pmatrix} 0 & d & h \end{pmatrix} && (5.8)\\
D_S &= \begin{pmatrix} 0 & -d & h \end{pmatrix} && (5.9)\\
D_E &= \begin{pmatrix} d & 0 & h \end{pmatrix} && (5.10)\\
D_W &= \begin{pmatrix} -d & 0 & h \end{pmatrix} && (5.11)
\end{aligned}$$

where d is the arm length of the flyer and h is the height of the rotors above the Centre of Gravity (CoG).

Vectors T_i and Q_i are the rotor thrust and torque, and M_i is the moment due to the thrust vector of the ith rotor – for a teetering rotor, the moment produced by the rotor flapping is due solely to the thrust vector acting around a displacement from the vehicle's centre of gravity.

Crucially, the thrust vector is tilted by the flapping angles, altering both the force and moments applied to the airframe. The first harmonic of the longitudinal

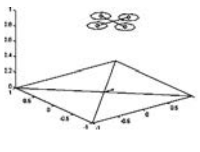

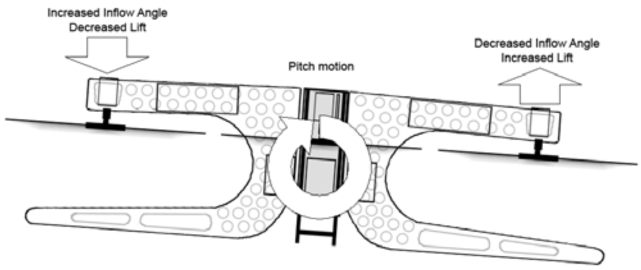

Figure 5.2: Inflow Due to Vertical Rotor Motion.

and lateral flapping angles of the ith rotor are denoted by a_{1s_i} and b_{1s_i}. The non-dimensionalised thrust and torque coefficients, C_T and C_Q, are treated as constants here. The speed of the ith rotor is given by ω_i. The non-dimensionalised thrust coefficient and flapping equations are discussed in more detail in Sections 5.2.3 and 5.2.4.

The rotation matrix R is constructed with the yaw-pitch-roll, $\eta = (\phi, \theta, \psi)$ Euler angles:

$$\mathrm{R} = \begin{pmatrix} c_\theta c_\phi & s_\psi s_\theta c_\phi - c_\psi s_\phi & c_\psi s_\theta c_\phi + s_\psi s_\phi \\ c_\theta s_\phi & s_\psi s_\theta s_\phi + c_\psi c_\phi & c_\psi s_\theta s_\phi - s_\psi c_\phi \\ -s_\theta & s_\psi c_\theta & c_\psi c_\theta \end{pmatrix} \tag{5.12}$$

where s_x and c_x notations represent $\sin x$ and $\cos x$ respectively.

5.2.3 Vertical Rotor Motion Inflow

A quadrotor necessarily has a horizontal displacement between its masts and CoG. When the craft rolls and pitches, the rotors experience a vertical velocity with respect to the established airflow through the rotor. This leads to a change in the apparent inflow angle observed at the blade (see Fig. 5.2). From Prouty [Prouty 2002, p 101], C_T can be related to the vertical velocity, V_z, by:

$$C_T/\sigma = \frac{a(\alpha)}{4}\left[\theta_t - \frac{v_i + V_z}{\omega R}\right] \tag{5.13}$$

where a is the polar lift slope, θ_{t} is the geometric blade angle at the tip of the rotor, v_i is the induced velocity through the rotor, and σ is the solidity of the disc - the ratio of the surface area of the blades and the rotor disc area.

The polar lift slope is itself a function of the rotor blade angle of attack, α. It is highly nonlinear for some airfoils and so the relation can be better expressed

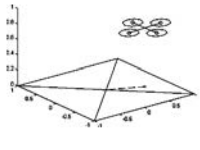

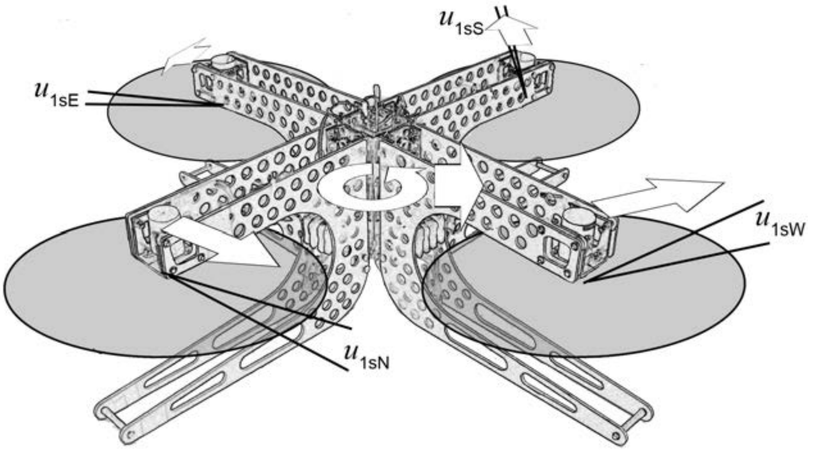

Figure 5.3: Principal Flapping Angles of General Quadrotor Motion.

as a variation around a set point, $C_{\mathrm{T}0}$:

$$C_{Ti} = C_{T0} + \Delta C_{Ti} \tag{5.14}$$

where ΔC_T is the change induced by the changing inflow conditions. From Equation 5.13, this is written as:

$$\Delta C_{Ti} = -\frac{a_0}{4}\frac{\sigma}{\omega_i R}(V_z + \Omega \times D_i)e_3 \tag{5.15}$$

where a_0 is the lift slope at the set point.

A consequence of this effect on the inflow velocity is a tendency for a quadrotor to damp pitch and roll velocities.

5.2.4 Generalised Rotor Flapping Equations

The dynamic model described in Pounds *et al* [Pounds *et al* 2004] added articulated flapping rotors to the basic quadrotor rigid body dynamics model of Hamel *et al* [Hamel *et al* 2002]. The current configuration of the X-4 Flyer does not incorporate the hub springs originally included in the model and as a result the flapping equations can be substantially simplified.

However, a quadrotor's flight is not limited to longitudinal motion — when the vehicle moves arbitrarily, the flapping motions of the rotors need not be in line with the nominal front of the aircraft (see Fig. 5.3). When the craft yaws the linear velocity of the rotor hubs about e_3 is added to the motion of the vehicle.

The flapping of the ith rotor due to planar motion is found by calculating the magnitude and direction of rotor's translation and defining a local frame of

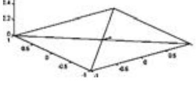

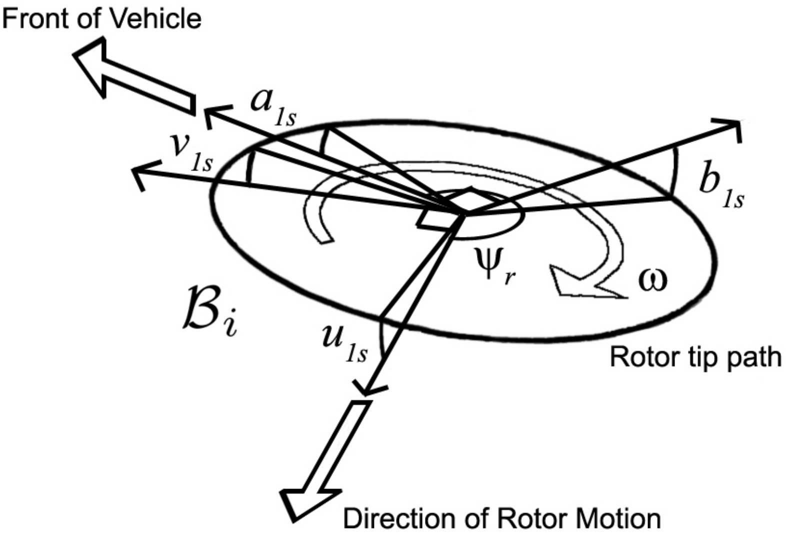

Figure 5.4: Blade Flapping Angle Rotation.

reference, $\mathcal{B}_i$, aligned in that direction. The longitudinal and lateral flapping angles are calculated in the rotor frame ($u_{1_s i}$ and $v_{1_s i}$) and then re-expressed in the body-fixed frame ($a_{1_s i}$ and $b_{1_s i}$ using a rotation matrix (see Fig. 5.4). This reduces computational complexity by using standard flapping equations in the local frame.

The per-rotor flapping is found by first computing the advance ratio and azimuthal direction of the rotor:

$$V_{ri} = V + \Omega \times D_i \tag{5.16}$$

$$\mu_{ri} = \frac{\|V_{r(1,2)i}\|}{\omega_i R} \tag{5.17}$$

$$\psi_{ri} = \arctan\left(\frac{V_{r(2)i}}{V_{r(1)i}}\right) \tag{5.18}$$

where $V_{r(n)i}$ is the nth element of the ith rotor's velocity vector, μ_{ri} is the ith rotor's advance ratio and ψ_{ri} is the azimuthal direction of motion.

The X-4 Flyer uses teetering hinges, and so has a zero hinge offset distance. Thus, the equations describing flapping motion given in Subsection 2.4.3 can be greatly simplified. The longitudinal and lateral flapping angle solutions of the ith rotor in the local frame, $\mathcal{B}_i$, are:

$$
\begin{aligned}
u_{1_si} &= \frac{1}{1-\frac{\mu_{ri}^2}{2}}\mu_{ri}\left(4\theta_t - 2\lambda_i\right) && (5.19)\\
v_{1_si} &= \frac{1}{1+\frac{\mu_{ri}^2}{2}}\frac{4}{3}\left(\frac{C_T}{\sigma}\frac{2}{3}\frac{\mu_{ri}\gamma}{a} + \mu_{ri}\right) && (5.20)
\end{aligned}
$$

respectively, where λ_i is the non-dimensionalised inflow of the ith rotor [Prouty 2002, p 167] and γ is the Lock Number [Leishman 2006, p 179]:

$$\gamma = \frac{\rho a_0 c r^4}{\mathrm{I}_b} \tag{5.21}$$

where $\mathrm{I_b}$ is the rotational inertia of the blade about the flapping hinge.

These are transformed back into the body-fixed frame by the frame mapping between $\mathcal{A}$ and $\mathcal{B}_i$, J_i to derive the body-frame flapping angles due to motion of the flyer:

$$
\begin{aligned}
{}^{\mathcal{A}}J_{\mathcal{B}_i} &= \begin{pmatrix} \cos\psi_{ri} & -\sin\psi_{ri} \\ \sin\psi_{ri} & \cos\psi_{ri} \end{pmatrix} && (5.22)\\
\begin{pmatrix} \overline{a}_{1_si} \\ \overline{b}_{1_si} \end{pmatrix} &= {}^{\mathcal{A}}J_{\mathcal{B}_i}\begin{pmatrix} u_{1_si} \\ v_{1_si} \end{pmatrix} && (5.23)
\end{aligned}
$$

The components of the flapping angles produced by the craft's pitch and roll rates [Prouty 2002] are added to those of the body-fixed frame:

$$
\begin{aligned}
a_{1_si} &= \overline{a}_{1_si} + \frac{-\frac{16}{\gamma}\left(\frac{q}{\omega}\right) + \left(\frac{p}{\omega}\right)}{1-\frac{\mu_i^2}{2}} && (5.24)\\
b_{1_si} &= \overline{b}_{1_si} + \frac{-\frac{16}{\gamma}\left(\frac{p}{\omega}\right) + \left(\frac{p}{\omega}\right)}{1-\frac{\mu_i^2}{2}} && (5.25)
\end{aligned}
$$

5.2.5 Unforced Stability Analysis

The dominant dynamics of a rotorcraft are associated with the longitudinal dynamics of the vehicle. Around hover, the motion is largely decoupled in each axis. The symmetry of quadrotors means that the important attitude dynamics can be described by a single equation. The natural stability of these dynamics is analysed to provide insight into the best airframe geometry for controllability of the system.

In earlier work [Pounds *et al* 2004], Prouty's stability derivation was applied to analyse the near-hover dynamics of quadrotors. This treatment furthers that

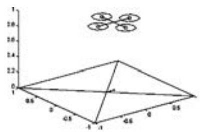

analysis through the addition of terms specific to quadrotors and the elimination of flapping due to hub springs that are not used in the current X-4 Flyer.

From the basic dynamic equations for a helicopter constrained to only translate in X and rotate in pitch, with a small advance ratio and flapping angles, and equal speed on all rotors, the stability derivative matrix is[1]:

$$\begin{vmatrix} -ms + \frac{\partial x}{\partial \dot{x}} & \frac{\partial x}{\partial \dot{\theta}}s - mg \\ \frac{\partial \theta}{\partial \dot{x}} & -\mathrm{I_{YY}}s^2 + \frac{\partial \theta}{\partial \dot{\theta}}s \end{vmatrix} \begin{vmatrix} \dot{x} \\ \theta \end{vmatrix} = 0 \tag{5.26}$$

This uses the standard stability derivatives given in Prouty [Prouty 2002, p 564] and listed in Appendix D – x is the longitudinal position, θ is the pitch angle, $\mathrm{I_{YY}}$ is the pitch rotational inertia and s is the Laplace transform of the differential operator. The standard treatment of helicopters is modified by multiplying the effect of main rotor derivatives by 4 for the four rotors, as well as by adding a relatively small term in $\partial\theta/\partial\dot{\theta}$ due to the vertical motion of the rotors in pitch and roll:

$$\frac{\partial \theta}{\partial \dot{\theta}} = \frac{\partial \theta}{\partial a_{1_s}} \frac{\partial a_{1_s}}{\partial \dot{\theta}} + \frac{\partial x}{\partial \dot{\theta}} h + \rho A_b (\omega R)^2 2d \frac{\partial C_{\mathrm{T}}/\sigma}{\partial \dot{\theta}} \tag{5.27}$$

where:

$$\frac{\partial C_T/\sigma}{\partial \dot{\theta}} = \frac{-a}{8} \frac{d}{\omega R} \tag{5.28}$$

The characteristic equation of the system matrix determinant becomes:

$$s^3 - \left(\frac{1}{m} \frac{\partial x}{\partial \dot{x}} + \frac{1}{\mathrm{I_{YY}}} \frac{\partial \theta}{\partial \dot{\theta}} \right) s^2 + \frac{g}{\mathrm{I_{YY}}} \frac{\partial \theta}{\partial \dot{x}} = 0 \tag{5.29}$$

The first order term

$$\frac{\partial x}{\dot{x}} \frac{\theta}{\dot{\theta}} - \frac{x}{\dot{\theta}} \frac{\theta}{\dot{x}} \tag{5.30}$$

does not appear in the characteristic polynomial because the two derivative products approximately cancel [Prouty 2002, p 597]:

$$\frac{\partial \theta}{\partial \dot{\theta}} = \frac{d\theta}{da_{1_s}} \frac{\partial a_{1_s}}{\partial \dot{\theta}}, \frac{x}{\dot{x}} = -\rho A_b (\omega R)^2 C_T/\sigma \frac{\partial a_{1_s}}{\partial \mu} \frac{\partial \mu}{\partial \dot{x}} \tag{5.31}$$

$$\frac{\partial \theta}{\partial \dot{x}} = \frac{d\theta}{da_{1_s}} \frac{\partial a_{1_s}}{\partial \mu} \frac{\partial \mu}{\partial \dot{x}}, \frac{\partial x}{\partial \dot{\theta}} = -\rho A_b (\omega R)^2 C_T/\sigma \frac{a_{1_s}}{\dot{\theta}} \tag{5.32}$$

Solving for the roots of the characteristic polynomial gives the exponential components of the dynamic behaviour of the system. Since:

$$\left(\frac{1}{m} \frac{\partial x}{\partial \dot{x}} + \frac{1}{\mathrm{I_{YY}}} \frac{\partial \theta}{\partial \dot{\theta}} \right) > 0 \tag{5.33}$$

---

[1] Prouty's aircraft coordinate notation is used in the stability and control analysis for clarity.

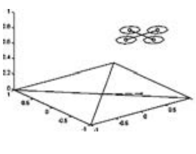

and:

$$\frac{g}{\mathrm{I}_{\mathrm{YY}}}\frac{\partial\theta}{\partial\dot{x}} > 0 \tag{5.34}$$

for any system, it is clear that the unforced, open-loop dynamics can never be stable for the X-4.

Application of Routh's Discriminant, as outlined in Prouty, uses the characteristic polynomial to determine the nature of the instability. The Routh's Discriminant, $R.D.$, is given by:

$$R.D. = AD - BC \tag{5.35}$$

where A, B, C and D are the coefficients of 5.29. If it is positive, the craft will exhibit pure divergence. If negative, the craft will exhibit unstable oscillation. If zero, the pitch dynamic will be neutral. In this case:

$$R.D. = -C_T\rho A\left(\omega R\right)^2 h \tag{5.36}$$

Of the composing terms, only h can change signs. For a conventional helicopter, where $h < 0$, the craft has an unstable pole pair. If the rotors and CoG are coplanar then the craft is marginally stable, with poles at the origin. If the rotors are inverted (above the CoG), the craft will diverge without unstable oscillation.

The idea of inverting the rotor not new: it has been applied in the past in De Lackner's HZ-1 [Starostin 2004] and has similarities with the well-known Hiller Flying Platform [Starostin 2004] and Charles Zimmerman's 'whirligig' [NASM 2006]. The Mesicopter micro quadrotor also has an inverted rotor configuration, but fixed, ducted rotors — it was found that increasing CoG distance from the rotor plane increases damping but does not benefit the natural frequency [Kroo *et al* 2000]. In all these cases the rigid (or near-rigid) rotors would produce small or zero flapping effect. The X-4 Flyer is different because it has true flapping hinges and can be adjusted into the correct dynamic mode.

5.2.6 Simulation

Before building the X-4 Flyer, a dynamic model was coded into Matlab Simulink. The simulator model is nonlinear, and includes effects such as the flyer's rotational velocity in calculating the advance ratio per rotor. The simulator consists of three Simulink blocks: the control input mixer, output graphical display and dynamics S-Function.

The control mixer takes roll, pitch, yaw and throttle demand signals and converts them into logical $NSEW$ motor demand inputs to the dynamics block.

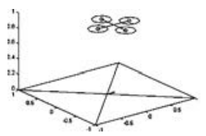

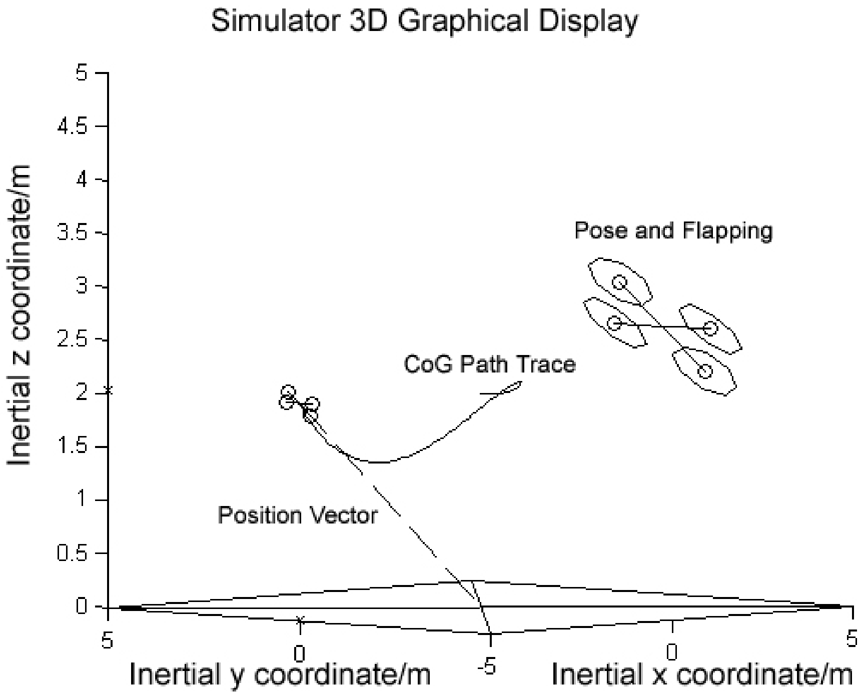

Figure 5.5: X-4 Flyer Simulator Graphical Output.

This follows the mixing scheme outlined in Pounds *et al* [Pounds *et al* 2002]. The same input logic is implemented on the flyer control boards.

The plotter animates a schematic flyer in a 3D window (fig. 5.5). An attitude display shows the pose of the flyer at the current moment and a CoG trail is plotted for the total flyer motion. An additional attitude display can be turned on to show the pose and relative rotor flapping angles when the flyer moves off-screen. Two plot animations can be seen as flip-books in the bottom corners of the pages. Each page represents 0.125 seconds of simulation time.

The dynamics block is a Simulink M-File S-Function block. The block implements the dynamic model with continuous states for the body motion. The system is solved with an Euler ODE1 fixed step solver, with a step-size of 0.02 seconds. The simulator runs until a set time elapses or until the flyer's altitude reaches zero (crashes). The flyer parameters are entered into the dynamic model to reflect the physical hardware.

Figure 5.6 shows the partial state, (x, z, θ), evolution of the X-4. In each case, the initial conditions are $x = 0$ m, $z = 2$ m. In the top row (A, B and C), the flyer is given an initial x velocity of 0.1 ms^{-1}. In the bottom row (D, E and F), the flyer is given an initial angle of initial pitch angle of -0.1 rad. All other angles and

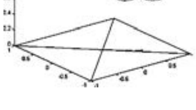

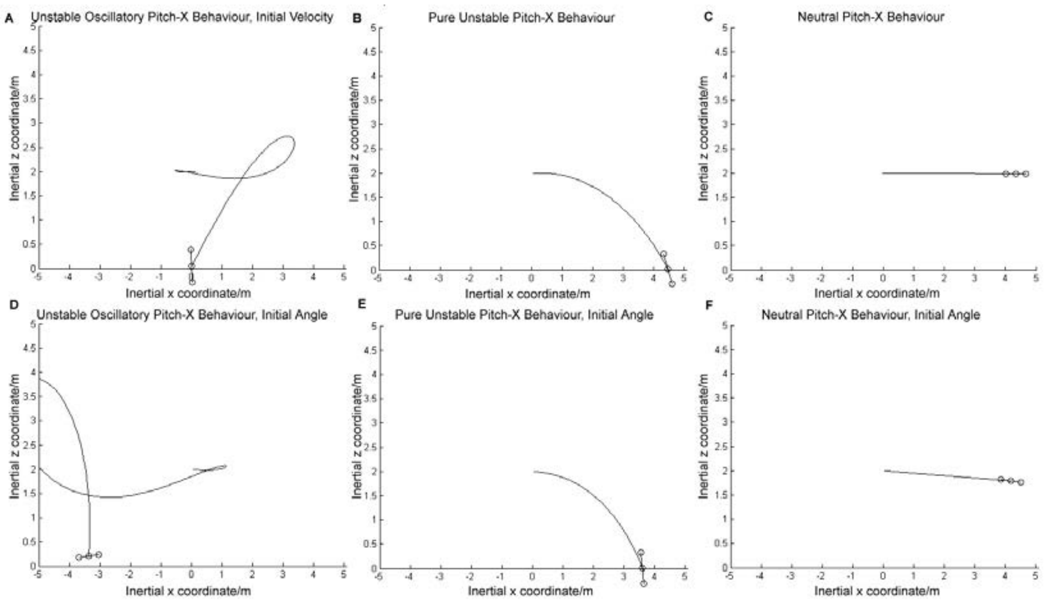

Figure 5.6: Simulated Open-Loop Dynamic Modes.

velocities are zero and hover thrust is applied at each rotor. Columns represent changes to the mast height and hinge offset, demonstrating the different dynamic modes. In A and D, the flyer has a 20 mm equivalent hinge offset and no mast height; it exhibits unstable oscillation. In B and E the flyer has no hinge offset (teetering rotor) and -35 mm mast height; it shows pure divergence. In C and F the flyer has a 20 mm hinge offset and -13.25 mm mast height; in this case the competing derivatives cancel and produce neutral stability.

5.3 Model Parameterisation and Stability

Designing a controller based on this model requires parameters of the physical system to be specified. Most of these values are dictated by the flight performance of the system; some, most importantly h, can be chosen freely. The error associated with each parameter defines the envelope of the plant model's dynamic response. The system behaviour across the range of parameters is used to determine the best value of h, the height of the rotor plane above the CoG.

5.3.1 Measured Values and Uncertainty

A set of parameter estimates are taken directly from measurements of the flyer or derived from experiments, and the associated errors estimated. In the case

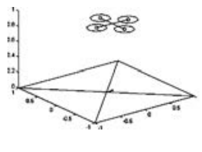

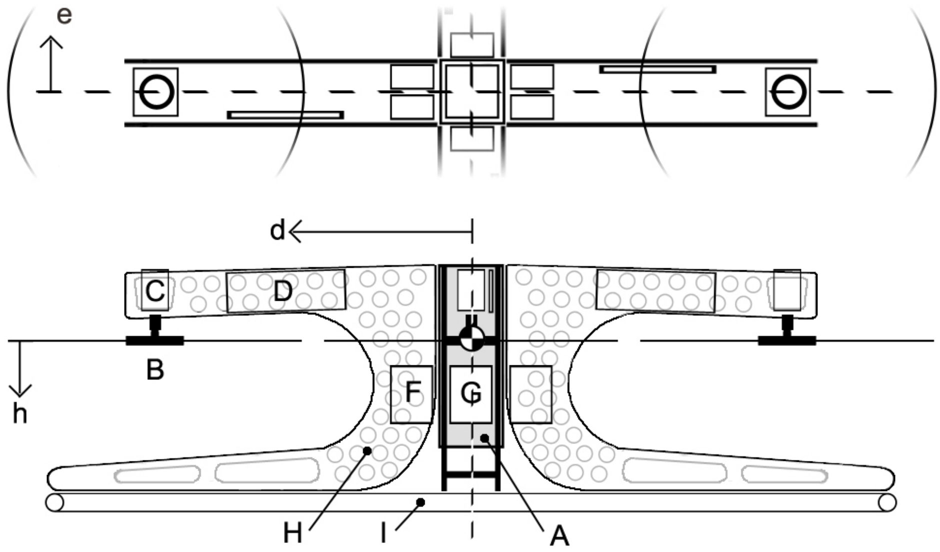

Figure 5.7: X-4 Component Offsets.

of parameters computed from other known values, the associated error was also computed:

- Aerodynamic parameters
  Rotor, blade and aerodynamic parameters are obtained through measurement, computation, simulation or from references. These are listed in Table 5.1.

- Masses and Displacements
  Component masses and distances measured with respect to the rotor plane, (masses ±0.005 kg, distances ±0.005 m) are given in Table 5.2. Note that this table is not a complete listing of all masses, but includes all major masses – screws and fasteners are omitted (see Fig. 5.7).

- Rotational Inertia Computed from the previous values by treating the masses as point masses, the diagonal entries of the inertial matrix are given in Table 5.3. The CoG is 0.0071 ± 0.005 m above the rotor plane.

5.3.2 Parameterised Model Envelope

Using the physical values for the flyer, the coupled pitch and ξ_x translational dynamical equations can be computed. The error range of the parameters maps the roots of the plant into a space on the complex plane. Linearised differential

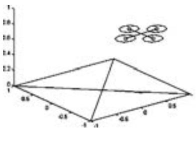

Parameter	Value	Error	Unit
a_0	5.5	±0.5	
c_t	0.012	±0.001	m
m	4.34	$\pm 5 \times 10^{-3}$	kg
A	0.0855	$\pm 0.1 \times 10^{-3}$	m^2
C_T	0.0047	$\pm 0.2 \times 10^{-3}$	
C_Q	0.228×10^{-3}	$\pm 0.015 \times 10^{-3}$	
I_b	40.887×10^{-6}	$\pm 3.655 \times 10^{-6}$	$\mathrm{kg{\cdot}m^2}$
R	0.165	$\pm 0.5 \times 10^{-3}$	m
ρ	1.184	Not available	$\mathrm{kg{\cdot}m^{-3}}$
γ	1.417	±0.133	
λ	0.049	$\pm 2 \times 10^{-3}$	
θ_t	4.4	±0.5	deg
σ	0.054	$\pm 1 \times 10^{-3}$	
ω_0	870	±5	$\mathrm{rad{\cdot}s^{-1}}$

Table 5.1: Aerodynamic Parameters and Associated Error.

	Part	mass/kg	d/m	e/m	h/m
A	Avionics	0.242	0	0	-0.02
B	Rotor	0.046	0.315	0	0
C	Motor	0.288	0.315	0	-0.06
D	ESC	0.074	0.15	0.035	-0.055
E	Powerbus	0.099	0	0	-0.13
F	$\mathrm{Batt_{long}}$	0.165	0.0125	0.06	0.035
G	$\mathrm{Batt_{lat}}$	0.165	0.0	0.04	0.035
H	Arm	0.039	0.157	0.035	0.04
I	Hoop	0.200	0	0	-0.17
	Chassis Core	0.600	0	0	0
	Fasteners	Rem.	0	0	0

Table 5.2: Component Masses and Offsets.

	Value	Error	Unit
$\mathrm{I_{XX}}$	0.0820	$\pm 7.2 \times 10^{-3}$	$\mathrm{kg{\cdot}m^2}$
$\mathrm{I_{YY}}$	0.0845	$\pm 7.7 \times 10^{-3}$	$\mathrm{kg{\cdot}m^2}$
$\mathrm{I_{ZZ}}$	0.1377	$\pm 9.7 \times 10^{-3}$	$\mathrm{kg{\cdot}m^2}$

Table 5.3: Diagonal Inertial Elements.

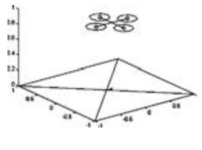

	Value	Error
p_1	-2.5477	± 0.8190
p_2	-0.1549	± 0.0155
p_3	0.1322	± 0.0067
z	-0.015	± 0.003

Table 5.4: Poles and Zeros of the Open Loop Pitch Dynamics.

equations for the flyer are:

$$\begin{aligned} m\ddot{x} &= -mga_{1_s} - mg\theta && (5.37) \\ \mathrm{I_{YY}}\ddot{\theta} &= 4dC_T\rho AR^2\omega_0\delta\omega + mgha_{1_s} - \frac{a}{2}\sigma\rho AR\omega_0 d^2\dot{\theta} && (5.38) \end{aligned}$$

The longitudinal flapping angle is approximated as a linear function of $\dot{x}$ and $\dot{\theta}$:

$$a_{1_s} = \frac{4\theta_t - 2\lambda}{\omega_0 R}\dot{x} - \frac{16}{\gamma\omega_0}\dot{\theta} \qquad (5.39)$$

These can be solved for a single transfer function $H = \Theta/\delta\omega$ between pitch angle, θ, and the input change in rotor speeds, $\delta\omega$:

$$H = \frac{4dC_T Rc_2(s + gc_1)}{(s + gc_1)(\mathrm{I_{YY}}s^2 + \frac{a_0}{2}\sigma c_2 d^2 s) + mgh\left(gc_3 s^2 - gc_1\right)} \qquad (5.40)$$

where:

$$\begin{aligned} c_1 &= \frac{4\theta_t - 2\lambda}{\omega_0 R} && (5.41) \\ c_2 &= \rho AR\omega_0 && (5.42) \\ c_3 &= \frac{16}{\gamma\omega_0} && (5.43) \end{aligned}$$

Using the previously given parameters and errors, the poles and zeros of the system are shown in Table 5.4. The rotor height above the CoG is a large contributor to error; accurate knowledge of the rotor height is important to determining the dynamic model.

The unforced stability analysis demonstrated that h is also important in determining the behaviour of the dynamic system. The root locus for h shows that the structure of the open-loop poles changes significantly as h changes sign (see Fig. 5.8). Analogous to the unforced case, the system exhibits an unstable oscillation when the CoG is below the rotor, pure divergence when it is above the rotor, and neutral stability when coincident with the rotor.

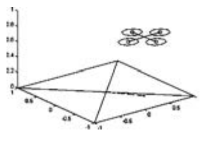

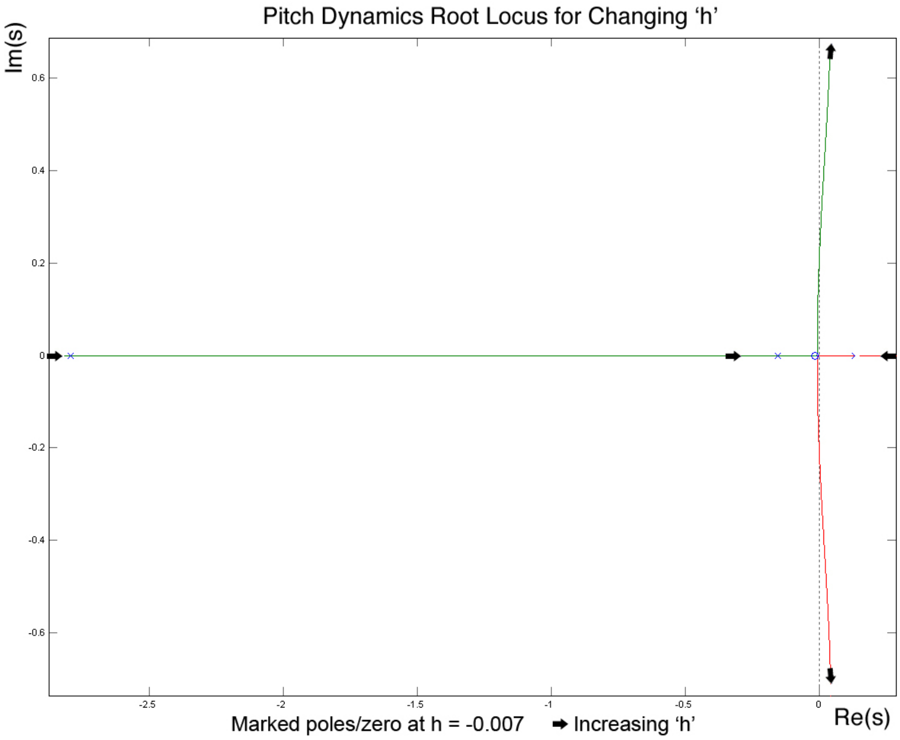

Figure 5.8: Root Locus of Pitch Dynamics for Changing Rotor Height Above CoG.

Prouty suggests that helicopters can benefit from an inverted rotor configuration, as pure divergence is easier for a human pilot to correct for than unstable oscillation [Prouty 2002, p 603].

5.4 Design for Optimal Sensitivity

The use of automatic compensators no longer requires that a system be intuitive for a human pilot, and so oscillatory systems are acceptable. Instead, the fundamental limits of control can be employed to adjust the plant for best controller performance.

Strong disturbance rejection and fast response to input commands are desired for good performance. However, the ‘water-bed effect’ of the Bode integral for the sensitivity function imposes a limit on arbitrary design targets for the controller across all frequencies: it states that any arbitrary reduction in the sensitivity of the system implies a corresponding increase in sensitivity over other frequencies [Seron *et al* 1997] (see Subsection 2.7.3).

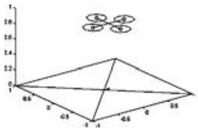

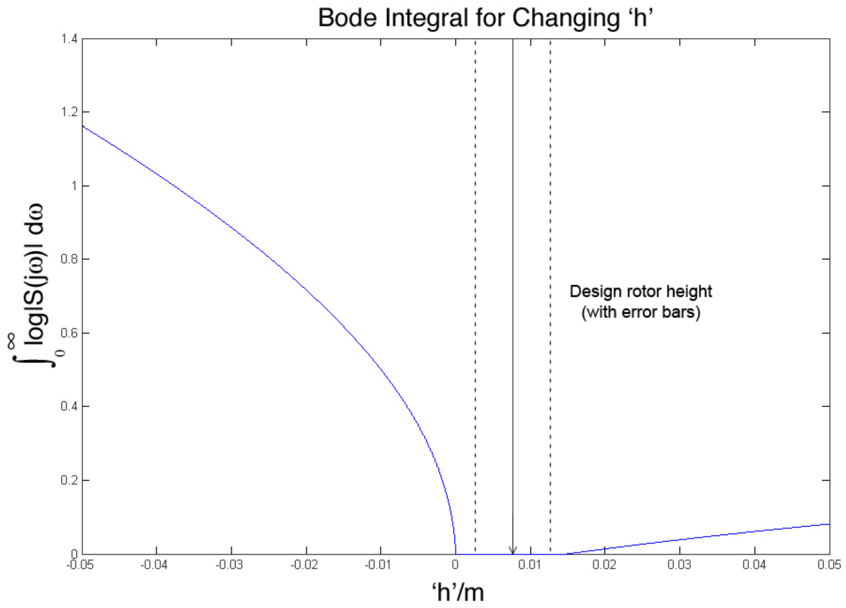

Figure 5.9: Bode Integral With Respect to Rotor Plane Placement.

In the case of the X-4 Flyer, both low frequency disturbances, which cause drift, and high frequency disturbances, which induce noise in the inertial sensors, must be rejected. For this reason, it is desirable to reduce the integral of sensitivity function across the underlying system, prior to the application of any control.

The sensitivity function can be related directly to the poles of the open-loop plant throuhg the Bode integral. From Seron *et al*:

$$\int_0^\infty \log|S(e^{j\omega})|d\omega = \pi \sum_{i=1}^{n_p} p_i \tag{5.44}$$

where S is the sensitivity function of the system, p_i are the poles of the open loop plant, and ω is frequency.

Calculating the Bode integral for a range of h from -0.05 to 0.05 m below the rotor demonstrates a sharp notch at $h = 0$ (see Fig. 5.9). When the rotor plane is coincident with the center of gravity, the Bode integral is zero. In this configuration, the pitch dynamic is neutral.

The magnitude of the integral changes sharply as the rotor plane moves away from the CoG. Given the strong correlation between h error and plant model structure, and the link between control sensitivity and h position, it is clear that close attention to the correct tuning and verification of rotor height is essential for the performance of the helicopter.

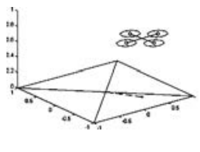

For the X-4 Flyer, the ideal rotor position is at $h = 0$. However, as the root locus with changing h demonstrates, the structure of the plant undergoes significant change with error around this point. For this reason, the CoG is set slightly away from the rotor plane so that small errors will not have an impact on stability. The Bode integral corresponding to the rotor position, with error bars, is shown on Fig. 5.9. Although more difficult to control by a human, this choice maximises the achievable performance of the closed-loop system.

5.5 Control and Simulation

A variety of control techniques have been implemented successfully on quadrotor UAVs – these include PID and LQ [Bouabdallah *et al* 2004b] and PD^2 [Tayebi and McGilvray 2004] control. Bouabdallah found that PID performed favourably compared with LQ due to the simpler method's tolerance for model uncertainty. This quality is desirable for the derived full-flapping model, which is especially sensitive to changes in h.

In addition to the attitude dynamics, the X-4 Flyer also has important motor dynamics. The motor dynamics act in series with the rigid body dynamics – fast motor response is important for authoritive attitude control of quadrotors. To this end, rotor speed controllers have been developed to improve the natural performance of the rotor-motor system [Pounds *et al* 2007a] (see Chapter 4). As the motor dynamics are so fast, the dominant pole has little interaction with the attitude mechanics. If they were slower, excess poles would diverge closer to the unit circle, leading to oscillation and possibly instability.

5.5.1 Discretised Model and Validation

The onboard controller runs at 50 Hz, the maximum frequency at which attitude data is updated, and so the dynamics of the plant are discretised at $t_{\mathrm{s}} = 0.02$ seconds for the control design. The IMU returns both angle and rate information, which allows for an improper PID controller to be realised.

From the parameter estimtion, the complete discretised model, $G = \theta/\delta\omega$, is:

$$G = \frac{3.6967 \times 10^{-5}(z+1)(z-0.9997)}{(z-1.0027)(z-0.9969)(-0.9457)} \tag{5.45}$$

where $\delta\omega$ is the differential variation in rotor speed about the operating condition, $\omega_0 = 870$ rad·s^{-1}. The additional zero at $z = -1$ comes from the matched pole-zero discretisation method.

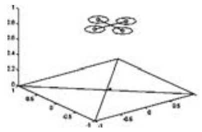

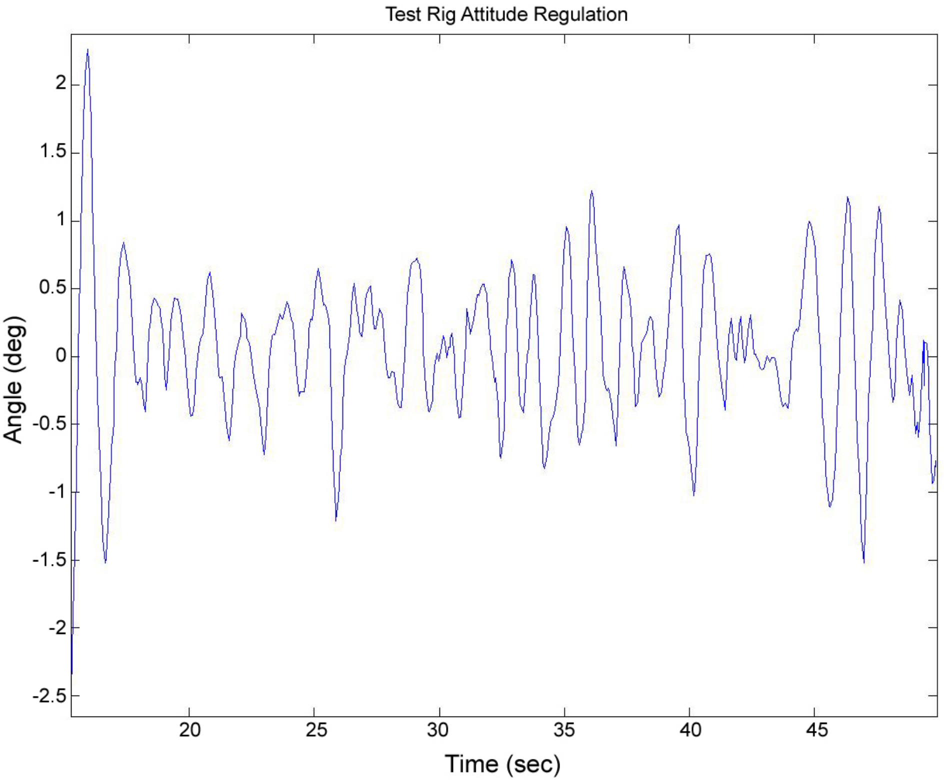

Figure 5.10: Zero Pitch Reference Tracking on the Gimbal Rig.

It is difficult to validate the full dynamic model in free flight conditions and so an intermediate identification test was run on the gimbal rig. As the flyer cannot translate on the rig, there is no flapping term associated with lateral motion, and the transfer function reduces to a two pole model:

$$H_{\text{rig}} = \frac{4dC_T R c_2}{\mathrm{I}_{\mathrm{YY}} s^2 + (hmgc_3 + a_0 2\sigma c_2 d^2)s} \tag{5.46}$$

The expected discretised transfer function is:

$$G_{\text{rig}} = \frac{3.4493 \times 10^{-5}(z+1)}{(z-1)(z-0.956)} \tag{5.47}$$

It is straight forward to design a PD controller for this plant. The controller used was:

$$C_{\text{rig}} = 400(1 + 0.1\frac{(z-1)}{0.02}) \tag{5.48}$$

The flyer successfully regulates attitude on the gimbal rig, within ±1° angle tracking (see Fig. 5.10 and 5.11). A series of 10° reference steps were used to identify the response of the plant (see Fig. 5.12).

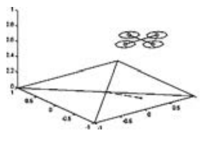

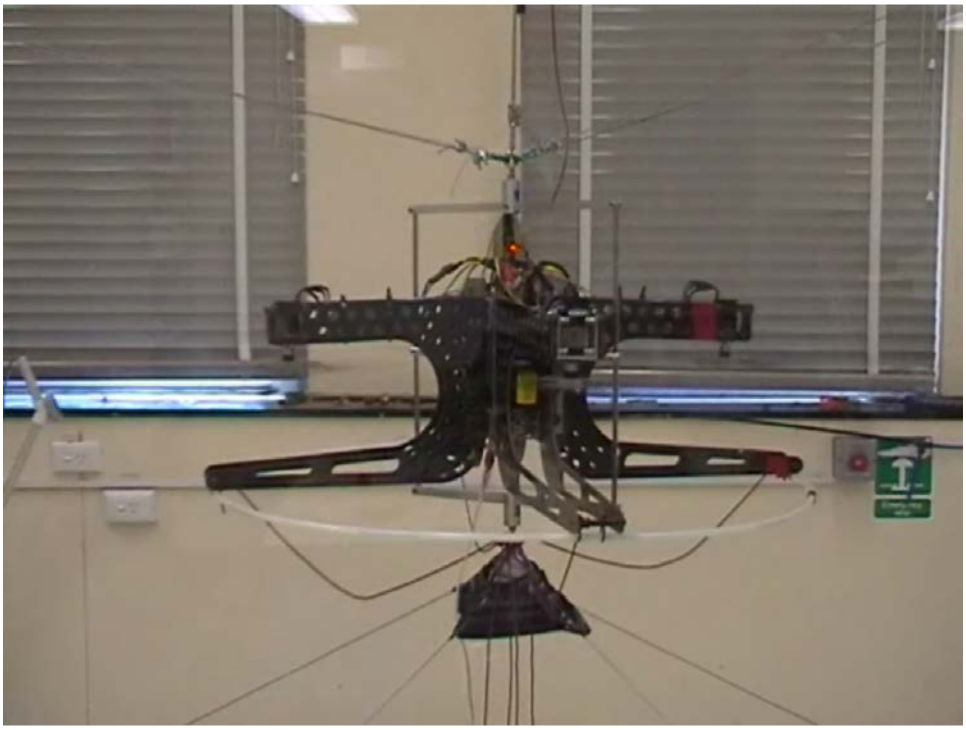

Figure 5.11: X-4 Flyer Stabilised in Pitch and Roll on the Gimbal Rig.

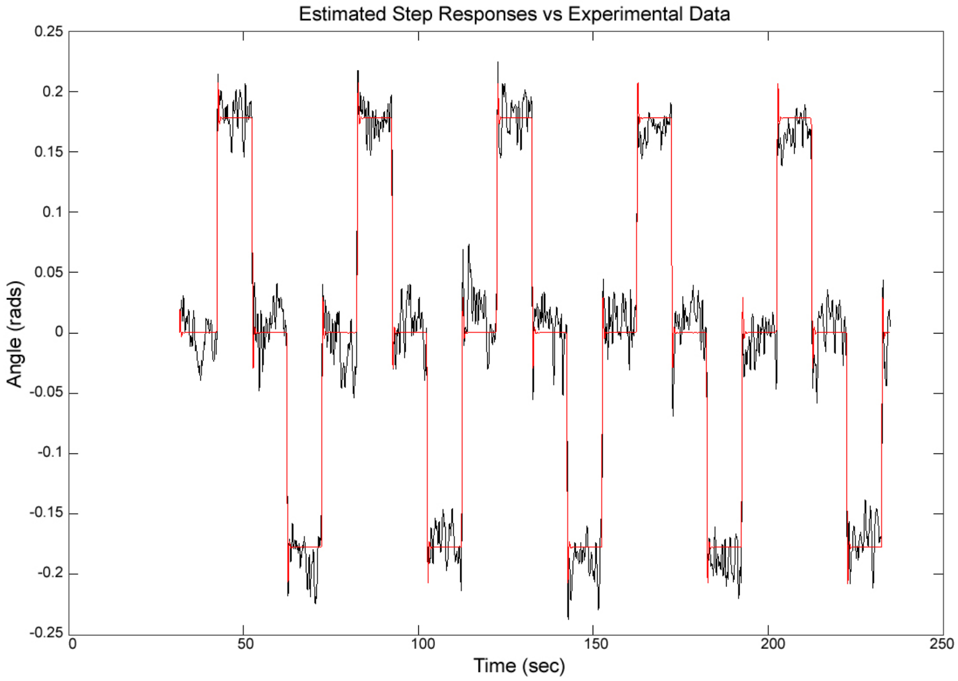

Figure 5.12: Gimbal Rig Experiment Step Response and Identified Plant Response.

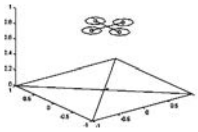

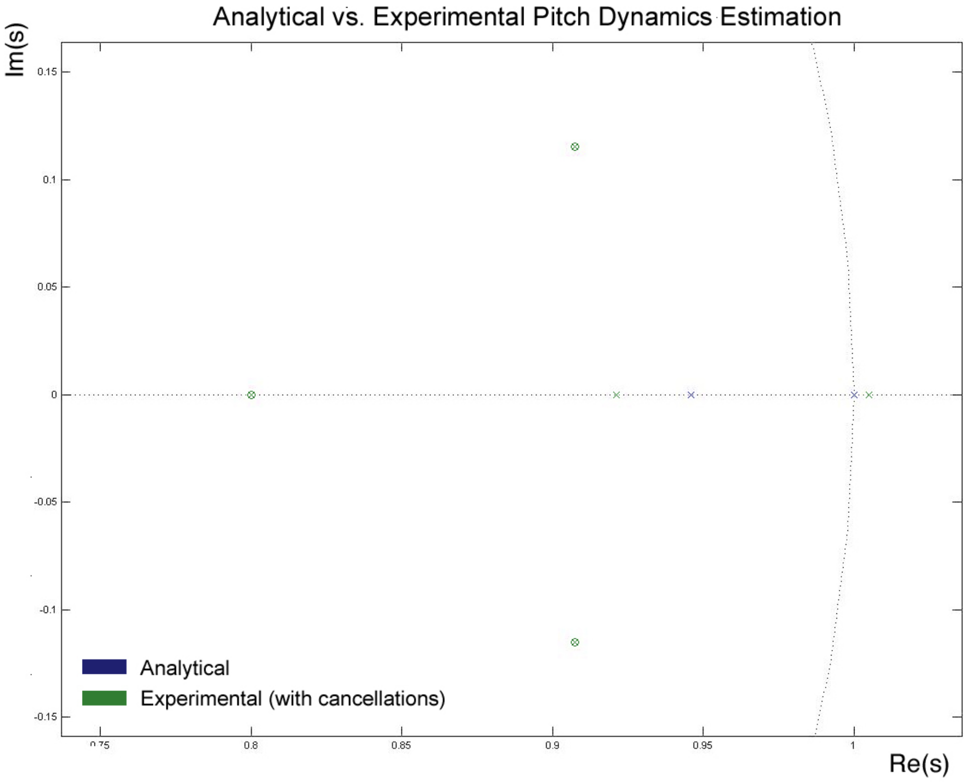

Figure 5.13: Gimbal Rig Experiment Estimated Poles vs Calculated Poles.

The experimentally derived plant is:

$$H_{\text{rig}} = \frac{5.557 \times 10^{-5}}{(z - 1.005)(z - 0.9211)} \tag{5.49}$$

The calculated pole positions show good agreement with the analytically derived system, indicating that the free flight model is likely to be reliable (see Fig. 5.13). The difference in the slow stable pole position is within the range due to the parameter estimation error. The identified model exhibits a slow unstable pole, rather than a pure integrator, likely due to the flyer being slightly top-heavy in the test rig.

5.5.2 Controller Design

The proposed controller consists of a pure integrator for zero angle tracking error and a real zero to stabilise the plant (see Fig. 5.14). The transfer function of the controller, C, is:

$$C = 400 \left(1 + 0.2 \frac{0.02}{(z - 1)} + 0.3 \frac{(z - 1)}{0.02} \right) \tag{5.50}$$

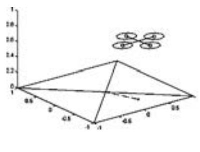

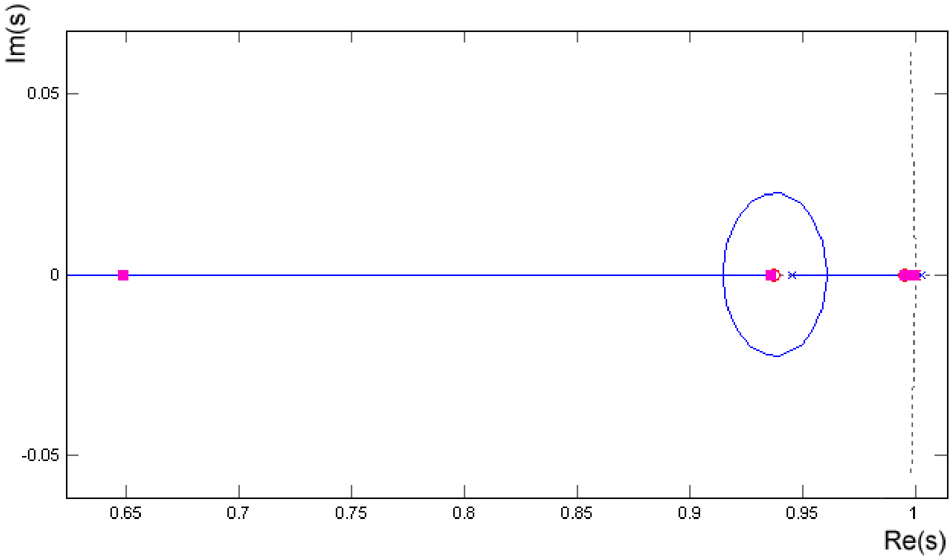

Figure 5.14: Attitude Control Design Root Locus.

As the motor dynamics are so fast, the dominant pole has little interaction with the attitude mechanics. If it were slower, the excess poles would diverge closer to the unit circle, leading to oscillation and possibly instability. The slow motor pole-zero cancellation is associated with the dynamics of the lithium ion polymer cells used to power the flyer. Sufficient gain causes the pole to close with the zero, reducing the influence of the effect.

5.5.3 Disturbance Rejection

The disturbances experienced by the attitude dynamics are expected to take the form of aerodynamic effects propagated through variations in the the rotor speed. The sensitivity model developed for the motor speed controller is used to predict the displacement in position due to a motor speed output disturbance (see Fig. 5.15). The X-4 Flyer position variation should be small — in the order of 0.1 m.

The rotor speed noise is modelled by an output disturbance to the rotor speed, d, characterised as white noise, $\eta(t)$, passed through a coloured filter, D [Pounds and Mahony 2005]:

$$D = \frac{0.0143(s+7)}{(s+0.1)} \tag{5.51}$$

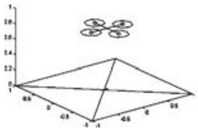

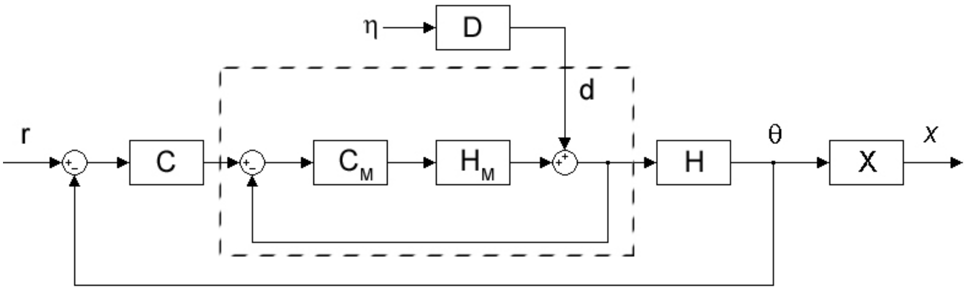

Figure 5.15: Disturbance Propagation Block Diagram.

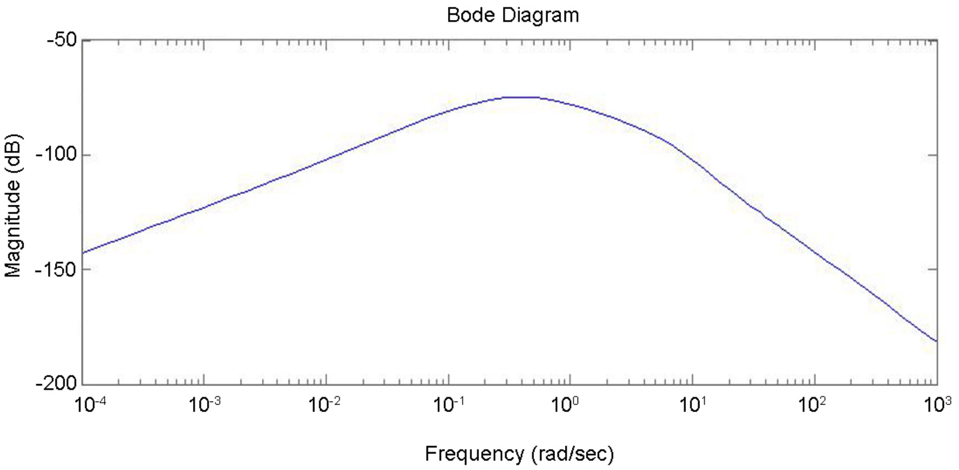

Figure 5.16: Pitch Angle Sensitivity Function Bode Plot.

The pitch angle sensitivity due to η is given by:

$$\frac{\Theta}{W} = \frac{H}{1 + C_M H_M} \frac{C_M H_M}{C_M H_M + CH(1 + C_M H_M)} D \tag{5.52}$$

where H_{M} is the motor plant and C_{M} is the motor compensator. The peak sensitivity in pitch angle is at 0.4 rad·s^{-1} (see Fig. 5.16).

Pitch angle is integrated to x position. Using equations 5.38 and 5.39, the transfer function, X, is:

$$X = \frac{-gc_3 - g}{s(s + gc_1)} \tag{5.53}$$

A unit disturbance at the peak angle sensitivity frequency yields a positional variation of 0.01 m, well within the target. However, due to the integral position dynamics, the peak sensitivity in x occurs at low frequencies to DC ($\omega < 0.01$ rad·s^{-1}) at -6.3 dB; a unit sinusoid in this range will produce a corresponding position deviation of 0.78 m with negligible angle deviation. Note that this de-

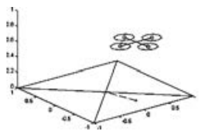

viation is very slow – a period of 600 s – and would be easily compensated for, given position measurement.

5.5.4 Simulation

A complete simulation of the attitude control system was coded in Matlab Simulink. This included nonlinearities in the system arising from multiple sample times in the microcontrollers, saturation of the motors, quantisation of measurements and slew limitation in the motor controller.

In simulation, the closed loop system has a unit impulse response settling-time of 2 seconds and 0.2 rad maximum angular displacement. A unit sinusoid disturbance applied at $w = 0.01$ rad·s^{-1} produced small angular displacements that were subsumed by the small nonlinear effects of the model and did not propagate into the output. It is likely that error measurements due to slow disturbance effects will be lost in the quantisation of the sensor readings.

5.6 Implementation and Performance

The attitude controller is implemented on the motor controller HC12 microprocessors. Each motor controller reads the IMU data packets broadcast over the CANbus and computes the corresponding speed for its motor. This eliminates potential latency problems that would arise from centralised control.

A series of tests were devised to ensure the correct operation of the vehicle in flight. These consisted of testing IMU trim calibration with respect to the vehicle axes, testing correct turn-on of attitude stabilisation functions, drift measurement in suspended flight and a ground-effect flight prior to full free flight.

Unfortunately, time constraints prevented an extensive testing program. The experiments reported here were obtained in the last week before submission and are provided as an indication of performance, rather than as a rigorous experimental verification. Failure of a control board in the ground effect test prevented completion of the experimental program. A replacement board will take four to six weeks to fabricate.

Two flight experiments were completed: a suspended flight and a ground effect flight. The first test was to measure the flyer's IMU calibration. The flyer was initialised while suspended off the ground and the X-4's attitude control was engaged and brought up to 90 per cent flight speed. The craft regulated roll and pitch angle to within ±0.5° of horizontal (see Fig. 5.17). Simple yaw damping

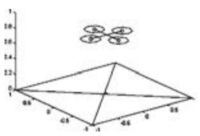

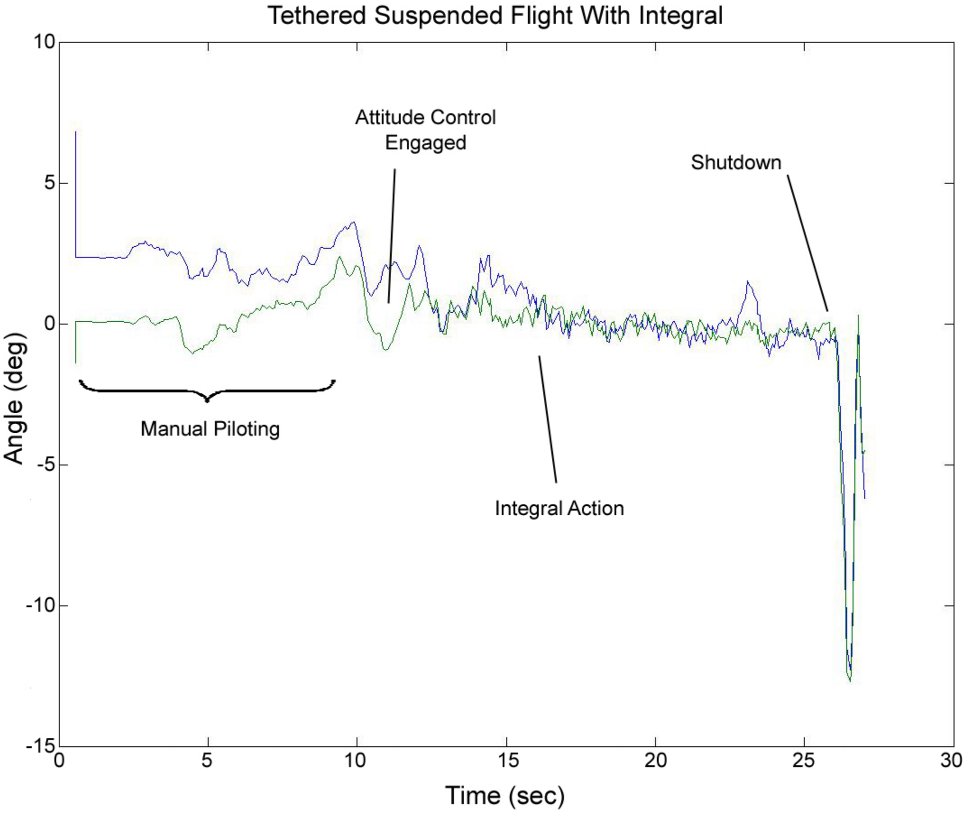

Figure 5.17: Suspended Stability Test Pitch Angle.

was implemented to reduce heading drift. The planar drift performance was found to be good, but difficult to gauge as the loose tether suspension induced a pendulum motion in the flyer that appears to be slowly unstable. The tethered dynamics are unrepresentative of the free flight dynamics of the vehicle, and only limited inference of the performance of the closed-loop system can be drawn from this experiment. Results obtained do show strong stability of the key attitude stability loop. In particular, the effective action of the integral term in regulating attitude to 0° is visible within the period 16–22 seconds.

The second flight experiment involved starting the X-4 from ground level to demonstrate ground-effect flight. The pitch/roll integral terms controller were turned off to prevent integral wind-up and saturation of the motors at takeoff. Yaw damping was disabled along with integral terms. The flyer was attached to a suspension line for safety, but lifted its entire weight without assistance.

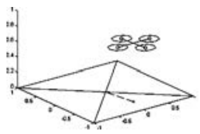

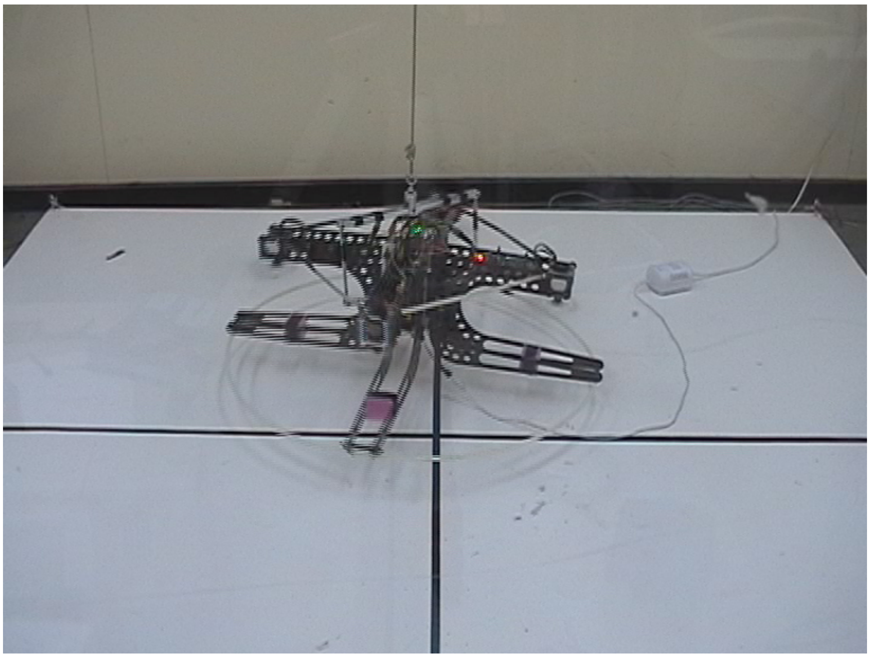

Figure 5.18: X-4 Flyer In Flight.

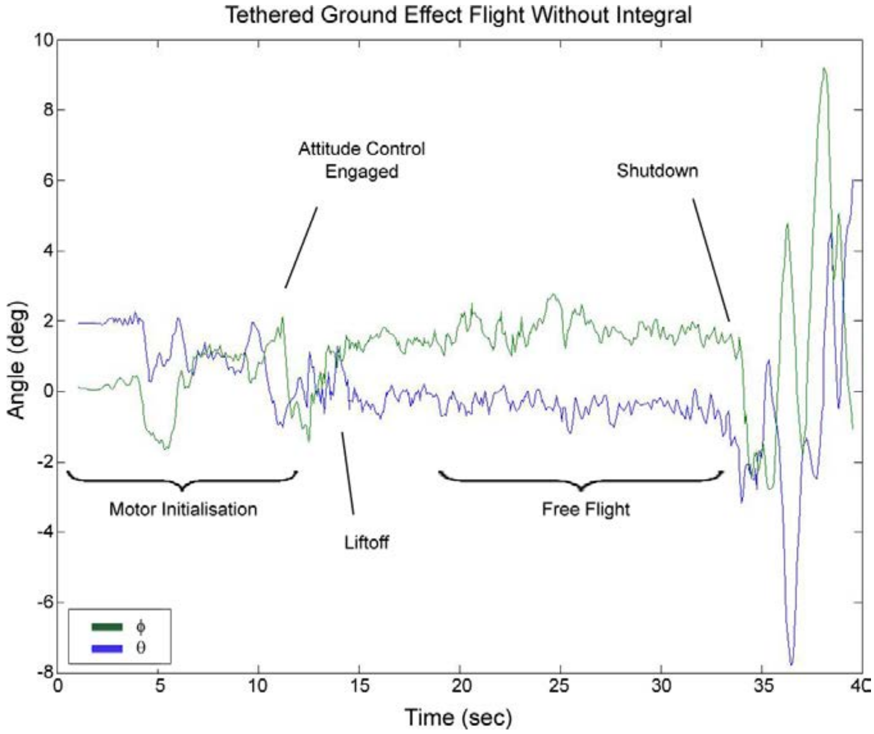

Figure 5.19: Ground Effect Flight Stability Test, Pitch and Roll Angles.

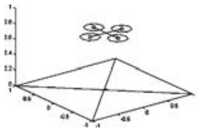

The X-4 flew at an altitude of approximately 0.4 m (see Fig. 5.18). The flyer stabilised at a pitch angle of $-0.5°$ and a roll angle of $1.6°$, associated with offsets due to the trim conditions in the rotors (see Fig. 5.19). The X-4 drifted 1.5 m across the testpad in approximately three seconds, corresponding with the expected induced lateral acceleration due to the angled vehicle thrust. Imbalance in the blades causes the craft to yaw once fully in the air. It is believed that the integral and yaw control terms would deal effectively with these small and slow deviations.

Before follow-up tests to these preliminary results could be run, an electronic speed control board failed due to a faulty MOSFET. The board failure requires a new board be manufactured, which has a lead time four to six weeks. Continuation of tests was outside the scope of this thesis.

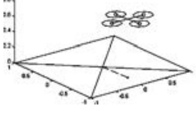

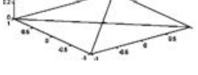
1
0.8
0.6
0.4
0.2
0
1
0.5
0
-0.5
-1
-1
-0.5
0
0.5

Chapter 6

Nonlinear Control and Estimation

6.1 Introduction

Small-scale UAVs (dimensions of the order of 60 cm) carry limited payload capacity and have compact embedded flight control systems. For these systems, the attitude sensing and stabilisation control avionics pose a particular challenge in making reliable and affordable craft. Such systems must work with limited computational resources in a small package with high robustness; however, the compact, low-cost MEMS accelerometers and gyroscopes used in these craft are typically noisy and prone to bias. An additional difficulty is that MAVs generally have poorly characterised and uncertain system models. As reported in Chapter 2, previously formulated complementary filters provide computationally cheap control schemes for non-linear rigid-body dynamics on S03 and quaternion formulations for the design of non-linear attitude filters.

This chapter provides an integrated and coupled non-linear estimation and control design for VTOL MAV stabilisation to systems with sensor bias. The control algorithm considered is an adaptation of the classical passivity-based control for mechanical systems [Wen and Kreutz-Delgado 1991] [Tayebi and McGilvray 2004] [Tayebi and McGilvray 2006]. A feed-forward control input transformation is used to compensate for the trajectory tracking inputs and model non-linearities. Stability is obtained using a Lyapunov control function design, based on the natural mechanical passivity of rigid-body dynamics. The estimation and control analysis is undertaken in the geometric framework of the rotation group and respects all the non-linearities of rigid-body (rotational)

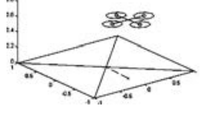

motion. Both the angular rate bias and the constant term associated with a bias cross-product are estimated. The interaction terms are bounded with respect to estimation and control errors and the full coupled system is shown to be (almost) globally stable for at least two inertial direction measurements (i.e. gravitational and magnetic fields). Simulations are provided that show the closed-loop system is well-conditioned and continues to function in the presence of significant noise and when only a single inertial direction (the gravitational field) is measured.

This chapter is organised into four parts, including this introduction. Section 6.2 presents the control of rigid body dynamics with estimated bias. Section 6.3 repeats the control design, without the use of a reconstructed rotation matrix. Section 6.4 reports the performance of the non-linear control design without rotation matrix reconstruction in simulation.

6.2 Control With Bias Estimation

Assuming that a reconstruction of the rotation matrix, R, is available, a controller with biased measurements can be derived. Section 6.3 provides a generalisation of this result to the case where only IMU measurements are available. The orientation is not specifically estimated, but rather the bias associated with the measurements is estimated, and used to control the system. The dynamics of the estimator and control are shown to be stable and the error shown to converge to zero.

Assuming that a^y and m^y are two direct inertial direction measurements: $a = e_3$, the direction of gravity, and $m \in \text{span}\{e_1, e_3\}$, the magnetic direction in the inertial frame $\mathcal{I}$. Let Ω^y be the measurement of the angular velocity Ω in the body-fixed frame $\mathcal{A}$. The velocity measurement comprises the actual velocity, the gyro measurement bias, b, and noise, μ_Ω: $\Omega^y = \Omega + b + \mu_\Omega$. In the derivation it is assumed that the noise is a high-frequency, low-power stochastic signal that can be neglected due to the operation of the control filter.

The system kinematic and dynamic equations are:

$$\dot{R} = R\Omega_\times \tag{6.1}$$

$$\mathrm{I}\dot{\Omega} = -\Omega_\times \mathrm{I}\Omega + \Gamma \tag{6.2}$$

Here the notation $\times$ represents the skew matrix operation. Define R^d to be the

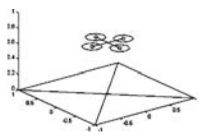

desired orientation, with the following dynamics:

$$\begin{aligned} \dot{R}^d &= R^d\Omega^d_\times && (6.3)\\ \mathrm{I}\dot{\Omega}^d &= \tau^d && (6.4) \end{aligned}$$

where Ω^d and τ^d are the desired angular velocity and torque applied to the system. The noise-free measurement of the angular velocity is the sum of the actual value and the bias: $\overline{\Omega} = \Omega + b$.

Define $\widetilde{R} = R_d^T R$ to be the orientation error:

$$\begin{aligned} \dot{\widetilde{R}} &= -\Omega^d_\times\widetilde{R} + \widetilde{R}\Omega_\times && (6.5)\\ &= -\Omega^d_\times\widetilde{R} + \widetilde{R}\Omega^d_\times - \widetilde{R}\Omega^d_\times + \widetilde{R}\Omega_\times && (6.6)\\ &= [\widetilde{R}, \Omega^d_\times] + \widetilde{R}(\Omega_\times - \Omega^d_\times) && (6.7)\\ &= [\widetilde{R}, \Omega^d_\times] + \widetilde{R}(\Omega - \Omega^d)_\times && (6.8) \end{aligned}$$

The estimate for b is denoted $\widehat{b}$, and the estimate error $\widetilde{b} = b - \widehat{b}$. Thus:

$$\begin{aligned} \dot{\widetilde{R}} &= [\widetilde{R}, \Omega^d_\times] + \widetilde{R}(\overline{\Omega} - \Omega^d - b)_\times && (6.9)\\ &= [\widetilde{R}, \Omega^d_\times] + \widetilde{R}(\overline{\Omega} - \Omega^d - \widehat{b})_\times - \widetilde{R}\widetilde{b}_\times && (6.10) \end{aligned}$$

The dynamics of $\widehat{b}$ will be specified during the control design.

Define $\varepsilon = \overline{\Omega} - \Omega^d - \widehat{b}$. Using the preceding definitions:

$$\begin{aligned} \mathrm{I}\dot{\Omega} &= (\mathrm{I}\Omega)_\times\Omega + \Gamma && (6.11)\\ \mathrm{I}\dot{\overline{\Omega}} &= (\mathrm{I}\overline{\Omega} - \mathrm{I}b)_\times\Omega + \Gamma && (6.12)\\ \mathrm{I}\dot{\widehat{b}} &= (\mathrm{I}\widehat{b})_\times\Omega - (\mathrm{I}\widehat{b})_\times\Omega + \mathrm{I}\dot{\widehat{b}} && (6.13)\\ \mathrm{I}\dot{\Omega}^d &= (\mathrm{I}\Omega^d)_\times\Omega - (\mathrm{I}\Omega^d)_\times\Omega + \tau^d && (6.14) \end{aligned}$$

Combining these derivative terms with the definition of ε provides its derivative:

$$\mathrm{I}\dot{\varepsilon} = (\mathrm{I}\varepsilon)_\times\Omega - (\mathrm{I}\widetilde{b})_\times\Omega + (\mathrm{I}\Omega^d)_\times\Omega + \Gamma - \mathrm{I}\dot{\widehat{b}} - \tau^d \qquad (6.15)$$

Rewriting this as:

$$\mathrm{I}\dot{\varepsilon} = (\mathrm{I}\varepsilon)_\times\Omega - (\mathrm{I}b)_\times\Omega + (\mathrm{I}\widehat{b})_\times\Omega + (\mathrm{I}\Omega^d)_\times\Omega + \Gamma - \mathrm{I}\dot{\widehat{b}} - \tau^d \qquad (6.16)$$

and knowing that $\Omega = \overline{\Omega} - b = \overline{\Omega} - \widehat{b} - \widetilde{b}$, it can be written:

$$\begin{aligned} \mathrm{I}\dot{\varepsilon} &= (\mathrm{I}\varepsilon)_\times\Omega - (\mathrm{I}b)_\times\overline{\Omega} + (\mathrm{I}b)_\times b + (\mathrm{I}\widehat{b})_\times\overline{\Omega}\\ &\quad -(\mathrm{I}\widehat{b})_\times\widehat{b} - (\mathrm{I}\widehat{b})_\times\widetilde{b} + (\mathrm{I}\Omega^d)_\times\overline{\Omega} - (\mathrm{I}\Omega^d)_\times\widehat{b}\\ &\quad -(\mathrm{I}\Omega^d)_\times\widetilde{b} + \Gamma - \mathrm{I}\dot{\widehat{b}} - \tau^d && (6.17) \end{aligned}$$

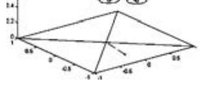

The estimator substitution of b with $\widehat{b}$ is effective for linear terms. The nonlinear term, $(\mathrm{I}b)_\times b$, must be handled separately - this is done by treating it as a constant, $a := (Ib) \times b$ that must be separately estimated in the control design. Gathering terms:

$$\begin{aligned} \mathrm{I}\dot{\varepsilon} &= (\mathrm{I}\varepsilon)_\times \Omega - (\mathrm{I}\widetilde{b})_\times \overline{\Omega} + (\mathrm{I}\widehat{b})_\times \overline{\Omega} + a - (\mathrm{I}\widehat{b})_\times \widetilde{b} \\ &\quad -(\mathrm{I}\Omega^d)_\times \widetilde{b} + (\mathrm{I}\widehat{b})_\times \overline{\Omega} - (\mathrm{I}\widehat{b})_\times \widehat{b} + (\mathrm{I}\Omega^d)_\times \overline{\Omega} \\ &\quad -(\mathrm{I}\Omega^d)_\times \widehat{b} + \Gamma - \mathrm{I}\dot{\widehat{b}} - \tau^d \end{aligned} \tag{6.18}$$

This is divided into known and unknown parts, by grouping known terms into:

$$\overline{\Gamma} := \Gamma - \tau^d - (\mathrm{I}\widehat{b})_\times \widehat{b} + (\mathrm{I}\Omega^d)_\times \overline{\Omega} - (\mathrm{I}\Omega^d)_\times \widehat{b} \tag{6.19}$$

That can be arbitrarily assigned by choice of Γ. Thus:

$$\mathrm{I}\dot{\varepsilon} = (\mathrm{I}\varepsilon)_\times \Omega + a + \overline{\Omega}_\times (\mathrm{I}\widetilde{b}) - (\mathrm{I}\widehat{b})_\times \widetilde{b} - (\mathrm{I}\Omega^d)_\times \widetilde{b} + \overline{\Gamma} - \mathrm{I}\dot{\widehat{b}} \tag{6.20}$$

The kinematics and dynamics of the error become:

$$\dot{\widetilde{R}} = [\widetilde{R}, \Omega^d_\times] + \widetilde{R}(\overline{\Omega} - \Omega^d - \widehat{b})_\times - \widetilde{R}\widetilde{b}_\times \tag{6.21}$$

$$\begin{aligned} \mathrm{I}\dot{\varepsilon} &= (\mathrm{I}\varepsilon)_\times \Omega + a + \overline{\Omega}_\times (\mathrm{I}\widetilde{b}) - (\mathrm{I}\widehat{b})_\times \widetilde{b} \\ &\quad -(\mathrm{I}\Omega^d)_\times \widetilde{b} + \overline{\Gamma} - \mathrm{I}\dot{\widehat{b}} \end{aligned} \tag{6.22}$$

Theorem 1. *Consider the system (6.1) and (6.2), along with desired trajectory (6.3) and (6.4), and the system error dynamics (6.21) and (6.22). Assume that gyro bias b is constant and that the rotation matrix R is reconstructed from measured sensor data. Let $\widehat{a}$ and $\widehat{b}$ represent estimates of $(\mathrm{I}b)_\times b$ and b, respectively.*

Choose Γ according to (6.19) such that:

$$\overline{\Gamma} = -k_\varepsilon \varepsilon - k_R \mathrm{I}^{-1} \mathrm{vex}(\mathbb{P}_a(\widetilde{R})) - \widehat{a} + \mathrm{I}\dot{\widehat{b}} \tag{6.23}$$

where k_R and k_ε are positive scalar gains, $\mathrm{vex} : so(3) \to \mathcal{R}^3$ is the inverse skew-symmetric matrix operator and $\mathbb{P}_a(\cdot)$ is the anti-symmetric matrix projection operator. Choose adaptive dynamics:

$$\dot{\widehat{a}} = k_a \mathrm{I}\varepsilon \tag{6.24}$$

$$\dot{\widehat{b}} = -k_b k_R \mathrm{vex}(\mathbb{P}_a(\widetilde{R})) + k_b((\mathrm{I}\overline{\Omega}) - \mathrm{I}\overline{\Omega}_\times)\mathrm{I}\varepsilon \tag{6.25}$$

where k_a and k_b are positive constants. Then, $(\mathrm{I}, 0)$ is an asymptotically stable limit point of $(\widetilde{R}, \varepsilon)$ and $\widehat{b} \to b$ and $\widehat{a} \to (\mathrm{I}b)_\times b$.

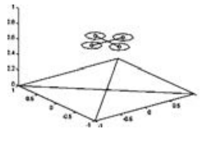

Proof. Lyapunov's method is used to prove the stability of the system. Let V be a storage function of $\widetilde{R}$ and ε:

$$\begin{aligned} V &= \frac{k_R}{2}\mathrm{tr}(\mathrm{I}_3 - \widetilde{R}) + \frac{1}{2}(\mathrm{I}\varepsilon)^T(\mathrm{I}\varepsilon) && (6.26)\\ \dot{V} &= -\frac{k_R}{2}\mathrm{tr}(\dot{\widetilde{R}}) + \frac{1}{2}(\mathrm{I}\varepsilon)^T(\mathrm{I}\dot{\varepsilon}) && (6.27)\\ &= -\frac{k_R}{2}\mathrm{tr}([\dot{\widetilde{R}}, \Omega^d_\times] + \widetilde{R}\varepsilon_\times - \widetilde{R}\widetilde{b}_\times) \\ &\quad +(\mathrm{I}\varepsilon)^T(-(\Omega + \widetilde{b})_\times \mathrm{I}\varepsilon + a \\ &\quad +(\overline{\Omega}_\times \mathrm{I} - (\mathrm{I}\overline{\Omega})_\times)\widetilde{b} + \overline{\Gamma} - \mathrm{I}\dot{\widehat{b}}) && (6.28) \end{aligned}$$

where k_R is a positive scalar gain. Note that:

$$\begin{aligned} \mathrm{tr}([\widetilde{R}, \Omega^d_\times]) &= \mathrm{tr}(\widetilde{R}\Omega^d_\times - \Omega^d_\times \widetilde{R}) && (6.29)\\ &= \mathrm{tr}(\widetilde{R}\Omega^d_\times) - \mathrm{tr}(\Omega^d_\times \widetilde{R}) && (6.30) \end{aligned}$$

Furthermore, due to skew symmetry, $(\mathrm{I}\varepsilon)^T(\Omega + \widetilde{b})_\times(\mathrm{I}\varepsilon) = 0$.

The derivative of V becomes:

$$\begin{aligned} \dot{V} &= -\frac{k_R}{2}\mathrm{tr}(\widetilde{R}\varepsilon_\times - \widetilde{R}\widetilde{b}_\times) \\ &\quad +(\mathrm{I}\varepsilon)^T(a + (\overline{\Omega}_\times \mathrm{I} - (\mathrm{I}\overline{\Omega})_\times)\widetilde{b} + \overline{\Gamma} - \mathrm{I}\dot{\widehat{b}}) && (6.31) \end{aligned}$$

Recalling (6.23):

$$\overline{\Gamma} = -k_\varepsilon \varepsilon - k_R \mathrm{I}^{-1}\mathrm{vex}(\mathbb{P}_a(\widetilde{R})) - \widehat{a} + \mathrm{I}\dot{\widehat{b}} \tag{6.32}$$

where k_R and k_ε are positive scalar gains. It follows that:

$$\begin{aligned} \dot{V} &= -\frac{k_R}{2}\mathrm{tr}(\widetilde{R}\varepsilon_\times - \widetilde{R}\widetilde{b}_\times) \\ &\quad +(\mathrm{I}\varepsilon)^T(\widetilde{a} + (\overline{\Omega}_\times \mathrm{I} - (\mathrm{I}\overline{\Omega})_\times)\widetilde{b} \\ &\quad -k_\varepsilon \varepsilon - k_R \mathrm{I}^{-1}\mathrm{vex}(\mathbb{P}_a(\widetilde{R}))) && (6.33) \end{aligned}$$

where $\widetilde{a} = a - \widehat{a}$. Note that for any matrix A and any vector m:

$$\mathrm{tr}(Am_\times) = \mathrm{tr}(\mathbb{P}_a(A)m_\times) = -2m^T\mathrm{vex}(\mathbb{P}_a(A)) \tag{6.34}$$

Thus

$$\begin{aligned}
\dot{V} &= -\frac{k_R}{2}\mathrm{tr}(\mathbb{P}_a(\widetilde{R})\varepsilon_\times - \mathbb{P}_a(\widetilde{R})\widetilde{b}_\times) \\
&\quad -k_\varepsilon\varepsilon^T\mathrm{I}\varepsilon - k_R\varepsilon^T\mathrm{vex}(\mathbb{P}_a(\widetilde{R})) \\
&\quad -\varepsilon^T\mathrm{I}(\widetilde{a} + (\overline{\Omega}_\times\mathrm{I} - (\mathrm{I}\overline{\Omega})_\times)\widetilde{b}) \qquad (6.35) \\
&= k_R\varepsilon^T\mathrm{vex}(\mathbb{P}_a(\widetilde{R})) - k_R\widetilde{b}^T\mathrm{vex}(\mathbb{P}_a(\widetilde{R})) \\
&\quad -k_\varepsilon\varepsilon^T\mathrm{I}\varepsilon - k_R\varepsilon^T\mathrm{vex}(\mathbb{P}_a(\widetilde{R})) \\
&\quad -\varepsilon^T\mathrm{I}(\widetilde{a} + (\overline{\Omega}_\times\mathrm{I} - (\mathrm{I}\overline{\Omega})_\times)\widetilde{b}) \qquad (6.36) \\
&= k_\varepsilon\varepsilon^T\mathrm{I}\varepsilon k_R\widetilde{b}^T\mathrm{vex}(\mathbb{P}_a(\widetilde{R})) \\
&\quad -\varepsilon^T\mathrm{I}(\widetilde{a} + (\overline{\Omega}_\times\mathrm{I} - (\mathrm{I}\overline{\Omega})_\times)\widetilde{b}) \qquad (6.37)
\end{aligned}$$

Define the Lyapunov function L:

$$L = V + \frac{1}{2}\widetilde{b}k_b^{-1}\widetilde{b} + \frac{1}{2}\widetilde{a}^T k_a^{-1}\widetilde{a} \qquad (6.38)$$

where k_b and k_a are positive definite matrices. The derivative:

$$\begin{aligned}
\dot{L} &= \dot{V} + \widetilde{b}^T k_b^{-1}(-\dot{\widehat{b}}) + \widetilde{a}^T k_a^{-1}(-\dot{\widehat{a}}) \qquad (6.39) \\
&= -k_\varepsilon\varepsilon^T\mathrm{I}\varepsilon + \widetilde{b}^T(k_R\mathrm{vex}(\mathbb{P}_a(\widetilde{R})) + ((\mathrm{I}\overline{\Omega})_\times - \mathrm{I}\overline{\Omega}_\times)\mathrm{I}\varepsilon \\
&\quad -k_b^{-1}\dot{\widehat{b}}) + \widetilde{a}^T(\mathrm{I}\varepsilon - k_a^{-1}\dot{\widehat{a}}) \qquad (6.40)
\end{aligned}$$

Recall (6.24) and (6.25):

$$\begin{aligned}
\dot{\widehat{a}} &= k_a\mathrm{I}\varepsilon \qquad (6.41) \\
\dot{\widehat{b}} &= -k_b k_R\mathrm{vex}(\mathbb{P}_a(\widetilde{R})) + k_b((\mathrm{I}\overline{\Omega}) - \mathrm{I}\overline{\Omega}_\times)\mathrm{I}\varepsilon \qquad (6.42)
\end{aligned}$$

Hence, it can be seen that $\dot{L} = -k_\varepsilon\varepsilon^T\mathrm{I}\varepsilon \Rightarrow \dot{L} = 0$ when $\varepsilon = 0$. It is assumed here that $\overline{\Omega}$ is a bounded and continuous. Slotine and Li's formulation of Barbalat's lemma is used to ensure the non-autonomous system is stable [Slotine and Li 1991]. For $\dot{L} = 0$, one has:

$$\begin{aligned}
\dot{\widehat{a}} &\equiv 0 \qquad (6.43) \\
\dot{\widehat{b}} &\equiv -k_b k_R\mathrm{vex}(\mathbb{P}_a(\widetilde{R})) \qquad (6.44) \\
\dot{\widetilde{R}} &\equiv [\widetilde{R}, \Omega^d_\times] - \widetilde{R}\widetilde{b}_\times \qquad (6.45) \\
\overline{\Gamma} &\equiv -k_R\mathrm{I}^{-1}\mathrm{vex}(\mathbb{P}_a(\widetilde{R})) - \widehat{a} + \mathrm{I}\dot{\widehat{b}} \qquad (6.46)
\end{aligned}$$

Consequently:

$$\begin{aligned}
\mathrm{I}\dot{\varepsilon} &\equiv \widetilde{a} + (\overline{\Omega}_\times\mathrm{I} - (\mathrm{I}\overline{\Omega})_\times)\widetilde{b} - k_R\mathrm{I}^{-1}\mathrm{vex}(\mathbb{P}_a(\widetilde{R})) \qquad (6.47) \\
L &= \frac{k_R}{2}\mathrm{tr}(\mathrm{I} - \widetilde{R}) + \frac{1}{2}\widetilde{b}^T k_b^{-1}\widetilde{b} + \frac{1}{2}\widetilde{a}^T k_a^{-1}\widetilde{a} \qquad (6.48) \\
&\equiv \text{constant} \qquad (6.49)
\end{aligned}$$

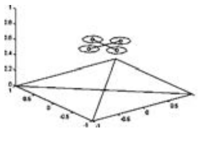

From the equation of $\dot{\varepsilon}$ and knowing that $\dot{\varepsilon}$ converges to zero, one can ensure that:

$$(\overline{\Omega}_\times \mathrm{I} - (\mathrm{I}\overline{\Omega}_\times))\widetilde{b} \equiv k_R \mathrm{I}^{-1}\mathrm{vex}(\mathbb{P}_a(\widetilde{R})) + \text{constant} \tag{6.50}$$

Knowing that:

$$\dot{\widehat{b}} = k_b k_R \mathrm{vex}(\mathbb{P}_a(\widetilde{R})) \Rightarrow \dot{\widetilde{b}} = -k_b k_R \mathrm{vex}(\mathbb{P}_a(\widetilde{R})) \tag{6.51}$$

$$\Rightarrow \mathrm{I}^{-1} k_b^{-1} \dot{\widetilde{b}} = -k_R \mathrm{I}^{-1}\mathrm{vex}(\mathbb{P}_a(\widetilde{R})) \tag{6.52}$$

Introducing this expression into (6.47), it yields:

$$\widetilde{a} + (\overline{\Omega}_\times \mathrm{I} - (\mathrm{I}\overline{\Omega})_\times)\widetilde{b} + \mathrm{I}^{-1} k_b^{-1} \dot{\widetilde{b}} = 0 \tag{6.53}$$

which is a first order system. If $\overline{\Omega}$ is independent of $\widetilde{b}$, the solutions of the system are:

$$\begin{cases} \widehat{b} \rightarrow & \text{constant} \\ \widehat{b} \rightarrow & \infty \end{cases} \tag{6.54}$$

If $\widehat{b} \rightarrow$ constant, then $\dot{\widehat{b}} \equiv 0 \Rightarrow \mathrm{vex}(\mathbb{P}_a(\widetilde{R})) \equiv 0$, and $\mathrm{vex}\left(\mathbb{P}_a\left(\widetilde{R}\right)\right) = 0$ implies that $\widehat{R}$ is symmetric; that is $\widehat{R} = \mathrm{I}$ or $\mathrm{tr}\left(\widehat{R}\right) = -1$. There exists a neighborhood of $(\mathrm{I}, 0)$ such that $\mathrm{vex}\,\mathbb{P}_a\left(\widehat{R}\right)\Big) = 0 \rightarrow \widehat{R} = \mathrm{I}$ Otherwise, if $\widehat{b} \rightarrow \infty$, then L diverges, which is impossible. Therefore, $\widetilde{b} \rightarrow 0$ and $\widetilde{a} \rightarrow 0$ and the result is proved. □

6.3 Control Without Reconstructed Rotation Matrix

The sensors available to the controller do not provide the rotation matrix directly, but rather R is calculated from the inputs of directional sensors. The computation of this matrix is not essential to the functioning of the controller. By rephrasing the design in terms of these raw sensor inputs, it is possible to eliminate this step, and so save on microprocessor cycles in the implemented system.

Given inertial directions v_{0i}, the measurements available from the sensors are:

$$v_i = R^T v_{0i} + \mu_i;\ i = 1 \ldots n \tag{6.55}$$

The desired measurements are defined to be $v_{di} = R^d v_{0i}$. Similar to the derivation in [Hamel and Mahony 2002], the natural attitude error for a single direction is:

$$\begin{aligned} 1 - \cos(\angle v^d, v) &= 1 - \langle v^d, v \rangle && (6.56) \\ &= 1 - v_{0i}^T R_d R^T v_{0i} && (6.57) \end{aligned}$$

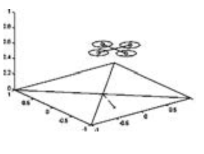

For multiple measurements, the cost function may be written as: where the gains $k_{i>0}$ are the relative weightings in each measurement, which may be adjusted according to the confidence of the measurement. The global cost is written:

$$E = \sum_{i=1}^{n} k_i - \mathrm{tr}(\widetilde{R}M) \tag{6.58}$$

where $M = R^T M_0 R$ and M_0 is a constant matrix:

$$M_0 = \sum_{i=1}^{n} k_i v_{0i} v_{0i}^T \tag{6.59}$$

In the storage function, (6.27), substitute:

$$\mathrm{tr}(\mathrm{I}_3 - \widetilde{R}) \rightarrow \sum k_i - \mathrm{tr}(\widetilde{R}M) \tag{6.60}$$

Thus, the proposed storage function is:

$$\begin{aligned} V &= \frac{k_R}{2}\sum k_i - \frac{k_R}{2}\mathrm{tr}(\widetilde{R}M) + \frac{1}{2}(\mathrm{I}\varepsilon)^T(\mathrm{I}\varepsilon) && (6.61)\\ \dot{V} &= -\frac{k_R}{2}\mathrm{tr}(\frac{d}{dt}(\widetilde{R}M)) + (\mathrm{I}\varepsilon)^T(\mathrm{I}\dot{\varepsilon}) && (6.62) \end{aligned}$$

Rewrite $\frac{d}{dt}(\widetilde{R}M)$ as follows:

$$\begin{aligned} (\dot{\widetilde{R}M}) &= \dot{\widetilde{R}}M - \widetilde{R}\dot{M} && (6.63)\\ &= -\Omega^d_\times\widetilde{R}M + \widetilde{R}\Omega_\times - \widetilde{R}\Omega_\times M + \widetilde{R}M\Omega_\times && (6.64)\\ &= -\Omega^d_\times\widetilde{R}M + \widetilde{R}M\Omega^d_\times \\ &\quad -\widetilde{R}M\Omega^d_\times + \widetilde{R}M\Omega_\times && (6.65)\\ &= [\widetilde{R}M, \Omega^d_\times] + \widetilde{R}M(\Omega - \Omega^d) && (6.66) \end{aligned}$$

This gives the similar form:

$$\begin{aligned} \dot{V} &= -\frac{k_R}{2}\mathrm{tr}(\widetilde{R}M\varepsilon_\times - \widetilde{R}M\widetilde{b}_\times) \\ &\quad +(\mathrm{I}\varepsilon)^T(a + (\overline{\Omega}_\times\mathrm{I} - (\mathrm{I}\overline{\Omega})_\times)\widetilde{b} + \overline{\Gamma} - \mathrm{I}\dot{\widetilde{b}}) && (6.67) \end{aligned}$$

Corollary 1. *Consider the system (6.1) and (6.2), along with desired trajectory (6.3) and (6.4), and the system error dynamics (6.21) and (6.22). Assume that there are at least two measurements of inertial direction of the form (6.55) available. Assume that gyro bias b is constant and, let $\widehat{a}$ and $\widehat{b}$ represent estimates of $(\mathrm{I}b)_\times b$ and b. Choose Γ according to (6.19) such that:*

$$\overline{\Gamma} = -k_\varepsilon\varepsilon + k_R\mathrm{I}^{-1}\frac{1}{2}\sum_{i=1}^{n} k_i v_i^d \times v_i - \widehat{a} + \mathrm{I}\dot{\widehat{b}} \tag{6.68}$$

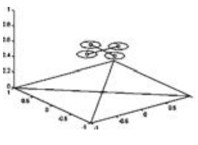

where k_R *and* k_ε *are positive scalar gains, and choose adaptive dynamics:*

$$\begin{aligned} \dot{\widehat{a}} &= k_a \mathrm{I}\varepsilon & (6.69) \\ \dot{\widehat{b}} &= k_b k_R \frac{1}{2} \sum_{i=1}^{n} k_i v_i^d \times v_i + k_b((\mathrm{I}\overline{\Omega}) - \mathrm{I}\overline{\Omega}_\times)\mathrm{I}\varepsilon & (6.70) \end{aligned}$$

where k_a *and* k_b *are positive definate matrices. Then,* $(\mathrm{I}, 0)$ *is an asymptotically stable limit point of* $(\widetilde{R}, \varepsilon)$ *and* $\widehat{b} \to b$ *and* $\widehat{a} \to (\mathrm{I}b)_\times b$.

Proof. It was shown in [Hamel and Mahony 2002] that:

$$-\frac{1}{2} \sum_{i=1}^{n} k_i v_i^d \times v_i = \mathrm{vex}(\mathbb{P}_a(\widetilde{R}M)) \quad (6.71)$$

where $v_i^d = R_d^T v_{0i}$. Substitution into (6.68) and (6.70) yield a form analogous to (6.23) and (6.25) where $\mathcal{P}_a(\widetilde{R})$ is replaced with $\mathcal{P}_a(\widetilde{R}M)$. From here the proof is analogous to the proof of Theorem 1 up to the final paragraph. Following (6.54) one concludes $\widehat{b} \to$ constant implies $\mathrm{vex}(\mathcal{P}_a(\widetilde{R}M)) \equiv 0$. In Mahony *et al* [Mahony *et al* 2008] it was shown that this also implies that either $\widetilde{R} = \mathrm{I}$ or $\mathrm{tr}(\widetilde{R}) = -1$. The conclusions follow as before.

□

6.4 Simulation

The non-reconstructed R matrix controller was tested in Matlab Simulink. The rotational inertia used is:

$$\mathrm{I} = \begin{pmatrix} 0.0797 & 0 & 0 \\ 0 & 0.0797 & 0 \\ 0 & 0 & 0.1490 \end{pmatrix} \quad (6.72)$$

The simulated system starts with a 10° initial yaw angle and 0.1 rad·s^{-1} pitch velocity. The bias vector is $(0.2\ \ 0.1 {-} 0.1)^T$. The measurement noise μ_Ω is a unit normal distribution. A test without noise was also performed, but the results were very similar to the test with noise and are not reported.

Combining (6.19) and (6.23), the controller for the non-reconstructed matrix simulation is:

$$\begin{aligned} \Gamma &= -k_\varepsilon \varepsilon - k_R \mathrm{I}^{-1} \mathrm{vex}(\mathbb{P}_a(\widetilde{R}M)) - \widehat{a} + \mathrm{I}\dot{\widehat{b}} \\ &\quad + \tau^d + (\mathrm{I}\widehat{b})_\times \widehat{b} - (\mathrm{I}\Omega^d)_\times \overline{\Omega} + (\mathrm{I}\Omega^d)_\times \widehat{b} & (6.73) \end{aligned}$$

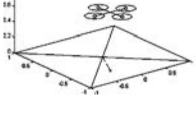

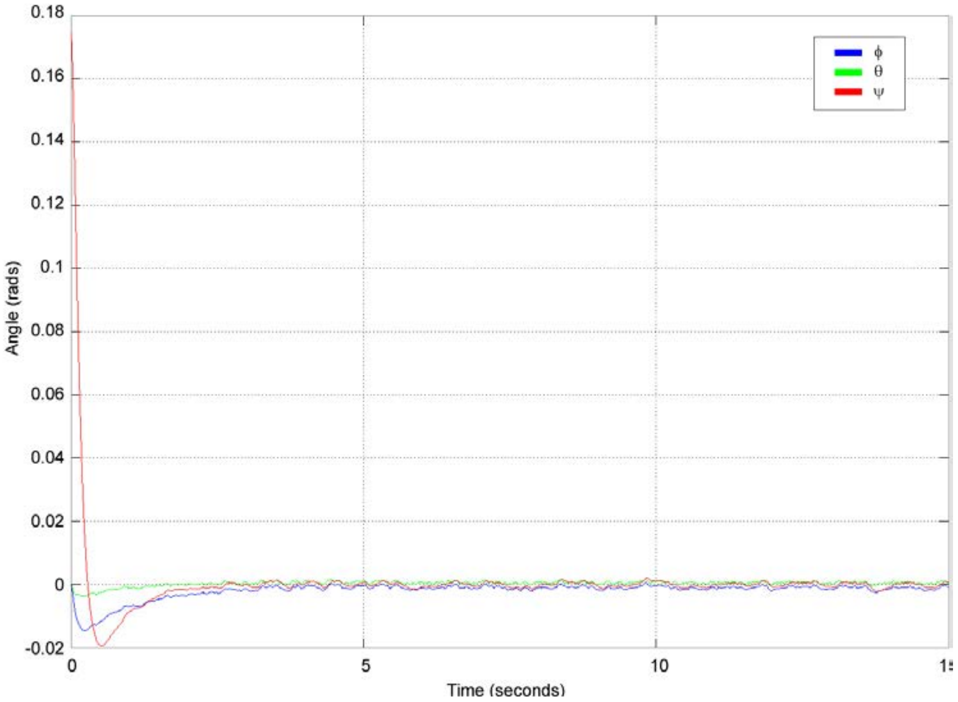

Figure 6.1: Aircraft Euler Angles ($R_d^T R$) Using Controller Without Rotation Matrix Reconstruction

Likewise, the bias estimators are:

$$\dot{\hat{a}} = k_a \mathrm{I}\varepsilon \tag{6.74}$$

$$\dot{\hat{b}} = -k_b k_R \mathrm{vex}(\mathbb{P}_a(\widetilde{R}M)) + k_b((\mathrm{I}\overline{\Omega}) - \mathrm{I}\overline{\Omega}_\times)\mathrm{I}\varepsilon \tag{6.75}$$

Plots for aircraft Euler angles, angular velocity, bias estimates and bias cross-product estimates are given below (see Fig. 6.1, 6.2, 6.3, 6.4 and 6.5).

It can be seen that the attitude angles converge quickly to around zero, with time-separated dynamics of the estimators that reduce the remaining error. The system is robust to measurement noise in the angular rate gyros.

For stability in practice, the transient response is most important - this provides robustness to disturbances such as wind gusts. The gains have been tuned to obtain a rise-time of 0.25 seconds. There is also a slow 15 second mode associated with the bias estimation dynamics, a 60 times time-scale separation. Bias tracking need not be any faster than this to cope with slow thermal transients in the sensors. The 0.002 radian angle offset present while the bias estimates converge will cause the craft to drift, but within this rise-time, the motion will be less than 30 mm.

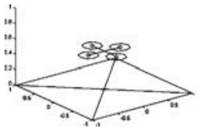

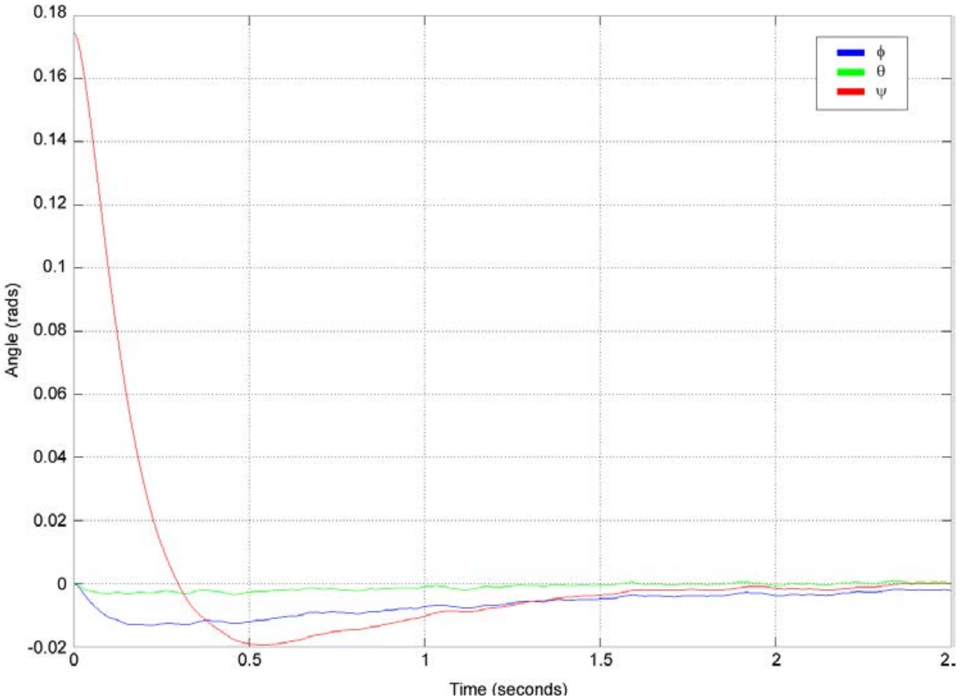

Figure 6.2: Aircraft Euler Angles ($R_d^T R$) Using Controller Without Rotation Matrix Reconstruction, First 2.5 Seconds

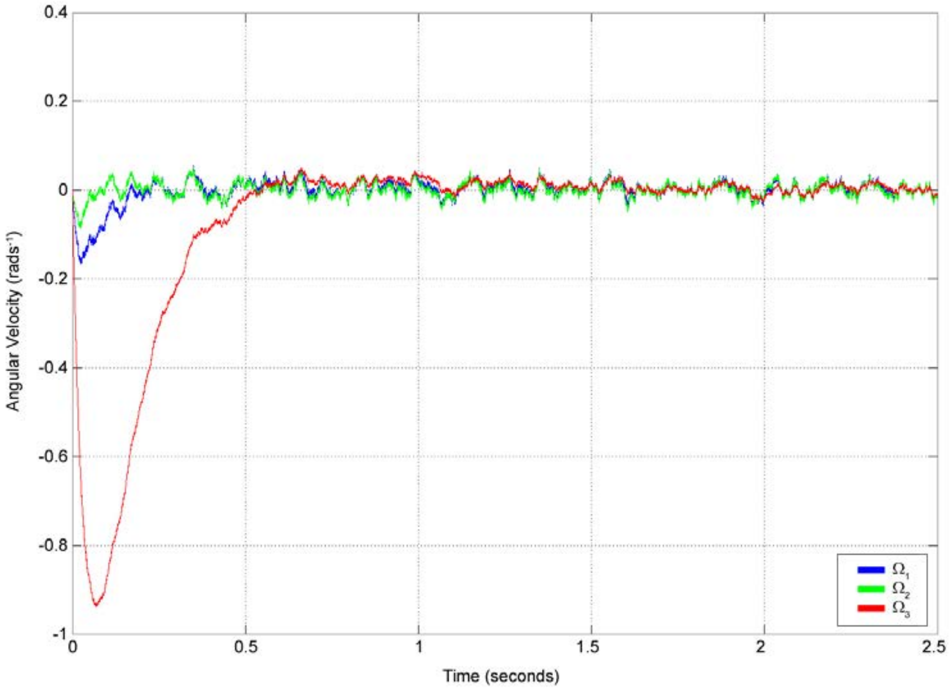

Figure 6.3: Aircraft Angular Velocity (Ω) Using Controller Without Rotation Matrix Reconstruction, First 2.5 Seconds

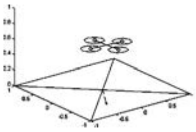

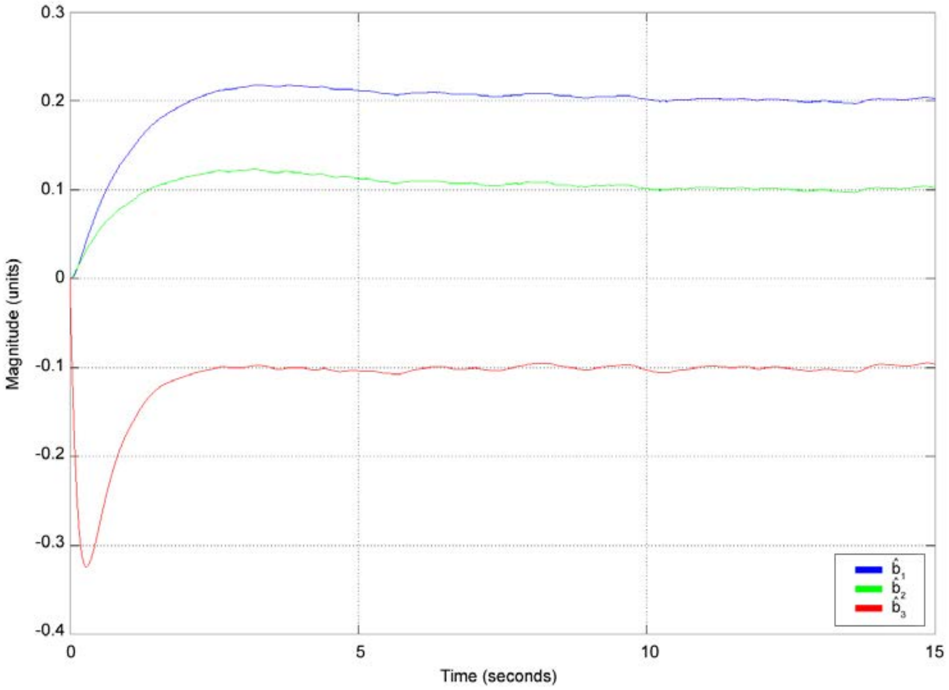

Figure 6.4: Aircraft Bias Estimates $(\widehat{b})$ Using Controller Without Rotation Matrix Reconstruction

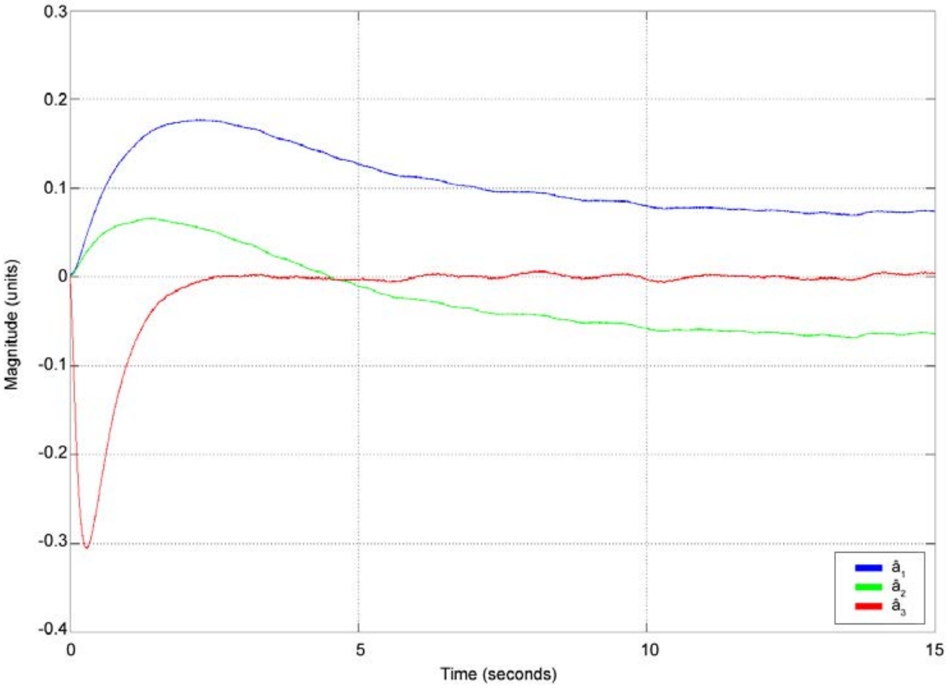

Figure 6.5: Aircraft Bias Cross-Product Constant Estimates $(\widehat{a})$ Using Controller Without Rotation Matrix Reconstruction

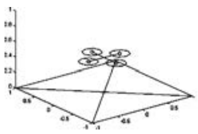

Chapter 7

Conclusion

In this thesis I reported the design, construction and control of the X-4 Flyer, a quadrotor UAV. The craft is designed to be compact, mechanically simple, with the intent of creating a robot that can be operated in the field without continuous skilled maintenance. Consequently, it is significantly heavier than most of the quadrotors reported in the literature. It is capable of carrying up to 1 kg of payload on top of its battery weight. I have shown that the key design challenges to be overcome when building a large quadrotor such as the X-4 are efficient aeroelastic rotor design, motor speed dynamics and attitude control.

7.1 Achievements

In Chapter 1 I list eight goals of the thesis. I have met each of these goals, although, in the case of goal seven, it was not possible to test the non-linear controller on the X-4 in flight.

1. Produce mechanically simple rotors to generate the required lift.
   The rotor design was developed using a mix of blade element theory, momentum theory and element-wise torsion analysis. A crucial part of the design was the development of a finite element analysis tool to find a robust balancing of lift moment and elastic torsion. The blades were manufactured from three-ply carbon fibre, using moulds milled in-house at the ANU. At maximum speed the rotors can provide 1.5 kg of thrust — a 50 per cent thrust margin above that required for hover.

2. Produce motor controllers for fast dynamic speed response.
   The rotors, motors and custom-built electronic speed controllers form a ro-

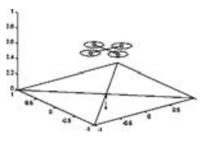

bust, high-performance drive unit. A local 1 kHz proportional feed-forward control loop improves the dynamic response of the motors, allowing for fast speed changes. I characterised the dynamic response and spectral disturbance behaviour of the assembled drive system. Interestingly, steady flow regimes induced more disturbance power than continually changing flow regimes.

The rise-time was reduced from 0.2 seconds to 0.05 seconds. Thruster performance is limited by an imposed rate-saturation; a proportional controller was tuned to exploit the gain to the maximum extent possible, and more complex control schemes would not provide a significant improvement in performance due to the rate constraint.

3. Devise a dynamic model incorporating rotor for specialised quadrotor vehicles.
   I have expanded the conventional dynamic model of quadrotors to include the effect of rotor flapping in generalised flight. Blade flapping occurs in all but the stiffest rotors and has a significant impact on vehicle dynamics. My dynamic model includes the effect of rotors translating vertically due to pitch and roll, and of flapping due to yawing motion of the craft.

4. Find the flyer configuration with the most favourable attitude dynamics.
   It is possible to exploit the flapping dynamics of a quadrotor to make the craft purely unstable or dynamically neutral, rather than unstable-oscillatory, the common configuration of commercial quadrotor toys . Using the Bode integral, I show that the sensitivity of the design can be optimised by setting the centre of gravity in the plane of the rotors, making the system dynamically neutral. At this point, the system is easiest to control, potentially simplifying the control design.

5. Build the complete flyer hardware system.
   The X-4 was fabricated in-house at the ANU, with avionics subsystems provided by CSIRO. The flyer is housed and operated in the ANU Mechatronics Laboratory.

6. Design and implement onboard attitude control. The attitude control system used on the X-4 was a distributed PID loop, implemented in each motor control board. The controller successfully regulates the attitude of the flyer to ±0.5° on the gimbal test rig and in flight tests.

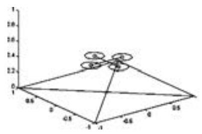

7. Improve attitude control with non-linear control-estimation methods.
   To reduce the complexity of the electronics needed for a robust quadrotor, a combined control-estimator for MAVs was proposed that performs angular velocity gyro sensor bias estimation and correction, without the need to explicitly reconstruct the rotation matrix. Its stability was proven using a Lyapunov function analysis and I demonstrated its functionality in simulation. The system exhibits good noise rejection, which makes it ideal for implementation on low-cost MAV craft, although time constraints precluded testing it on the X-4.

8. Demonstrate the X-4 Flyer's flight worthiness. The flyer has successfully flown in the ANU Mechatronics test cage. It demonstrated $\pm 0.5^\circ$ attitude stability and hovered a short distance. The failure of a motor control board while on the ground halted testing before longer flights could be carried out. The X-4 has produced commercially-viable stabilisation precision, payload capacity and flight-time performance.

   Currently, the X-4 Flyer is awaiting a replacement motor control board. Flight tests are ongoing.

7.2 Future Direction

The results of this research suggest some natural extensions to my work:

- Chassis and Hardware
  The X-4's chassis can be optimised to reduce weight and vibration. Replacing the foam and aluminium construction for a one-piece carbon-fibre structure could save almost 1 kg of weight and drastically simplify the chassis. Engineering the craft for vibration reduction and integrating isolation mounts directly into the chassis will save further weight and improve control. New motor and battery technology is now available that can save 0.5 kg and extend flight time.

- Rotors
  The rotors have performed beyond expectations, but there are a few possible improvements. Obviously, the faulty blade mould can be replaced. It is also possible to integrate the individual blades into a single mould for one rotor. Eliminating the aluminium hub clamp structure will further reduce weight and improve the speed response of the blades, reducing vibration.

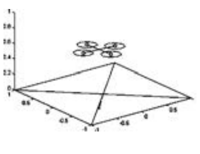

The danger posed by the high-speed rotors is a clear area of concern. The physics of generating great thrust in such a small area makes fast rotors inescapable. The trend in quadrotors is to construct shrouds around the blades to shield them from collision. It is expected that the improvement in safety and increased thrust from the duct will offset the added weight.

- Control and Avionics

  The obvious next step in control design is to test the non-linear controller on the flyer. Solid data should provide an indication of the suitability of this control scheme to the current design.

  It may be possible to further reduce the complexity of the electronics by integrating inertial sensors with the motor control boards. This will eliminate the need for any inter-board communication, outside of user commands and telemetry. Consequently, the attitude control speed could occur at the rate of the motor control, allowing for greatly improved attitude regulation.

In summary, the X-4 Flyer is a large, robust quadrotor capable of lifting 1 kg of payload with excellent control performance. I believe this thesis and the prototype X-4 Flyer provides a step towards constructing quadrotors that can carry useful payloads and perform challenging real-world tasks, without expert support — a commercially useful quadrotor for everybody.

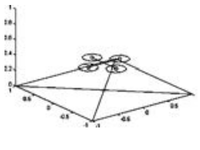

Appendix A

Flapping Angle Equation Derivation

A.1 Flapping in Horizontal Flight

There are many books that provide a derivation of flapping equations for a helicopter [Leishman 2006] [Done and Balmford 2001] [Prouty 2002]. The following derivation is based primarily on that presented in Prouty [Prouty 2002, pp 463–469].

Equations for flapping angles induced by a helicopter in forward flight can be found by solving for the aerodynamic-weight-centripedal moment equilibrium:

$$M_{\text{C.F.}} + M_A + M_W = 0 \tag{A.1}$$

Each of these moment elements is derived, and the constant and sinusoidal component equations are solved in turn. There are several assumptions made in this solution:

- Aerodynamic forces act over the blade, from the hinge outwards
- There is no reverse flow on the retreating blade
- Airfoils have a linear lift slope
- The rotor has no second order or higher harmonic effects
- The rotor flapping angles are small
- The hinge angle-rotor length ratio is small
- Centrifugal effects lie in the plane of the rotor

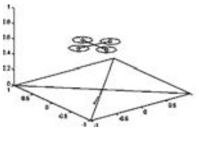

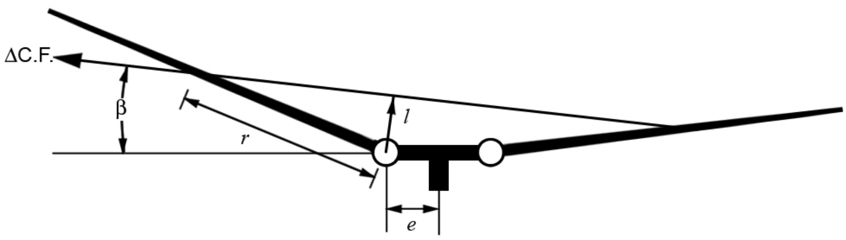

Figure A.1: Geometry of Flapping Centripedal Forces.

A.1.1 Centrifugal Moment

The effect of centripedal force on the blades is to induce a moment about the hinge. This moment is the product of the outward centripedal force and the moment arm described by the hinge angle β and the coning angle a_0:

$$\begin{aligned} \Delta M_{C.F.} &= -\Delta \text{C.F.} l & \text{(A.2)} \\ \Delta \text{C.F.} &= m \Delta r (r+e) \omega^2 & \text{(A.3)} \end{aligned}$$

where r is the element distance from the hinge to the centre of mass of the blade, e is the hinge offset, l is the centripedal moment arm. The length of the moment arm can be found from the geometry of the rotorhead (see Fig. A.1):

$$l = r a_0 + \frac{e}{r+e}(r\beta - r a_0) \tag{A.4}$$

The angle observed at the hinge, β is composed of the coning angle, and azimuthal components of longitudinal and lateral flapping:

$$\beta = a_0 - a_{1_s} \cos\psi - b_{1_s} \sin\psi \tag{A.5}$$

where a_{1_s} and b_{1_s} are the Fourier coefficients of the longitudinal and lateral rotor flapping angles.

Substituting (A.5) into (A.3) and integrating from the hinge outwards gives:

$$M_{\text{C.F.}} = -\omega^2 \left[a_0 \left(\text{I}_b + e\frac{M_b}{g} \right) - (a_{1_s} \cos\psi + b_{1_s} \sin\psi) e \frac{M_b}{g} \right] \tag{A.6}$$

where I_b is the rotational inertia of the blade, M_b is the static blade moment, and g is acceleration due to gravity.

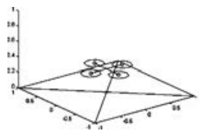

A.1.2 Aerodynamic Moment

The moment due to aerodynamic forces is:

$$\Delta M_A = r\frac{\rho}{2}U_T^2 a\alpha c\Delta r \tag{A.7}$$

where U_T is the velocity at the rotor tip, α is the blade angle of attack. These are respectively given by:

$$U_T = \omega R\left[\frac{r+e}{R} + \mu\sin\psi\right] \tag{A.8}$$

where μ is the advance ratio, and

$$\alpha = \theta + \frac{U_T}{U_P} \tag{A.9}$$

where θ is the geometric angle and U_T/U_P is the induced angle of the blade inflow, U_T.

The inflow through the rotor is given by the sum of the flow velocity components normal to the rotor plane: the component of horizontal velocity passing through the rotor tilted by the shaft angle, the induced velocity of the rotor and components due to flapping:

$$\begin{aligned} U_P = \omega R\Bigg[&\mu\alpha_s - \frac{v_i}{\omega R}\left(1+\frac{r}{R}\cos\psi\right) - \frac{r}{R}(a_{1_s}\sin\psi - b_{1_s}\cos\psi) \\ &-\mu(a_0 - a_{1_s}\cos\psi - b_{1_s}\sin\psi)\cos\psi\Bigg] \end{aligned} \tag{A.10}$$

where α_s is the structural rotor shaft tilt angle and v_i is the induced velocity of the rotor airflow at the rotor disc.

The geometric angle of the blades is a function of the blade twist and applied pilot longitudinal and lateral feathering control angles:

$$\theta = \theta_0 + \frac{r}{R}\theta_1 - A_1\cos\psi - B_1\sin\psi \tag{A.11}$$

where A_1 and B_1 are the longitudinal and lateral feathering angles.

Integrating the aerodynamic moment element outward from the hinge to the tip for the total moment, M_A, produces a complex equation that can be written as a sum of constant and sinusoidal components. Higher order and higher frequency components of M_A are discarded in this derivation:

$$M_A = M_{A_{\text{const}}} + M_{A_{\text{sine}}}\sin\psi + M_{A_{\text{cosine}}} \tag{A.12}$$

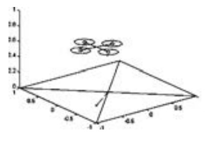

These components are:

$$
\begin{aligned}
M_{A_{\text{const}}} &= \frac{\rho}{2} ac(\omega R)^2 \left(1-\frac{e}{R}\right)^2 R^2 \Bigg\{ \frac{\theta_0}{4}\left[1+\mu^2+\frac{2}{3}\frac{e}{R}+\frac{1}{3}\left(\frac{e}{R}\right)^2\right] \\
&+\theta_1\left[\frac{1}{5}+\frac{\mu^2}{6}\left(1-\frac{e}{R}\right)-\frac{1}{10}\left(\frac{e}{R}\right)-\frac{1}{15}\left(\frac{e}{R}\right)^2-\frac{1}{30}\left(\frac{e}{R}\right)^3\right] \\
&+\left(\mu\alpha_s-\frac{v_i}{\omega R}\right)\left(\frac{1}{3}+\frac{1}{6}\frac{e}{R}\right)-B_1\mu\left(\frac{1}{3}+\frac{1}{6}\frac{e}{R}\right)+\mu\frac{e}{R}\frac{a_{1_s}}{4}\Bigg\} \qquad \text{(A.13)} \\
M_{A_{\text{sine}}} &= \frac{\rho}{2} ac(\omega R)^2 \left(1-\frac{e}{R}\right)^2 R^2 \Bigg\{ 2\theta_0\mu\left[\frac{1}{3}+\frac{1}{6}\frac{e}{R}\right] \\
&+2\theta_1\mu\left[\frac{1}{4}-\frac{1}{6}\frac{e}{R}-\frac{1}{12}\left(\frac{e}{R}\right)^2\right]-B_1\left[\frac{1}{4}+\frac{3}{8}\mu^2+\frac{1}{6}\frac{e}{R}+\frac{1}{12}\left\{\frac{e}{R}\right\}^2\right] \\
&+\frac{\mu}{2}\left(\mu\alpha_s-\frac{v_i}{\omega R}\right)-a_{1_s}\left[\frac{1}{4}-\frac{\mu^2}{8}-\frac{1}{6}\frac{e}{R}-\frac{1}{12}\left(\frac{e}{R}\right)^2\right]\Bigg\} \qquad \text{(A.14)} \\
M_{A_{\text{cosine}}} &= \frac{\rho}{2} ac(\omega R)^2 R^2 \Bigg\{ -A_1\left[\frac{1}{4}+\frac{\mu^2}{8}+\frac{1}{6}\frac{e}{R}+\frac{1}{12}\left(\frac{e}{R}\right)^2\right] \\
&+b_{1_s}\left[\frac{1}{4}+\frac{\mu^2}{8}-\frac{1}{6}\frac{e}{R}-\frac{1}{12}\left(\frac{e}{R}\right)^2\right] \\
&-\frac{v_i}{\omega R}\left[\frac{1}{4}-\frac{1}{6}\frac{e}{R}-\frac{1}{12}\left(\frac{e}{R}\right)^2\right]-\mu a_0\left[\frac{1}{3}+\frac{1}{6}\frac{e}{R}\right]\Bigg\} \qquad \text{(A.15)}
\end{aligned}
$$

In general, the hinge-blade length ratio, e/R is small, and so is eliminated from terms in square brackets.

A.1.3 Weight Moment

The contribution to the hinge moment from weight, M_W is:

$$M_W = -M_b = -\int_0^{R-e} mgr\ dr \qquad \text{(A.16)}$$

where m is the weight of the blade.

A.1.4 Constant Component Solution

The solution of the constant component of the moment balance,

$$M_{\text{C.F.}_{\text{const}}} + M_{A_{\text{const}}} + M_{W_{\text{const}}} = 0 \qquad \text{(A.17)}$$

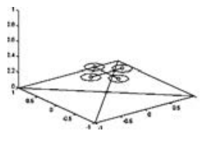

is the coning angle of the blades:

$$\begin{aligned} a_0 &= \frac{\frac{1}{6}\rho a c R^4 \left(1-\frac{e}{R}\right)^2}{\mathrm{I}_b + e\frac{M_b}{g}} \left[\theta_0\left(\frac{3}{4}+\frac{3}{4}\mu^2\right) + \theta_1\left(\frac{3}{5}+\frac{\mu^2}{2}\right)\right. \\ &\quad \left. +\mu(\alpha_s - B_1) - \frac{v_i}{\omega R}\right] - \frac{M_b}{\omega^2\left(\mathrm{I}_b + e\frac{M_g}{g}\right)} \end{aligned} \tag{A.18}$$

This can be simplified using the approximation

$$C_T/\sigma = \left(1-\frac{e}{R}\right)\frac{a}{4}\left[\theta_0\left(\frac{2}{3}+\mu^2\right)+\theta_1\left(\frac{1}{2}+\frac{\mu^2}{2}\right)+\mu(\alpha_s - B_1) - \frac{v_i}{\omega R}\right] \tag{A.19}$$

to become:

$$a_0 = \frac{\frac{2}{3}\rho c R^4\left(1-\frac{e}{R}\right)^2 C_T/\sigma}{\mathrm{I}_b + e\frac{M_b}{g}} - \frac{M_b}{\omega^2\left(\mathrm{I}_b + e\frac{M_g}{g}\right)} \tag{A.20}$$

In the case of blades with uniform mass distribution, this can be rewritten:

$$a_0 = \frac{\frac{2}{3}\gamma C_T/\sigma}{a}\left[\frac{\left(1-\frac{e}{R}\right)^2}{1+\frac{1}{2}\frac{e}{R}}\right] - \frac{\frac{3}{2}gR}{(\omega R)^2}\left[\frac{1}{1+\frac{1}{2}\frac{e}{R}}\right] \tag{A.21}$$

A.1.5 Sinusoidal Component Solution

The sinusoidal components of the flapping moment must sum to zero:

$$M_{\mathrm{C.F.}_{\mathrm{sine}}} + M_{A_{\mathrm{sine}}} = 0 \tag{A.22}$$

$$M_{\mathrm{C.F.}_{\mathrm{cosine}}} + M_{A_{\mathrm{cosine}}} = 0 \tag{A.23}$$

The mass moment has no sinusoidal components. Expanding, the sine and cosine balances are written:

$$\begin{aligned} \omega^2 b_{1_s} e\frac{M_b}{g} + \frac{\gamma \mathrm{I}_b}{2}\omega^2\left(1-\frac{e}{R}\right)^2\left[\frac{2}{3}\theta_0\mu + \frac{1}{2}\theta_1\mu\right. & \\ \left. -B_1\left(\frac{1}{4}+\frac{3}{8}\mu^2\right) + \frac{\mu}{2}\left(\mu\alpha_s - \frac{v_i}{\omega R}\right) - a_{1_s}\left(\frac{1}{4}-\frac{\mu^2}{8}\right)\right] &= 0 \end{aligned} \tag{A.24}$$

and

$$\begin{aligned} \omega^2 a_{1_s} e\frac{M_b}{g} + \frac{\gamma \mathrm{I}_b}{2}\omega^2\left(1-\frac{e}{R}\right)^2 & \\ \left[-A_1\left(\frac{1}{4}+\frac{\mu^2}{8}\right) - \frac{\mu a_0}{3} - \frac{1}{3}\frac{v_i}{\omega R} + b1_s\left(\frac{1}{4}+\frac{\mu^2}{8}\right)\right] &= 0 \end{aligned} \tag{A.25}$$

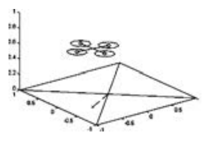

Solving these equations simultaneously gives the equations for a_{1_s} and b_{1_s}. The following approximations are used:

$$\frac{eM_b/g}{\mathrm{I}_b} = \frac{\frac{3}{2}\frac{e}{R}}{1-\frac{e}{R}} \tag{A.26}$$

$$\frac{v_i}{\omega R} = C_T/\sigma\frac{\sigma}{2\mu} \tag{A.27}$$

$$a_0 = \frac{2}{3}\gamma\frac{C_T/\sigma}{a}\frac{\left(1-\frac{e}{R}\right)^2}{1+\frac{1}{2}\frac{e}{R}} \tag{A.28}$$

The equation for longitudinal flapping is:

$$a_{1_s} = \frac{\frac{8}{3}\theta_0\mu + 2\theta_1\mu - B_1\left(1+\frac{3}{2}\mu^2\right) + 2\mu\left(\mu\alpha_s - C_T/\sigma\frac{\sigma}{2\mu}\right)}{\left(1-\frac{\mu^2}{2}\right) + \frac{144\left(\frac{e}{R}\right)^2}{\gamma^2\left(1-\frac{e}{R}\right)^6\left(1+\frac{\mu^2}{2}\right)}}$$
$$+\frac{12\left(\frac{e}{R}\right)}{\gamma\left(1-\frac{e}{R}\right)^3\left(1+\frac{\mu^2}{2}\right)} \times \left[\frac{A_1\left(1+\frac{\mu^2}{2}\right) + \frac{4}{3}C_T/\sigma\left(\frac{\frac{2}{3}\frac{\mu\gamma}{a}}{1+\frac{3}{2}\frac{e}{R}} + \frac{\sigma}{2\mu}\right)}{\left(1-\frac{\mu^2}{2}\right) + \frac{144\left(\frac{e}{R}\right)^2}{\gamma^2\left(1-\frac{e}{R}\right)^6\left(1+\frac{\mu^2}{2}\right)}}\right] \tag{A.29}$$

The second term in each denominator is generally small and can be discarded to produce:

$$a_{1_s} = \frac{\frac{8}{3}\theta_0\mu + 2\theta_1\mu - B_1\left(1+\frac{3}{2}\mu^2\right) + 2\mu\left(\mu\alpha_s - C_T/\sigma\frac{\sigma}{2\mu}\right)}{\left(1-\frac{\mu^2}{2}\right)}$$
$$+\frac{12\left(\frac{e}{R}\right)}{\gamma\left(1-\frac{e}{R}\right)^3\left(1+\frac{\mu^2}{2}\right)} \times \left[A_1\left(1+\frac{\mu^2}{2}\right) + \frac{4}{3}C_T/\sigma\left(\frac{\frac{2}{3}\frac{\mu\gamma}{a}}{1+\frac{3}{2}\frac{e}{R}} + \frac{\sigma}{2\mu}\right)\right] \tag{A.30}$$

Likewise for lateral flapping, the solution is:

$$b_{1_s} = A_1 + \frac{\frac{4}{3}C_T/\sigma}{1+\frac{\mu^2}{2}}\left(\frac{\frac{2}{3}\frac{\mu\gamma}{a}}{1+\frac{3}{2}\frac{e}{R}} + \frac{\sigma}{2\mu}\right) + \frac{12\left(\frac{e}{R}\right)}{\gamma\left(1-\frac{e}{R}\right)^3\left(1-\frac{\mu^4}{4}\right)}$$
$$\times\left[\frac{8}{3}\theta_0\mu + 2\theta_1\mu - B_1\left(1+\frac{3}{2}\mu^2\right) + 2\mu\left(\mu\alpha_s - C_T/\sigma\frac{\sigma}{2\mu}\right)\right] \tag{A.31}$$

A.2 Flapping Due to Pitch and Roll

Where pitch and roll are to be considered, the preceding derivation must be modified to take into account the gyroscopic effects of the rotor:

$$M_{\text{C.F.}} + M_A + M_W + M_{\text{gyro}} = 0 \tag{A.32}$$

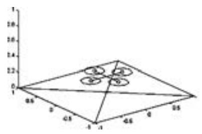

The gyroscopic effect can be represented as a correction applied to a the steady-state flapping. Consider only the sinusoidal components of the centrifugal moment:

$$M_{\text{C.F.}} = \omega^2(a_{1_s}\cos\psi + b_{1_s}\sin\psi)e\frac{M_b}{g} \tag{A.33}$$

Recall the aerodynamic hinge moment increment, (A.7). The pitch and roll-rate dependency of the aerodynamics is the angle of attack — considering the only the inflow components of the AoA:

$$\alpha = \frac{U_P}{U_T} \tag{A.34}$$

where:

$$\begin{aligned} U_P = {} & (r+e)(\dot\theta\cos\psi + \dot\phi\sin\psi) - r\omega(a_{1_s}\sin\psi - b_{1_s}\cos\psi) \\ & +V(a_{1_s}\cos\psi + b_{1_s}\sin\psi)\cos\psi \end{aligned} \tag{A.35}$$

and U_T is rewritten:

$$U_T = \omega R\left[\frac{r+e}{R} + V\sin\psi\right] \tag{A.36}$$

recalling $\mu = V/\omega R$.

Substituting into (A.7) and integrating for constant and sinusoidal components yields:

$$\begin{aligned} M_A = \frac{\rho}{8}ac(\omega R)^2\left(1-\frac{e}{R}\right)^2 R^2 \Bigg\{ & \left[\frac{\dot\phi}{\omega} - \left(1-\frac{\mu^2}{2}\right)a_{1_s}\right]\sin\psi \\ & + \left[\frac{\dot\theta}{\omega} + \left(1+\frac{\mu^2}{2}\right)b_{1_s}\right]\cos\psi\Bigg\} \end{aligned} \tag{A.37}$$

The gyroscopics hinge moment is found using the vertical acceleration of the blade with respect to the tip path plane. The kinematics of motion due to rotation produces two vertical velocity components each for pitch and roll — one for instantaneous pitch or roll rate and one for angular acceleration:

$$V_{\text{gyro}} = -\dot\theta r\cos\psi - \dot\phi r\sin\psi + \omega r\sin\psi\ \dot\theta dt - \omega r\cos\psi\ \dot\phi dt \tag{A.38}$$

The kinematics give the resulting acceleration:

$$a_{\text{gyro}} = 2\dot\theta r\omega\sin\psi - 2\dot\phi r\omega\cos\psi \tag{A.39}$$

The resultant hinge moment element is:

$$\Delta M_{\text{gyro}} = r(-a_{\text{gyro}}m)dr \tag{A.40}$$

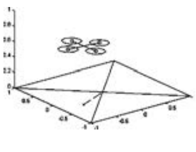

Substituting for a_{gyro} and integrating yields the sinusoidal components:

$$M_{\text{gyro}_{\text{sine}}} = -2\dot{\theta}\omega \mathrm{I}_b \tag{A.41}$$

$$M_{\text{gyro}_{\text{cosine}}} = 2\dot{\phi}\omega \mathrm{I}_b \tag{A.42}$$

Substituting into and solving (A.32) gives a_{1_s} and b_{1_s} as functions of pitch and roll rate:

$$a_{1_s} = \frac{\frac{-\frac{16}{\gamma}\left(\frac{\dot{\theta}}{\omega}\right)}{\left(1-\frac{e}{R}\right)^2} + \left(\frac{\dot{\phi}}{\omega}\right)}{1-\frac{\mu^2}{2}} + \frac{\frac{\frac{12}{\gamma}\frac{e}{R}}{\left(1-\frac{e}{R}\right)^3}\left[\frac{-\frac{16}{\gamma}\left(\frac{\dot{\phi}}{\omega}\right)}{\left(1-\frac{e}{R}\right)^2} - \left(\frac{\dot{\theta}}{\omega}\right)\right]}{1-\frac{\mu^2}{4}} \tag{A.43}$$

and

$$b_{1_s} = \frac{\frac{-\frac{16}{\gamma}\left(\frac{\dot{\phi}}{\omega}\right)}{\left(1-\frac{e}{R}\right)^2} + \left(\frac{\dot{\theta}}{\omega}\right)}{1-\frac{\mu^2}{2}} + \frac{\frac{\frac{12}{\gamma}\frac{e}{R}}{\left(1-\frac{e}{R}\right)^3}\left[\frac{-\frac{16}{\gamma}\left(\frac{\dot{\theta}}{\omega}\right)}{\left(1-\frac{e}{R}\right)^2} - \left(\frac{\dot{\phi}}{\omega}\right)\right]}{1-\frac{\mu^2}{4}} \tag{A.44}$$

A.3 Sprung Teetering Hinge

Although it is not used in the current X-4 flyer, the original proposed rotor design used a torsional spring attached to the teetering rotor hub to emulate the effect of a flapping hinge offset. Replacing the spring with one of a different spring constant allowed the effective hinge offspring to be changed quickly. The apparent offset of this ‘virtual hinge’ can be calculated from the spring constant and blade centripetal behaviour.

For a torsional spring of stiffness k_0 mounted at the teetering hub:

$$M_{\text{spring}} = \omega^2\beta \mathrm{I}_b + \beta k_0 \tag{A.45}$$

It can be seen that the spring will behave the same as a hinge offset, such that:

$$e_{\text{spring}} = \frac{k_0 g}{\omega^2 \mathrm{I}_b} \tag{A.46}$$

where e_{spring} is the equivalent hinge offset distance of the sprung rotorhead.

The spring is not a perfect offset replacement, as the apparent offset will change with changing ω. However, around hover (near constant rotor speed) the spring will reproduce hinge offset behaviour, allowing standard helicopter formulae to be applied. In practice, hub springs were found to cause vibration in the rotorhead, particular to the two-blade teetering mast. Consequently, although hub springs could be used to tune the stiffness of the rotor flapping, they are not implemented on the X-4.

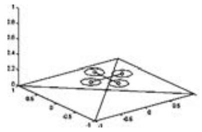

Appendix B

Data Software Interfaces

B.1 Telemetry Logfiles

Telemetry is stored in five log files, referenced by the logged session name (e.g. ‘xxxx’) appended with the type of log file. The logs are stored in a .dat format that is easily interpreted by Mathworks Matlab. Every entry in each logfile is time-stamped.

`xxxx_can_in.dat` records every COS packet received over the Bluetooth link, preserving extended CAN packet fragmentation. Defragmented received packets are logged in `xxxx_comms_in.dat`, which allows for lost packet fragments to be cross-referenced against complete packets. All transmitted packets are stored in `xxxx_comms_out.dat` in their non-fragmented format (although no extended packets are currently sent via the uplink). The vehicle motion, rotor speeds, sensor readings, subsystems statuses and handset control positions are recorded in `xxx_states.dat`. Any flagged occurrences, conditions or errors are recorded in `xxxx_events.dat`.

B.2 Extended CANbus Packet

The EiMU uses a multi-packet CANbus interface, not specified in the CANbus standard. We term these multi-part packets ‘extended packets’. Extended CAN packets consist of a series of chained data fragments. In each fragment, the lead byte value (`buf[0]`) is the number of remained packets in the series; 0x80 set high indicates that the fragment is the leading fragment of a chain.

To avoid confusion between standard single-frame CAN packets and extended packets, a bitmask is used in the ID value to differentiate betwen the two. The

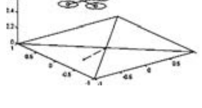

Byte	Value
Header	0xff
ID1	Identifier MSB
ID2	Identifier LSB
Format	Number of payload bytes
Payload	data0
...	data1
...	...
Parity	CRC-8 parity byte

Table B.1: COS Packet Structure.

11th bit, 0x0400 set high indicates a multi-part packet. If a received packet indicates it is part of an extended packet, it is stored until the remaining packets are received. By the CANbus bus contention rules, single-frame packets are always given priority over extended packets. This guarantees that priority messages such as panic packets can always seize the bus.

B.3 CAN Over Serial

The X-4 uses a hybrid CANbus/CAN Over Serial (COS) architecture developed for the project. All inter-device communications are implemented as CAN or virtualised CAN packets implemented as serial packets. A COS packet is all the data contained in a CAN packet, represented as bytes with simple CRC8 parity. The serial packet structure is given in Tab. B.1. The maximum number of data bytes is 8; there is a maximum of 13 bytes in a packet. Reconstruction and delivery of COS packets from serial data is performed by the application layer code.

B.4 Defragmentation and Packetisation

Extended CAN packets are combined into concatenated CAN (CON) packets that are identical except for a greatly enlarged data buffer capacity. In practice, CAN packets can be stored in CON packets to simplify function IO.

The software communications stack consists of four routines; two for Rx, two for Tx. These routines have been implemented on both PC and embedded microprocessor platforms:

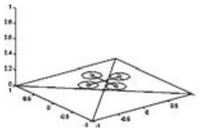

- `get_can_packet_crc_8` — Read from the line until a valid COS CAN packet is found
- `get_con_packet` — Read from the line; return the first valid CON packet
- `send_can_packet_crc_8` — Write the passed CAN packet as COS bytes
- `send_con_packet` — Fragment and transmit the CON packet as COS bytes.

Function `get_can_packet_crc_8` reads through the serial buffer until a complete packet is found. The function reads a number of data bytes specified by the format byte. An additional parity byte is used to validate the whole packet. If the header is not found, the format tests out of bounds, or parity check fails, the function will loop back to searching for a header.

Function `get_con_packet` defragments multi-part CAN packets and returns CON packets. A hash table is used to store incomplete packet data until all of the fragments are collected. When a packet request is sent, the function calls `get_can_packet_crc_8`. If the returned packet is a single-part packet, it is passed out as a CON packet. If the fragment is a lead fragment, it starts an entry in the hash table; any previous entries are overwritten — this assumes that only one device will transmit multi-part packets using a given ID at any time. If the fragment is a final fragment, the complete packet is passed out; otherwise the fragment is slotted into the hash table `get_can_packet_crc_8` is called again. If any fragments from a currently incomplete run are read out of order, the entire hash table entry is scrapped. This function is entirely independent of the COS implementation, including parity. This is the most complex unit of code in the system and a good candidate for speed improvement.

Function `send_can_packet_crc_8` reads the input data and transmits the packet header and data bytes over serial with CRC8 parity. It will return an error if more than eight bytes are requested to be sent.

Function `send_con_packet` calculates the number of fragments a passed packet will require, and then passes them to `send_can_packet_crc_8` for transmission. Function `send_can_packet_crc_8` writes the passed data into a COS packet buffer array that is then written sequentially out over the serial line.

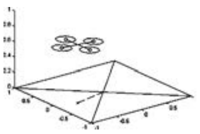

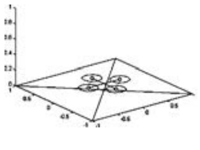

Appendix C

Device Packet Structures

C.1 EiMU

The EiMU transmits its data in a four-part extended CAN packet format. Two values, roll rate and Y magnetometer reading, are split between two packets. Table C.1 shows the EiMU packet structure, with sub-fragments denoted by horizontal rules.

C.2 RC Receiver

The RC receiver transmits radio handset PWM stick and switch position data in two extended COS packets. Unlike other devices that transmit CAN packets over RS-232 via a converter, the RC receiver outputs COS packets natively without need for an interface board. Table C.2 shows the RC receiver packet structure, with sub-fragments denoted by horizontal rules.

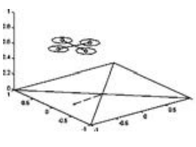

Packet	Byte	Value
3	0	Roll Angle (MSB)
	1	Roll Angle (LSB)
	2	Pitch Angle (MSB)
	3	Pitch Angle (LSB)
	4	Heading Angle (MSB)
	5	Heading Angle (LSB)
	6	Roll Rate (MSB)
2	7	Roll Rate (LSB)
	8	Pitch Rate (MSB)
	9	Pitch Rate (LSB)
	10	Yaw Rate (MSB)
	11	Yaw Rate (LSB)
	12	X Acceleration (MSB)
	13	X Acceleration (LSB)
1	14	Y Acceleration (MSB)
	15	Y Acceleration (LSB)
	16	Z Acceleration (MSB)
	17	Z Acceleration (LSB)
	18	X Magnetometer (MSB)
	19	X Magnetometer (LSB)
	20	Y Magnetometer (MSB)
0	21	Y Magnetometer (LSB)
	22	Z Magnetometer (MSB)
	23	Z Magnetometer (LSB)
	24	Temperature (MSB)
	25	Temperature (LSB)
	26	Time Reference (MSB)
	27	Time Reference (LSB)

Table C.1: EiMU Extended Packet Structure.

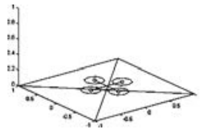

Packet	Byte	Value
1	0	Throttle (MSB)
	1	Throttle (LSB)
	2	Aileron (MSB)
	3	Aileron (LSB)
	4	Elevator (MSB)
	5	Elevator (LSB)
	6	Rudder (MSB)
0	7	Rudder (LSB)
	8	Gear (MSB)
	9	Gear (LSB)
	10	Auxillary 1 (MSB)
	11	Auxillary 1 (LSB)
	12	Auxillary 2 (MSB)
	13	Auxillary 2 (LSB)

Table C.2: RC Receiver Extended Packet Structure.

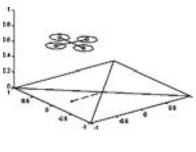

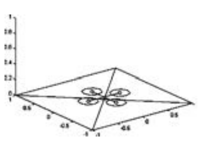

Appendix D

Quadrotor Stability Derivatives in Hover

The behaviour of an aircraft around equilibirum conditions can be represented by a sum of state variables and associated stability derivatives for each axis of motion [Prouty 2002, p 361]. In the case of the X-4 Flyer's longitudinal motion in hover:

$$-m\ddot{x} + \frac{\partial x}{\partial \dot{x}}\dot{x} + \frac{\partial x}{\partial \dot{\theta}}\dot{\theta} - mg\theta = 0 \tag{D.1}$$

$$-\mathrm{I}_{\mathrm{YY}}\ddot{\theta} + \frac{\partial \theta}{\partial \dot{x}}\dot{x} + \frac{\partial \theta}{\partial \dot{\theta}}\dot{\theta} = 0 \tag{D.2}$$

These equations are used in Section 5.2.5 to analyse the longitudinal stability of the flyer.

Unlike conventional helicopters, quadrotors do not have tail rotor or stabiliser stability derivatives; instead, they have the effect of four main rotors and the additional vertical and yaw motion effects that come from widely spaced rotors. Selected longitudinal and yaw stability derivatives for near-hover flight are presented here. Also included is the yaw derivative due to flapping, unique to tandem and quad-rotor helicopters. It is given that all blade feathering derivatives are zero.

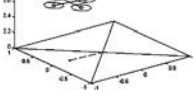

Derivative	Equation	X-4 Flyer
$\frac{\partial\mu}{\partial\dot{x}}$	$\frac{1}{\omega R}$	0.007
$\frac{\partial a_{1_s}}{\partial\mu}$	$4\theta_t - 2\lambda$	0.2092
$\frac{\partial b_{1_s}}{\partial\mu}$	$\frac{4}{3}a_0$	0.0257
$\frac{\partial C_\mathrm{T}/\sigma}{\partial\lambda}$	$\frac{1}{\frac{8}{a}+\frac{\sqrt{\frac{\sigma}{2}}}{\sqrt{C_\mathrm{T}/\sigma}}}$	0.4991
$\frac{\partial a_{1_s}}{\partial\dot{\theta}}, \frac{\partial b_{1_s}}{\partial\dot{\phi}}$	$-\frac{16}{\gamma\omega\left(1-\frac{e}{R}\right)^2} - \frac{12\frac{e}{R}}{\gamma\omega\left(1-\frac{e}{R}\right)^3}$	-0.0103
$\frac{\partial a_{1_s}}{\partial\dot{\phi}}, \frac{\partial b_{1_s}}{\partial\dot{\theta}}$	$\frac{1}{\omega}\left[1 - \frac{192\frac{e}{R}}{\gamma^2\left(1-\frac{e}{R}\right)^3}\right]$	0.0011
$\frac{\partial C_H/\sigma}{\partial a_{1_s}}$	$\frac{3}{2}C_\mathrm{T}/\sigma\left(1 - \frac{a}{12}\frac{\theta_t}{C_\mathrm{T}/\sigma}\right)$	0.0811
$\frac{\partial\theta}{\partial a_{1_s}}$	$\frac{3}{4}\frac{e}{R}\frac{A_b\rho R(\omega R)^2 a}{\gamma}$	0
$\frac{\partial x}{\partial\dot{x}}$	$-\rho A_b(\omega R)^2\frac{\partial C_\mathrm{H}/\sigma}{\partial a_{1_s}}\frac{\partial a_{1_s}}{\partial\mu}\frac{\partial\mu}{\partial\dot{x}}$	-0.0133
$\frac{\partial x}{\partial\dot{\theta}}$	$-\rho A_b(\omega R)^2\frac{\partial C_\mathrm{H}/\sigma}{\partial a_{1_s}}\frac{\partial a_{1_s}}{\partial\dot{\theta}}$	0.0938
$\frac{\partial x}{\partial\dot{\phi}}$	$-\rho A_b(\omega R)^2\frac{\partial C_\mathrm{H}/\sigma}{\partial a_{1_s}}\frac{\partial a_{1_s}}{\partial\dot{\phi}}$	-0.01
$\frac{\partial\theta}{\partial\dot{x}}$	$\frac{\partial\theta}{\partial a_{1_s}}\frac{\partial a_{1_s}}{\partial\mu}\frac{\partial\mu}{\partial\dot{x}} - \frac{\partial x}{\partial\dot{x}}h$	9.23×10^{-6}
$\frac{\partial\theta}{\partial\dot{\theta}}$	$\frac{\partial\theta}{\partial a_{1_s}}\frac{\partial a_{1_s}}{\partial\dot{\theta}} + \frac{\partial x}{\partial\dot{\theta}}h + \rho A_b(\omega R)^2 2d\frac{\partial C_\mathrm{T}/\sigma}{\partial\dot{\theta}}$	0.2201
$\frac{\partial\theta}{\partial\dot{\phi}}$	$\frac{\partial\theta}{\partial a_{1_s}}\frac{\partial a_{1_s}}{\partial\dot{\phi}} + \frac{\partial x}{\partial\dot{\phi}}h + \rho A_b(\omega R)^2 2d\frac{\partial C_\mathrm{T}/\sigma}{\partial\dot{\phi}}$	0.2201
$\frac{\partial C_\mathrm{T}/\sigma}{\partial\dot{\theta}}$	$-\frac{a}{4}\frac{d}{\omega R}$	-0.003
$\frac{\partial C_\mathrm{T}/\sigma}{\partial\dot{\phi}}$	$-\frac{a}{4}\frac{d}{\omega R}$	-0.003
$\frac{\partial\psi}{\partial\dot{\psi}}$	$(4\theta_t - 2\lambda)\frac{4d}{\omega R}$	0.0018

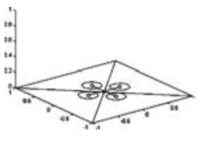

Bibliography

[UAD 2001] 2001 Air Demo, *Yamaha RMAX*, `www.strikenet.js.mil/uavairshow/RMAX.htm` (2001).

[Altŭg *et al* 2002] E. Altŭg, J. Ostrowski and R. Mahony, Control of a Quad-Rotor Helicopter Using Visual Feedback, In *Proc. International Conference on Robotics and Automation*, Washington, United States, 2002.

[Altŭg *et al* 2003] E. Altŭg, J. Ostrowski and C. Taylor, Quadrotor Control Using Dual Camera Visual Feedback, In *Proc. IEEE International Conference on Robotics and Automation*, Taipei, Taiwan, 2003.

[Anderson and Stone 2007] P. Anderson and H. Stone, Predictive Guidance and Control for a Tail-Sitting Unmanned Aerial Vehicle, In *Proc. Information, Decision and Control*, Adelaide, Australia, 2007.

[Armitage 1988] M. Armitage, *Unmanned Aircraft*, Brassey's Defence Publishers, London, UK, 1988.

[Bachmann *et al* 2001] E. Bachmann, J. Marins, M. Zyda, R. Mcghee and X. Yun, An Extended Kalman Filter for Quaternion-Based Orientation Estimation Using MARG Sensors, In *Proc. 2001 IEEE/RSJ International Conference on Intelligent Robots and Systems*, 2001.

[Bhandari and Colgren 2006] S. Bhandari and R. Colgren, 6-DoF Dynamic Model for a Raptor 50 UAV Helicopter Including Stabilizer Bar Dynamics, In *Proc. AIAA Modeling and Simulation Technologies Conference and Exhibit*, Keystone, Colorado, United States, 2006.

[Bell 2006] Bell Helicopter, The Eagle Eye UAV, `www.bellhelicopter.textron.com/en/aircraft/military/bellEagleEye.cfm` (2006, Jan).

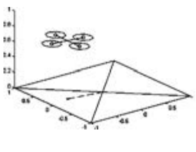

[Benallegue *et al* 2006] A. Benallegue, A. Mokhtari and L. Fridman, Feedback Linearization and High Order Sliding Mode Observer For A Quadrotor UAV, In *Proc. International Workshop on Variable Structure Systems*, Alghero, Italy, 2006.

[Bode 1945] H. Bode, *Network Anaylsis and Feedback Amplifier Design*, D. van Nostrand, New York, United States, 1945.

[Boeing 2006] Boeing, Phantom Works Advanced Systems Canard Rotor/Wing, `www.boeing.com/phantom/advsystems/canard.html` (2006, Jan).

[Bohorquez and Pines 2003] F. Bohorquez and D. Pines, Hover Performance of Rotor Blades at Low Reynolds Numbers for Rotary Wing Micro Air Vehicles, In *Proc. "Unmanned Unlimited" Conf. and Workshop and Exhibit*, San Diego, United States, 2003.

[Borenstein 1992] J. Borenstein, The Hoverbot — An Electrically Powered Flying Robot, Unpublished paper, University of Michigan, 1992, `ftp://ftp.eecs.umich.edu/people/johannb/paper99.pdf` (2004).

[Bouabdallah *et al* 2004a] S. Bouabdallah, P. Murrieri and R. Siegwart, Design and Control of an Indoor Micro Quad-Rotor, In *Proc. International Conference on Robotics and Automation*, New Orleans, United States, 2004.

[Bouabdallah *et al* 2004b] S. Bouabdallah, A. Noth and R. Siegwart, PID vs LQ Control Techniques Applied to an Indoor Micro Quadrotor, In *Proc. IEEE/RSJ International Conference on Intelligent Robots and Systems*, Sendai, Japan, 2004.

[Bouabdallah and Siegwart 2005a] S. Bouabdallah and R. Siegwart, Towards Intelligent Miniature Flying Robots, In *Proc. Field and Service Robotics*, Port Douglas, Australia, 2005.

[Bouabdallah and Siegwart 2005b] S. Bouabdallah and R. Siegwart, Backstepping and Sliding-Mode Techniques Applied to an Indoor Micro Quadrotor, In *IEEE International Conference on Robotics and Automation*, Barcelona, Spain, 2005.

[Bourquardez *et al* 2007] O. Bourquardez, R. Mahony, N. Guenard, F. Chaumette, T. Hamel and L. Eck, Kinematic Visual Servo Control of a

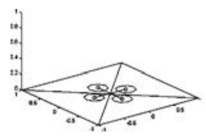

Quadrotor Aerial Vehicle, Institut de Recherche en Informatique et Systémes Aléatoires, Rennes Cedex, France, 2007.

[Bradley 1996] R. Bradley, The Flying Brick Exposed: Nonlinear Control of a Basic Helicopter Model, Technical Report, Department of Mathematics, Glasgow Caledonian University, 1996.

[Brown and Houston 2000] R. Brown and S. Houston, Comparison of Induced Velocity Models for Helicopter Flight Mechanics, In *Journal of Aircraft*, Vol. 37, No. 4, 2000.

[Carpenter and Fridovitch 1953] P. Carpenter and B. Fridovitch, Effect of Rapid Blade Pitch Increase on the Thrust and Induced Velocity Response of a Full Scale Helicopter Rotor, National Advisory Committee for Aeronautics TN-3044, 1953.

[Castillo *et al* 2004a] P. Castillo, R. Lozano and A. Dzul, Stabilization of a Mini-Rotorcraft Having Four Rotors, In *Proc. IEEE International Conference on Intelligent Robots and Systems*, Sendai, Japan, 2004.

[Castillo *et al* 2004b] P. Castillo, A. Dzul and R. Lozano, Real-Time Stabilization and Tracking of a Four-Rotor Mini Rotorcraft, In *IEEE Transactions on Control Systems Technology*, Vol. 12, No. 4, 2004.

[Castles and De Leeuw 1954] W. Castles and J. De Leeuw, The Normal Component of the Induced Velocity in the Vicinity of a Lifting Rotor and Some Examples of Its Application, National Advisory Committee for Aeronautics TR 1184, 1954.

[Chen 1990] R. Chen, A Survey of Nonuniform Inflow Models for Rotorcraft Flight Dynamics and Control Applications, In *Vertica*, Vol. 14, No. 2, 1990.

[Cogdell 1999] J. Cogdell, *Foundations of Electrical Engineering*, 2nd Ed., Prentice Hall, Upper Saddle River, United States, 1999.

[Coleman *et al* 1945] R. Coleman, M. Feingold and C. Stempin, Evaluation of the Induced-Velocity Field of an Idealized Helicopter Rotor, National Advisory Committee for Aeronautics WR L-126, 1945.

[Coleman 1997] C. Coleman, A Survey of Theoretical and Experimental Coaxial Rotor Aerodynamic Research, NASA Technical Paper 3675, March 1997.

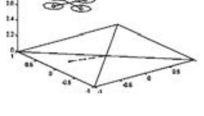

[Crassidis *et al* 2007] J. Crassidis, F. Markley, and Y. Cheng, Nonlinear Attitude Filtering Methods, In *Journal of Guidance, Control, and Dynamics*, Vol. 30, No. 1, 2007.

[Done and Balmford 2001] G. Done and D. Balmford, *Bramwell's Helicopter Dynamics*, American Institute of Aeronautics and Astronautics Inc., Reston, United States, 2001.

[Draganfly Innovations 2006] Draganfly Innovations, Draganflyer V Ti Thermal Intelligence Gyro Stabilized Helicopter, `www.rctoys.com/draganflyer5.php` (2006, Jan).

[Drela 2003] M. Drela, *MIT 16.82 Flight Vehicle Engineering Course Demonstrator*, `http://student.mit.edu/catalog/m16b.html` (2004).

[Drela 2004] M. Drela, X-Foil Subsonic Airfoil Development System, `http://raphael.mit.edu/xfoil/` (2004, Aug).

[Dunbabin *et al* 2004] M. Dunbabin, S. Brosnan, J. Roberts and P. Corke, Vibration Isolation for Autonomous Helicopter Fight, In *Proc. International Conference on Robotics and Automation*, New Orleans, United States, 2004.

[Fjellstad and Fossen 1994] O-E. Fjellstad and T. Fossen, Comments on the Attitude Control Problem, In *IEEE Transactions on Automatic Control*, Vol. 39, No. 3, 1994.

[Francis and Zames 1984] B. Francis and G. Zames, On H_∞-Optimal Sensitivity Theory for SISO Feedback Systems, In *IEEE Transactions on Automatic Control*, Vol. 29, No. 1, 1984.

[Franklin *et al* 1994] G. Franklin, J. Powell and A Emami-Naeini, *Feedback Control of Dynamic Systems*, Reading, Massachusetts, United States of America: Addison-Wesley Publishing Company, 1994.

[Freudenberg and Looze 1987] J. Freudenberg and D. Looze, A Sensitivity Tradeoff for Plants With Time Delay, In *IEEE Transactions on Automatic Control*, Vol. 32, No. 2, 1987.

[Friedmann 1977] P. Friedmann, Feedback Control of Dynamic Systems, In *Journal of Aircraft*, Vol. 14, No. 11, 1977.

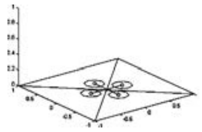

[Gao *et al* 2002] L. Gao, S. Liu and R. Dougal, Dynamic Lithium-Ion Battery Model for System Simulation, In *Transactions on Components and Packaging Technologies*, Vol. 25, No. 3, Sept. 2002.

[Goebel 2007] G. Goebel, Cruise Missiles, `www.vectorsite.net/twcruz.html` (2007, Aug).

[Golightly and Jones 2005] I. Golightly and D. Jones, *Visual Control of an Unmanned Aerial Vehicle for Power Line Inspection*, In *Proc. International Conference on Advanced Robotics*, Seattle, United States, 2005.

[Gordon *et al* 1993] M. Gordon, S. Kondof, E. Corban, D. Schrage, Rotorcraft Aerial Robot - Challenges and Solutions, In *Proc. Digital Avionics Systems Conference*, 1993.

[Grace 2001] M. Grace, Unsteady Blade Response: The BVI Model VS. the Gust Model, In *Proc. 7th AIAA/CEAS Aeroacoustics Conference*, Maastricht, The Netherlands, 2001.

[Green 2003] S. Green, Design of an X-4 Flyer, Australian National University Dept. Engineering Honours Thesis, 2003.

[Green and Oh 2005] W. Green and P. Oh, A MAV That Flies Like an Airplane and Hovers Like a Helicopter, In *Proc. International Conference on Advanced Intelligent Mechatronics*, Monterey, United States, 2005.

[Guenard *et al* 2006] N. Guenard, T. Hamel and L. Eck, Control Laws For The Tele Operation Of An Unmanned Aerial Vehicle Known As An X4-flyer, In *Proc. IEEE/RSJ International Conference on Intelligent Robots and Systems*, Beijing, China, 2006.

[Guenard *et al* 2005] N. Guenard, T. Hamel and V. Moreau, Dynamic Modeling and Intuitive Control Strategy for an "X4-Flyer". In *Proc. International Conference on Control and Automation*, Budapest, Hungary, 2005.

[Guenard *et al* 2007] N. Guenard, T. Hamel and R. Mahony, A Practical Visual Servo Control for a Unmanned Aerial Vehicle. In *Proc. IEEE International Conference on Robotics and Automation*, Rome, Italy, 2007.

[GHHF 2007] Gyrodyne Helicopter Historical Foundation, Gyrodyne Helicopter Historical Foundation, `www.gyrodynehelicopters.com/` (2007, Aug).

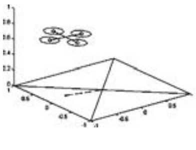

[Hamel *et al* 2002] T. Hamel, R. Mahony, R. Lozano and J. Ostrowski, Dynamic Modelling and Configuration Stabilization for an X4-Flyer, In *Proc. 15th Triennial World Congress of the International Federation of Automatic Control*, Barcelona, Spain, 2002.

[Hamel and Mahony 2002] T. Hamel and R. Mahony, Attitude estimation on $SO(3)$ based on direct inertial measurements, In *Proc. International Conference on Robotics and Automation*, Orlando, United States, 2006.

[Hepperle 2004] M. Hepperle, *Airfoils for Tailless Airplanes*, `www.mh-aerotools.de/airfoils/nf_1.htm` (2004, Aug).

[Herwitz *et al* 2002] S. Herwitz, L. Johnson, J. Arvesen, J. Leung, and S. Dunagan, Precision Agriculture as a Commercial Application for Solar-Powered UAVs, In *Proc. AIAA UAV Conference*, Portsmouth, United States, 2002.

[Heyson and Katzoff 1957] H. Heyson and S. Katzoff, Induced Velocities Near a Lifting Rotor With Nonuniform Disk Loading, National Advisory Committee for Aeronautics TR 1319, 1957.

[Hoffmann *et al* 2004] G. Hoffmann, D. Rajnarayan, S. Waslander, D. Dostal, J. Jang and C. Tomlin, The Stanford Testbed of Autonomous Rotorcraft for Multi Agent Control (STARMAC), In *Proc. Digital Avionics Systems Conference*, Salt Lake City, United States, 2004.

[Honnery 2000] D. Honnery, *Introduction to the Theory of Flight*, Gracie Press, Northcote, Victoria, 2000.

[Hyvārinen and Kjellgren 1997] J. Hyvārinen and P. Kjellgren, MSC/PATRAN as a Part of a Tool in the Field of Static and Dynamic Aeroelasticity, In *Proc. MSC 1996 World Users' Conference*, 1996.

[Innovatia 2006] Innovatia Design Center, Motor Theory, `www.innovatia.com/Design_Center/Electronic_Design_for_Motor_Control_1.htm` (2006, Jun).

[Jones 1940] R. Jones, The Unsteady Lift of a Wing of Finite Aspect Ratio, National Advisory Committee for Aeronautics, Report No. 681.

[Jun *et al* 2006] M. Jun, S. Roumeliotis and G. Sukhatme, State Estimation of an Autonomous Helicopter using Kalman Filtering, In *Proc. IEEE/RSJ International Conference on Intelligent Robots and System*, 1999.

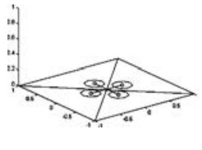

[Jung *et al* 2006] D. Jung, E. J. Levy, D. Zhou, R. Fink, J. Moshe, A. Earl and P. Tsiotras, Design and Development of a Low-Cost Test-Bed for Undergraduate Education in UAVs , In *Proc. IEEE Conference on Decision and Control*, Seville, Spain, 2005.

[Khalil 1995] H. Khalil, *Nonlinear Systems*, 2nd Ed., Prentice Hall, New Jersey, United States, 1995.

[Kroo *et al* 2000] I. Kroo, F. Prinz, M. Shantz, P. Kunz, G. Fay, S. Cheng, T. Fabian and C. Partridge, *The Mesicopter: A Miniature Rotorcraft Concept Phase II Interim Report*, Stanford University, 2000.

[Leishman 2002a] J. Leishman, The Bréguet-Richet Quad-Rotor Helicopter of 1907, `www.enae.umd.edu/AGRC/Aero/Breguet.pdf`, (2002, May).

[Leishman 2002b] J. Leishman, Challenges in Modeling the Unsteady Aerodynamics of Wind Turbines, In *Wind Energy*, John Wiley & Sons, Vol. 5, 2002.

[Leishman 2006] J. Leishman, *Principles of Helicopter Aerodynamics*, 2nd Ed., Cambridge University Press, Cambridge, United Kingdom, 2006.

[Loewy 1969] R. Loewy, Review of Rotary-Wing V/STOL Dynamic and Aeroelastic Problems, In *Journal of the American Helicopter Society*, 1969.

[Mahony *et al* 2006] R. Mahony, S. Cha and T. Hamel, A Coupled Estimation and Control Analysis for Attitude Stabilisation of Mini Aerial Vehicles, In *Proc. Australasian Conference on Robotics and Automation*, Auckland, New Zealand, 2006.

[Mahony *et al* 2005] R. Mahony, T. Hamel and J-M. Pflimlin, Complementary Filter Design on the Special Orthogonal Group $SO(3)$, In *Proc. IEEE Conference on Decision and Control*, Seville, Spain, 2005.

[Mahony *et al* 2008] R. Mahony, T. Hamel and J-M. Pflimlin, Non-Linear Complementary Filters on the Special Orthogonal Group, In *Transactions on Automatic Control*, Accepted for publication, 2008.

[Martinez-Val and Hernández 1999] R. Martinez-Val and C. Hernández, Preliminary Design of a Low Speed, Long Endurance Remote Piloted Vehicles (RPV) for Civil Applications, In *Aircraft Design*. vol. 2, 1999.

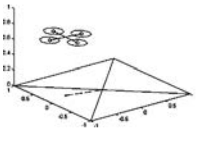

[McCormick 1999] B. McCormick, *Aerodynamics of V/STOL Flight*, Dover Publications, Mineola, New York, 1999.

[AHS 2006] M. McKee, VTOL UAVs Come of Age: US Navy Begins Development of VTUAV, `www.vtol.org/uavpaper/NavyUAV.htm` (2006, Jan).

[McKerrow 2004] P. McKerrow, Modelling the Draganflyer Four-Rotor Helicopter, In *Proc. IEEE International Conference on Robotics and Automation*, 2004.

[Mettler *et al* 2004] B. Mettler, C. Dever and E. Feron, Scaling Effects and Dynamic Characteristics of Miniature Rotorcraft, In *Journal of Guidance, Control, and Dynamics*, Vol.27, No.3, 2004.

[Middleton 1991] R. Middleton, Trade-offs in Linear Control Systems Design, In *Automatica*, Vol. 27, No. 2, 1991.

[Middleton and Goodwin 1990] R. Middleton and G. Goodwin, *Digital Control and Estimation. A Unified Approach*, Prentice-Hall, 1990.

[Mistler *et al* 2001] V. Mistler, A. Benallegue and N. M'Sirdi, Exact Linearization and Noninteracting Control of a 4 Rotors Helicopter via Dynamic Feedback, In *Proc. IEEE International Workshop on Robot and Human Interactive Communication*, 2001.

[Mokhtari and Benallegue 2004] A. Mokhtari and A. Benallegue, Dynamic Feedback Controller of Euler Angles and Wind parameters estimation for a Quadrotor Unmanned Aerial Vehicle, In *Proc. IEEE International Conference on Robot and Automation*, New Orleans, Louisiana, United States, 2004.

[Mokhtari *et al* 2005] A. Mokhtari, A. Benallegue and B. Daachi, Robust Feedback Linearization and GH$_\infty$ Controller for Quadrotor Unmanned Aerial Vehicle, In *Proc. IEEE/RSJ International Conference on Intelligent Robots and Systems*, 2005.

[Nice 2004] E. Nice, Design of a Four Rotor Hovering Vehicle, Cornell University, 2004.

[Nicoud and Zuffery 2002] J. Nicoud and J. Zufferey, Toward indoor flying robots, In *Proc. IEEE/RSJ International Conference on Intelligent Robots and System*, 2002.

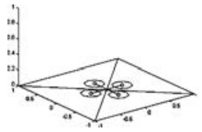

[NASG 2004] Nihon University Aero Student Group, *Airfoil Database*, `www.nasg.com/afdb/index-e.phtml` (2004, Aug).

[Park *et al* 2005] S. Park, D. Won, M. Kang, T. Kim, H. Lee and S. Kwon, RIC (Robust Internal-loop Compensator) Based Flight Control of a Quad-Rotor Type UAV, In *Proc. International Conference on Intelligent Robots and Systems*, 2005.

[Parsch 2005] A. Parsch, Directory of U.S. Military Rockets and Missiles, `www.designation-systems.net/dusrm/app4/sperry-fb.html` (2005).

[Pflimlin *et al* 1997] J. Pflimlin, P. Soueres and T. Hamel, Position control of a ducted fan VTOL UAV in crosswind, In *International Journal of Control*, Vol. 80, No. 5, 2007.

[Pope 2002] R. Pope, Hybrid Concept Flyer, Australian National University Dept. Engineering Honours Thesis, 2002.

[Potter and Wiggert 1997] M. Potter and D. Wiggert, *Mechanics of Fluids*, Prentice-Hall, Upper Saddle River, New Jersey, 1997.

[Pounds *et al* 2002] P. Pounds, R. Mahony, P. Hynes and J. Roberts, Design of a Four-Rotor Aerial Robot, In *Proc. Australasian Conference on Robotics and Automation*, Auckland, New Zealand, 2002.

[Pounds *et al* 2004] P. Pounds, R. Mahony, J. Gresham, P. Corke, J. Roberts, Towards Dynamically-Favourable Quad-Rotor Aerial Robots, In *Proc. Australasian Conference on Robotics and Automation*, Canberra, Australia, 2004.

[Pounds and Mahony 2005] P. Pounds and R. Mahony, Small-Scale Aeroelastic Rotor Simulation, Design and Fabrication, In *Proc. Australasian Conference on Robotics and Automation*, Sydney, Australia, 2005.

[Pounds *et al* 2007a] P. Pounds, R. Mahony and P. Corke, System Identification and Control of an Aerobot Drive System, In *Proc. Information, Decision and Control*, Adelaide, Australia, 2007.

[Prouty 2002] R. Prouty, *Helicopter Performance, Stability, and Control*, Krieger Publishing Company, 2002.

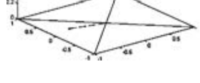

[Pullin and Wang 2003] D. Pullin and Z. Wang, Unsteady Forces on an Accelerating Plate and Application to Hovering Insect Flight, In *Journal of Fluid Mechanics*, Vol. 509, 2003.

[Quackenbush *et al* 2004] T. Quackenbush, D. Wachspress, A. Boschitsch, C. Solomon, Aeromechanical Analysis Tools for Design and Simulation of VTOL UAV Systems, `www.continuum-dynamics.com/documents/MSA001.pdf` (2004).

[Rehbinder and Hu 2004] H. Rehbinder and X. Hu, Drift-free Attitude Estimation for Accelerated Rigid Bodies, In *Automatica*, Vol. 4, No. 4, 2004.

[Roberts *et al* 2003] J. Roberts, P. Corke and G. Buskey, Low-Cost Flight Control System for a Small Autonomous Helicopter, In *Proc. IEEE International Conference on Robotics and Automation*, Taipai, 2003.

[Romero *et al* 2003] H. Romero, R. Benosman and R. Lozano, Stabilization and Location of a Four Rotor Helicopter Applying Vision, In *Proc. American Control Conference*, Minneapolis, Minnesota, United States, 2006

[Roylance 1996] D. Roylance, *Mechanics of Materials*, John Wiley & Sons, New York, 1996.

[Ruddell 1976] A. Ruddell, Advancing Blade Concept (ABC) Development, In *Journal of The American Helicopter Society*, January 1977.

[Rutherford and Wells 1999] J. Rutherford and V. Wells, An Air-launched, Self-recovering Autonomous Vehicle Concept, In *Aircraft Design*. vol. 2, 1999.

[Salazar-Cruz *et al* 2005] S. Salazar-Cruz, A. Palomino and R. Lozano, Trajectory Tracking for a Four Rotor Mini-Aircraft, In *Proc. IEEE Conference on Decision and Control and the European Control Conference 2005*, Seville, Spain, 2005.

[Salcudean 1991] S. Salcudean, A Globally Convergent Angular Velocity Observer for Rigid Body Motion, In *IEEE Transactions on Automatic Control*, Vol. 46, No. 12, 1991.

[Seddon 1996] J. Seddon, *Basic Helicopter Aerodynamics*, Blackwell Science, Oxford, United Kingdom, 1996.

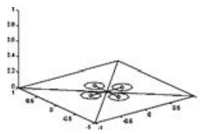

[Seron *et al* 1997] M. Seron, J. Braslavsky and G. Goodwin, *Fundemental Limitations in Filtering and Control*, Springer-Verlag, London, United Kingdom, 1997.

[Seron and Goodwin 1995] M. Seron and G. Goodwin, Design Limitations in Linear Filtering, In *Proc. Conference on Decision and Control*, New Orleans, Louisiana, United States, 1995.

[Seron and Goodwin 1996] M. Seron and G. Goodwin, Sensitivity Limitations in Nonlinear Feedback Control, In *Systems and Control Letters*, 1996.

[Slotine and Li 1991] J-J. Slotine and W. Li, *Applied Nonlinear Control*, Prentice Hall, Englewood Cliffs, United States, 1991.

[Shakernia *et al* 1999] O. Shakernia, Y. Ma, J. Koo and S. Sastry, Landing an Unmanned Air Vehicle: Vision Based Motion Estimation and Nonlinear Control, In *Asian Journal of Control*, Vol. 1, No. 3, 1999.

[Shiau and Chen 1991] B-S. Shiau and Y-B Chen, Observation on Wind Turbulence Characteristics and Velocity Spectra Near the Ground at the Coastal Region, In *Journal of Wind Engineering and Industrial Aerodynamics*, Vol. 90, 2002.

[NASM 2006] Smithsonian Air and Space Museum, Smithsonian Institute, Principles of Helicopter Aerodynamics, `www.nasm.si.edu/research/aero/aircraft/zimmerman.htm` (2006, Jan.)

[Starostin 2004] M. Starostin, All the World's Rotorcraft, `http://avia.russian.ee` (2004, Aug).

[Stein 2003] G. Stein, Respect the Unstable, In *Control Systems Magazine*, Vol. 23, No. 4, 2003.

[Stepniewski and Keys 1984] W. Stepniewski and C. Keys, *Rotary-Wing Aerodynamics*, Dover Publications, New York, 1984.

[Tayebi and McGilvray 2004] A. Tayebi and S. McGilvray, Attitude Stabilization of a Four-Rotor Aerial Robot, In *Proc. 43rd IEEE Conference on Decision and Control*, Atlantis, Paradise Island, Bahamas, 2004.

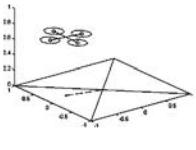

[Tayebi and McGilvray 2006] A. Tayebi and S. McGilvray, Attitude Stabilization of a VTOL Quadrotor Aircraft, In *IEEE Transactions on Control Systems Technology*, Vol. 14, No. 3, 2006.

[Taamallah *et al* 2005] S. Taamallah, A. de Reus and J. Boer, Development of a Rotorcraft Mini-UAV System Demonstrator, In *Proc. Digital Avionics Systems Conference*, Vol. 2, 2005.

[Thienel and Sanner 2003] J. Thienel and R. Sanner, A Coupled Nonlinear Spacecraft Attitude Controller and Observer With an Unknown Constant Gyro Bias and Gyro Noise, In *IEEE Transactions on Automatic Control*, Vol. 48, No. 11, 2003.

[Tournier *et al* 2006] G. Tournier, M. Valenti, J. How and E. Feron, Estimation and Control of a Quadrotor Vehicle Using Monocular Vision and Moire Patterns, In *Proc. AIAA Guidance, Navigation and Control Conference*, Keystone, Colorado, United States, 2006.

[Veratech 2007] Veratech Aero Corportation, Single Rotor Phantom Sentinel, `www.veratech.aero/phantom.html` (2007, Aug).

[Vik and Fossen 2001] B. Vik and T. Fossen, A Nonlinear Observer for GPS and INS Integration, In *Proc 40th IEEE Conference on Decision and Control*, 2001.

[Wagner 1925] H. Wagner, Über die Entstehung des Dynamishen Auftriebes von Tragflüeln, In *Z. f. a. M. M.*, Bd. 5, Heft 1, S. 17-35, 1925.

[Wang 2005] Z. Wang, Dissecting Insect Flight, In *Annual Review of Fluid Mechanics*, Vol. 37, 2005.

[Waslander *et al* 2005] S. Waslander, G. Hoffmann, J. Jang and C. Tomlin, Multi-Agent Quadrotor Testbed Control Design: Integral Sliding Mode vs. Reinforcement Learning, In *Proc. IEEE/RSJ International Conference on Intelligent Robots and Systems*, Edmonton, Canada, 2005.

[Wells 2004] V. Wells, Propeller, `www.eas.asu.edu/~harvee/papers/propeller.pdf` (2004, Aug).

[Wen and Kreutz-Delgado 1991] J. Wen and K. Kreutz-Delgado, The Attitude Control Problem, In *IEEE Transactions on Automatic Control*, Vol. 36, No. 10, 1991.

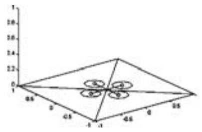

[Wie *et al* 1989] B. Wie, H. Weiss and A. Arapostathis, Quaternion Feedback Regulator for Spacecraft Eigenaxis Rotation, In *AIAA Journal of Guidance and Control*, 1989, Vol. 12, No. 3, 1989.

[Winchester 2005] J. Winchester, *X-Planes and Prototypes*, Amber Books, London, United Kingdom, 2005.

[Yang *et al* 2000] Z. Yang, L. Sankar, M. Smith and O. Bauchau, Recent Improvements to a Hybrid Method for Rotors in Forward Flight, In *Proc. Aerospace Sciences Meeting and Exhibit*, Reno, Nevada, United States, 2000.

[Yassini and Syrovy 2002] S. Yassini and G. Syrovy, Advanced Tiltrotor Technology VTOL Aircraft With a Single Rotor, In *Aircraft Technology, Integration, and Operations*, Los Angeles, United States, 2002.

[Young *et al* 2002] L.A. Young, E.W. Aiken, J.L. Johnson, R. Demblewski, J. Andrews and J. Klem, New Concepts and Perspectives on Micro-Rotorcraft and Small Autonomous Rotary-Wing Vehicles, Ames Research Center, Moffett Field, California, 2002.